A REMOTE ANALYSIS OF THE LUNAR LANDSCAPE

A DISSERTATION SUBMITTED TO THE GRADUATE DIVISION OF THE UNIVERSITY OF HAWAIʻI AT MĀNOA IN PARTIAL FULFILLMENT OF THE REQUIREMENTS FOR THE DEGREE OF

DOCTOR OF PHILOSOPHY

IN

GEOLOGY AND GEOPHYSICS

DECEMBER 2014

By

David Trang

Dissertation Committee:

Jeffery J. Gillis-Davis, Chairperson
Paul G. Lucey
B. Ray Hawke
Scott K. Rowland
Michael C. Liu

Keywords: Moon, Lunar Surface, Lunar Geomorphology, Lunar Volcanism, Impact Cratering, Near-Infrared Spectroscopy, Lunar Remote Sensing

ACKNOWLEDGEMENTS

First and foremost, I would like to thank Jeff Gills-Davis for being an amazing advisor, mentor, teacher, and father-like figure. Jeff always listened and understood my frustrations in graduate school. He also dealt with my spontaneous reports and updates of my progress throughout the years. His advice and suggestions in both academic and personal situations were always helpful.

I would also like to give a big thank you to Ed Scott and Jeff Taylor for helping me reverse my decision due to unexpected circumstances with SUNY-Buffalo. They immediately helped me find my place at the University of Hawai‘i at Mānoa. I would not have been here without them.

I would not have made it this far if it wasn’t for my qualifying, comprehensive, and dissertation committee members, which included Steve Martel, James Foster, Scott Rowland, and Michael Liu. Most of all, I would like to thank my co-advisors, B. Ray Hawke and Paul Lucey. Not only did they give great suggestions and advice on my projects, they also encouraged me on my tough days and helped pick me up mentally. I will never forget the seven topics Paul gave me for my comprehensive exam, in which I had to write a 2000 word paper for each topic over a 3.5-month period. I gained so much from this study, such as becoming a faster writer and learning to catch up in a topic over 1.5 weeks. Also, B. Ray’s stories about lunar science and the Apollo missions have always been a pleasure to listen to. These stories not only cover the publications, but the background thinking from the authors.

My knowledge of both planetary science and geology was expanded in part to Gary Huss, Julia Hammer, Mike Garcia, John Mahoney, Eric Gaidos, Paul Wessel, Peter Englert, Sasha Krot, Barbara Bruno, Michele Guannel, and Sarah Sherman, the Department of Geology and Geophysics and the Hawai‘i Institute of Geophysics and Planetology. They shared their knowledge and their expertise of their field, which I continuously found useful even in the most unexpected places.

I would also like to thank Ethan Costner and Eric Pilger for their technical support. I would also like to thank Brooks Bays for his illustration expertise.

Additionally, I would like to thank Vi Nakahara, Rena Lefevre, and Leona Anthony for helping me settle at the University and dealing with my administrative paperwork.

I would also like to thank collaborators, Josh Cahill, Joe Boyce, Myriam Lemelin, Elyse Iseke, Rachel Klima, Peter Isaacson, Rebecca Ghent, and Tom Giguere, have shared their knowledge and expertise and helped improve my manuscripts and projects.

I would like to thank the various NASA teams on the Lunar Reconnaissance Orbiter, in particular the Mini-RF team (Wes Patterson, Catherine Neish, Brad Thomson, Lynn Carter, Ben Bussey, and Paul Spudis) for including me in their discussions, meetings, and offering suggestions on my various projects. I would also like to thank people from the LROC team including Sam Lawrence, Julie Stopar, Tom Giguere, and Mark Robinson and the Diviner team, including Paul Haynes, and Josh Bandfield. I would like to thank, Junichi Hayamara, from the Kaguya team for teaching me how to obtain the wonderful Kaguya data sets. Also, I would also like to thank Eugenie Song for her help in retrieving Diviner and Kaguya data and convincing me to learn DaVinci.

There are many young scientists within the University of Hawai‘i who I would like to thank for academic advice and most importantly, their support, which include but not limited to Carolyn Parcheta, Alice Colman, Kimberly Aller, Sarah Crites, Myriam Telus, Ryan Ogliore, Manavi Jadhav, Emily First, Elise Rumpf, Matt Markley, Patrick Gasda, Christie Jilly, Laura Corley, Chris Hamilton.

Also there are researchers I would like to thank who are outside the University of Hawai‘i, especially Casey Lisse, Catherine Elder, Christian Schrader, Alexandra Farrell and Lillian Ostrach, for their encouragement and support. Also, I would like to thank Michael Poland who continued to teach me and support me even after I left the Hawaiian Volcano Observatory.

I would also like to thank May Salcedo, Cody Parmley, and others who worked at Coffee Bean and Tea Leaf Mānoa for their performance-enhancing tea latte and letting me work there when I needed to be away from the office.

Finally, I would like to thank my family for their support and helping me achieve this dream. I would to thank my best friend, Heather Kaluna, who has been there for me since our undergraduate days at University of Hawai‘i at Hilo. Most importantly, I would like to thank Alyssa Anderson. She supported and listened to me on my final months of my graduate studies and has always been there for me even on the hardest days.

Lastly, I would like to thank NASA LRO Mini-RF Participating Scientist for their financial support.

ABSTRACT

The integration of remote sensing data sets is important to producing accurate interpretations of geomorphological features on the lunar surface. Studies of the surface can reveal the geological history of the Moon and Earth, provide key observations to the early Solar System, assist in refining surface process models, and find important resources for future exploration. The dissertation goals are to advance current remote sensing tools and techniques and use new global data sets and products from Kaguya and the Lunar Reconnaissance Orbiter missions to better understand impact craters and volcanic features. We improved remote sensing tools by characterizing the optical properties of olivine and pyroxene and producing a technique that uses crater degradation state to determine the crater age. We used these tools along with the new data sets and derived products to understand the changes in crater morphology with time, determine the origin of concentric craters, and classify localized pyroclastic deposits based upon physical and compositional properties. From these projects, we successfully modeled the optical properties of olivine and pyroxene by using the Modified Gaussian Model. Also, we calibrated the degree of freshness scale to absolute model ages. In studying lunar geomorphology, we deduced that igneous intrusions underneath small craters (<15 km in diameter) are likely to produce concentric craters. Finally, we found a relationship between surface rock abundance, glass proportion and maximum deposit thickness of localized pyroclastic deposits, which we used to categorize these deposits into four groups.

TABLE OF CONTENTS

TABLE OF TABLES

TABLE OF FIGURES

LIST OF ABBREVIATIONS AND SYMBOLS

Abbreviation/Symbols	Definition
A	Absolute Model Age
C	Continuum or cumulative crater per unit area
CPR	Circular Polarization Ratio
D	Crater diameter
Diam.	Diameter
Di	Diopside
DTM	Digital Terrain Model
E	Error magnitude in degree of freshness
En	Enstatite
Err.	Error
F	Corrected degree of freshness
f	Observed degree of freshness
Fa	Fayalite
Fo	Forsterite
Fs	Ferrosilite
G	Gaussian
g	Gaussian
GRAIL	Gravity Recovery and Interior Laboratory
H	Density Scale Height
HOSERLab	Hyperspectral Optical Sensing for Extraterrestrial Reconnaissance Laboratory
k	Imaginary index of refraction
Lat.	Latitude
LOLA	Lunar Orbiter Laser Altimeter
Long.	Longitude
LSCC	Lunar Spectral Characterization Consortium
LRO	Lunar Reconnaissance Orbiter
LROC	Lunar Reconnaissance Orbiter Camera

M^3	Moon Mineralogy Mapper
MESSENGER	Mercury Surface Space Environment Geochemistry and Ranging
MDIS	Mercury Dual Imaging System
Mg#	(MgO/[FeO+MgO]) • 100
MGM	Modified Gaussian Model
MI	Multispectral Imager
Mini-RF	Miniature Radio Frequency
Mn'	$(Mn^{2+}/[Fe^{2+}+Mg^{2+}+Mn^{2+}]) \bullet 100$
n	Real index of refraction
n	Index of Refraction
n.d.	Not determined
NAC	Narrow Angle Camera
NEAR	Near Earth Asteroid Rendezvous
No.	Number
R_D	Ratio of concentric ridge diameter to parent crater diameter
RELAB	Reflectance Experiment Laboratory
s	Absorption strength
SELENE	Selenological and Engineering Explorer (Kaguya)
Std. Dev.	Standard Deviation
TC	Terrain Camera
tr.	Trace amount
USGS	United States Geological Survey
UV	Ultraviolet
UVVIS	Ultraviolet-Visible
vol.%	Volume Percent
WAC	Wide Angle Camera
Wo	Wollastonite
wt.%	Weight Percent

ΔH	Density scale height difference between background and pyroclastic deposit
λ	Wavelength
μ	Absorption center
ν	Energy
σ	Absorption width or standard deviation

CHAPTER 1

INTRODUCTION

1.1 Remote Sensing of the Lunar Surface

This dissertation focuses on integrating remote sensing data sets to produce accurate interpretations of geomorphological features on the lunar surface. There are two reasons to integrate remote sensing data sets. First, a diverse set of remote sensing data would reveal the various properties of a geomorphological feature or surface unit. Accordingly, a detailed model must incorporate the wide range of observations. Second, measurements of a dimension or property of a geomorphological feature with different techniques could reinforce confidence in the observations. In this dissertation, we use the new data sets (e.g., albedo maps, radar backscatter, surface temperature maps) and derived products (e.g., mineral maps, digital terrain models (DTM), surface rock abundance map, circular polarization ratio maps) from recent missions (i.e., Lunar Reconnaissance Orbiter and Kaguya) to study impact craters and pyroclastic deposits.

After a hiatus of missions to the Moon in the 1980s, exploration has revitalized starting with the Clementine mission, a United States Department of Defense mission. The Clementine mission resulted in diverse first-of-its-kind global data sets, such as topographic and gravity [*Zuber et al.*, 1994] maps. From the Clementine data sets, several workers derived new data products like, the color ratio [*Pieters et al.*, 1994], FeO, TiO_2 abundance [*Lucey et al.*, 2000b], optical maturity [*Lucey et al.,* 2000a], and mineral maps [*Lucey*, 2004]. Studies of these various data sets and derived products began to reveal the composition and shape of the Moon. One of these investigations studied the bistatic radar data of the poles, which led to the discovery of water ice [*Nozette et al.*, 1996]. Later, NASA launched Lunar Prospector; this mission resulted in various elemental abundance maps including the thorium abundance maps. Studies of the thorium maps led to identifying the compositional diversity of the crust [*Jolliff et al.*, 2000] and the origin of red spots [*Hagerty et al.*, 2006]. Afterward, missions such as the Lunar Reconnaissance Orbiter (LRO), Kaguya, Chandraayan-1, and GRAIL (Gravity Recovery and Interior Laboratory) provided new or improved data sets. These new data sets contributed to the identification of skylights on lava tubes [*Haruyama et al.*, 2009], the detection of spinel [*Pieters*

et al., 2011], the presence of high-silica volcanism [*Glotch et al.*, 2010; 2011; *Jolliff et al.*, 2011], the improved descriptions of impact melt [*Bray et al.*, 2010; *Carter et al.*, 2012; *Stopar et al.*, 2014], and the existence of a large igneous rift [*Andrews-Hanna et al.*, 2014]. As a result of these missions, there is an assortment of data sets that measures different properties of the surface and interior.

1.2 The Importance of Studying Lunar Geomorphology and Stratigraphy

Studying the lunar surface can reveal the geological history of the Moon and Earth-Moon system, provide key observations to the early Solar System, and assist in refining models of surface processes. On Earth, plate tectonics and atmospheric weathering erased the first billion years of its geological history. The Moon, on the other hand, has continued to keep a geological record for the past four billion years. A crucial discovery from studying the geological history of the Moon is the impact flux for the Earth-Moon system. Analysis of the impactor flux have provided insight of potential present and future hazards from impacts.

Another importance is that studies of the surface may assist in understanding the early Solar System. For example, the interpretations from radiometric dating of several impact basins hypothesized the Late Heavy Bombardment event [*Tera et al.*, 1974]. This event corresponds to a spike in the impactor flux, which is possibly related to the repositioning of planets [e.g., *Levison et al.*, 2001; *Gomes et al.*, 2005]. Stratigraphic analysis cannot verify the existence of the Late Heavy Bombardment, but it can determine the oldest basin [*Wilhelms*, 1987]. A future sample-return mission to the oldest basin could verify the Late Heavy Bombardment hypothesis [*Jolliff et al.*, 2010].

Features on the lunar surface could test current Earth-based models of surface processes because of the contrasting environment between the Earth and the Moon (e.g., gravity). For instance, *McGetchin and Head* [1973] predicted through modeling that the Moon would produce low-rimmed pyroclastic rings instead of steeper cone-like structures because the lunar environment lacks an atmosphere and has a lower gravitational acceleration than Earth. In return, inaccuracies in the predictions based upon observations of localized pyroclastic deposits could indicate the need in amending the model.

An additional reason to study the surface is to prepare for future exploration and human colonization. Future explorers will need to know the types of resources that are available, locate the potential resources, and assess the accessibility of the resources to build a self-sustaining

settlement. Furthermore, understanding surface processes could help locate areas and features containing useful materials.

1.2.1 Impact Cratering

Impact cratering is a ubiquitous process that occurs on all planetary bodies. The impacting process to form a simple bowl-shaped crater is well understood (i.e., compositionally homogeneous projectile and a compositionally homogenous rigid target). However, the impact crater geometry sometimes deviates from the "ideal" bowl-shaped crater due to the environmental conditions and surface processes that affect them. Therefore, impact craters are a great test to identify the crustal composition and surface processes of a planetary body. In fact, there are some unique crater classes that exist on other planetary bodies, but absent on the Moon. The absence of these other crater classes is because the Moon has a different environment to other planetary bodies (e.g., different surface processes, reduced gravity, no atmosphere, contrasting crustal composition). Examples of crater classes that are absent from the Moon include, central-pit craters (Mars, Callisto, and Ganymede) [e.g., *Passey and Shoemaker*, 1982], pit-floor craters (Mercury) [*Gillis-Davis et al.*, 2009], and palimpsests (Ganymede) [e.g., *Croft*, 1983].

The dominant geomorphological feature on the surface is impact craters. Studying these numerous craters has significantly advanced current understanding of impact craters. Impact craters display an evolution of crater classes (e.g., simple, complex craters) with increasing crater diameter [e.g., *Wood and Andersson*, 1978; *Pike*, 1980; *Melosh*, 1989; *Baker et al.*, 2011] and age [e.g., *Pohn and Offield*, 1970; *Trask*, 1971]. In addition to these crater classes, other impact crater classes such as bench craters, doublet craters, floor-fractured craters, concentric craters, and primary crater chains, exemplify the importance of understanding the target and the projectile properties as well as post-impact processes [e.g., *Quaide and Oberbeck*, 1968; *Oberbeck*, 1973; *Schultz*, 1976a; *Wood*, 1978; *Melosh and Whitaker*, 1994].

1.2.2 Lunar Volcanism

Basaltic volcanism is a ubiquitous process that has occurred throughout the inner Solar System. Products from basaltic volcanism provide insight into the physical and compositional nature of the mantle as well as the environmental properties of the surface [*Basaltic Volcanism Study Project*, 1981].

The maria comprises of basaltic lava, which covers about 17% of the lunar surface, mostly on the nearside [*Head*, 1976]. Features within the maria include a diversity of volcanic features such as, lava flows, sinuous rilles, domes, cones, and explosive deposits. Lava flows are identified in several ways, such as flow boundaries [*Schaber*, 1973; *Schaber et al.*, 1976], compositional differences [*Pieters,* 1978], age differences [e.g., *Heisinger et al.*, 2000; 2003; 2010], and radar backscatter [*Campbell et al.*, 2014]. *Haruyama et al.* [2009] found skylights, an indicator that lava traveled through lava tubes. Lava also traversed through long meandering channel, called sinuous rilles, which usually fades into the maria on one end and on the other end is a pit crater [*Greeley*, 1971]. Several workers found constructional features such as domes [*Guest and Murray*, 1976] and cones [*Head and Wilson*, 1979]. Studies noted the presence of pyroclastic deposits, which range in area from a few tens to thousands of square kilometers [e.g., *Gaddis et al.*, 2003].

1.3 Goals and Dissertation Structure

The overarching dissertation goals are to: 1) advance current remote sensing tools and techniques and 2) use new global data sets and products from Kaguya and the Lunar Reconnaissance Orbiter missions to better understand impact craters and volcanic features. Four projects compose this dissertation, which could be divided into two sections: Chapter 2 and 3 involve improving remote sensing tools for studying geomorphological features. Chapter 3, 4, and 5 concern the analyses and interpretations of geomorphological features. In particular, we set out to understand the degradation of craters with time, determine the origin of concentric craters, and classify localized pyroclastic deposits.

Chapter 2 and 3 pertain to the improvement of remote sensing tools. The primary objective in Chapter 2 is to model the optical properties of two common mafic minerals throughout the Solar System, olivine and pyroxene. Our model refinements may improve mineral maps [i.e., *Lucey*, 2004], which support works such as investigations of the lunar crust [e.g., *Lucey et al.*, 2014; *Lemelin et al.*, in prep].

Chapter 3 describes a calibration to link crater degradation states to absolute model ages. *Pohn and Offield* [1970] created a measurement system to determine the relative age of a crater based upon its degradation state. Their dating technique, however, only determined relative ages between craters. The primary objective is to establish a relationship between absolute model ages

through crater density measurements and the degradation states of 1–20 km in diameter craters. As a result, we provide a reconnaissance method of estimating ages of craters.

Chapters 3, 4, and 5 study three geomorphological features, degraded impact craters, concentric craters, and localized pyroclastic deposits. Chapter 3 uses the relationship between degradation states of craters and absolute model ages to describe the changes in morphology of impact craters with time. These descriptions could support future models of crater degradation.

In Chapter 4, we investigate the enigmatic lunar concentric crater. The interior of these craters exhibits a concentric topographic ring of an unknown origin. The primary objective is to examine the concentric crater properties and evaluate the origin of concentric craters through the method of multiple hypotheses.

Finally, Chapter 5 examines the properties of localized pyroclastic deposits. The primary objective is to characterize the volume and structure of localized pyroclastic deposits as well as the regolith and mineralogical properties. Analyses of these properties may shed light on the different types of localized pyroclastic deposits. Furthermore, the different types of pyroclastic deposits could hint at their unique origins. As a result of this study, future workers could use these observations to produce eruptive models for each pyroclastic deposit type [e.g., *Head and Wilson*, 1979] and evaluate their resource potential [e.g., *Hawke et al.*, 1990].

CHAPTER 2

NEAR-INFRARED OPTICAL CONSTANTS OF NATURALLY OCURRING OLIVINE AND SYNTHETIC PYROXENE AS A FUNCTION OF MINERAL COMPOSITION

Published: Trang, D., P. G. Lucey, J. J. Gillis-Davis, J. T. S. Cahill, R. L. Klima, and P. J. Isaacson (2013), Near-infrared optical constants of naturally occurring olivine and pyroxene as a function of mineral compositon, J. Geophys. Res. Planets, 118, doi:10.1002/jgre.20072

Abstract – Radiative transfer theory will assist in determining olivine and pyroxene proportions and compositions from the surface of a planetary body composed of intimately mixed minerals. In order to use radiative transfer techniques, the model requires the optical constants of olivine and pyroxene. Optical constants are parameters that describe the degree light is absorbed (k) and refracted (n) in a medium. Here, we only parameterize k in the near-infrared from 0.6–2.5 μm of natural olivine as a function of forsterite number and synthetic pyroxene with respect to wollastonite and ferrosilite number. In contrast to previous work, this study is an improvement on previous work because we have a diverse and larger sample size leading to robust optical parameters. Additionally, we characterize each k-spectrum with the modified Gaussian model (MGM). MGM is a physically realistic model of near-infrared absorptions due to electronic transitions. In each spectrum, we model each absorption and continuum with Gaussians and an inverse of a linear function, respectively. We find that our fitting routine characterizes the olivine and pyroxene k-spectra in a robust and consistent manner. Then, we use regression analysis to characterize each parameter of the Gaussians and the continuum as a function of mineral composition. The developed optical parameters from this work will allow calculations of mineral proportions and compositions on planetary surfaces with use of data from missions such as, Dawn, MESSENGER, SELENE, and Chandrayaan-1.

2.1 Introduction

Characterization of common mafic mineral proportions/composition of the surface of a planetary surface is often a critical first step for accurate petrologic characterization and analysis of igneous surfaces. Specifically, quantifying the mineral proportions and composition of a surface can determine its lithology, how petrologically and chemically evolved the rock is, the likely compositions of its primary melt, and the conditions in which this melt crystallized [*Basaltic Volcanism Study Project*, 1981]. From here, petrologic experiments and models developed for igneous processes on Earth can be applied to physically test or simulate the potential crystallization path of a rock and its origin [e.g., *Ghiorso and Sack*, 1995; *Longhi*, 1991]. On Earth, samples of igneous rocks are collected from the field for laboratory analysis. However, when celestial body sampling is limited or nonexistent, remotely sensed spectra are the best way to access the global surface composition of a body.

Spectroscopic tools have successfully detected the presence of olivine and pyroxene in the near infrared on bodies such as the Moon [e.g., *McCord and Johnson*, 1970; *Pieters*, 1982] and asteroids [e.g., *McCord and Gaffey*, 1974]. Radiative transfer theory is a common method used to interpret remotely sensed spectra of surfaces composed of intimately mixed minerals. This method allows a planetary spectrum to be modeled on the basis of optical properties determined for suspected constituents and assumptions regarding the physical state of the surface. Initial applications of radiative transfer theory, based upon work from Bruce Hapke [e.g., *Hapke,* 1981; 1993], to planetary spectra yield encouraging results [e.g., *Harker et al.*, 2002; *Birlan et al.*, 2007; *Cahill et al.*, 2010, *Emery et al.*, 2011]. The accuracy of such models is limited by the quality of the inputs (i.e., optical constants). The presence of the mafic mineral groups (e.g., olivine and pyroxene), as evidence from spectra and samples, is ubiquitous on rocky planetary surfaces (e.g., Moon, Mars, and asteroids). Hence, optical properties of these minerals are required for 'Hapke' modeling of planetary spectra. Both iron-bearing olivine and pyroxene group minerals show continuous and strong variation in optical properties with composition and wavelength in the near infrared, so models must include this effect. These models will be valuable to past (e.g., Earth-based telescopic spectra, Clementine, Chandrayaan-1, SELENE, NEAR, Galileo) and current missions (e.g., MESSENGER, Dawn) to developing mineral maps of the surface of airless bodies. Here, we model the near-infrared optical constants of natural olivine and synthetic pyroxene as a function of mineral composition.

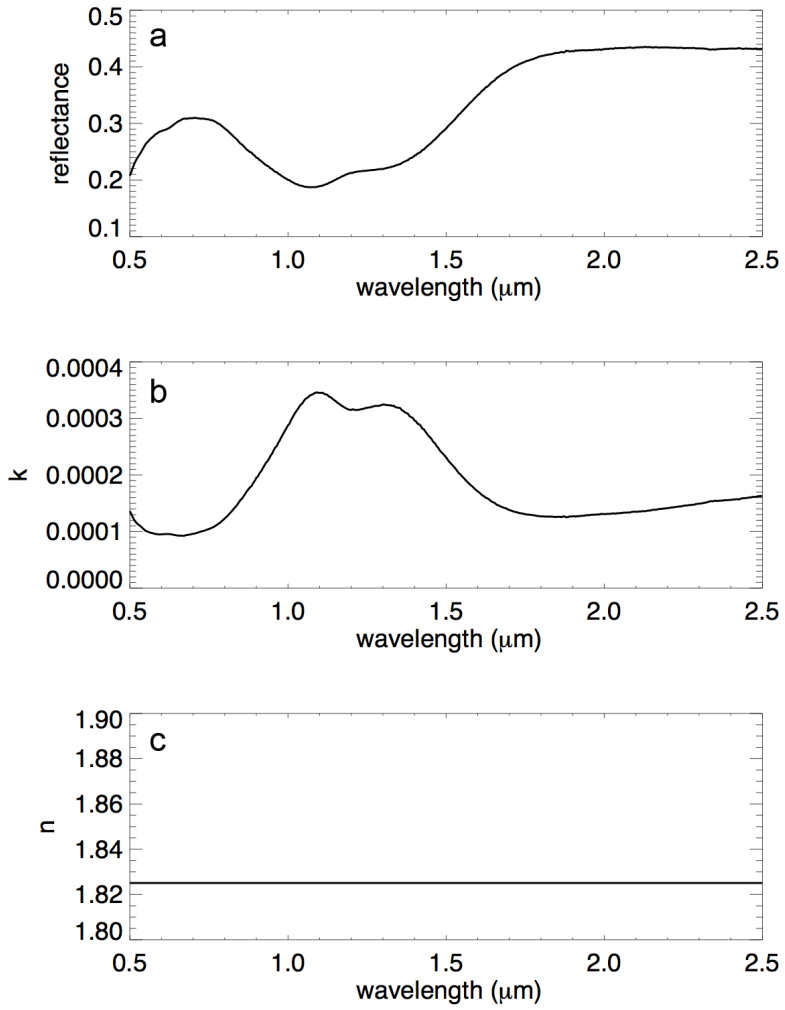

Figure 2.1: A comparison of the real and imaginary indices of refraction for olivine (Fo_{01}). Both *n* and *k* were calculated using techniques from *Lucey* [1998]. (a) reflectance, (b) *k*-, (c) and *n*-spectrum. When there is a strong absorption in reflectance, the efficiency of absorbing photons is large (*k*) at the same.

Optical constants are physical parameters that describe how electromagnetic radiation interacts with a medium [*Hapke*, 1993]. Quantitatively, the optical constants are comprised of two components: the real and imaginary part of the index of refraction (**n** = n – ik), where for transparent material, *n*, the real index of refraction, describes the degree light refracts in a material and *k*, the imaginary index of refraction, relates to how efficiently light is absorbed. For

silicate minerals, *n* is nearly constant in the visible and near-infrared portions of the electromagnetic spectrum (**Figure 2.1c)** [*Hiroi and Pieters*, 1994], whereas *k* varies with wavelength in this region of the spectrum and is manifested in reflectance spectra as absorption features (**Figure 2.1b)**. Greater values in *k* indicate photons are efficiently absorbed at that particular wavelength as a function of its crystallography and composition. On this basis, mineral proportion and composition is encoded within any given reflectance spectrum including of intimately mixed materials, which can be estimated using both Hapke modeling and a complete set of characterized optical constants of each individual mineral.

In this paper, we derive the optical constant parameters of olivine and pyroxene by first converting laboratory reflectance of natural olivines and synthetic pyroxenes to *k*-spectra using equations (1)–(8) found in *Lucey* [1998]. Next, we characterize the resulting *k*-spectra features with the modified Gaussian model (MGM). Specifically, each Gaussian approximates a spectral absorption feature by defining the band strength, width, and center. Then, we use regression analysis to determine how these parameters vary as a function of mineral composition. This project produces models needed to reconstruct the *k*-spectrum of olivine as a function of Fe^{2+} and Mg^{2+} proportion and mafic pyroxene at any relative proportions of Fe^{2+}, Mg^{2+}, and Ca^{2+}.

2.2 Background

2.2.1 Olivine

The absorption feature located at the one-micron wavelength in olivine is due to the interaction between electromagnetic radiation and the cation constituents housed within a well-defined crystal lattice [*Burns*, 1993]. The crystal structure of olivine includes two distinct distorted octahedral sites occupied by metal cations denoted M1 and M2, where M2 is larger than M1 [*Burns*, 1993]. The cations are usually Mg^{2+} and Fe^{2+}. The composition of olivine makes up a solid solution series $(Fe,Mg)_2SiO_4$, where the endmembers are Mg_2SiO_4 (forsterite or Fo) and Fe_2SiO_4 (fayalite or Fa). The proportions of Mg^{2+} and Fe^{2+} based upon molar concentration are quantitatively represented by Fo number, which is defined by $Fo=[Mg^{2+}/(Fe^{2+}+Mg^{2+})] \times 100$.

In reflectance spectra, olivine exhibits a broad absorption centered at one-micron [e.g., *Burns*, 1970; *Adams*, 1975; *Hazen*, 1977; *King and Ridley*, 1987; *Burns*, 1993; *Sunshine and Pieters*, 1998]. This broad absorption is a superposition of three absorption features centered near 0.9, 1.1, and 1.3 μm [e.g., *Burns*, 1970; *Sunshine and Pieters*, 1998]. The presence of the

three absorption features is due to the crystallographic sites containing Fe^{2+}, whereas Mg^{2+} does not produce near-infrared absorptions [see *Burns*, 1993].

As Fo content increases (increasing magnesium and decreasing iron content) in olivine, the 0.9-, 1.1-, and 1.3-μm absorptions shift towards shorter, higher-energy wavelengths [*Burns*, 1993; *Sunshine and Pieters*, 1998]. In general, these absorption shifts are related to the size of the crystallographic sites where Fe^{2+} enlarges the sites in contrast to Mg^{2+} [*Burns*, 1993]. From this concept, increasing the proportion of Fe^{2+} will shift the absorptions towards longer wavelengths.

Sunshine and Pieters [1998] showed that the 0.9- and 1.3-μm absorption band centers, widths, and strengths are coupled (see **Figure 4, 6, 7** in *Sunshine and Pieters* [1998]). This supports *Burns* [1993] interpretation that the two absorptions are due to Fe^{2+} in the M1 sites and the 1.1-μm absorption is from Fe^{2+} in the M2 sites.

2.2.2 Pyroxene

The crystal structure of pyroxene is more complex than olivine due to the additional interplay of Ca^{2+} with Fe^{2+} and Mg^{2+} among the crystallographic sites. The molar proportion of Mg^{2+}, Fe^{2+} and Ca^{2+} in pyroxene is defined by the ferrosilite (Fs) and wollastonite number (Wo) respectively, where $Fs=[Fe^{2+}/(Ca^{2+}+Fe^{2+}+Mg^{2+})] \times 100$ and $Wo=[Ca^{2+}/(Ca^{2+}+Fe^{2+}+Mg^{2+})] \times 100$. The pyroxene structure forms a single chain of silica tetrahedral and cations occupy two crystallographic sites: a relatively symmetrical octahedral site, denoted M1, and a larger polyhedral site, M2 [*Burns*, 1993]. The size of the cation is important to their distribution between the M1 and M2 sites. Due to Ca^{2+} larger size than Fe^{2+} and Mg^{2+}, Ca^{2+} will dominantly occupy M2 sites. Any remaining M2 sites unoccupied by Ca^{2+} are preferentially filled with Fe^{2+}.

Similar to olivine, Fe^{2+} is the only cation directly responsible for near-infrared absorptions in pyroxene spectra [*Burns*, 1993], but Mg^{2+} and Ca^{2+} have indirect roles in affecting the overall characteristics. Placement of Fe^{2+} in either the M1 or the M2 sites will display unique absorptions and intensities at 1.0, 1.2, and 2.0 μm due to contrasting geometries of the sites [e.g., *Hazen et al.*, 1978; *Cloutis and Gaffey*, 1991; *Burns*, 1993; *Denevi et al.*, 2007; *Klima et al.*, 2007, 2011]. When Fe^{2+} is in the relatively symmetric M1 site, weak absorptions are displayed at 1.0 and 1.2 μm. In contrast, Fe^{2+} in the more distorted M2 sites produce prominent 1.0 and 2.0 μm absorptions. Notably, when Fe^{2+} is in both the M1 and M2 site, the 1.0-μm feature is a superposition of two absorptions, one from each site.

In addition, the absorption properties of the 1.0-, 1.2-, and 2.0-µm change with the proportions of various cation species and their distribution among the crystallographic sites [e.g., *Hazen et al.*, 1978; *Cloutis and Gaffey,* 1991; *Burns*, 1993; *Klima et al.*, 2011]. There are two general patterns: 1) Substitution of Mg^{2+} for Fe^{2+} or Fe^{2+} for Ca^{2+} will enlarge the crystallographic sites causing the absorption bands to shift toward longer wavelengths. 2) Increasing the Fe^{2+} proportion in either crystallographic site will strengthen the absorptions caused by those respective sites. For instance, substitution of Ca^{2+} for Fe^{2+} results in the 1.0- and 1.2-µm absorption centers shifting towards shorter wavelengths and strengthening of the 2.0-µm absorption band because Fe^{2+} are filling M2 sites that were occupied by Ca^{2+}. Also, substituting Mg^{2+} for Fe^{2+} will cause the 1.0- and 1.2-µm absorptions to shift towards longer wavelength.

Klima et al. [2011] observed that the 2.0-µm absorption band is an exception to the general patterns. In pyroxenes with $Wo_{<20}$, increasing the proportion of Ca^{2+} will result in a shift of the 2-µm absorption towards longer wavelengths. However, at $Wo_{>20}$, the 2.0-µm absorption center is constant at ~2.3 µm regardless of increasing portions of Ca^{2+} or Fe^{2+}. This lack of shift in the 2.0-µm band is related to the geometry of the crystallographic sites in these high-calcium pyroxenes [see *Klima et al.*, 2011].

2.2.3 Building on Previous Work

In previous work, *Lucey* [1998] characterized the optical constants of olivine using samples from *King and Ridley* [1987] and pyroxene from [*Cloutis*, 1985; *Cloutis et al.*, 1986, 1990a,b]. *Lucey* [1998] used a linear least-squares fit to model compositional variations in *k* at each measured wavelength from ~0.22 to 2.4 µm as a function of iron content. Consequently, this method resulted in over a hundred parameters that only define the spectrum at particular wavelengths. In this work, we fit a set of olivine and pyroxene spectra with Gaussians and regress the Gaussian parameters with respect to composition. Gaussian analysis has four advantages over the previous method: 1) A Gaussian is a physically realistic model that can accurately represent spectral manifestation of electronic transitions due to Fe^{2+} contained in the crystallographic sites. 2) Gaussian analysis uses fewer parameters to characterize an entire *k*-spectrum by an order of magnitude. 3) This method improves the signal to noise of the result. 4) Gaussians enable calculation of *k* at any arbitrary wavelength without resampling. We build upon *Denevi et al.* [2007]'s work by characterizing a larger and more diverse database of synthetic

pyroxene that better represents the Fe^{2+}-rich portion of the pyroxene quadrilateral. In section 5.2, we contrast our parameters of synthetic pyroxene to the parameters of *Denevi et al.* [2007].

2.3 Methods

2.3.1 Samples

In this study, we use samples from two suites, which contain a large compositional range and several available diffuse bidirectional reflectance spectra. Our olivine spectra were collected at the NASA/Keck Reflectance Experiment LABoratory (RELAB) at Brown University [*Pieters*, 1983] and the United States Geological Survey (USGS) Library [*Clark et al.*, 2007]. In the USGS olivine samples, the composition is well distributed along the solid solution and covers the entire range. In addition, we model the olivine spectra from RELAB as a comparison to the USGS spectra and also to increase the overall sample size. Also, we choose to model the synthetic pyroxene spectral data, also collected at RELAB because of their larger compositional coverage of the pyroxene quadrilateral relative to the work by *Denevi et al.* [2007]. An increase in the compositional range will result in improved accuracy of current pyroxene optical parameters.

2.3.1.1 Naturally-Occurring Olivines

The RELAB data set consists of reflectance spectra measured by E. A. Cloutis and J. M. Sunshine with their compositions as well as minimum and maximum sieve fractions reported in **Table A.1**. Sample descriptions can be found in *Sunshine and Pieters* [1998] and the University of Winnipeg HOSERLab website (http://psf.uwinnipeg.ca/Home.html). For USGS contributed spectra, sample descriptions are found in *Hunt et al.* [1973], *Salisbury et al.* [1987], and *King and Ridley* [1987]. Major oxide compositions as well as minimum and maximum sieve fractions for the USGS olivine samples are also reported in **Table A.1**.

The RELAB olivine data set includes 31 spectra with 19 compositionally unique samples that span between $Fo_{0.1}$ to $Fo_{96.9}$ (**Figure 2.2a**). These spectral data were collected at RELAB with 0° emergence and 30° incidence angles. The spectral range of these reflectance spectra is from about 0.3 to 2.6 μm with measurements at 5 nm intervals. Only five of the 31 samples have $Fo_{<80}$. The sieve fraction of each sample was either <45 or 45–90 μm.

The USGS olivine data set contains 17 spectra. The compositions of the samples range between Fo_{11} to Fo_{92} (**Figure 2.2a**); seven of the samples have $Fo_{<80}$. This data set covers a wider range of iron content than those of the RELAB samples. The iron-rich olivine samples (e.g.,

$Fo_{<66}$) from the Kiglipait intrusion in Labrador, Canada were sieved to <60 µm [*King and Ridley*, 1987]. Other olivines with $Fo_{>66}$ are derived from areas including Papakōlea (Green Sand Beach) on Hawai‘i; Twin Sister Peak, Washington; Arizona; and Chavira Mine, Kamargo, Chihuahua, Mexico (**Table A.1**). Some samples feature more than one range of sieve sizes. All of these USGS sample spectra were acquired using the Beckman double-beam spectrometer at the United States Geological Survey (USGS) with a spectral range from ~0.22 µm to 2.4 µm and a spectral resolution of ~15 nm. We omit one of the spectra due to an oversaturation in the reflectance spectrum.

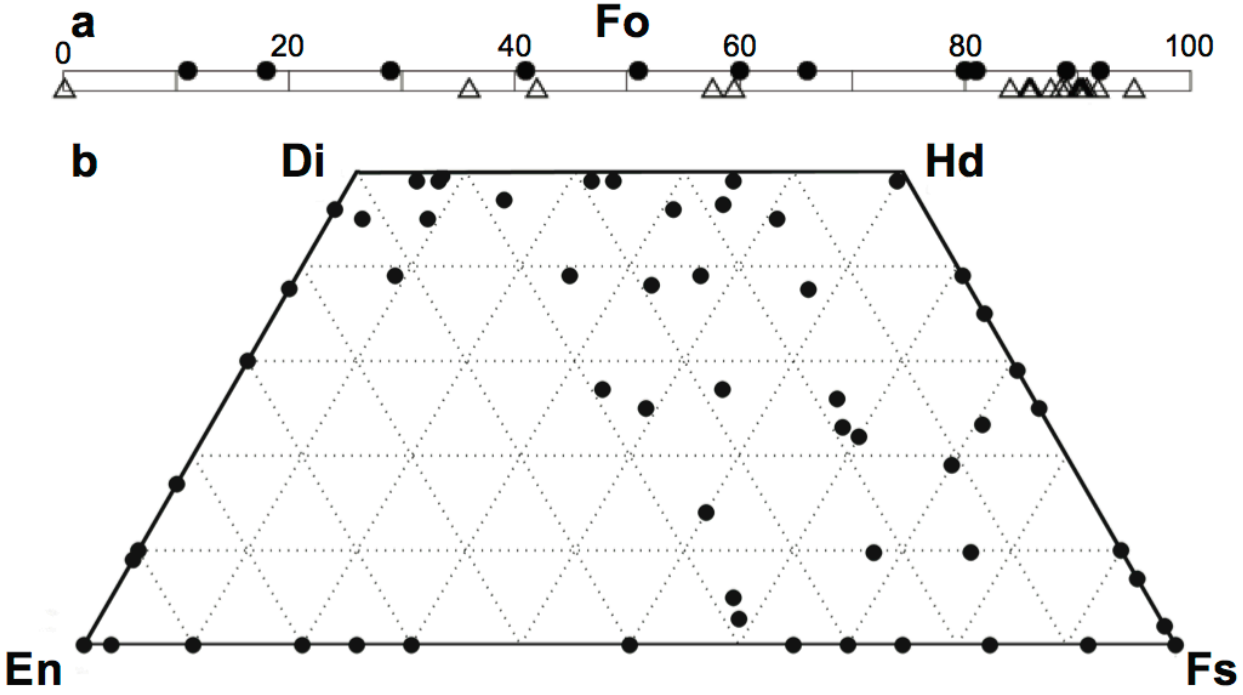

Figure 2.2: (a) The Forsterite (Fo) number of the USGS (solid circles) and RELAB (open triangle) olivine samples. (b) The composition of the synthetic pyroxenes on a pyroxene quadrilateral, where En (enstatite) is the magnesium-rich endmember, Fs (ferrosilite) is the iron-rich endmember, Di (diopside) is the magnesium-calcium-rich endmember, and Hd (hedenbergite) is the iron-calcium-rich endmember. One sample is missing because it is considered a pyroxenoid ($En_{00}Fs_{49}Wo_{51}$).

2.3.1.2 Synthetic Pyroxenes

Synthetic pyroxene samples used in this study were synthesized by D. H. Lindsley and others between 1972 and 2007; the experimental procedure used is given by *Turnock et al.*

[1973]. The starting compositions of these pyroxenes were synthesized from reagent-grade chemicals and five methods were employed to produce the variety of compositions available and also to avoid crystallization of unwanted pyroxenoids and olivines. Additionally, iron is maintained in the ferrous state (Fe^{2+}). To validate the synthetic pyroxene compositions, *Turnock et al.* [1973] examined the samples with X-ray diffraction. Later, composition and its spatial homogeneity within single grain samples were re-evaluated by *Klima et al.* [2007, 2011] using the CAMECA SX-100 electron probe microanalyzer at Brown University (**Table A.2**). *Klima et al.* [2007, 2011] sieved the samples to <45 μm and obtained the spectra using the bidirectional spectrometer at RELAB with incidence and emission angles of 30° and 0°, respectively. The data are composed of pyroxene compositions between the enstatite-diopside, enstatite-ferrosilite, and ferrosilite-hedenbergite solid solutions and also pyroxene with either $Fs_{>30}$ or $Wo_{>35}$ (**Figure 2.2b**). One of our samples (not shown in **Figure 2.2**) is actually classified as a pyroxenoid based upon its composition (Wo_{51}). Reflectance measurements have a spectral range of 0.3 to 2.6 nm and spectral sampling resolution of 5 nm.

2.3.2 Reflectance- to k-spectra conversion

Olivine and pyroxene diffuse bidirectional laboratory reflectance spectra are converted to *k*-spectra using equations (1)–(8) from *Lucey* [1998] based upon the work of *Hapke* [1981]. This conversion requires knowledge of the grain size of the samples. However, the range of grain sizes in these samples is based upon the maximum and minimum sieve diameters. *Lucey* [1998] found that computing the mean of the largest and smallest sieve diameter adequately represented the sample as a whole. From this, we use 22.5 μm as the grain size for the synthetic pyroxene samples and for olivine the computed grain sizes are found in **Table A.1**.

2.3.3 Fitting k-spectra with the Modified Gaussian Model

We fit our *k*-spectra with the Modified Gaussian Model (MGM), a type of Gaussian analysis [*Sunshine et al.*, 1990]. In contrast to previous Gaussian analyses [e.g., *Roush and Singer*, 1986], MGM is a physically realistic model because it can account for the shape of the absorption, which is due to thermal effects on the crystallographic sites [*Sunshine et al.*, 1990]. In this analysis, absorptions are superimposed on a background referred to as the continuum in reflectance. Our analysis includes fitting of the continuum background and the Gaussians appropriate to the mineral under analysis. Finally, we regress the derived Gaussian and continuum parameters against mineral composition.

Each absorption is modeled with a Gaussian based upon the MGM method, which is defined by,

$$g(\upsilon) = s \cdot \exp\left(\frac{-(\upsilon^n - \mu^n)^2}{2\sigma^2}\right) \quad (2.1)$$

where s is the Gaussian strength, μ is the center, σ is the width, and υ is in energy. The exponent, n (not to be confused with the real index of refraction), controls the symmetry of the Gaussian or the slopes of the wings of the Gaussian. *Sunshine et al.* [1990] found that a value of n equal to -1 is an optimal fit for a spectrum in units of energy. The units in our model are wavelength, inversely proportional to energy. Hence, our value of n is equal to 1; mathematically, the MGM function is identical to the traditional Gaussian, but with wavelength rather than energy as the variable. In this paper, Gaussian parameters are defined with respect to equation (2).

$$g(\lambda) = s \cdot \exp\left(\frac{-(\lambda - \mu)^2}{2\sigma^2}\right). \quad (2.2)$$

Some authors have hypothesized that the continuum represents specular reflectance (photons that reflect, but never penetrated the crystals) [*Huguenin and Jones*, 1986] or a broad ultraviolet absorption [*Clark*, 1999; *Denevi et al.*, 2007]. The continuum functional form varies based upon the units used for interpretation (i.e., energy or wavelength). In energy space, the continuum is linear, but is the inverse of a linear function in wavelength space [*Sunshine et al.*, 1990; *Denevi et al.*, 2007].

The continua of olivine and pyroxene *k*-spectra are modeled with a line,

$$C(\lambda) = y_{C1} + \left(\frac{y_{C2} - y_{C1}}{1/\lambda_{C2} - 1/\lambda_{C1}}\right) \cdot \left(1/\lambda - 1/\lambda_{C1}\right) \quad (2.3)$$

The two points (λ_{C1},y_{C1}) and (λ_{C2},y_{C2}), where λ is wavelength and y is k, are used to define the continuum. These points must be adjacent to and outside of any observed absorption features. Specifically, these points are chosen from k minima between 0.6–0.9 μm and 1.3–2.0 μm for olivine and between 0.5–0.7 μm and 1.85–2.0 μm for pyroxene. Instead of tabulating the (λ_{C1},y_{C1}) and (λ_{C2},y_{C2}) used to fit the continuum for each *k*-spectrum, we consistently measure the continuum based upon two discrete points, 0.6 and 1.85 μm for olivine and 0.6 and 1.3 μm for pyroxene.

We characterize *k*-spectra of olivine and pyroxene using equation (2.2) for the absorptions and (2.3) for the continuum. The fitting routine consists of Gaussians superimposed upon the continuum with initial guesses of the Gaussian parameters. We initially place each

absorption at their respective position (e.g., 1.0-µm absorption positioned at 1.0 µm) or near the closest local *k* maximum. The initial input for the absorption widths and strengths are orders of magnitude smaller than the resulting strengths and widths. The goal of this fitting routine is to minimize the mean and median of the absolute differences between the measured *k*-spectrum and the MGM model within the spectral range of interest. The spectral region of interest for olivine is between 0.60 to 1.85 µm. As for pyroxene, we isolate and fit the 1.0 µm and 2.0 µm region to simplify and expedite the fitting routine. The two spectral regions of interest are: 0.7 µm to the local *k* minimum and the local *k* minimum to 2.6 µm, where the local *k* minimum is located between the 1.2 and 2.0 µm. Then, an iterative fitting routine freely adjusts the Gaussian parameters based upon a robust manual search through the parameter space until the mean and median absolute difference is minimized.

2.3.3.1 MGM modeling of Olivine k-spectra

In olivine *k*-spectra, we have three absorptions that are centered near 0.9, 1.1, and 1.3 µm. Per *Sunshine and Pieters* [1998], the 0.9- and 1.3-µm absorptions are strongly coupled in reflectance spectra and vary proportionally in absorption strength, width, and center. To ensure that the coupling is evident in *k*-spectra, we examine preliminary results from *Trang et al.* [2011], in which it was not assumed that the 0.9- and 1.3-µm absorptions were coupled. In the preliminary analyses, we normalize the strengths and widths of all the absorptions to the 1.3-µm absorption. Regardless of Fo number, the strength of the 0.9-µm absorption relative to the strength of the 1.3-µm absorption is 0.46±0.11 and the width ratio between the two absorptions (width of 0.9-µm absorption/width of 1.3-µm absorption) is 0.85±0.07 (**Figure 2.3**). Additionally, the separation between the 0.9- and 1.3-µm band centers is constantly 0.30±0.03 µm. These proportionalities (e.g., relative strength, width, and band center separation) indicate that the two absorptions are coupled; similar to the coupling observed by *Sunshine and Pieters* [1998]. In this work, we couple the 0.9- and 1.3-µm absorptions in our MGM fit of *k*-spectra until it optimized. After optimization based upon coupling of the two Gaussians, we refine the model by allowing the two Gaussians to decouple and find a better fit.

2.3.3.2 MGM Modeling of Pyroxene k-spectra

For pyroxene, we use three to four absorptions to fit a *k*-spectrum. The three main absorptions of interest are centered at 1.0, 1.2, and 2.0 µm. Occasionally, in pyroxenes with $Wo_{>20}$, an additional Gaussian centered near 0.8 µm is required in order to prevent the 1.2-µm

absorption from becoming too wide and stretching across the 1.0-µm absorption from ~0.8 µm to ~1.2 µm. Physically, the 0.8-µm absorption may actually be part of a larger absorption 1.0-µm absorption. The 1.0-µm absorption is actually the superposition of two absorptions, one absorption from each crystallographic site. Attempting to model both 1.0-µm absorption features will result in a non-unique solution [*Klima et al.*, 2011]. Thus, we only use one Gaussian to represent the 1.0-µm feature and use a second Gaussian centered near the 0.8-µm to prevent the model from generating unrealistic solutions.

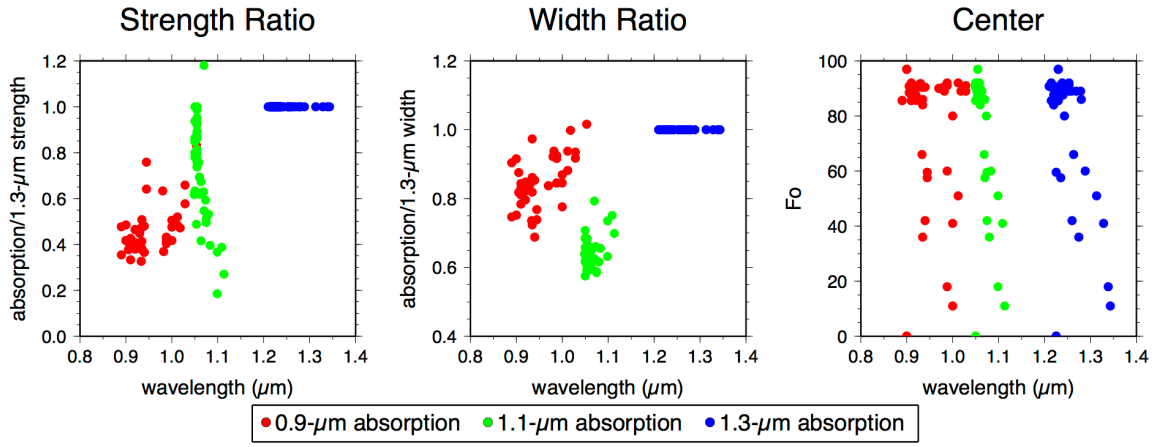

Figure 2.3: Preliminary fitting results for olivine from *Trang et al.* [2011] assumed no coupling between the 0.9- and 1.3-µm absorptions. Here, the width ratio of the 0.9- to 1.3-µm absorption is ~0.46 and the strength ratio of the same bands is 0.85. In addition, the 0.9- and 1.3-µm absorption centers are always separated by 0.30 µm. This proportionality suggests a coupling does exist in *k*-space and is similar to figures shown by *Sunshine and Pieters* [1998]. The modeled normalized strengths and the widths of the 0.9- and 1.1-µm absorptions appear similar to *Sunshine and Pieters* [1998]. However, the 0.9- to 1.3-µm displacement and the widths of the 1.1-µm absorption are different.

2.3.4 Optical Parameters as a Function of Mineral Composition

We regress each optical parameter to mineral composition in order to produce a model that accurately predicts the *k*-spectrum at any Fo number for olivine and for pyroxene, at any Fs number, but only for $Wo_{\leq 50}$. Only three main absorptions of olivine and pyroxene are modeled. Thus, we produce eleven parameters that characterize each *k*-spectrum (three parameters for each absorption and two parameters for the continuum). For each parameter, we use a least-squares

polynomial fit between Fo and each parameter in olivine. In contrast, pyroxene varies by two independent variables, Fs and Wo. Therefore, we apply a multi-linear regression between mineral composition and each parameter.

2.4 Results

2.4.1 Olivine

Figure 2.4 shows an example of the high-quality fit typical for our modeling of laboratory-derived *k*-spectra for olivine. In **Table A.3** and **Figure 2.5**, we report the MGM and continuum parameters as well as the mean and median absolute difference as the error. In some of our spectra, the continuum exhibits a negative slope (**Figure 2.4**), which results in negative *k* values at wavelengths shorter than the ultraviolet portion of the spectrum. Negative and positive sloped artifacts within this region typically occur when the minimum *k* values at the shortest continuum points are less than the longest continuum points; this is unavoidable. Regardless of which direction the continuum is realistically pointing, the slope is steeper towards shorter wavelengths beyond the visible. This region of the spectrum is not critical because most spacecraft spectral data are concentrated in the visible and near infrared; the region of the electromagnetic spectrum that our study models.

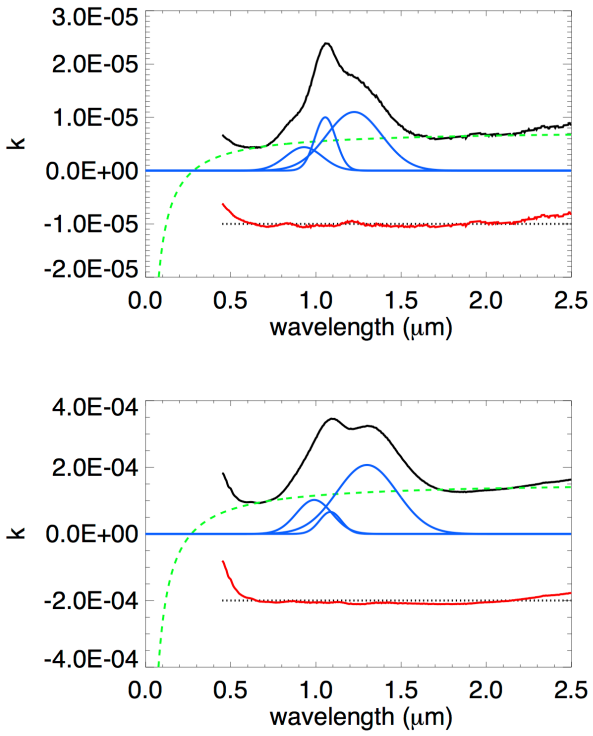

Figure 2.4: Model k-spectra fits for RELAB olivines with compositions $Fo_{96.9}$ (top) and $Fo_{0.01}$ (bottom). The solid black line indicates the measured k-spectrum, the dashed green line is the continuum, the solid blue lines are the Gaussians, and the solid red line is the residual or the difference between the measured k-spectrum and the modeled k-spectrum.

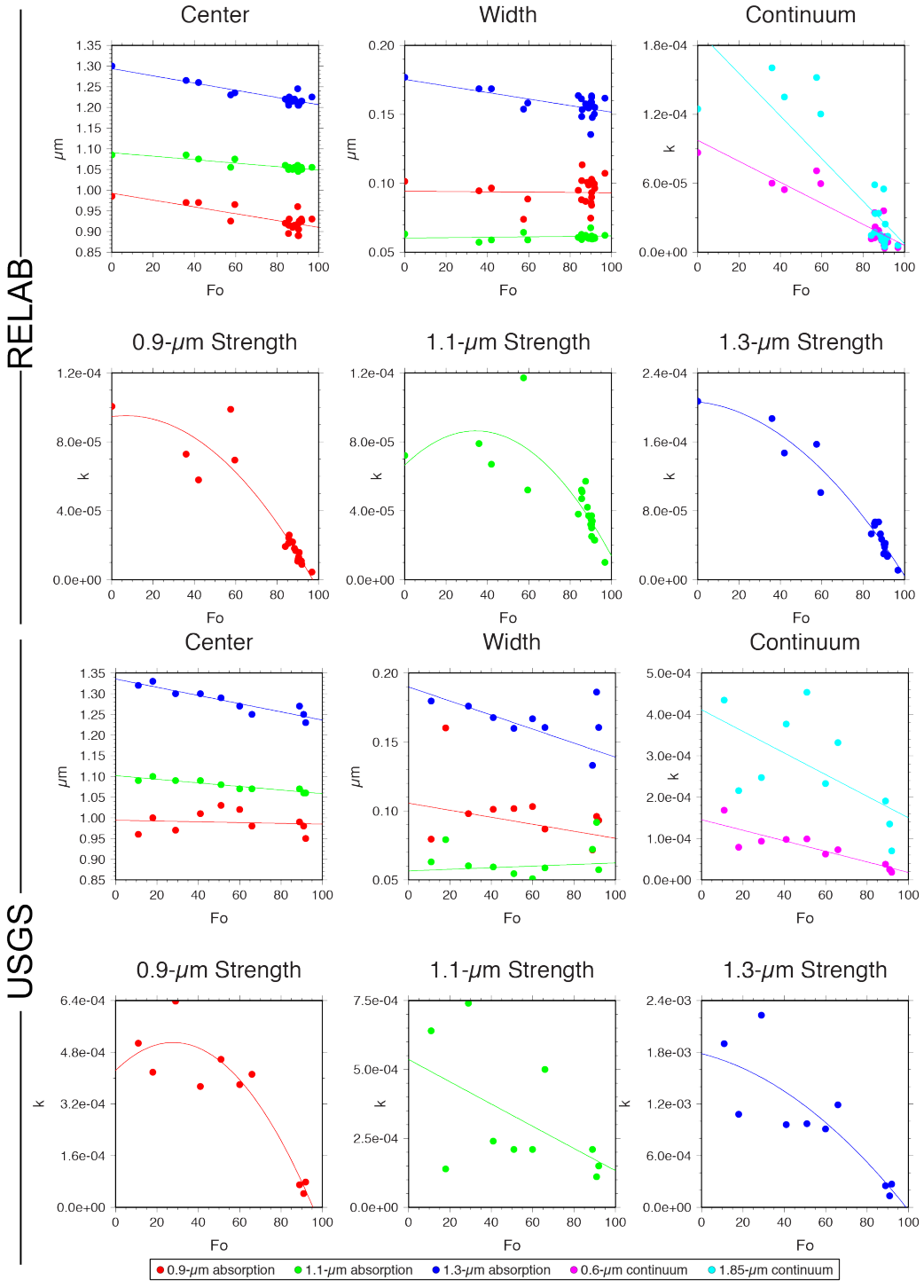

Figure 2.5: The results of the modeled fits for each optical parameter. Here, the parameters are shown relative to Fo number. The centers and widths of the absorptions and the 0.6- and 1.85-μm continuum points were regressed with a linear least-squares regression, but the strengths were regressed with a second-order least-squares fit.

We use a least-squares linear and polynomial fit for the USGS and RELAB olivine sample spectra. For the widths and centers of the Gaussian and continuum, we apply a least-squares linear regression. As for the absorption strengths, they exhibit a non-linear trend with respect to Fo. Instead of a linear regression, we find that a 2^{nd}-order polynomial is appropriate due to the shape of the 0.9- and 1.3-μm absorption strengths with respect to Fo in the RELAB data set. Consequently, this regression increases the quality of the model prediction. Although the absorption widths and centers are similar in both USGS and RELAB data sets (**Figure 2.5**), the absorption strengths and continuum are an order of magnitude stronger in the USGS relative to RELAB spectral data set. Due to contrasting absorption strengths and continuum, we produce an optical parameter for each data set instead of one for both data sets. The cause of this difference in absorption strengths is apparently not dependent on the origin of the samples because all the samples show increase *k* even though the samples were processed by different workers. Thus, we speculate the difference may be due to the use of different spectrometers.

We do not use all the results of the model fits from olivine *k*-spectra in producing the optical properties. In the RELAB data set, we use olivine samples that have sieve fractions <45 μm and for the USGS data set, we use samples where the sieve fraction is <60 μm and <74 μm. These samples are chosen because a well-characterized grain size is needed to convert from reflectance to *k*-spectra. Recall that our olivine samples widely range in sieve fractions resulting in various calculated grain sizes. A slight deviation between the input grain size during conversion and the actual grain size will result in an over- or underestimate of the continuum and absorption strength.

To visualize how important it is to input the correct grain size, we investigate how the *k*-spectrum changes as a function of grain size in the synthetic orthopyroxenes. **Figure 2.6a** and **b** show the potential variation in the continuum and 2.0-μm absorption of Ca^{2+}-free pyroxenes with input grain sizes ranging between 5–45 μm at intervals of 5 μm. The resulting absorption strength of Ca^{2+}-free pyroxenes can vary by up to an order of magnitude; meanwhile the

absorption center and width are constant. To minimize these potential errors due to grain size and for consistency, we constrain our regression analysis to the aforementioned grain size ranges. Furthermore, most of our spectra were measured within these sieve fraction ranges.

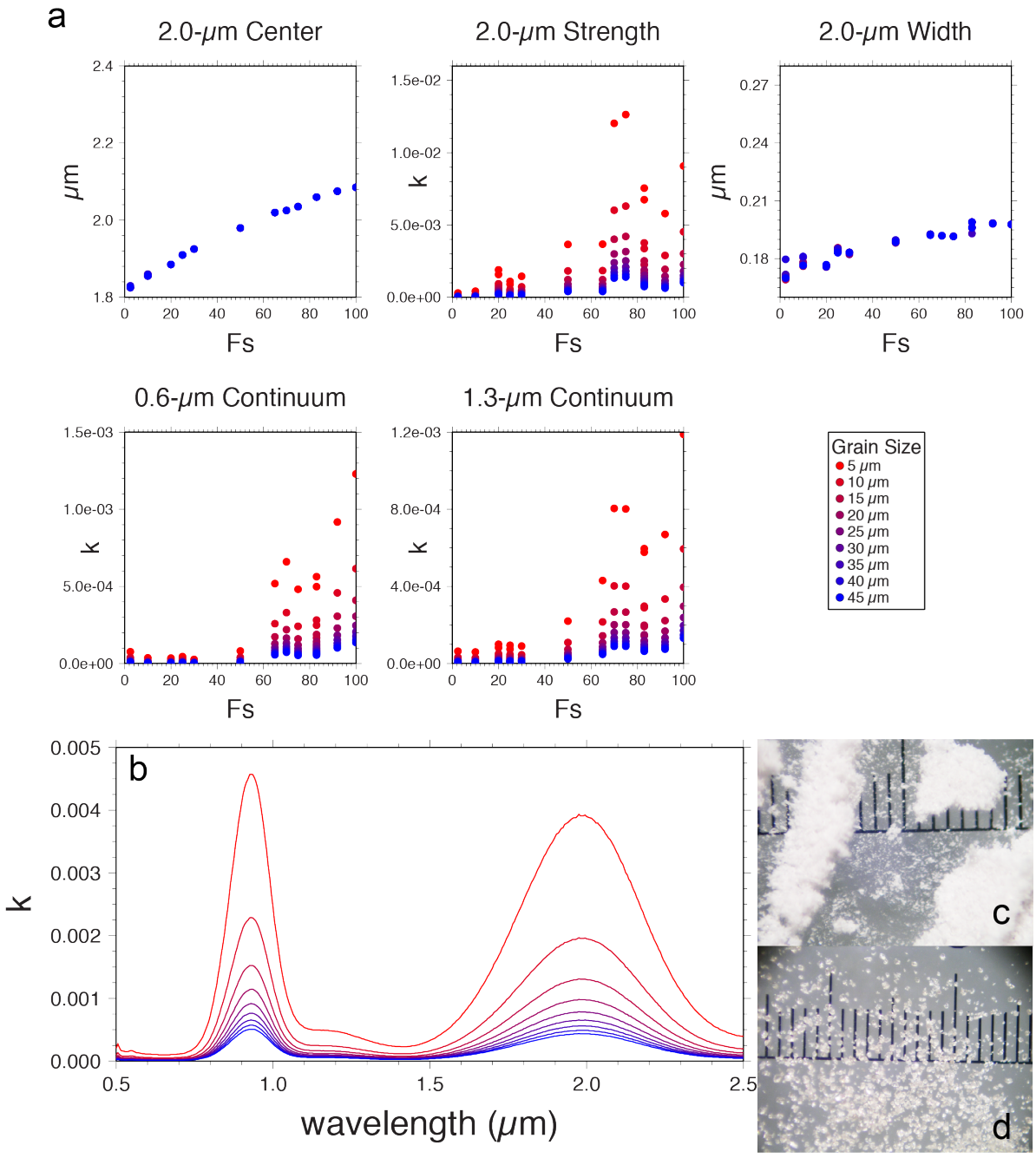

Figure 2.6: (a) The variation in each parameter of the continuum and 2.0-µm absorption in synthetic Ca-free pyroxene as a function of different assumed grain size. Regardless of grain size, the 2.0-µm width and center do not vary, but the strength and continuum can vary by an order of

magnitude. (b) The k-spectrum of a Ca-free pyroxene as a function of grain size. Colors match those in (a). (c–d) Each tick mark is 100 μm. The synthetic pyroxenes vary in average grain size, which we assumed was 22.5 μm. Figures (c) and (d) represent two different Ca-free synthetic pyroxene, which displays two contrasting grain sizes. This grain size variation may attribute to the larger scatter in the absorption strengths and continuum parameters.

The fit coefficients of olivine are displayed in **Table 2.1**. We use a least-squares linear regression for each parameter except for absorption strengths, which form the equation,

$$\mathrm{p(Fo)} = \mathrm{A} + \mathrm{B} \cdot \mathrm{Fo} \quad (4),$$

and for absorption strengths, the second-order least-squares regression takes the form of,

$$\mathrm{p(Fo)} = \mathrm{A} + \mathrm{B} \cdot \mathrm{Fo} + \mathrm{C} \cdot (\mathrm{Fo})^2 \ (5)$$

where *p(Fo)* represents any of the eleven optical constant parameters, *Fo* is the Fo number and *A*, *B*, and *C* are constants (**Table 2.1**). In **Figure 2.5**, we superimpose the regression along with the model fit results to visually demonstrate the goodness-of-fit. In **Figure 2.7**, the model fit for each olivine spectrum is compared to the predicted parameter value based upon the optical parameters (**Table 2.2**). We can see that the absorption centers, widths, strengths, and continuum are well predicted for the RELAB and the USGS data sets, although the USGS data set does show somewhat more scatter in the continuum and strength parameters.

Table 2.1: Olivine optical constants

Olivine/RELAB

Parameter	A	B	C	A 1σ	B 1σ	C 1σ
0.60-μm Continuum	9.74E-05	-9.15E-07		8.63E-06	1.05E-07	
1.85-μm Continuum	1.93E-04	-1.85E-06		2.11E-05	1.05E-07	
0.9-μm Strength	9.46E-05	1.62E-07	-1.17E-08	9.84E-06	3.91E-07	3.49E-09
0.9-μm Center	9.93E-01	-8.25E-04		1.50E-02	1.83E-04	
0.9-μm Width	9.43E-02	-1.07E-05		7.79E-03	9.52E-05	
1.1-μm Strength	6.64E-05	1.16E-06	-1.68E-08	1.30E-05	5.15E-07	4.60E-09
1.1-μm Center	1.09E+00	-4.20E-04		4.14E-03	5.05E-05	
1.1-μm Width	6.03E-02	1.50E-05		1.89E-03	2.31E-05	
1.3-μm Strength	2.06E-04	-2.50E-07	-1.77E-08	1.20E-05	4.76E-07	4.25E-09
1.3-μm Center	1.29E+00	-8.72E-04		8.91E-03	1.09E-04	
1.3-μm Width	1.75E-01	-2.38E-04		5.80E-03	7.08E-05	

Table 2.1: Olivine optical constants (continued)

Olivine/USGS

Parameter	A	B	C	A 1σ	B 1σ	
0.60-µm Continuum	1.45E-04	-1.28E-06		1.55E-05	2.52E-07	
1.85-µm Continuum	4.11E-04	-2.61E-06		7.31E-05	2.52E-07	
0.9-µm Strength	4.24E-04	6.21E-06	-1.12E-07	9.62E-05	4.19E-06	3.79E-08
0.9-µm Center	9.94E-01	-9.46E-05		1.88E-02	3.04E-04	
0.9-µm Width	1.06E-01	-2.54E-04		9.18E-03	1.49E-04	
1.1-µm Strength	5.36E-04	-4.05E-06	1.67E-10	2.63E-04	1.15E-05	1.04E-07
1.1-µm Center	1.10E+00	-4.34E-04		3.59E-03	5.81E-05	
1.1-µm Width	5.65E-02	5.79E-05		4.11E-03	6.66E-05	
1.3-µm Strength	1.78E-03	-6.06E-06	-1.21E-07	5.00E-04	2.18E-05	1.97E-07
1.3-µm Center	1.34E+00	-9.93E-04		9.22E-03	1.49E-04	
1.3-µm Width	1.90E-01	-5.09E-04		6.45E-03	1.04E-04	

2.4.2 Pyroxene

Fitting of our models to synthetic pyroxene *k*-spectra is exemplified in **Figure 2.8**. We report the fit coefficients to the Gaussian parameters, the continuum, and the mean and median absolute differences as the error in **Table A.4** and **Figure 2.9 and 2.10**. Of the sixty-two synthetic pyroxene *k*-spectra, we determine model fits to fifty-four sample spectra and omit eight sample spectra due to being featureless. One sample spectrum is excluded from the regression analyses due to its composition (Wo_{51}, making it a pyroxenoid).

The optical constants of synthetic pyroxene are divided into low- and high-calcium pyroxene groups. We base this division upon the existence of two trends found in the 1.0- and 2.0-µm absorption center as a function of Fs (**Figure 2.9a and c).** As a result, we produce two sets of optical parameters for synthetic pyroxene based upon low-Ca pyroxene and high-Ca pyroxene, where the separation is at Wo_{20}. The Gaussian and continuum parameters are defined by,

$$\mathrm{p(Fs, Wo)} = \mathrm{A} \cdot \mathrm{Fs} + \mathrm{B} \cdot \mathrm{Wo} + \mathrm{C} \quad (6),$$

where *Fs* is the Fs number, *Wo* is the Wo number, and *A*, *B*, and *C* are constants (**Table 2.2**). Similar to **Figure 2.7**, in **Figure 2.11** we compare the model fit of each parameter against the predicted parameter value based upon the multi-linear regression (**Table 2.2**). We observe the absorption centers and the widths present a tighter fit, but the strength and continuum present some scatter.

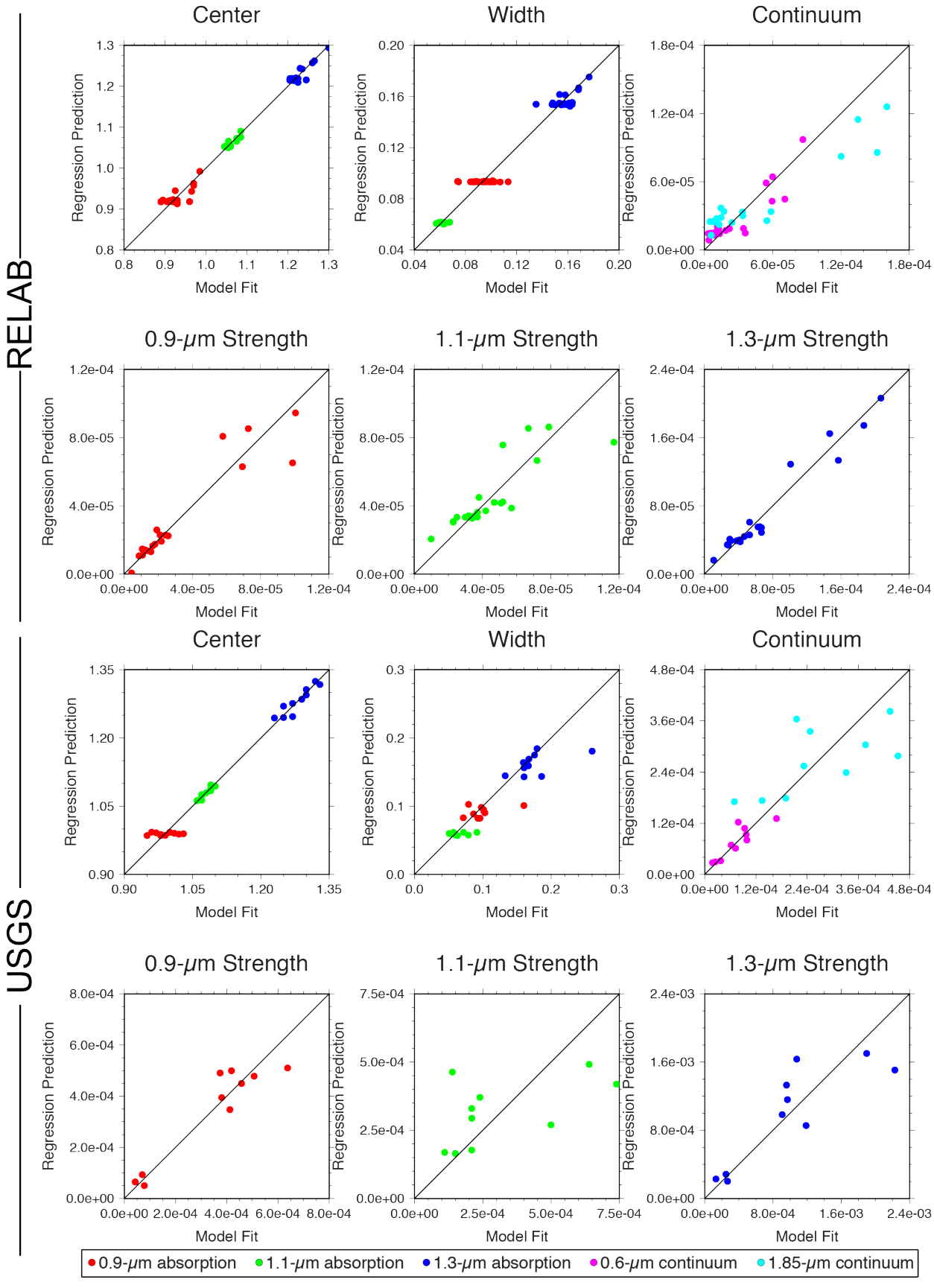
RELAB
USGS
Center
Width
Continuum
0.9-μm Strength
1.1-μm Strength
1.3-μm Strength
Regression Prediction
Model Fit
0.9-μm absorption
1.1-μm absorption
1.3-μm absorption
0.6-μm continuum
1.85-μm continuum

Figure 2.7: We compared the model fitting results to the predicted parameters for olivine, which is based upon our regression. Points that cluster along the 1:1 line indicate the samples are well predicted by the optical parameters. The RELAB data set showing tighter fits along the 1:1 line than the USGS data set.

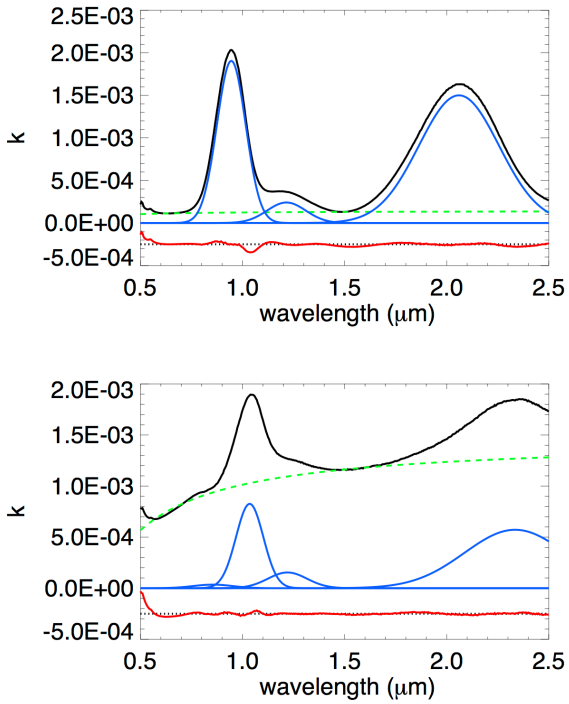

Figure 2.8: Model *k*-spectra fits for synthetic pyroxene with compositions $En_{17}Fs_{83}Wo_0$ (top) and clinopyroxene $En_{18}Fs_{35}Wo_{46}$ (bottom). The solid black line indicates the measured *k*-spectrum, the dashed green line is the continuum, the solid blue lines are the Gaussians, the solid red line is the residual or the difference between the measured *k*-spectrum and the model *k*-spectrum.

Similarly to the olivine, the assumed grain size of the pyroxene samples may affect the goodness-of-fit between the fit coefficient and predicted coefficient of the absorption and continuum parameters. Our observations of the binocular microscope images of synthetic pyroxene (**Figure 2.6c and d**) show that the samples vary in grain size, which support the

assumption that scatter in absorption strength and continuum is due to errors in the assumed grain size.

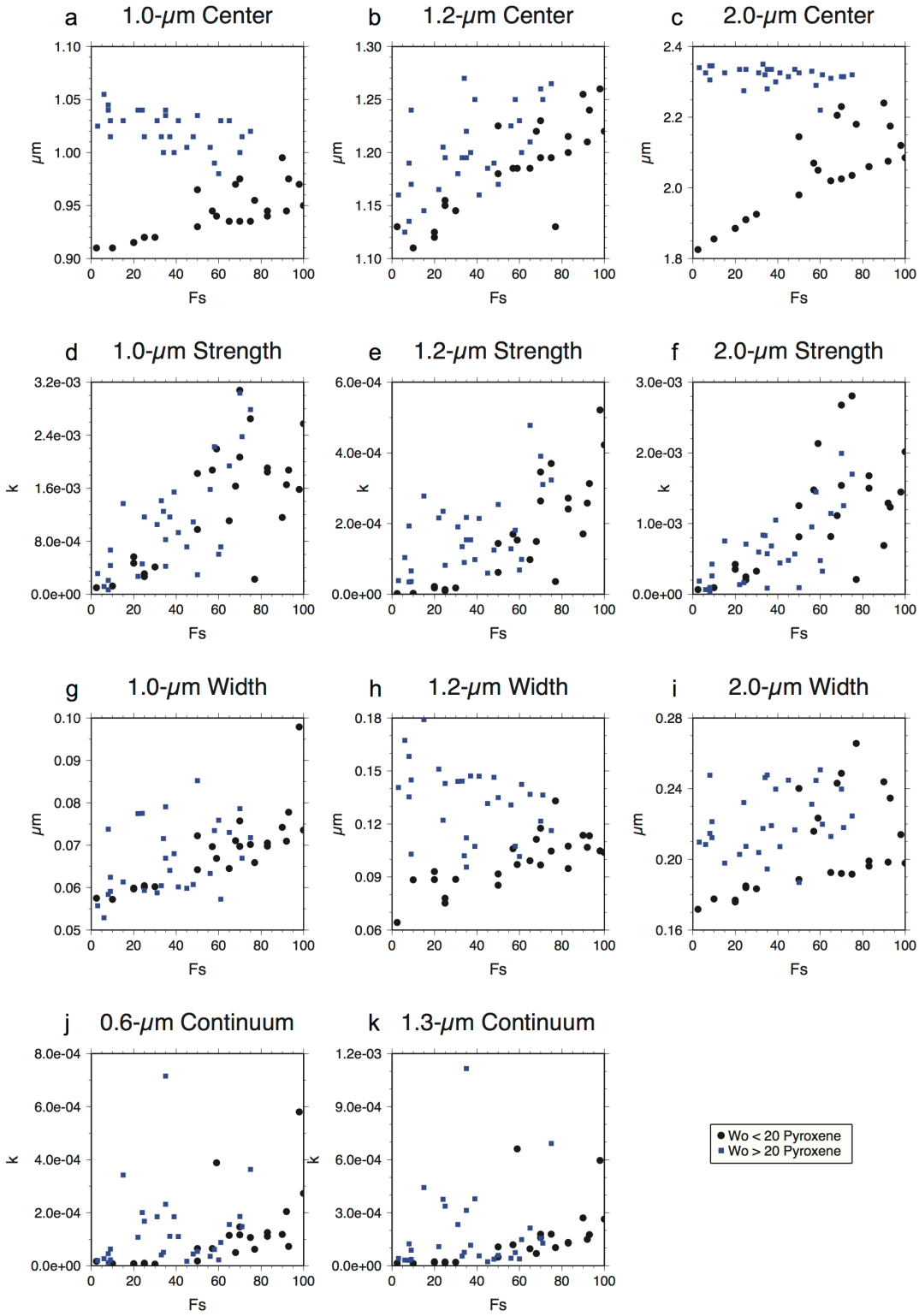

Figure 2.9: Results for each optical parameter with respect to Fs number of the modeled fits to synthetic pyroxene k-spectra. Based upon the 1.0 and 2.0 μm absorption centers (a and c), we produced two optical parameters because of the two different trends (blue squares vs. black circles). We found that the difference in trend was dependent on Wo number and separated at Wo~20. Blue squares represent pyroxene with Wo> 20, and black circles represent pyroxene with Wo<20.

Table 2.2: High- and low-calcium pyroxene optical constants

High-Ca Pyroxene					
Parameter	**A (Fs)**	**B (Wo)**	**C**	**Fs 1σ**	**Wo 1σ**
0.6 μm Continuum	2.92E-06	5.95E-06	-2.04E-04	1.76E-06	3.87E-06
1.3 μm Continuum	3.44E-06	7.09E-06	-2.07E-04	2.94E-06	3.87E-06
1.0 μm Strength	1.58E-05	-3.40E-05	1.79E-03	6.25E-06	1.38E-05
1.0 μm Center	1.79E-04	1.89E-03	9.43E-01	9.29E-05	2.05E-04
1.0 μm Width	2.25E-04	2.21E-04	4.99E-02	9.70E-05	2.14E-04
1.2 μm Strength	4.70E-06	6.31E-06	-2.45E-04	1.04E-06	2.29E-06
1.2 μm Center	3.71E-04	-2.43E-03	1.28E+00	3.24E-04	7.14E-04
1.2 μm Width	-4.60E-05	9.17E-04	9.93E-02	2.32E-04	5.12E-04
2.0 μm Strength	7.01E-06	-2.93E-05	1.49E-03	3.84E-06	8.46E-06
2.0 μm Center	-2.87E-04	4.61E-04	2.31E+00	3.13E-04	6.90E-04
2.0 μm Width	-3.03E-04	-1.59E-03	2.94E-01	1.67E-04	3.69E-04

Low-Ca Pyroxene					
Parameter	**A (Fs)**	**B (Wo)**	**C**	**Fs 1σ**	**Wo 1σ**
0.6 μm Continuum	2.97E-06	-4.83E-06	-4.72E-05	8.05E-07	4.42E-06
1.3 μm Continuum	3.16E-06	-1.51E-06	-3.26E-05	1.05E-06	4.42E-06
1.0 μm Strength	2.11E-05	-2.35E-06	1.22E-04	4.77E-06	2.62E-05
1.0 μm Center	4.89E-04	2.48E-03	9.05E-01	5.36E-05	2.94E-04
1.0 μm Width	2.19E-04	2.51E-04	5.46E-02	3.90E-05	2.14E-04
1.2 μm Strength	4.34E-06	-4.01E-06	-7.24E-05	6.30E-07	3.46E-06
1.2 μm Center	1.14E-03	1.84E-03	1.11E+00	1.72E-04	9.45E-04
1.2 μm Width	3.32E-04	1.06E-03	7.54E-02	6.07E-05	3.34E-04
2.0 μm Strength	1.81E-05	-1.99E-05	1.03E-04	4.59E-06	2.52E-05
2.0 μm Center	2.73E-03	1.29E-02	1.84E+00	1.38E-04	7.59E-04
2.0 μm Width	3.25E-04	3.91E-03	1.74E-01	7.02E-05	3.86E-04

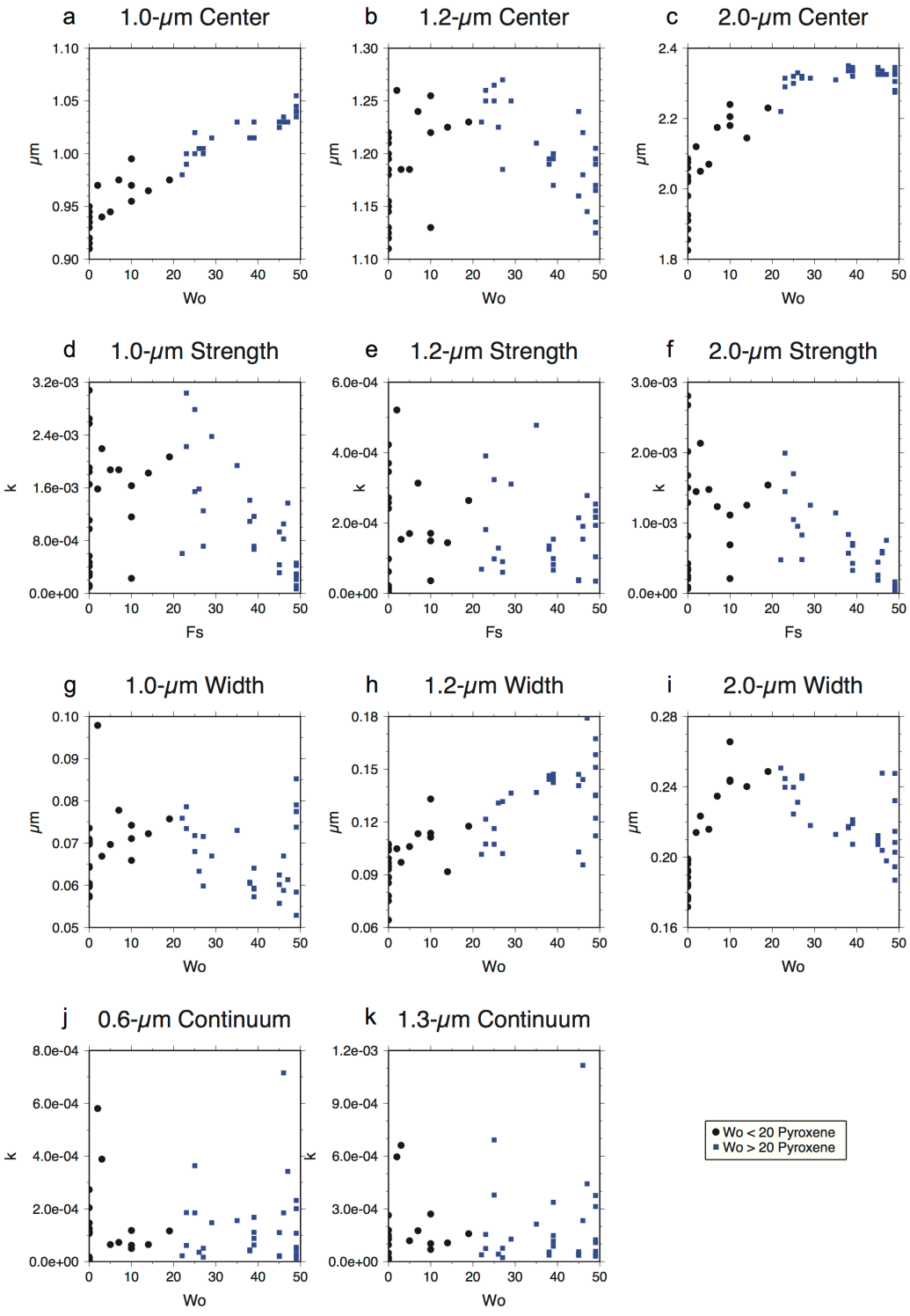

Figure 2.10: Results for each optical parameter with respect to Wo number of the modeled fits to synthetic pyroxene k-spectra. Blue squares represent pyroxene with Wo >20, and black circles represent pyroxene with Wo <20.

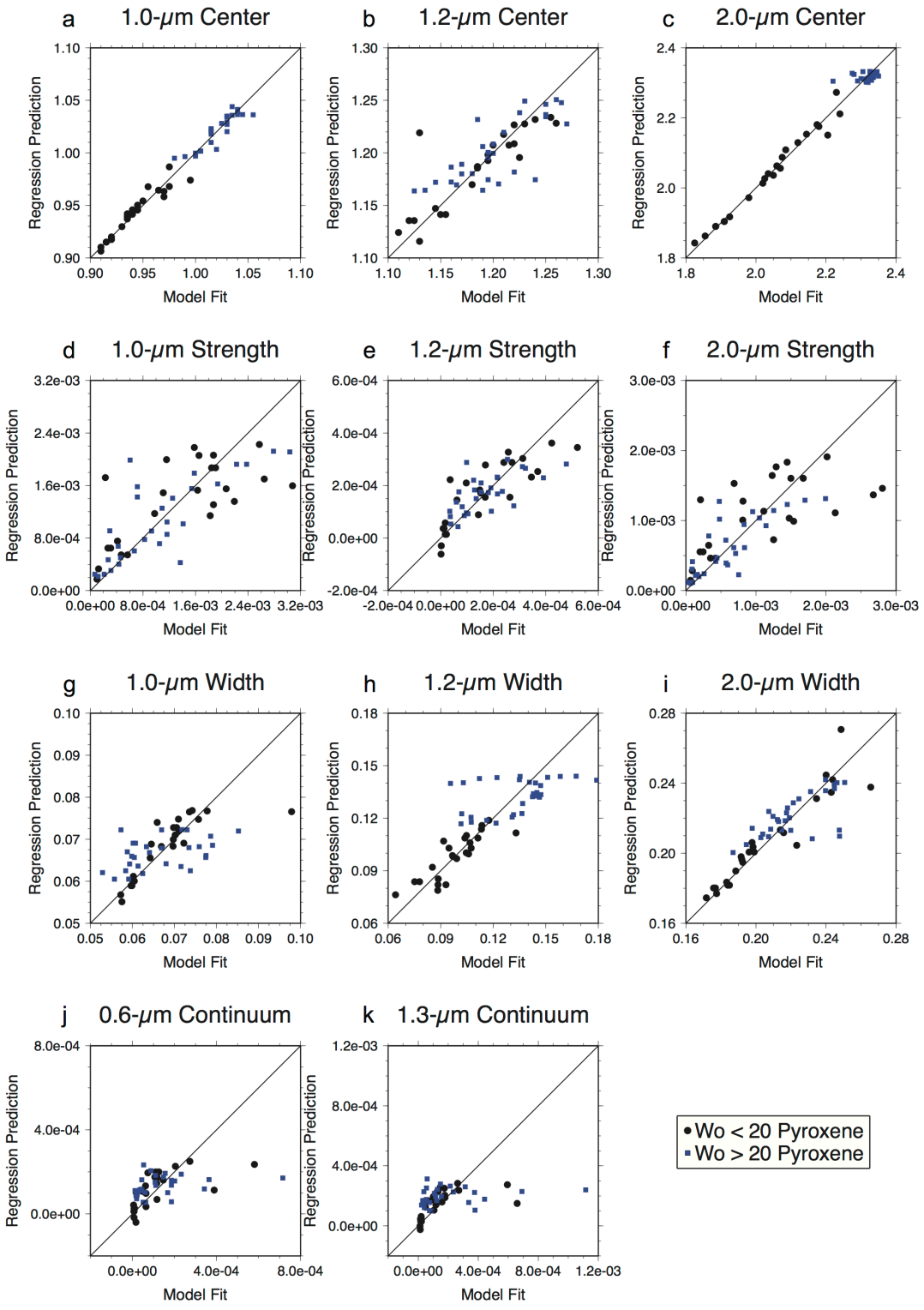

Figure 2.11: We compared the model fits results to the multi-linear regression of the synthetic pyroxenes. For the absorption centers and the widths, they show much tighter fit. However, the absorption strengths exhibit more scatter.

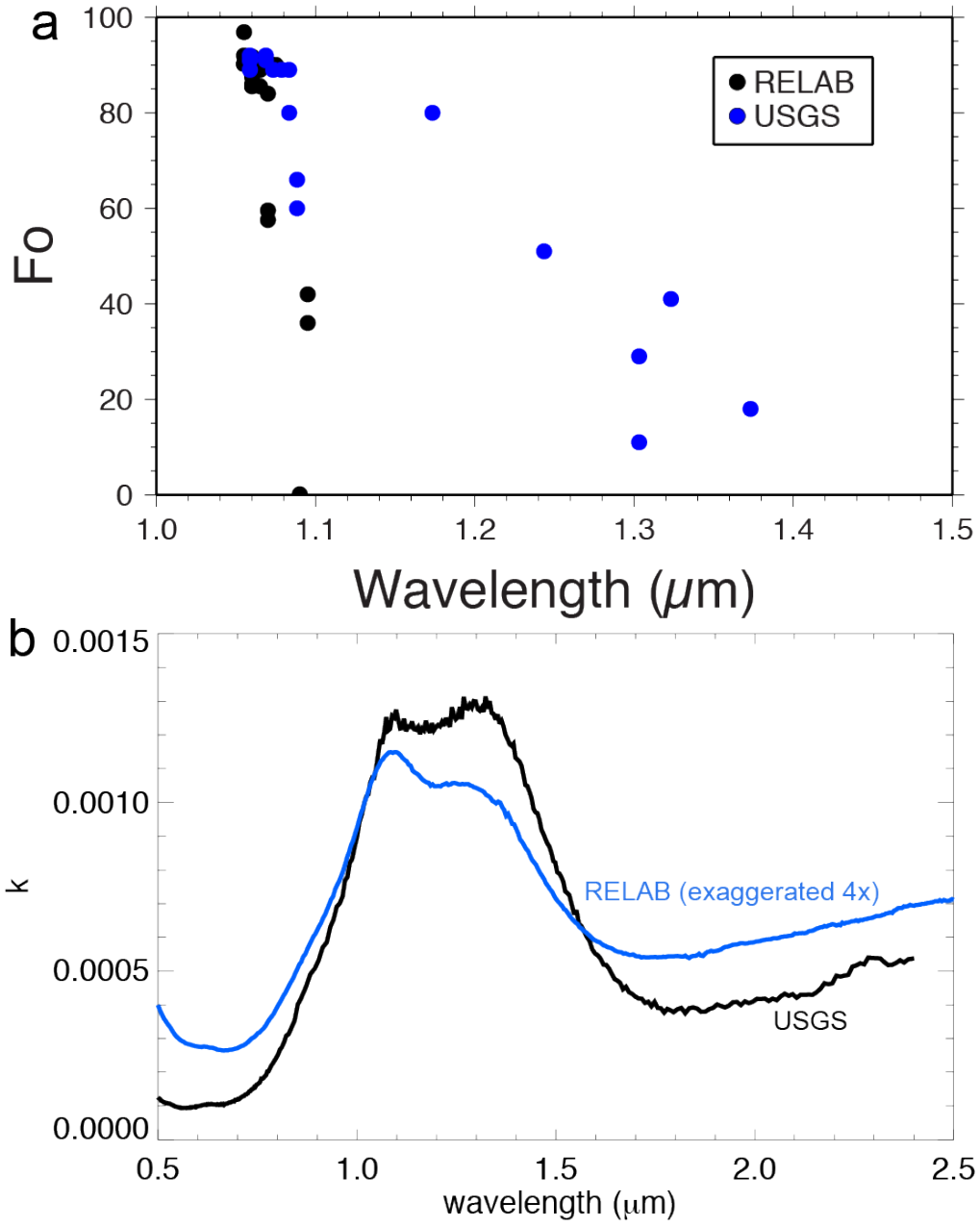

Figure 2.12: The olivine k-spectra of the RELAB and USGS data for olivine are quite different even though the compositions are similar. a) The peak of the absorption on the USGS Fe-rich olivine is unusual because it is near ~1.3 μm, whereas reflectance spectra of olivine tend to show the peak closer to 1.0 μm. b) The USGS k-spectra is much darker than the RELAB. In this case, the USGS olivine k-spectrum (Fo41) is four times darker than the RELAB k-spectrum (Fo_{42}).

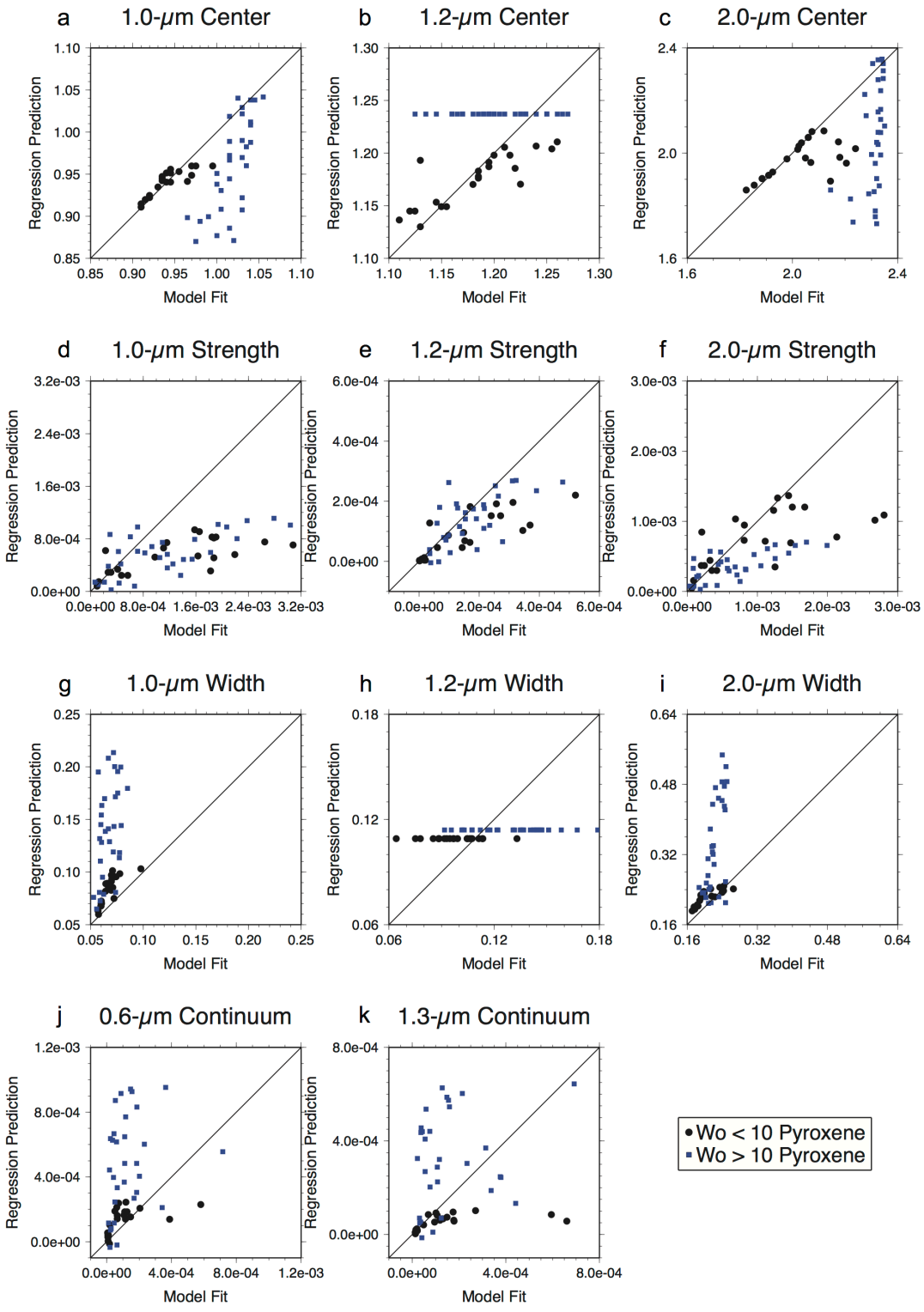

Figure 2.13: We compared the results of the model fits of the synthetic pyroxene to the predicted results based upon the optical parameters from Denevi et al. [2007]. Synthetic pyroxenes with composition of Wo>10 show considerable scatter are not well predicted by

Denevi et al. [2007]'s optical parameters. On the other hand, the orthopyroxene optical parameters can somewhat predict the model fits of the synthetic pyroxenes.

2.5 Resulting Optical Parameter Implications and Lessons

2.5.1 Olivine Optical Parameters: RELAB vs. USGS Sample Sets

For the reasons mentioned in section 4.1, we produce two sets of optical parameters for olivine based upon the USGS and RELAB data. Of the two optical parameters, we recommend using the RELAB parameters even though the USGS data set has the advantage of covering a larger range of Fo number. We favor the RELAB parameters for the following reasons: First, RELAB Fe-rich olivine has a maximum *k*-value near 1 μm, which is consistent with the location of the absorption minimum in reflectance spectra. In contrast, the maximum *k* value in Fe-rich olivines in the USGS data set unusually occurs at longer wavelengths, closer to 1.3 μm (**Figure 2.12a**). This result is considered suspect because it is inconsistent with the absorption minimum of olivine in reflectance spectra. Second, the USGS *k*-spectra absorption strengths for olivine are an order of magnitude stronger than the RELAB olivines, which suggests that the olivines are anomalously dark (**Figure 2.12b**). Therefore, using the USGS parameters on unknown *k*-spectra will result in overestimates of Fo number; an example is shown in section 6.1. For these reasons, we urge the reader to use the RELAB based parameters.

2.5.2 Comparison to Previous Work

We compare our optical parameters to previous work. We did not make comparisons with *Lucey* [1998]'s olivine and pyroxene optical parameters because their parameters are based upon modeling the changes in *k* with iron content at every wavelength, whereas our parameters are based upon Gaussians. Thus, there is not a direct or indirect method of comparing the two models.

As for pyroxenes, we compare our model fit results of the synthetic pyroxenes to the predicted values for each Gaussian and continuum parameter based upon *Denevi et al.* [2007]'s optical parameters of mostly natural pyroxenes, which in a sense, is comparing the two optical parameters indirectly. *Denevi et al.* [2007] produced two sets of optical parameters, including a set for ortho- ($Wo_{\leq 10}$) and a set for clinopyroxene ($Wo_{>10}$), respectively. Roughly speaking, the optical parameters for orthopyroxenes ($Wo_{\leq 10}$) derived by *Denevi et al.* [2007] somewhat match our model fits for synthetic orthopyroxenes with ($Wo_{\leq 10}$; **Figure 2.13-black circles**). However,

when using the optical parameters derived for clinopyroxene ($Wo_{\geq 10}$), by *Denevi et al.* [2007], an inadequate model prediction of synthetic clinopyroxene is determined (**Figure 2.13-blue squares**). And conversely, our optical parameters would produce poor model fits to the natural pyroxenes of *Denevi et al.* [2007].

This contrast between natural and synthetic pyroxenes *k*-spectra is not clear, but the difference is important in predicting pyroxene abundances and composition on planetary surfaces. We indicate two possibilities for the observed differences. First, zonation of pyroxenes causes the absorptions to appear wider [*Sunshine and Pieters*, 1993] and produces erroneous centers [*Hazen et al.,* 1978; *Cloutis and Gaffey,* 1991]. The natural clinopyroxenes examined here and their absorption widths and centers are plausibly consistent with this interpretation. Another possibility is that these natural pyroxenes are accommodating minor and/or trace elements that are modifying the crystal structure. If the differences between the two-pyroxene suites are due to zonation, then determination of two pyroxenes from spectral data will improve petrological modeling. Future petrographic and spectroscopic studies in examining the difference in natural and synthetic pyroxene will be key to resolving this issue.

2.5.3 Ordering of Cations Among the Cation Sites.

The strengths of olivine and pyroxene absorptions are dependent upon the proportion of Fe^{2+} present in each crystallographic site. Also, the strength of each absorption is linked to how Fe^{2+} is ordered among the crystallographic sites. Two studies compiled data on the ordering between Fe^{2+}-Mg^{2+} in the M1 and M2 sites in olivine for temperatures between 0–800 °C [*Princivalle*, 1990; *Rinaldi et al.*, 2000]. Within these temperatures, *Burns* [1993] found that the effects of cation ordering on olivine spectra are negligible. Thus, we can safely assume that olivine cation ordering does not affect our optical parameters significantly.

The effects from Mg^{2+}-Fe^{2+} ordering are more prominent in pyroxene than olivine [*Burns*, 1993]. As mentioned above, Fe^{2+} prefers the M2 to M1 sites in pyroxenes. When each Fe^{2+} ions is in its preferred site, the pyroxene is considered "ordered", where the reverse is called "disordered". The degree of ordering in orthopyroxene is dependent upon the rate of cooling. Pyroxenes that cool slowly, such as pyroxenes originating from metamorphic and plutonic rocks, are more ordered than rapidly-cooled pyroxenes from volcanic rocks [*Ghose and Hafner*, 1967; *Virgo and Hafner*, 1970]. *Burns et al.* [1991] reheated samples of orthopyroxenes to 500–700°C to enhance disorder and compared the near-infrared spectra before and after disorder. Using

Mössbauer spectroscopy, they found that with increasing disorder, where the proportion of Fe^{2+} in the M1 sites increased, the strengths of the 1.0- and 2.0-μm absorptions weakened and the 1.2-μm absorption strengthened. On this basis, even though a correlation between absorption strengths and pyroxene composition exist, the absorption strength may not be the lone indicator of mineral composition [*Denevi et al.*, 2007]. For example, during pyroxene synthesis the samples were quenched, which promotes disordering in the samples. Thus, cation ordering may be a contributing factor to the scatter in our model absorption strengths.

Determining cation ordering from a pyroxene spectrum could be used to model cooling rates on asteroids and planetary surfaces. A number of authors have worked on a method using cation ordering to derive cooling rates in terrestrial orthopyroxenes [e.g., *Virgo and Hafner*, 1970; *Besancon*, 1981; *Stimpfl et al.*, 1999], pigeonite [*Pasqual et al.*, 2000], and clinopyroxenes [*McCallister et al.*, 1976; *Brizi* et al., 2000]. *Ganguly and Stimpel* [2000] successfully demonstrated that orthopyroxene cation ordering in orthopyroxenes in meteorites could be used to derive mineral cooling rates. If the absorption strength indicates the proportion of Fe^{2+} in each site (i.e., order/disorder), then correlating pyroxene absorption strength with cation ordering in pyroxene may result in spectroscopy-based derived cooling rates.

2.5.4 True Proportion of Fe^{2+}

Optical parameters formulated here are based upon Fo for olivine, and Fs and Wo number for pyroxene. These parameters are generally relied upon for characterization of chemical species within these minerals. In the context of remote sensing, spectral variations are generally attributed to changes in bulk Fe^{2+}, Mg^{2+}, and Ca^{2+} contents of olivine and pyroxene. However, the cation constituents in natural olivine and pyroxene compositions are not restricted to Fe^{2+}, Mg^{2+}, and Ca^{2+}. Minor cations (e.g., Ni^{2+}, Mn^{2+} for olivine and Mn^{2+}, Al^{3+}, Na^{+} for pyroxene) are often present at percent levels in these minerals. As a result, the relative Fe^{2+} proportions to all major (e.g., Mg^{2+}, Ca^{2+}) and minor cations are not accurately reflected in Fs and Fo numbers because they determine the proportions relative to three major elements. For instance, the overall abundance of Fe^{2+} and Mg^{2+} can vary while the proportionality of the two species can remain constant due to an increase in the abundance of minor elements. What is important, however, is whether these accessory elements influence the abundance and/or crystallographic site of Fe^{2+}, Mg^{2+}, or Ca^{2+} in a way that would influence our interpretation of a reflectance spectrum. If the effects of minor elements on spectra are observable, then the

reported absorption strengths, centers, widths, and continuums may not be as adequately related to Fo, Wo, and Fs number.

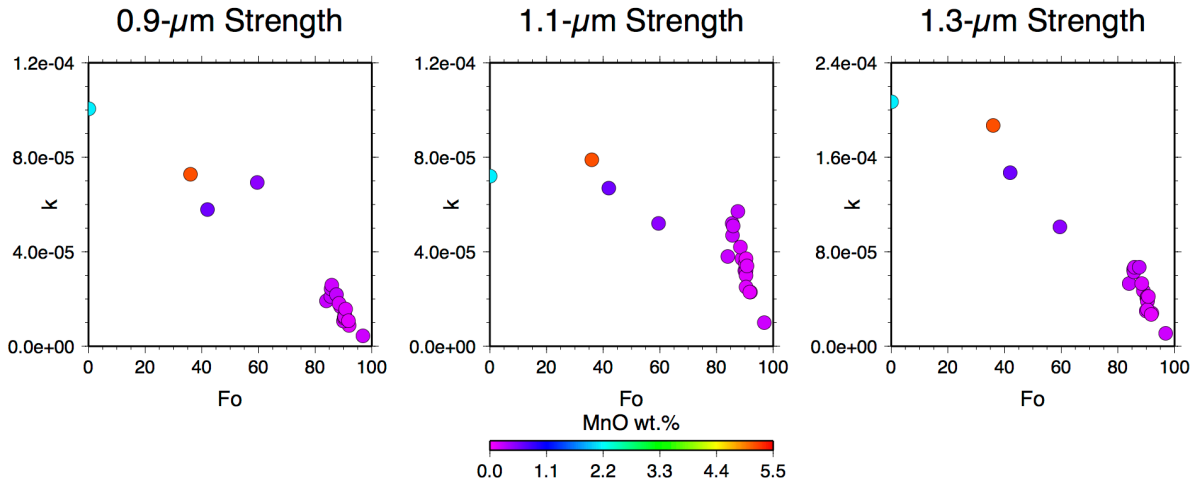

Figure 2.14: The presence of Mn^{2+} in Fe-rich olivine is abundant enough to cause the 1.1 μm absorption strength to become non-linear and also affects the 0.9 and 1.3 μm absorption strength.

2.5.5 The Presence and Potential Influence of Mn^{2+}

The RELAB olivine data set exhibits a near linear relation between Fo number and the 0.9- and 1.3-μm absorption strength, but a non-linear correlation between Fo number and the 1.1-μm strength (**Figure 2.14**). The relation between Fo number and strength of the 1.1-μm absorption appears to bifurcate into two trends. We hypothesize that this non-linear behavior in the 1.1-μm absorption and near-linear behavior in the 0.9- and 1.3-μm absorption may be attributed to the presence of the minor element Mn^{2+}. The influence of Mn^{2+} in mineral spectra has been inferred before. Previous authors have investigated the effects of Mn^{2+} on olivine spectra [*Burns*, 1970; *Burns*, 1993] as well as the proportions needed for a spectral effect to be observable [*Cloutis*, 1997]. These studies found that the presence of Mn^{2+} has two major effects on near-infrared absorptions of olivine. First, the 1.1-μm absorption becomes weakens relative to the 0.9- and 1.3-μm absorptions as Mn' proportions increase [*Burns*, 1993] (in atomic proportions, $Mn' = [Mn^{2+}/(Fe^{2+}+Mg^{2+}+Mn^{2+})] \times 100$). This weakened absorption is due to Mn^{2+} tendency to occupy M2 sites, forcing Fe^{2+} into M1 sites. In extreme cases (70–78% mole % of Mn_2SiO_4), the 1.1-μm absorption of olivine is no longer visually resolvable [*Cloutis*, 1997]. Second, an increase in Mn' will also shift the 1.1-μm absorption towards longer wavelengths

because Mn^{2+} is a larger cation than Fe^{2+} [*Huggins*, 1973; *Burns, 1993*]. *Cloutis* [1997] found that at ~10 % mole % Mn_2SiO_4, the 1.1-µm absorption will begin shifting beyond the potential positions for this absorption observed for the forsterite-fayalite solid solution.

Upon examining the oxides in the RELAB samples, we observe an increase in Mn^{2+} (and Mn') in olivine as Fo number decreases (**Figure 2.15**). Specifically, the proportion of Mn' is >0.5% at ~$Fo_{,<60}$ with one sample having a Mn' as high as ~ 7%. We also notice that with increasing Mn^{2+} content, the scatter is greater in the 1.1-µm absorption strength at samples of $Fo_{<80}$ relative to olivines with $Fo_{>80}$. At $Fo_{>80}$, the 1.1-µm absorption strength increases linearly with decreasing Fo number, but at $Fo_{<80}$ the absorption strength deviates from this linear trend and becomes weaker relative to the 0.9- and 1.3-µm absorption strength (**Figure 2.14**); a pattern that is expected due to positioning the Mn^{2+} into the M2 sites and forcing more Fe^{2+} into the M1 sites. Additionally, the 0.9- and 1.3-µm absorptions are not perfectly linear due to Mn^{2+}-induced cation ordering.

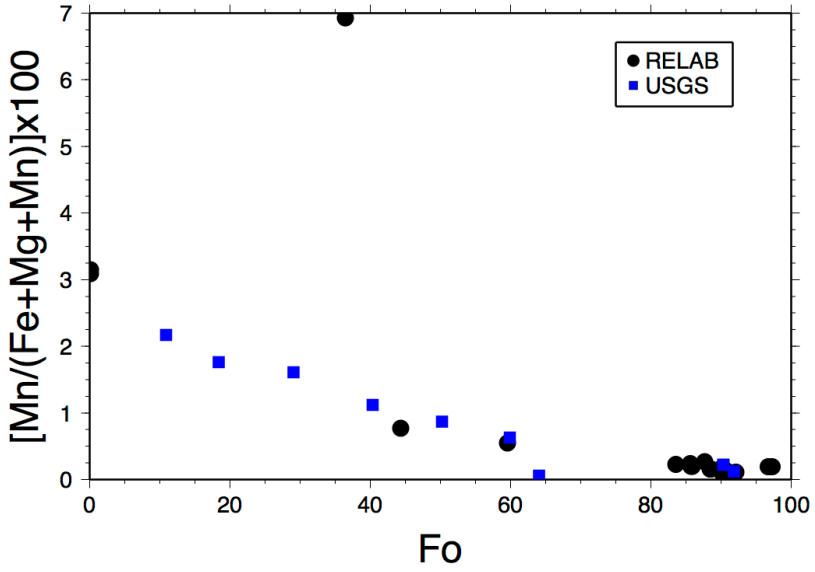

Figure 2.15: In both the RELAB and USGS olivine samples, as the Fe^{2+} content increases, so does the Mn^{2+} content.

The optical parameters we derive for olivine are preliminary because we find that the presence of Mn^{2+} in the crystal structure is significant enough to alter our spectral models. Aside from the presence of Mn^{2+}, we observe that the two points that define the continuum (i.e., 0.6 and 1.85 µm) in the RELAB data are still quite scattered with respect to Fo number, indicating

the possible influence from our grain size assumption. Consequently, the absorption strengths may be stronger or weaker than the reported strengths. Future work that constrains grain size as well as modeling with optical parameters through natural and synthetic olivine samples with respect to Fe^{2+}, Mg^{2+}, and Mn^{2+} content will produce more accurate models of olivine spectra. Furthermore, this future study will result in determination of Mn^{2+} proportion in olivine studies of planetary surfaces. This determination of abundance and composition of this additional cation will improve future petrologic modeling.

2.6 Application

2.6.1 Olivine Example- Lunar Dunite

To demonstrate the practical application of the olivine optical parameters, we determine the mineral composition of olivine separates from a lunar dunite (72415), which were previously studied by *Isaacson and Pieters* [2010]. *Isaacson and Pieters* [2010] produced a reflectance spectrum at RELAB with an incidence angles and emission angles of 30º and 0º, respectively. The sieve fraction of this spectrum is from <125 μm olivine separates. We convert the reflectance spectrum to *k* based upon the equations (1)–(8) from *Lucey* [1998] and using a grain size of 66.2 μm. Next, we compare the *k*-spectrum of the sample to modeled *k*-spectra, based upon the optical parameters with compositions ranging from Fo_0 to Fo_{100} at intervals of 1. The best matching olivine *k*-spectrum is determined by the lowest mean absolute difference between the model and the sample *k*-spectrum at wavelengths between 0.6 to 1.55 μm. We limit the spectral range of interest due to the presence of chromite. Chromite produces a broad absorption, which becomes apparent at ~1.5 μm [*Isaacson and Pieters*, 2010]. The model determines that the composition of the lunar olivine is Fo_{83} (**Figure 2.16a**), which could be considered approximate to the actual (Fo_{88}). We perform the same routine with the USGS optical parameters, which predict the sample is of Fo_{100} (**Figure 2.16b**). This result is unsurprising because the USGS optical parameters predict olivines of a particular Fo number to be darker than the actual. Thus, the USGS optical parameters would over predict the Fo number of the sample.

2.6.2 Pyroxene Example- Tatahouine Meteorite

We apply our pyroxene optical parameters to determine the mineral composition of a diogenite meteorite, Tatahouine. Diogenites are pyroxene-dominated meteorites thought to derive from 4 Vesta. *Hiroi et al.* [2001] presented the spectrum (0.3 to 2.6 μm) of a sample of Tatahouine ground to <25 μm grain size. For this analysis, we use a grain size of 12.5 μm. We

assume that they used an incidence angle of 30° and emission angle of 0°. Next, we convert the spectrum from reflectance to *k* by applying equations (1)–(8) from *Lucey* [1998], the grain size of the sample, and viewing geometry. After the conversion, we compare the Tatahouine *k*-spectrum to the modeled pyroxene *k*-spectra based upon the optical parameters. The best matching pyroxene *k*-spectrum is obtained by comparing every combination of En, Fs, and Wo that summed to 100 at intervals of 1 until the mean absolute difference between the Tatahouine and pyroxene *k*-spectrum was close to zero. The actual pyroxene composition of Tatahouine is $En_{75}Fs_{23.5}Wo_{1.5}$ [*Barrat et al.*, 1999] and we predict the mineral composition to be $En_{68}Fs_{31}Wo_{1}$, which is a good approximation of the sample (**Figure 2.16c**).

2.7 Conclusion

Here, we have determined optical parameters for natural olivines and synthetic pyroxenes in the near-infrared from 0.6–2.5 μm. These optical parameters will be important for determining abundance and proportion of olivine and pyroxene in intimately mixed soils on bodies such as, the Moon and asteroids using a variety of available data sets (e.g., Earth-based telescopic spectra, Clementine, Chandrayaan-1, SELENE, NEAR, Galileo, MESSENGER, Dawn). Natural olivine optical properties are effectively characterized with two sets of model parameters derived from examination of RELAB and USGS spectra. Of these two sets of parameters, the RELAB set is more robust. However, these newly derived optical constants do have some caveats resulting largely to compositional impurities. The olivine optical constants we report are derived from Mn-bearing olivine samples with up to ~5 MnO wt%. The abundance of Mn^{2+} is found to increase systematically with decreasing Fo number. Due to Mn^{2+} in these olivine samples, the optical parameters of Fe^{2+}-rich olivine spectra are less than robust and limits accuracy of modeling of Fe-rich olivines, especially for olivine samples that are Mn free/depleted relative to the calibration set of olivine. Mg-rich olivine samples modeled here are better predicted largely because of a larger sample size and lower trace-element abundances.

In this study, pyroxene optical parameters were derived from synthetic samples. Due to the concentration of samples towards the Fe^{2+}-rich region of the pyroxene quadrilateral, the optical parameters describe this region better. Future work is necessary in examining the petrographic and geochemical differences that reveal the discrepancies between the natural and synthetic optical parameters shown here. Such a study would be highly beneficial for more accurate modeling of the pyroxene optical parameters.

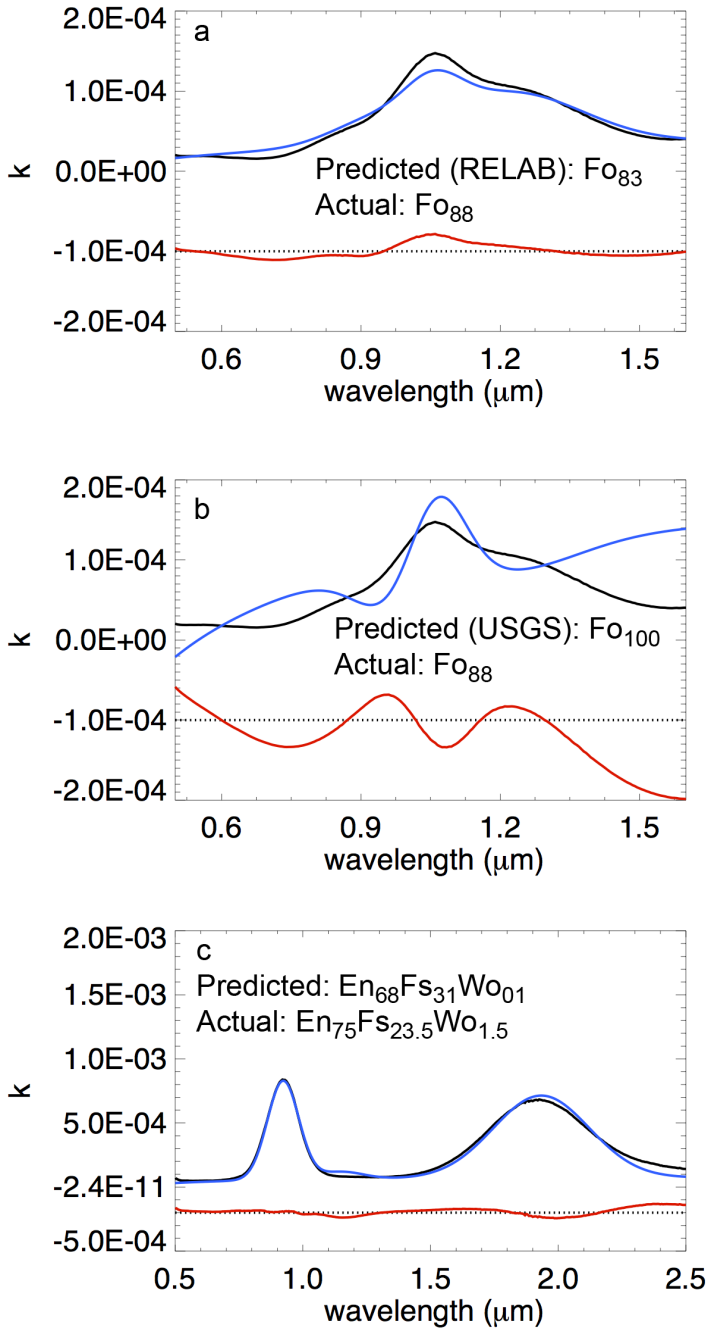

Figure 2.16: The solid black line is the lunar olivine separate k-spectrum for (a–b) and the Tatahouine spectrum in (c). The violet line is the best-fit spectrum. The solid red line represents the residuals between the two spectra. The fitting for the lunar olivine separate was limited to the relevant wavelengths from 0.6 to 1.55 μm. This limitation is due to the additional absorption beyond 1.5 μm caused by chromite. a) The best model olivine spectrum based upon the RELAB

optical parameters has a mineral composition of Fo83, close to the actual composition (Fo88). b) The best model olivine spectra based upon the USGS optical parameters is Fo100. However, the fit is not very good based on the residuals. c) The pyroxene model appears to replicate the Tatahouine k-spectrum well and also predict the mineral composition.

CHAPTER 3

ABSOLUTE MODEL AGES FROM LUNAR CRATER MORPHOLOGY

Accepted: Trang, D., J. J. Gillis-Davis, J. M. Boyce, Absolute Model Ages from Lunar Crater Morphology, J. Geophys. Res. Planets.

Abstract – Impact craters exhibit an array of degradation states, which is an indicator of their age. Previous workers have used crater degradation states to obtain ages of surfaces or geomorphological features; one example is the degree of freshness method developed by *Pohn and Offield* [1970]. We created an empirical calibration that yields absolute model ages based upon the degree of freshness technique for 1–20 km craters. To produce the calibration, first we used fifteen craters with degree of freshness ranging from 6.3–2.5. Next, we use the Kaguya Terrain Camera data set to date fifteen craters by crater density to yield an absolute model age. The resulting absolute model ages ranged from 0.9–4.0 Ga. We find two linear regressions can describe the relationship between the absolute model age and degree of freshness of the fifteen craters. We fit each trend with two least-squares linear regressions, where the first regression represents craters with a degree of freshness from 0.0–4.9 and the second regression from 5.0–7.0. Craters <8 km degrade at a faster rate than larger craters, which causes the degree of freshness to overestimate their age. Therefore, we provide a numerical correction to allow this calibration to work on 1–8 km craters. We tested our calibration on North and South Ray craters and the Apollo 12 landing site. Using the degree of freshness, we calculated an age of 0.6 and 0.2 Ga for North and South Ray crater, respectively, and 3.1 Ga for the Apollo 12 landing site.

3.1 Introduction

There are several dating methods that rely on lunar impact craters to calculate an age of a surface or a morphological feature. These methods include crater density [e.g., *Neukum et al.*, 2001 and references therein], detection of the impact ejecta optically [*Shoemaker and Hackman*, 1962] and in radar [*Thompson,* 1981; *Bell et al.*, 2012; *Thomson et al.*, 2013], degree of regolith maturity [*Grier et al*., 2001], and degradation of crater morphology [*Pohn and Offield*, 1970; *Trask*, 1971; *Soderblom and Lebofsky*, 1972; *Boyce and Dial*, 1975; *Fassett*, 2013]. Only several of these techniques result in absolute ages. Some examples include crater density studies and degradation of ≤3 km in diameter craters [*Soderblom*, 1970; *Swann and Reed*, 1974]. The majority of these methods only yield a relative sequence of events. In this study, we calibrate a previous relative dating method based upon crater degradation states to absolute model ages so that future studies can easily and quickly estimate ages of small-scale spatial features.

We calibrate the degree of freshness, a relative dating category created by *Pohn and Offield* [1970], which shown to be successful in the past [*Wilhelms*, 1987]. In this work, we adopt their relative dating method to yield absolute model ages for lunar impact craters ~1–20 km in diameter. As a result, this project provides a reconnaissance tool to constrain absolute model ages of surfaces and features based upon the morphology of craters. Additionally, we can document the changes in crater morphology with time and increasing degradation. This calibration is only applicable to the Moon, however, future work could expand this method to larger crater diameters and other planetary bodies.

3.2 Background

There are several surface processes that change the appearance of a crater over time (**Figure 3.1**). These physical changes include a decrease in crater ray brightness, the disappearance of secondary craters, degradation of rim and terrace sharpness, loss of rim texture, change in crater shape, channel development on crater walls, and an increase in number of superimposed craters (**Figure 3.2)**. The surface processes that degrade impact craters include space weathering [e.g., *Gold*, 1955; *McKay et al.*, 1991; *Hapke*, 2001], seismic shaking [e.g., *Titley*, 1966, *Schultz and Gault*, 1975], mass wasting [*Pike*, 1971; *Lindsay*, 1976; *Xiao et al.*, 2013], and impacts [*Soderblom*, 1970; *Oberbeck*, 1975; *Head,* 1975].

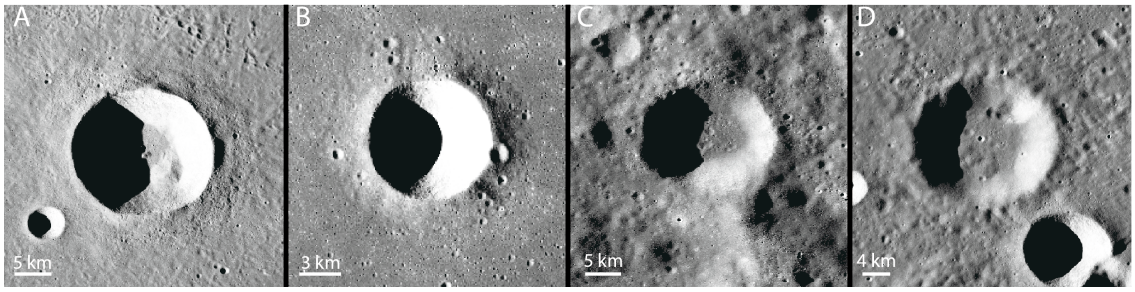

Figure 3.1: Kaguya Terrain Camera images of lunar craters with increasing degradation or decreasing degree of freshness from left to right. A) Diophantus (6.3) B) Marius D (5.4) C) Hainzel L (4.2) D) Rothmann C (3.4).

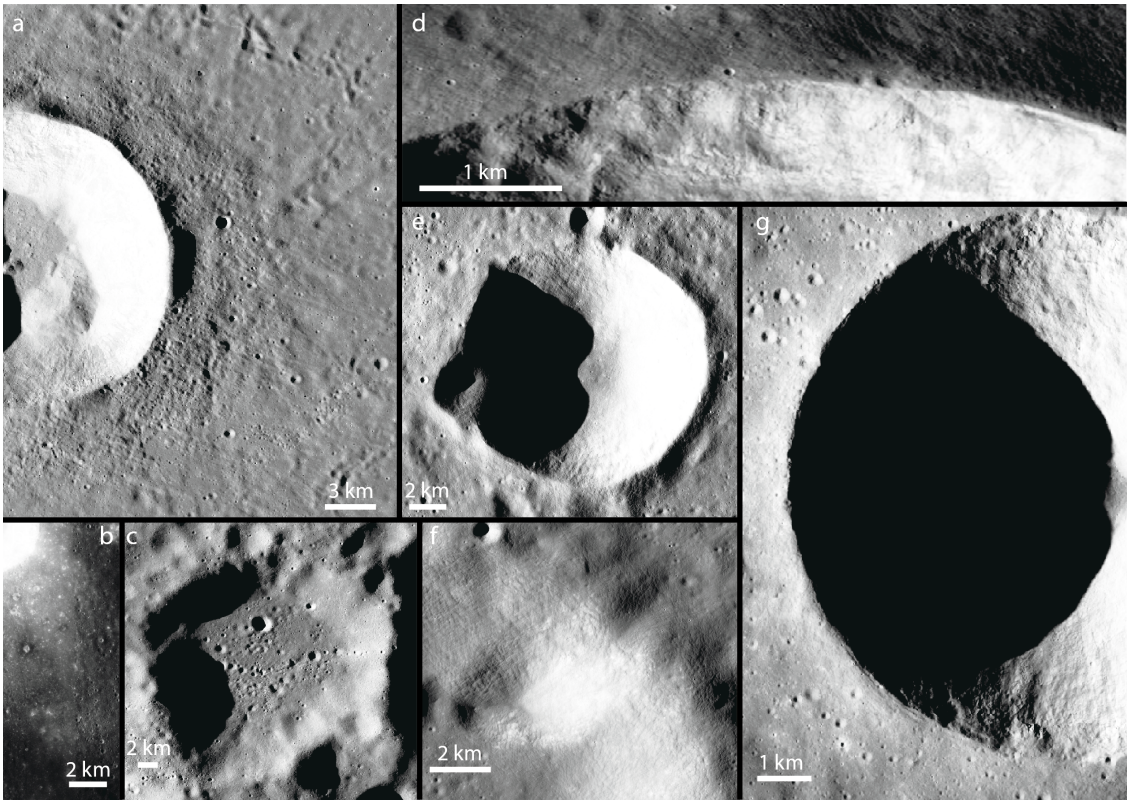

Figure 3.2: Kaguya Terrain Camera and Multispectral Imager images of seven crater features observed by Pohn and Offield [1970] to appear and disappear as a crater degrades with time. a) Secondary crater field b) Bright crater ejecta over mare c) Polygonality or circularity of a crater and the shallower depth of the crater d) Rim sharpness and texture e) Superimposing craters on the main crater f) A channel sloping to the bottom left on a crater wall g) Rim shadow shape and the smoothness of the crater wall.

Each lunar surface process degrades different aspects of impact craters. For instance, the effects of space weathering erases crater rays [e.g., *Adams and Jones*, 1970; *Hapke*, 2001]. The length of time required for crater rays to blend into the background is dependent on latitude and crater size [*Werner and Medvedev*, 2010]. However, a minor class of crater rays, called compositional crater rays, does not blend into the surrounding area [see *Hawke et al.*, 2004]. In another degradation process, seismic shaking from nearby impacts can initiate mass wasting [*Titley*, 1966; *Schultz and Gault*, 1975; *Lindsay*, 1976; *Howard*, 1973; *Xiao et al.*, 2013]. *Titley* [1966] suggested that seismic shaking results in compaction, debris creep, and slope failures. Consequently, the downslope movement of material causes the degradation of the crater rim, wall, and terraces, which fills in the crater [*Head*, 1975]. Also, the wall slope becomes gentler and the crater diameter becomes wider. Another surface process involves the addition of material from nearby impacts. The ejecta from new impacts could drape or destroy the preexisting ejecta deposits and also fill craters through lateral sedimentation [*Oberbeck*, 1975; *Head*, 1975]. Another contributor to crater degradation is direct impacts into a pre-existing crater. Direct hits into the crater wall results in radial indentations [*Head*, 1975].

After studying the images of more than a thousand lunar impact craters, *Pohn and Offield* [1970] observed a degradation continuum for impact craters, which they assumed to reflect crater age. Within the continuum, they noticed seven easily identifiable degradation stages. These seven stages became the base of their relative dating category. *Pohn and Offield* [1970] developed a decimalized ranking system from 0.0 (highly degraded and oldest) to 7.0 (very fresh and youngest), where each positive integer represents one of the seven major stages. Intermediate ranks are craters transitioning between stages. In this study, we call their ranking system the degree of freshness. The degree of freshness of a crater is dependent on the overall crater morphology such as the presence of continuous ejecta, crater rays, channels on the wall, and the smoothness of the crater wall and rim. Other features that contribute to the ranking system include the crater geometry, crater depth, the shape of the shadow of the crater rim imposed on the crater floor, and the number of smaller superimposing craters. In relation to time, *Pohn and Offield* [1970] inferred that their relative age dating categories do not represent equal spans of time because they hypothesized that erosional rates are not linear.

Pohn and Offield [1970] noticed that the degradation continuum of a crater is dependent on its initial crater geometry. As a result, *Pohn and Offield* [1970] divided the craters into three

classes based upon the initial plan-view shape of the rim crest. They developed three different degree of freshness systems for each class. The first class, Class I, contains circular craters with rim crenulations. Class I craters are typically craters with diameters >45 km. Class II craters have polygonal rim crests, which are usually representative of 20–45 km in diameter craters. The last class, Class III, are round in plan view and are typically ~8–20 km in diameter. *Wilhelms* [1987] simplified the classes where Class I and II craters are complex craters and Class III craters are simple craters [*Wilhelms*, 1987]. In this study, we focus on Class III craters.

Initially, the minimum diameter of Class III craters is 8 km because *Pohn and Offield* [1970] observed that craters <8 km in diameter degrade at an accelerated rate. *Offield and Pohn* [1970] investigated the accelerated degradation of <8 km craters. First, they looked for the most subdued craters at various diameters on each of the four regional geologic units (i.e., Corpernicus ejecta, Orientale blanket, Imbrium blanket, and Crisium rim). They assumed that the most subdued craters at the various diameters for each geologic unit have the same age. Thus, these craters should have the same degree of freshness. However, for <8 km craters, they found a decrease in degree of freshness with decreasing crater diameter. In other words, the smaller the crater, the faster it degrades. To account for the increase degradation rate in smaller craters, *Offield and Pohn* [1970] provided graphical offset curves (see **Figure 3** in *Offield and Pohn,* [1970]) to adjust the observed degree of freshness to the correct degree of freshness. Therefore, Class III includes craters down to 1 km in diameter with the offset curves. However, the use of the offset curves require visual interpolation, which could result in unreliable corrections to the degree of freshness.

Previously, *Swann and Reed* [1974] and *Head* [1975] attempted to relate crater degradation states to absolute ages. *Swann and Reed* [1974] calibrated a ranking system formed by *Trask*, [1971] to absolute ages. However, *Trask's* [1971] ranking system is only applicable to craters ≤3 km in diameter. Later, *Head* [1975] linked the degree of freshness of Copernicus crater, Eratosthenes crater, and Imbrium basin to absolute ages. Based upon the absolute ages of returned samples, *Head* [1975] estimated that the start of the Imbrian, Eratosthenian and Copernican periods to be a degree of freshness of 4.2, 5.5 and 6.0, respectively. In contrast to previous work, we calibrate the degradation state of larger craters than the craters in *Swann and Reed* [1974] and smaller craters than the ones in *Head* [1975]. Additionally, our calibration relies on more points to calibrate the degree of freshness to absolute model ages than previous workers.

The primary objective of this project is to calibrate *Pohn and Offield's* [1970] degree of freshness ranking system for Class III craters to absolute model ages. Our sample consists of fifteen Class III craters that were previously ranked by *Pohn and Offield* [1969; 1970] and *Offield and Pohn* [1970]. For each Class III crater, we calculate their absolute model ages through crater density measurements on their continuous ejecta blankets. Next, we fit a regression through the fifteen Class III craters to find an equation that calculates absolute model ages from the degree of freshness. The second objective is to empirically fit a function to *Offield and Pohn's* [1970] graphical offset curves. The use of *Offield and Pohn's* [1970] graphical offset curves relies on visual interpolation. To remove possible errors from visual interpolation, we create an equation that will estimate the corrected degree of freshness for <8 km craters.

There are three advantages in using the degree of freshness to date geomorphological features and surfaces: 1) dating through crater degradation is quick, best applied as a reconnaissance tool, especially for dating a large number of areas or features 2) unlike crater density measurements, statistical requirements do not limit the degree of freshness method (e.g., size of the area of interest) 3) crater counting becomes an unreliable method when the continuous ejecta lies on rough topography or underneath subsequent lava flows. Hence, the degree of freshness is another dating method that allows more reliable ages for certain scenarios than previous methods.

3.3 Methods

3.3.1 Crater Counting

In this study, we use fifteen primary Class III craters to calibrate the degree of freshness to absolute model ages (**Table 3.1**). We choose craters from tables and figures within *Pohn and Offield* [1969, 1970] and *Offield and Pohn* [1970] (see **Figure 2** of *Pohn and Offield* [1969,1970] and **Table 1** of *Offield and Pohn* [1970]) because the assigned degree of freshness of these craters already vetted through peer review. We try to select craters that sample a wide degree of freshness range at equal intervals. Also, we want craters that occur on flat topography and exhibit minimal superposed secondary impacts. As a result, our sample spans from very fresh (6.3) to highly degraded (2.5) with diameters ranging from 4.7–22.1 km in diameter. The sample craters with degree of freshness of 5.0 to 6.3 are mostly from the maria, whereas older craters are from the highlands (**Table 3.1**). This bias exists because the most ideal crater for this study occurs in the maria (i.e., least affected by pre-existing topography). On the other hand, our

older crater samples originate from the highlands because of the lack of very degraded craters in the maria. For five of our sample craters, *Pohn and Offield* [1969, 1970] and *Offield and Pohn* [1970] assigned a range of possible degree of freshness ranks instead of a discrete rank. When this is the case, we use the mean of the range of degree of freshness and round to the nearest tenth.

We employ high and low sun-angle basemaps derived from Kaguya Terrain Camera to measure crater density. The Terrain Camera is a panchromatic push-broom stereoscopic imager with a spatial resolution of ~10 m/pixel [*Haruyama et al.*, 2008]. The data from the Terrain Camera resulted in three global data sets, a high solar-elevation map, and two low solar-elevation maps called, "evening" and "morning". The morning and evening maps have solar incidence angles of <30°. The low sun-angle allows for easier detection of sub-kilometer sized craters and more accurate measurements of apparent crater diameter [*Young*, 1975; *Ostrach et al.*, 2011]. In addition, we use high solar-elevation maps to detect any craters hidden in shadow in the evening and morning maps. Although higher resolution images exist, specifically, the Lunar Reconnaissance Orbiter Camera (LROC)-Narrow Angle Camera (NAC), the Terrain Camera data has complete areal coverage of the continuous ejecta at consistent sun angles. Furthermore, we only need to count craters that are >100 m in diameter. We downloaded the Terrain Camera data products from the SELENE data archive (http://l2db.selene.darts.isas.jaxa.jp/). Next, we added the georeferencing information and mosaicked the data with the Integrated Software for Imagers and Spectrometers (ISIS 3). Afterward, we import the data into ArcGIS for crater counting.

We limit the counting area to the continuous ejecta deposit of each crater. The continuous ejecta deposit constitutes the crater rim to one-crater radii beyond the crater rim (**Figure 3.3**). In some cases, especially craters with high degree of freshness, we avoid counting near the rim of the main crater because the slope of the rim tends to be steep. The relative steepness may promote mass wasting, which causes craters to disappear quickly [*Xiao et al.*, 2013]. Consequently, the rim may contain an artificially low crater density. In addition, we excluded areas within the continuous ejecta that contain a high proportion of secondary craters. We identify secondary craters from their tight crater clusters with similar preservation states, shapes and sizes.

For each Class III impact crater, we estimate the absolute model age from our crater counts on the continuous ejecta. We count craters using the crater counting extension tool created by *Kneissl et al.* [2011] in ArcGIS. Next, we import the crater counts into *craterstats2*, a program developed by *Michael and Neukum* [2011]. Afterward, we use *Neukum et al.'s* [2001] production and chronology functions to calculate an absolute model age of each crater in our sample. We bin the counted craters in such that the ratio of the largest to smallest crater diameter interval is equal to the square root of two [*Crater Analysis Techniques Working Group*, 1979]. The absolute model age calculation only includes craters >100 m in diameter (i.e., Diophantus, Manilius D) because experts can only consistently detect craters ≥10 pixels across [*Robbins et al.*, 2014]. For most craters in our sample, we observe that the continuous ejecta have reached the

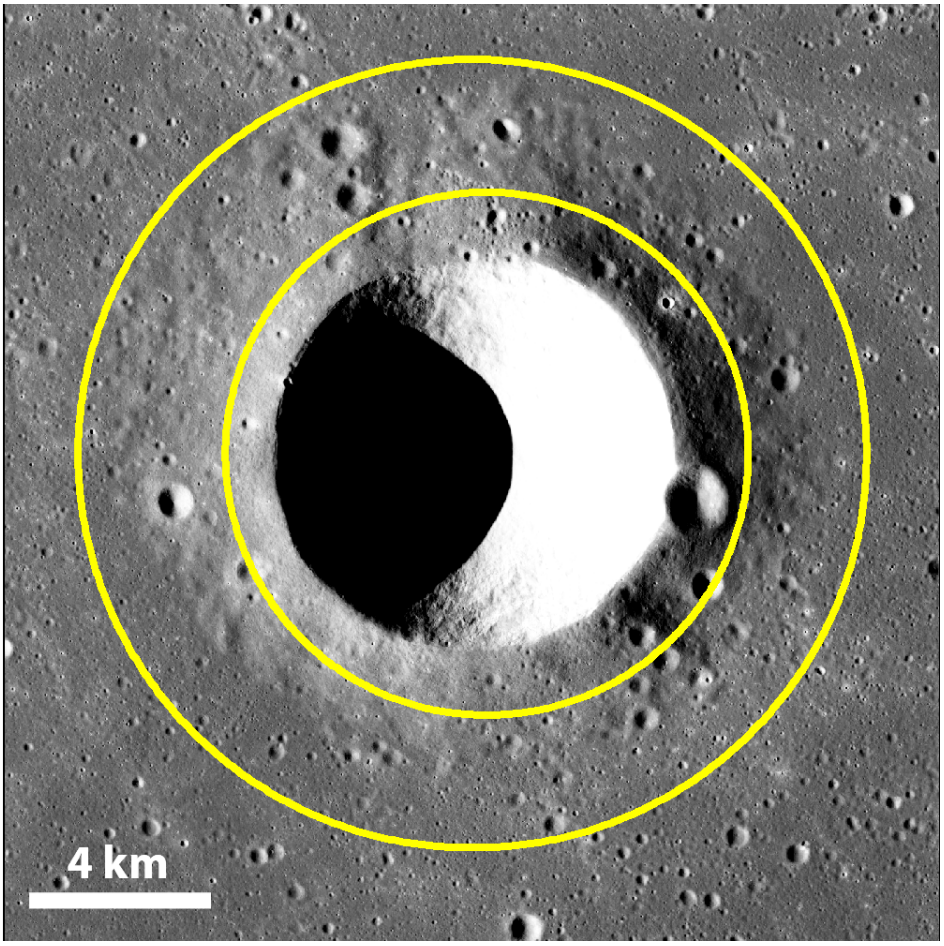

Figure 3.3: The yellow annulus represents the continuous ejecta where the craters were counted. Between the rim crest and the inner annulus is where the density of craters is much smaller due to higher erosion rates of small craters.

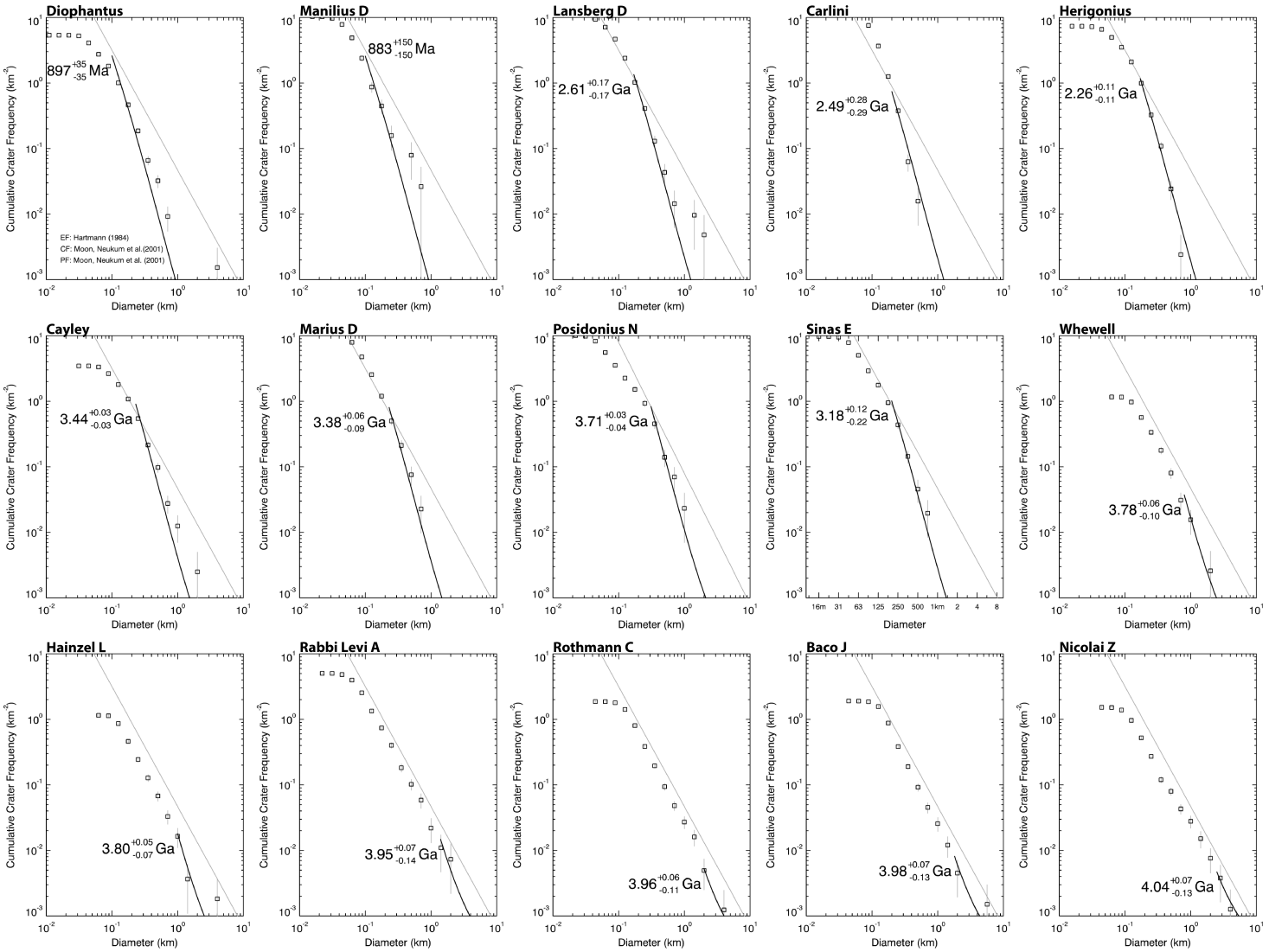

Figure 3.4: Cumulative size-frequency distribution of fifteen craters. The gray solid line is the saturation line from Hartmann [1984].

Table 3.1: Data of the fifteen craters and crater counting

Crater	Lat.	Long.	Diam. (km)	Region	Degree of Freshness			Age								
					Degree of Freshness	Mean	Error	Area [km^2]	No. of Craters	Age	Age +Error	Age - Error	Diameter Range (km)	Saturation Diam.	N(1)	N(0.3)
Diophantus	27.6	-34.3	17.6	Mare	6.3	6.3	0.1	652	656	0.9	0.0	0.0	0.1–∞	0.10	0.002	0.106
Manilius D	13.2	7.0	4.7	Mare	6.0–6.1	6.1	0.1	38	33	0.9	0.2	0.2	0.1–∞	0.10	0.000	0.079
Lansberg D	-3.0	-30.6	10.5	Mare	6.0	6.0	0.1	208	213	2.6	0.2	0.2	0.17–∞	0.17	0.010	0.250
Carlini	33.8	-24.1	10.7	Mare	5.6–5.8	5.7	0.1	191	72	2.5	0.3	0.3	0.2–∞	0.20	0.000	0.178
Herigonius	-13.4	-34.0	14.9	Mare	5.5–5.6	5.6	0.1	414	411	2.3	0.1	0.1	0.17–∞	0.17	0.000	0.179
Cayley	3.9	15.1	14.2	Highlands	5.5	5.5	0.1	399	217	3.4	0.0	0.0	0.23–∞	0.23	0.013	0.348
Marius D	11.4	-45.1	8.7	Mare	5.3–5.4	5.4	0.1	132	66	3.4	0.1	0.1	0.23–∞	0.23	0.000	0.333
Posidonius N	29.7	21.0	6.2	Mare	5.3	5.3	0.1	86	39	3.7	0.0	0.0	0.31–∞	0.31	0.023	0.628
Sinas E	9.7	31.0	8.7	Mare	5.0	5.0	0.2	153	67	3.2	0.1	0.2	0.2–∞	0.20	0.000	0.222
Whewell	4.2	13.7	13.1	Highlands	4.9	4.9	0.2	386	12	3.8	0.1	0.1	0.8–∞	0.35	0.016	0.254
Hainzel L	-38.1	-35.0	15.2	Highlands	4.1–4.2	4.2	0.2	547	9	3.8	0.1	0.1	1–∞	0.50	0.016	0.181
Rabbi Levi A	-34.4	22.7	11.5	Highlands	4.2	4.2	0.2	273	3	4.0	0.1	0.1	1.4–∞	0.70	0.022	0.289
Rothmann C*	-28.6	25.0	17.9	Highlands	3.4	3.4	0.2	809	4	4.0	0.1	0.1	2–∞	1.00	0.027	0.274
Baco J	-54.8	19.3	16.6	Highlands	3.0	3.0	0.3	663	3	4.0	0.1	0.1	1.8–∞	0.90	0.026	0.264
Nicolai Z	-41.0	21.5	22.1	Highlands	2.5	2.5	0.3	791	3	4.0	0.1	0.1	2.5–∞	2.50	0.028	0.188

*Rothmann C is listed as Rothmann H in *Pohn and Offield* [1969]. However, the figure and the description in *Pohn and Offield* [1969] match Rothmann C.

Hartmann [1984] crater saturation line (**Figure 3.4**). When crater saturation occurs, we only include bins that are below the *Hartmann* [1984] saturation line into the absolute model age calculation (**Table 3.1**) (i.e., Lansberg D, Carlini, Herigonius, Cayley, Marius D, Posidonius N, Sinas E). For highlands craters, except Cayley, the positions of the bins exhibit a similar slope as the *Hartmann* [1984] saturation curve, but at a lower cumulative crater frequency (**Figure 3.4**) (i.e., Whewell, Hainzel L, Rabbi Levi A, Rothmann C, Baco J, Nicolai Z). This displacement of the *Hartmann* [1984] saturation line is probably because the continuous ejecta is overlaying rough topography, which causes craters to disappear at an accelerated rate. Therefore, for highlands craters, the smallest bin diameter included in the absolute model age calculation is twice the diameter of the smallest bin before saturation. Occasionally, we use the smallest bin before the saturation line to boost the number of craters for the absolute model age calculation. After computing the absolute model age of each crater, we fit a function that best describes the relationship between the degree of freshness and absolute model age.

3.4 Results

3.4.1 Calibration of Class III Craters (8–20 km in Diameter)

Figure 3.5 and **Table 3.1** summarizes the results of the degree of freshness to absolute model age calibration. The craters in **Figure 3.5a** show two linear trends, a steeper linear trend for relatively fresh craters and a flatter linear trend for relatively degraded craters. The intersection of the two trends is sharp and occurs at a degree of freshness of ~5. We model these two trends with two separate least-squares linear regressions **Figure 3.5b**. The fresher crater regression relies on ten craters with the highest degree of freshness (4.9 to 6.3) within our samples. The linear regression has a form of

$$A = -2.000 \cdot F + 13.821 \qquad (3.1),$$

where A is the absolute model age in Ga and F is the degree of freshness. The correlation coefficient of this fit is 0.74. Interestingly, our trend for fresher craters intersects the present day (0.0 Ga) at a degree of freshness of about 6.9, which is close to the highest rank in the scale, 7.0. If we extrapolate equation (3.1) to an age of 4.5 Ga, a rough approximation of the age of the Solar System, we get a degree of freshness of 4.7. Hence, this calibration requires two regressions.

The more degraded crater regression relies on the six most degraded craters (2.5–4.9) in our sample. The fit result is

$$A = -0.104 \cdot F + 4.302 \qquad (3.2).$$

The correlation coefficient for this linear regression is 0.78. If we extrapolate this function to a degree of freshness of 0.0, we find that the age would be about 4.3 Ga. On the other side, if we extrapolate this function to a degree of freshness of 7.0, the calculated age is 3.6 Ga.

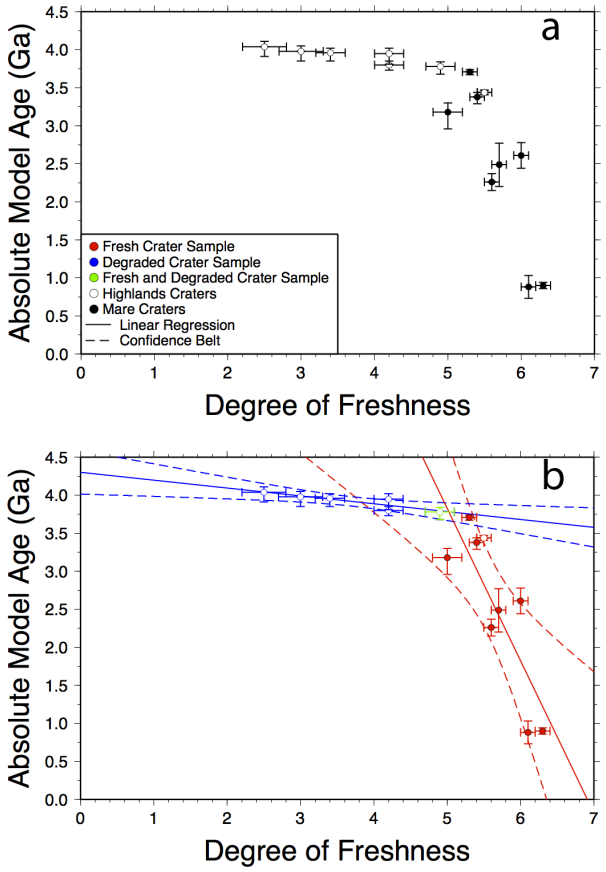

Figure 3.5: a) Degree of freshness versus absolute model ages and. Hollow points are craters in the highlands and solid points are craters in the maria. b) The degree of freshness against absolute model ages where red points used for the fresher crater regression (red solid), blue points used in calculating the degraded crater regression (blue solid) and green points used in both fresher and degraded crater regression. The dotted lines are the 95% confidence belts.

To force our calibration to be continuous, we calculate the intersection between the two linear regressions. The two linear regressions intersect at a degree of freshness of 5.0 or around

3.8 Ga. Therefore, we recommend using equation (3.1) for craters with a degree of freshness between 5.0–7.0 and equation (3.2) for craters with a degree of freshness between 0.0–4.9.

Pohn and Offield [1970] tested the consistency of the degree of freshness method by asking several lunar mappers to assign degrees of freshness ranks for several craters. They observed that the older the crater, the larger the error in ranking the degree of freshness. Specifically, at degrees of freshness of 6.0, 4.0, and 1.0, the error is ±0.1, ±0.2, and ±0.4, respectively. We calculate the linear regression for these errors so that in future studies, the degree of freshness error is known at other ranks. The degree of freshness error takes the form of

$$E = -0.061 \cdot F + 0.455 \quad (3.3),$$

where E is the magnitude of the degree of freshness error.

We compute the 95% confidence levels around the two regressions (**Figure 3.5b**) (descriptions of this calculation can be found in *Davis* [2002]). For the fresher crater regression, the 95% confidence is at worst at a degree of freshness of ~6.4 with an error of ±1.1 Gyr. At best, the predicted absolute model age is ±0.5 Gyr at a degree of freshness of 5.6. As for the more degraded crater regression, the 95% confidence is at worse ±0.3 Gyr at the degree of freshness of 0.0. At best, the error is ±0.1 Gyr at a degree of freshness of 3.7. Based upon the 95% confidence belt of the degraded crater trend, the degraded crater trend appears more reliable than the fresher crater trend, but the degraded crater trend varies over 5.0 ranks for a small time interval of 500 Myr. This time interval is smaller than the narrowest section of the 95% confidence belt of the fresher crater trend (±0.5 Ga).

3.4.2 Corresponding Lunar Geologic Periods with Degree of Freshness

After calibrating the degree of freshness to absolute model ages, we estimate the corresponding degree of freshness to each lunar period boundary (**Table 3.2**). Here, we use the period boundaries defined by *Wilhelms* [1987]. The five periods are the Pre-Nectarian (>3.92 Ga), Nectarian (3.92–3.85 Ga), Imbrian (3.85–3.2 Ga), Eratosthenian (3.2–1.1 Ga), and Copernican (<1.1 Ga). From our conversion, we find that the base of the Nectarian (3.92 Ga), Imbrian (3.85 Ga), Eratosthenian (3.2 Ga), and Copernican period (1.1 Ga) is 3.7, 4.4, 5.3, and 6.4, respectively. In **Table 3.2**, we summarize the degree of freshness range within the 95% confidence belt for each period.

The corresponding degree of freshness to each period in our work is different from predictions by [*Head*, 1975]. *Head* [1975] related the degree of freshness from *Pohn and Offield*

[1970] and *Offield and Pohn* [1970] to return sample ages of Imbrium basin, Eratosthenes, and Copernicus crater and used these three features as the base to their respective time periods (i.e., Imbrian, Eratosthenian, Copernican, respectively). The results of this study and *Head* [1975] for the base of Imbrian, Eratosthenian and Copernican periods are within a degree of freshness of 0.2–0.4 (**Table 3.2**). There are two possible reasons for the difference between the results of this study and *Head* [1975]: 1) *Head* [1975] used Class I craters (i.e., Eratosthenian and Copernican), which relies on a different degree of freshness system 2) the base of each period is slightly different between the two studies due to improved interpretation of lunar sample data over time.

Table 3.2: Corresponding Degree of Freshness to Periods

Corresponding Degree of Freshness to Periods

	Base Age	Degree of Freshness [Head, 1975]	Degree of Freshness	95% Confidence Range
Nectarian	3.92		3.7	2.7–4.6
Imbrian	3.85	4.2	4.4	3.7–5.2
Eratosthenian	3.2	5.5	5.3	5.0–5.5
Copernican	1.1	6	6.4	6.0–7.0

3.4.3 An Additional Correction for 1–8 km Craters

So far, we produced an equation that relates the degree of freshness to absolute model ages for craters approximately between 8–20 km. The lower diameter limit for Class III craters is 8 km because *Pohn and Offield* [1970] observed that craters <8 km in diameter degrade at an accelerated rate relative to larger craters. *Offield and Pohn* [1970] investigated the relationship between degree of freshness and crater diameter on four different regional geologic units: Crisim rim, the Imbrium and Orientale ejecta blanket, and Copernicus ejecta. Within each regional geologic unit, *Offield and Pohn* [1970] plotted the most degraded craters at various diameters. They assumed that the oldest craters at the various diameters within each unit formed at the same time (same age); thus the oldest craters at the various diameters should have the same degree of freshness. However, they observed that for all four surfaces, the degree of freshness decreases nonlinearly (**Figure 3.6**) for <8 km craters.

To account for this accelerated deterioration rate as a function of crater size, *Offield and Pohn* [1970] constructed graphical offset curves (**Figure 3.6** and **Figure 3.3** in *Offield and Pohn*, [1970]). The offset curves aids the user to readjust the degree of freshness of <8 km craters to an

equivalent degree of freshness of a crater >8 km. The weakness in this graphical solution is that correcting the degree of freshness of a small crater requires visual interpolation. For instance, if a user ranks a 4 km crater with a degree of freshness of 4.9, the user must visually interpolate from the *Offield and Pohn's* [1970] offset curves to correct the degree of freshness without any points in the vicinity to guide the user to the correct degree of freshness. In this section, we create an empirical fit through the data in **Figure 3.6** that allows accurate interpolation of the graphical offset curves. Therefore, we extend the lower diameter limit of this calibration between degree of freshness and absolute model ages from 8 km in diameter to 1 km.

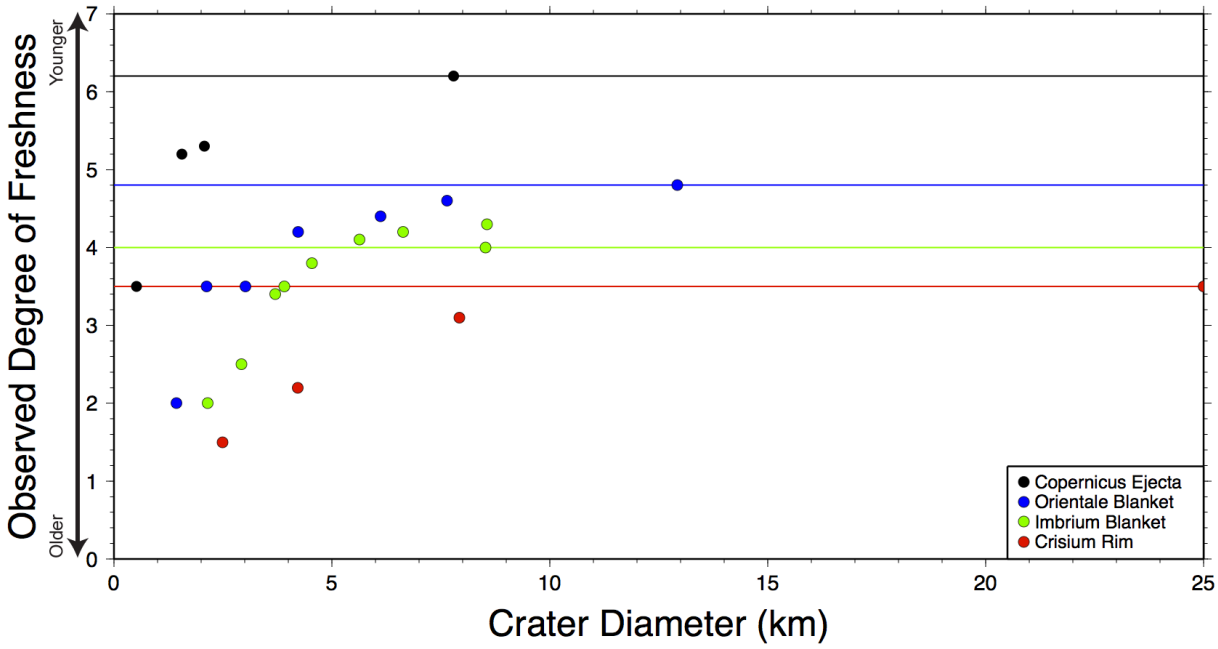

Figure 3.6: Each color represents a regional isochronous geologic unit: Copernicus ejecta (black), Orientale blanket (blue), Imbrium blanket (green), and Crisium rim (red). The points are the most subdued crater of that given diameter. The lines represent the approximate correct degree of freshness of that surface. The observed degree of freshness of <8 km in diameter craters appears older with decreasing crater size assuming that the craters in each set are of the same age. The points are taken from *Offield and Pohn* [1970].

For each point in **Figure 3.6**, we need three variables, 1) the observed and 2) corrected degree of freshness, and 3) the crater diameter. In **Figure 3.6**, four different sets of points represent the most subdued craters on the four different isochronous regional geologic units

[*Offield and Pohn,* 1970]. *Offield and Pohn* [1970] assumed each set of points to have formed at the same time. We estimate the relative age of each unit from the most degraded >8 km crater or the degree of freshness of the largest crater in each set (the lines in **Figure 3.6**). The corrected degree of freshness for each set of points is the relative age of each unit. The correct degree of freshness is approximately 6.2 (**Figure 3.6**, black) for the Copernicus ejecta, 4.8 (**Figure 3.6**, blue) for the Orientale blanket, 4.0 (**Figure 3.6**, green) for the Imbrium blanket, and 3.5 (**Figure 3.6**, red) for Crisium rim.

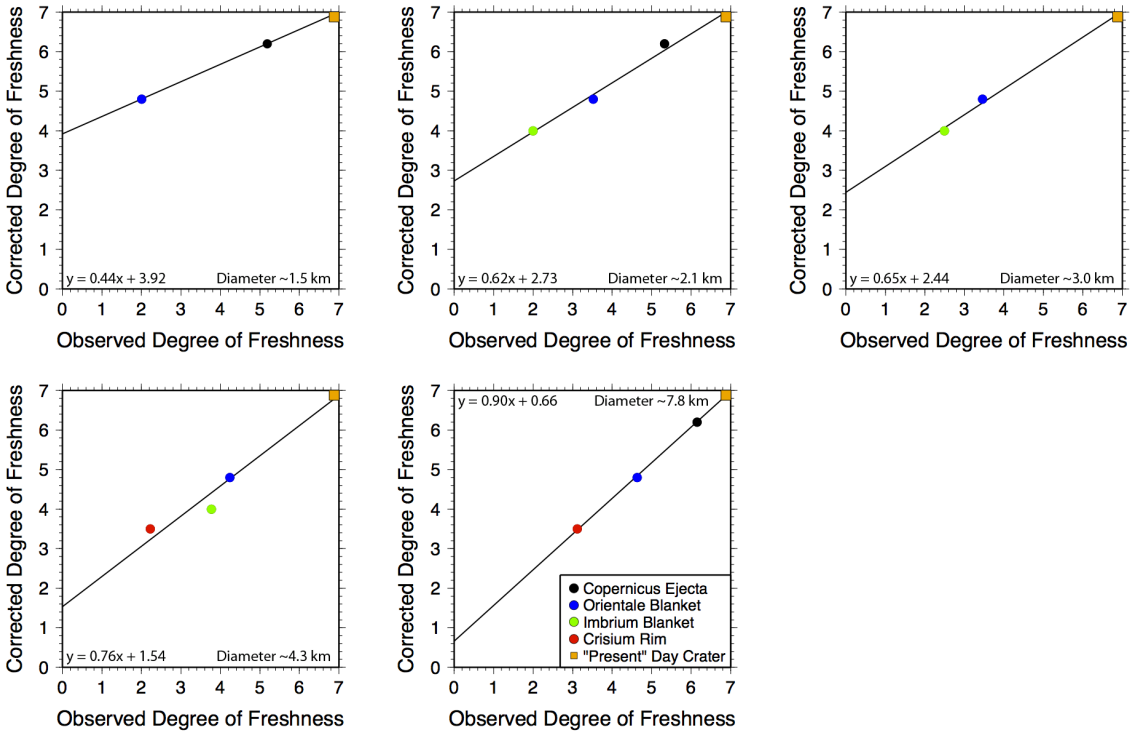

Figure 3.7: Each point in **Figure 3.6** contains a diameter, observed, and corrected degree of freshness. This is a replot of points from **Figure 3.6** with respect to the observed degree of freshness and the corrected degree of freshness. An additional point (orange square) was added at an observed and corrected degree of freshness of 7.0 because the freshest crater should have the same observed and corrected degree of freshness because they had no time to degrade. This added point helps gauge the relationship between the observed and corrected degree of freshness. Again, the colors are craters from Copernicus ejecta (black), Orientale blanket (blue), Imbrium blanket (green), and Crisium rim (red).

To create an empirical fit through the points in **Figure 3.6**, first we examine how the correct degree of freshness changes as a function of the observed degree of degradation at approximately constant crater diameter (i.e., 1.5, 2.1, 3.0, 4.3, and 7.8 km) (**Figure 3.7**). We also include additional points at an observed degree of freshness of 7.0 (orange squares in **Figure 3.7**), the youngest possible degree of freshness, which we assume represents 0.0 Ga or present day. Thus, a crater with an observed degree of freshness of 7.0 should have a corrected degree of freshness of 7.0 because the crater had no time to degrade. We find that the relationship between the observed and corrected degree of freshness is linear. As a result, at all five separate constant diameters, we use a linear regression (**Figure 3.7**), which has a generic form of

$$F = m \cdot f + b \,, \quad (3.4)$$

where F is the corrected degree of freshness, f is the observed degree of freshness, and m and b are constants. From smallest to largest crater diameter, we observe the slope of the linear regression (m) becomes steeper and the y-intercept (b) shift to lower ranks (**Figure 3.7**). Next, we compare the m and b constants as a function of crater diameter (**Figure 3.8**). We find that m behaves linearly and b changes exponentially as a function of crater diameter. Afterward, we substitute in the regressions for m and b into equation (3.4), which transforms into

$$F = (p \cdot D + q) \cdot f + (r \cdot exp^{s \cdot D}) \,, \quad (3.5)$$

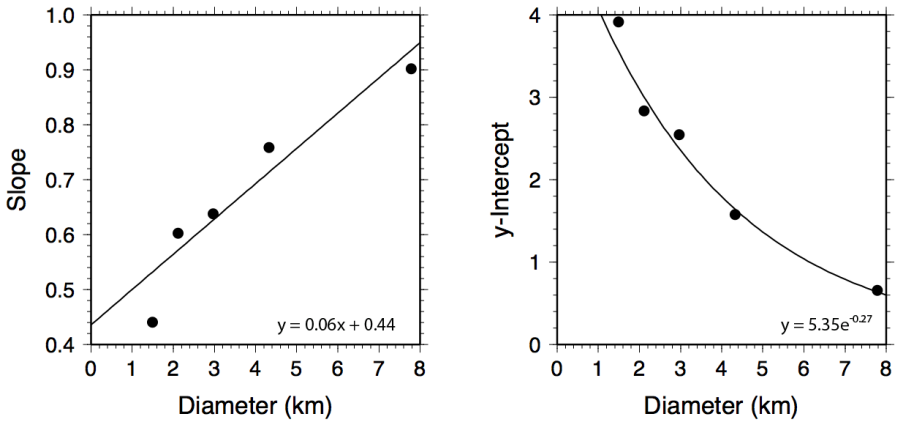

Figure 3.8: Graph of the slope (m) and y-intercept (b) from the linear regression in **Figure 3.7** to investigate how they change with respect to crater diameter. The slope (m) is linear and the y-intercept (b) is an exponential.

where D is the crater diameter in kilometers and p, q, r, and s are constants. We fine-tune the constants using MPFIT, a user-produced curve-fitting routine for IDL (Interactive Data Language) [*Markwardt*, 2009], to all <8 km craters in *Offield and Pohn* [1970]'s graphical offset curves. The results of this program find that p, q, r, and s are 0.057, 0.445, 5.321, and -0.272 respectively. Thus, equation (3.5) becomes

$$F = (0.057 \cdot D + 0.445) \cdot f + (5.321 \cdot exp^{-0.272 \cdot D}). \quad (3.6)$$

The degree of freshness error for craters <8 km in diameter must propagate through equation (3.6) too. To determine the degree of freshness error, first find the degree of freshness error for the associated observed degree of freshness. Next, add the errors to the observed degree of freshness, which results in a maximum and minimum degree of freshness. Then, propagate the maximum and minimum degree of freshness through equation (3.6) in order to determine the error associated with the corrected degree of freshness. For example, if a 3 km crater has an observed degree of freshness of 4.8, it would have a degree of freshness error of 0.2 where the minimum and maximum observed degree of freshness is 4.6 and 5.0, respectively. When correcting the degree of freshness with equation (3.6), the corrected degree of freshness of this crater is 5.3 with a corresponding maximum and minimum error of 5.4 and 5.2, respectively.

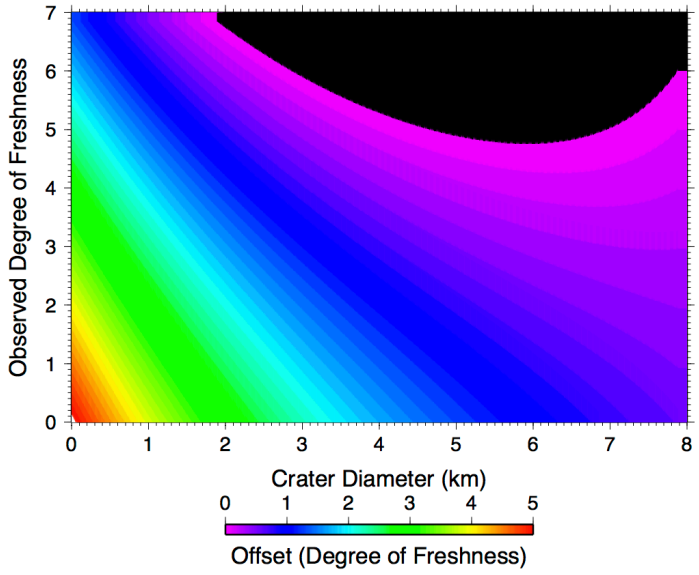

Figure 3.9: Each color represent the amount of offset in the degree of freshness with respect to the given crater diameter and observed degree of freshness. The lower the observed degree of freshness and smaller the crater, the larger the correction that is required. Conversely, a high

observed degree of freshness with a large crater requires smaller corrections. The black area represents where the offset is negative, in which this area is producing solutions that suggests craters should be more degraded than observed.

Manilius D, one of the fifteen craters used in this study has a diameter less than 8 km (**Table 3.1**). Thus, we should apply this correction to find the corrected degree of freshness of this crater. However, Manilius D is a young crater with a degree of freshness of 6.1. When applying equation (3.6), we calculate the new degree of freshness to 5.8, which incorrectly increases the age of the crater. From this example, we note that the empirical fit of the offset curve should not be used on young craters. The black area in **Figure 3.9** represents where the equation predicts an increase in crater age. Thus, craters <8 km in diameter with a degree of freshness in this black area of **Figure 3.9** should retain their observed degree of freshness.

3.4.4 Relationship Between Crater Density and Degree of Freshness

The relationship between degree of freshness and absolute model age is variable. Several researchers are constantly refining the relationship between cumulative crater frequency and absolute ages of return samples [e.g., *Neukum et al.*, 2001; *Robbins*, 2013], which is the relationship used to calculate an absolute model age from crater density. Consequently, equation (3.1 and 3.2) will be outdated in the future. Therefore, we present the results between the degree of freshness and cumulative crater frequency. Due to crater saturation in the degraded craters and the absence of kilometer-sized craters in the fresher craters, we derive two different relationships between the degree of freshness and cumulative crater frequency (**Figure 3.10**). The fresher crater relationship relies on the cumulative crater ≥300 m (**Figure 3.10a**) and the degraded crater relationship uses the cumulative craters ≥1 km craters (**Figure 3.10b**). The linear regression that describes the relationship between the degree of freshness and fresher cumulative craters ≥300 m is,

$$C_{\geq 0.3} = -0.232 \cdot F + 1.571 \qquad (3.7),$$

where $C_{\geq 0.3}$ is the cumulative ≥300 m craters per square kilometer and F is the degree of freshness. The correlation coefficient for the fresher crater regression is 0.34. This regression only includes nine craters with a degree of freshness of ≥5.0. The linear regression that describes the relationship between the degree of freshness and cumulative craters ≥1 km is,

$$C_{>1.0} = -0.006 \cdot F + 0.043 \qquad (3.8),$$

where $C_{\geq 1.0}$ is the cumulative craters ≥1 km craters per square kilometer, with a correlation coefficient of 0.81. When we compare the fresher crater regression from *Section 4.1* (degree of freshness versus absolute model ages) to the degree of freshness against crater density, we observe that there is more variation between the degree of freshness and crater density relationship. We observe that Sinas E is an outlier in the degree of freshness to absolute model regression. If Sinas E is also an outlier in the degree of freshness versus crater density regression, then an exponential function would appear to be more appropriate, which would tighten our fit.

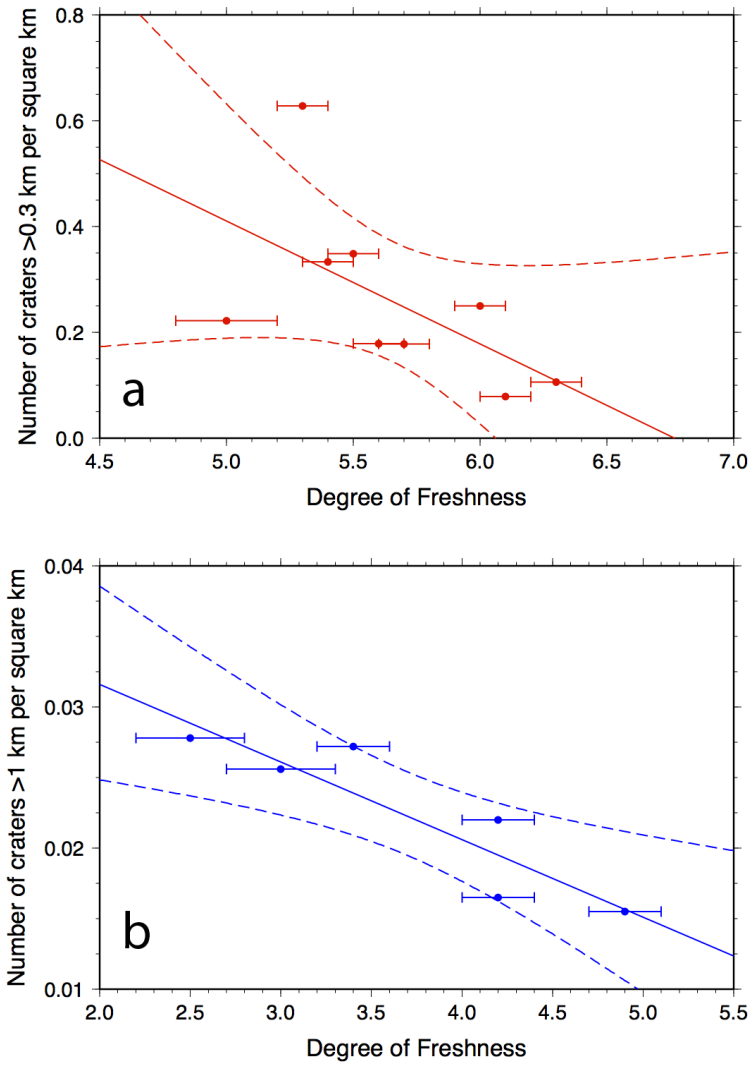

Figure 3.10: a) A fresher crater trend for cumulative craters ≥300 m per sq. km against degree of freshness. b) A degraded crater trend for cumulative craters ≥1 km per sq. km against degree of freshness.

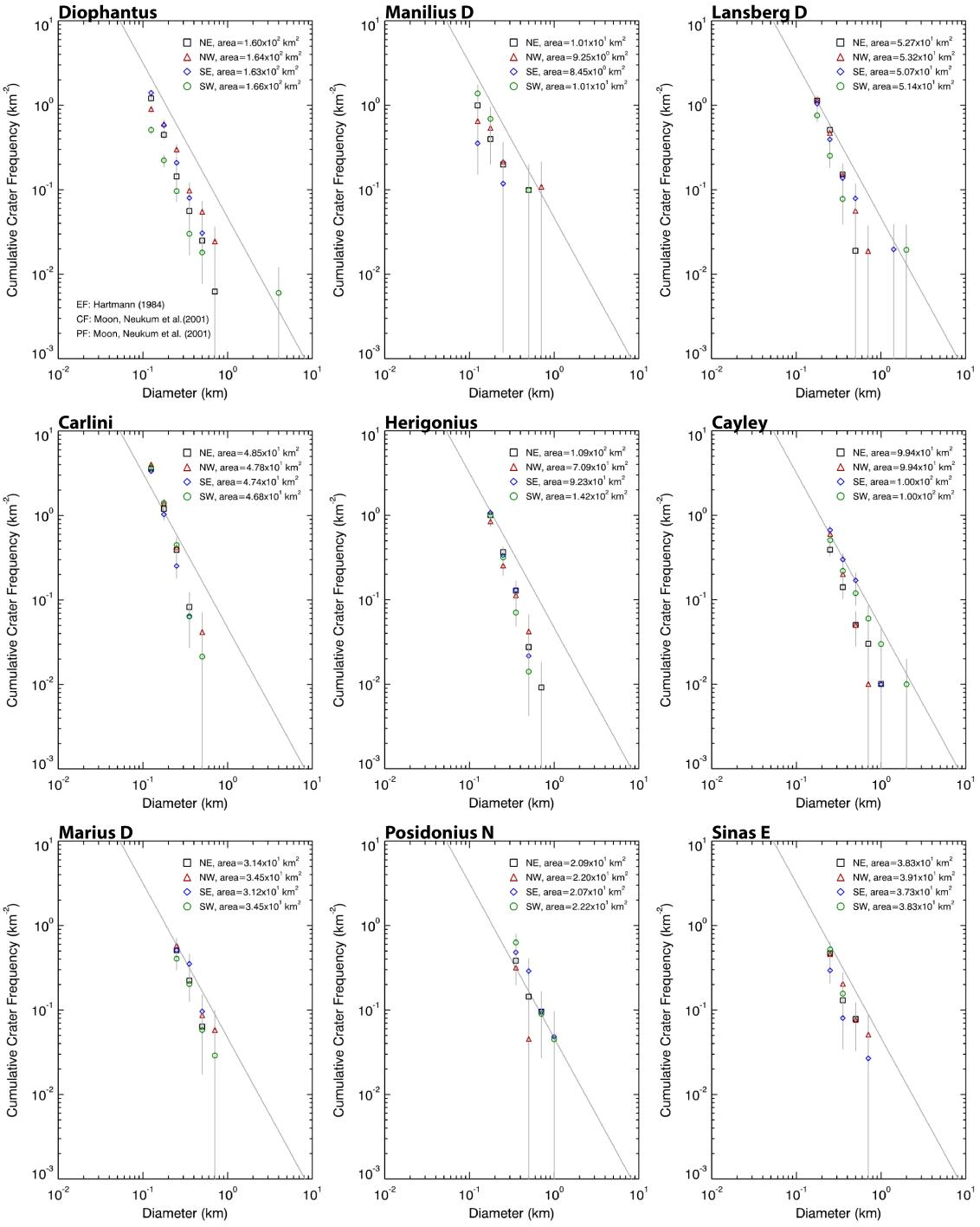

Figure 3.11: Plot of cumulative size-frequency distribution for the four quadrants of the nine of the freshest craters.

3.5 Discussion

3.5.1 Potential Variables Affecting Calibration

We investigated three variables that potentially affected the relationship between the degree of freshness and the absolute model ages. These variables include, material strength, variation in crater density on the continuous ejecta, and the observer counting the craters. One notable observation is that we use mostly mare craters to derive the fresher crater regression and highlands crater to derive the degraded crater regression. Recent preliminary studies show that material strength may affect other crater-related dating methods as well (e.g., *van der Bogert et al.* [2010] and *Fassett and Combellick* [2014]). *Van der Bogert et al.* [2010] suggested that impacts into highlands area produce larger craters than similar impacts into cohesive rock, such as the maria [*van der Bogert et al.*, 2010]. As a result, a crater density measurement of a set of craters on the highlands would indicate the surface is older than if the set of craters existed on the maria. We test the effects of material strength on our calibration by including the crater Cayley into our sample. In **Figure 3.5**, Cayley falls along the fresher crater trend instead of the degraded crater trend. Therefore, we infer that the effects of material strength on our calibration are negligible.

Another potential variable is the crater density variation throughout the continuous ejecta. *Zanetti et al.* [2013] measured the crater density on the continuous ejecta deposit of Aristarchus and Copernicus and found that the crater density is irregular throughout the deposit. They interpreted that at first, autosecondaries uniformly covered the continuous ejecta of the parent crater followed by an uneven distribution of impact melt covering some of the autosecondaries. Thus, this process led to the crater density variation throughout the continuous ejecta. Their preliminary study inclined us to study the crater density variation on craters.

We divide our count areas into quadrants with boundaries running north-south and east-west. This investigation only involves the nine youngest craters because the crater saturation diameter is limited to smaller crater diameters; hence more craters are available for the absolute model age calculation. In this investigation, we use the same minimum crater size from **Table 3.1** in determining the age of the quadrant. From this analysis, the standard deviation between the four quadrants decreases towards older craters, except for Sinas E. A potential explanation is that the crater density varies in younger craters due to uneven distribution of impact melt, but in older craters, such as Marius D (degree of freshness of 5.4), primary impact cratering dominates the

Table 3.3: Crater Density Variation for Nine Craters

Crater Density Variation

Crater	Area	Craters	Age	Age +error	Age -error	Mean Age	Std. Dev.
Diophantus	1.60E+02	194	0.93	0.07	0.07	0.91	0.31
	1.64E+02	148	1.12	0.09	0.09		
	1.63E+02	229	1.14	0.07	0.07		
	1.66E+02	85	0.47	0.05	0.05		
Manilius D	1.01E+01	10	0.94	0.29	0.29	0.89	0.39
	9.25E+00	6	1.05	0.42	0.42		
	8.45E+00	3	0.34	0.19	0.19		
	1.01E+01	14	1.24	0.33	0.33		
Lansberg D	5.27E+01	60	2.87	0.25	0.34	2.60	0.48
	5.32E+01	61	2.89	0.24	0.34		
	5.07E+01	53	2.75	0.29	0.36		
	5.14E+01	39	1.89	0.30	0.30		
Carlini	4.85E+01	174	2.56	0.18	0.19	2.62	0.25
	4.78E+01	192	2.88	0.15	0.19		
	4.74E+01	160	2.31	0.18	0.18		
	4.68E+01	173	2.74	0.18	0.20		
Herigonius	1.09E+02	109	2.40	0.22	0.23	2.26	0.21
	7.09E+01	60	1.98	0.25	0.25		
	9.23E+01	99	2.44	0.24	0.24		
	1.42E+02	142	2.20	0.18	0.18		
Cayley	9.94E+01	39	3.17	0.15	0.34	3.40	0.17
	9.94E+01	60	3.40	0.06	0.08		
	1.00E+02	67	3.54	0.03	0.04		
	1.00E+02	51	3.50	0.04	0.06		
Marius D	3.14E+01	16	3.38	0.10	0.27	3.41	0.09
	3.45E+01	20	3.46	0.07	0.13		
	3.12E+01	16	3.49	0.07	0.13		
	3.45E+01	14	3.29	0.14	0.50		
Posidonius N	2.09E+01	8	3.70	0.06	0.10	3.71	0.09
	2.20E+01	7	3.58	0.08	0.16		
	2.07E+01	10	3.78	0.05	0.07		
	2.22E+01	14	3.77	0.04	0.06		
Sinas E	3.83E+01	18	3.26	0.14	0.45	3.07	0.50
	3.91E+01	18	3.40	0.09	0.21		
	3.73E+01	11	2.33	0.64	0.70		
	3.83E+01	20	3.30	0.12	0.36		

continuous ejecta deposit and the crater density in the deposit becomes more uniform. (**Figure 3.11** and **Table 3.3**). Hence, errors associated with uneven distribution of impact melt are more important for younger craters than older craters.

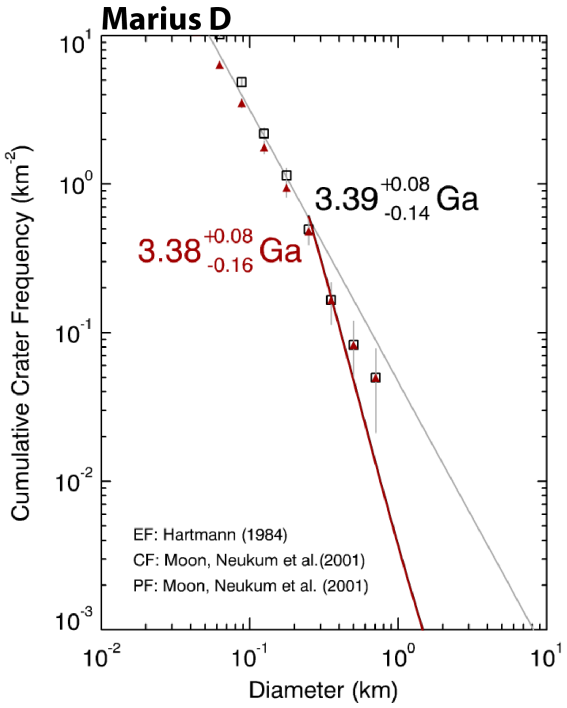

Figure 3.12: Crater size-frequency distribution for Kaguya Terrain Camera (red solid triangles) and LROC NAC (black hollow squares).

We count craters on the continuous ejecta of Marius D using Kaguya Terrain Camera and the LROC-NAC data to check the consistency of our absolute model age results. This comparison is important to evaluate because the differences in the two instruments may affect our crater counts. The LROC NAC cameras are monochromatic linescan imagers and have a spatial resolution of 0.5 m/pixel [*Robinson et al.*, 2010]. For both data sets, we count craters on the western half of the continuous ejecta of Marius D. The Terrain Camera image of this area had a phase angle of 30° with an incidence angle of 30° and an emission angle of 0°. As for LROC-NAC data, we use an image with a phase angle of 68.9°, where the incidence angle was 67.1° and the emission angle was 1.75°. We computed the crater counts for each data set and the age is 3.4 Ga for both data sets (**Figure 3.12**). The agreement between these two model ages indicates that the absolute model ages in this study are consistent across data sets.

Another factor that may affect our overall results is the observer. *Robbin et al.* [2014] noticed that among expert counters, uncertainty in absolute model ages could vary up to ±10–35% dispersion on a single bin, depending on the difficulty of the terrain. On this basis, the calculated absolute model ages may deviate enough to affect our overall calibration.

3.5.2 Testing the Degree of Freshness to Absolute Model Ages Calibration

We validate our calibration by comparing the degree of freshness with exposure ages of impact craters. Unfortunately, there are no known absolute ages of Class III craters. The best craters for this test are North Ray and South Ray craters even though the diameters of both these two craters are <1 km in diameter, which is below the minimum crater diameter threshold as recommended by *Pohn and Offield* [1970] and *Offield and Pohn* [1970].

The first noticeable feature on both craters is their crater rays (**Figure 3.13**). The presence of the rays suggests the craters degree of freshness is between 6.0 and 7.0 [*Pohn and Offield*, 1970]. Next, we examine the blocks along the rim, radial striations on the ejecta, and the shape of the crater rim crest shadow casted onto the crater floor. As a result, we rank North Ray crater at 6.6 and South Ray crater at 6.8. If we translate these degrees of freshness to absolute model ages, we find that the North Ray and South Ray craters are 0.6 and 0.2 Ga. Cosmic-ray exposure ages show that these craters are 0.05 Ga and 0.002 Ga [*Drozd et al.*, 1974], which is within the 95% confidence belt.

In another trial, we test our calibration on the mare surface immediate to the Apollo 12 landing site (3.01°S, 23.42°W). To restrict files to a manageable size, we downsample the Terrain Camera morning maps to 50 m/pixel. The map ranges from 0–6°S and 21–27°W. Within this area, we search for completely imaged primary impact craters within the maria that are >2 km in diameter. We did not use <2 km craters to avoid accidently dating secondary craters. We find and determine the observed degree of freshness for nine craters (**Figure 3.14)**. In **Table 3.4**, we justify the rank for each crater. Next, we convert the observed degree of freshness to the corrected the degree of freshness for each crater with equation (3.6) because the diameter of all nine craters are <8 km. We find that the oldest crater is a 2.9 km crater located at 335.52°E and 1.97°S with an observed degree of freshness of 4.8 and a corrected degree of freshness of 5.4. Converting the corrected degree of freshness to an absolute model age, this crater is 3.1 Ga. The age of the oldest crater on the surface suggests that the surface is at least 3.1 Ga. In comparison, sample analyses indicate this region is 3.08–3.29 Ga [*Basaltic Volcanism Study Project*, 1981].

Crater density measurements of this area resulted in absolute model ages between 3.14 and 3.65 Ga [*Hiesinger et al*., 2003]. Hence, we observe a consistency between the degree of freshness, samples age, and crater density measurements.

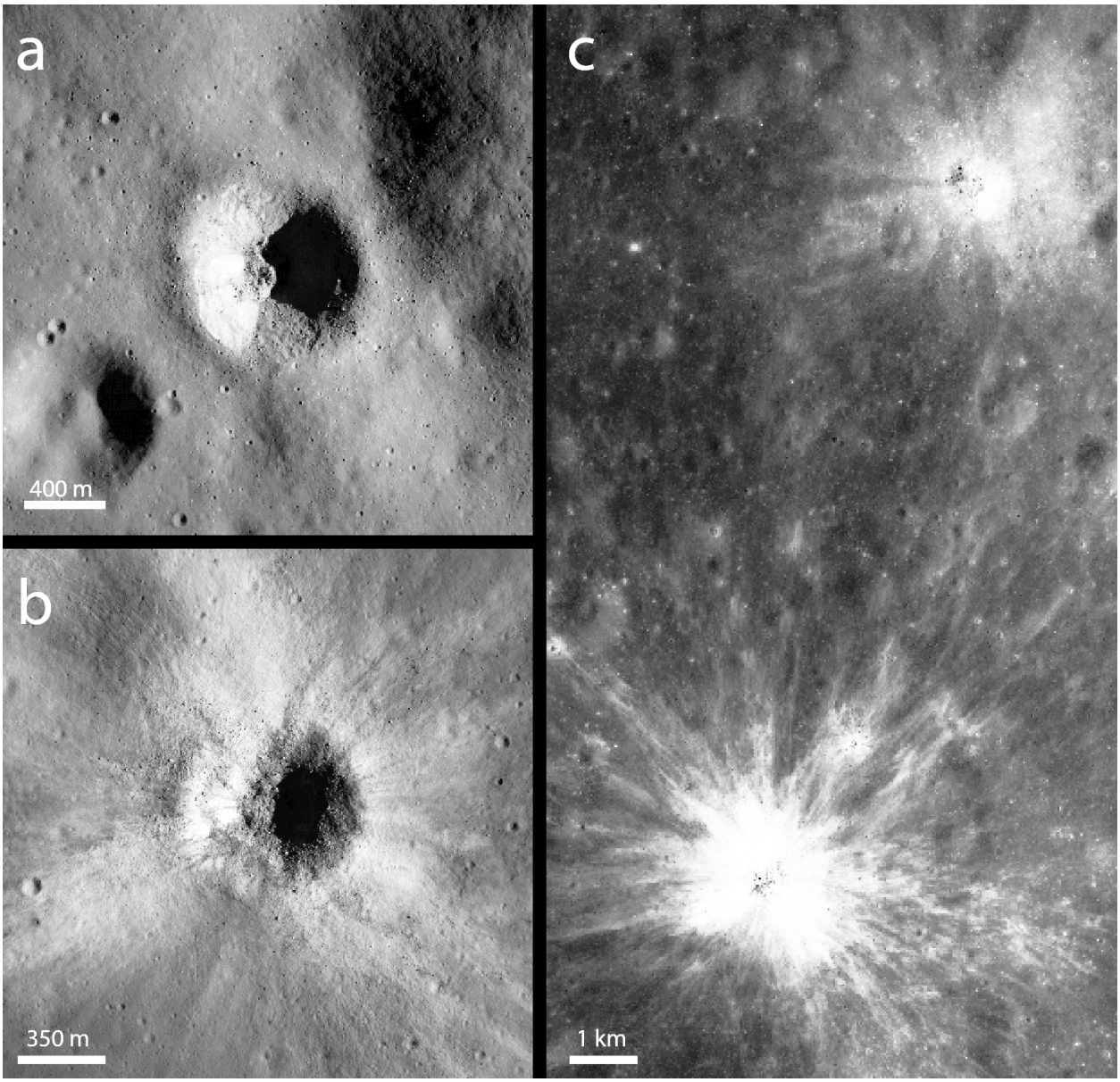

Figure 3.13: LROC-NAC images a) North Ray Crater. b) South Ray Crater. c) North and South Ray Craters imaged at high sun to show the crater rays.

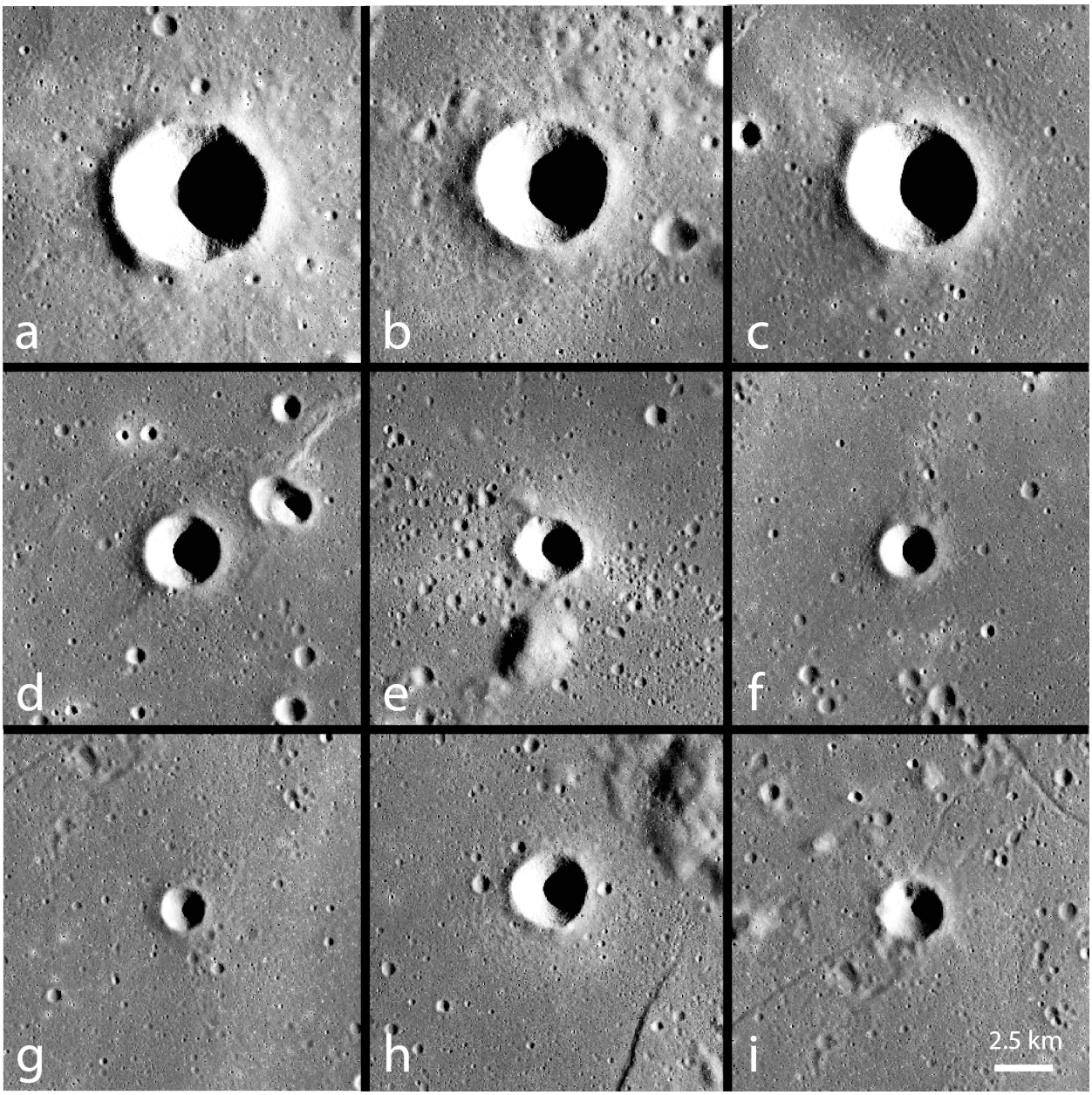

Figure 3.14: Class III mare craters around the Apollo 12 site used to determine the minimum absolute model age of the surface. The nine craters and associated letters are described in **Table 3.4**. Scale is applicable to all nine panels.

Table 3.4: Description of >2 km craters near Apollo 12

Degree of Freshness of >2 km Craters near Apollo 12

Fig. 3.14 Crater	Lat.	Long.	Diam.	Degree of Freshness		Age (Ga)	Description
				Observed	Corrected		
a	-4.0	338.3	6.7	6.1	6.1	1.6	Crater rays with a barely visible secondary crater field. Strong parabolic shadow casted into the crater and on the western rim. Sharp rim crests and obvious rim structure. Circular crater without any indentations.
b	-4.2	335.3	5.8	6.3	6.3	1.2	Crater rays with a strong secondary crater field. Strong parabolic shadow casted into the crater with a flatten top and a strong shadow west of the crater. Obvious rim structure. Sharp rim crest without any indentations.
c	-5.4	338.3	5.7	5.9	5.9	2.0	Noticeable secondary crater field. Distinguishable rim structure with sharp rims and no indentations. A circular crater. The shadow within the crater is a bit wider.
d	-5.5	337.7	3.3	5.5	5.6	2.5	A circular crater with slightly subdued rim crests, which lacks indentation. The rim structure is still apparent with the shadow on the western side of the crater. Shadow of the rim within the crater is sharp. Secondary crater field is not easily observed.

Table 3.4 (continued)

e	-2.5	333.1	2.8	6.1	6.2	1.5	A circular crater that shows crater rays with a noticeable secondary crater field to the north. Sharp parabolic shadow within the crater. Crisp rim crests.
f	-2.4	336.9	2.6	5.6	6.0	1.9	Secondary crater field is noticeable, but not very obvious. No crater rays. Circular crater with slightly subdued rim crests. Rim structure is still apparent from shadows on the west. The parabolic shadow within the crater is wide.
g	-2.3	336.6	2.1	4.9	5.8	2.2	No evidence of a secondary crater field. The rim structure is barely distinguishable with subdued rims. The crater walls is still smooth and lacks indentation. The shadow within the crater is wide.
h	-1.9	333.6	3.3	5.9	5.9	2.0	Apparent secondary crater field, but lacks crater rays. The rim structure is apparent with sharp rim crests. Crater is circular without any indentations on the wall. This crater has a sharp parabolic shadow in the interior.
i	-2.0	336.5	2.9	4.8	5.4	3.1	Lacks crater rays and a secondary crater field. The rim crest is subdued and the rim structure is barely distinguishable. The crater walls show some slight indentations and the shadow is not as strong and somewhat wide. Crater floor appears shallow.

3.5.3 The Interpretation of the Kink

In **Figure 3.5**, the relationship between the degree of freshness and absolute model age displays a prominent kink at a degree of freshness of 5.0 (3.8 Ga). We have three hypotheses that describe the origin of the kink. 1) The kink is an indicator of a change in degradation rate on the Moon, 2) The kink is a coincidence of the ranking system and is not geologically significance, 3) the kink represents the point where the continuous ejecta of Class III craters is saturated with craters.

The first interpretation suggests that the kink represents a change in degradation rate. The kink occurs around 3.8 Ga, which is approximately when the cratering flux decreases and the end of multi-ring basin forming events. Recall the various processes that act to degrade impact craters. The impacting process causes almost all the surfaces processes that degrade impact craters. Thus, an increase in impacts would result in faster degradation of craters. If the rate of crater degradation or the change in degree of freshness with respect to absolute model ages depends on the impact flux, then the slope of the two linear regressions suggests two periods with different cratering flux. Therefore, the rate of crater degradation was faster before 3.8 Ga and slower after 3.8 Ga. This interpretation agrees with *Head's* [1975] findings of two different degradation periods.

An alternative interpretation is that the kink is a coincidence of the ranking system and has no physical meaning. Recall that *Pohn and Offield* [1970] chose seven distinct types based upon their examination of thousands of craters. If *Pohn and Offield* [1970] divided or merged the craters into more or less number of types, the relationship between the degree of freshness and absolute model age may result in a different function than **Figure 3.5**.

Another explanation is that the kink represents when the continuous ejecta deposit of Class III crater is saturated with primary craters. The majority of the craters used to calculate the degraded crater regression rely on less than fifteen craters to determine an absolute model age. These absolute model ages rely on a small number of craters because bins representing crater diameters ≤500 m are saturated. Additionally, our older crater samples face two new problems. First, the area of the continuous ejecta cannot support several craters ≥500 m in diameter because these ≥500 m in diameter craters cover a sizable portion of the area. Secondly, the ejecta of ≥500 m craters would drape a sizable portion of our counting area and erase any preexisting craters. If

crater saturation is the cause of the kink, then we must interpret any crater with a degree of freshness ≤5.0 as older than 3.8 Ga.

There are several methods to resolve the significance of the kink. One potential solution is to relate the degree of freshness to crater diffusion models, such as the model created by *Soderblom and Lebofsky* [1972] and *Fassett* [2013]. Crater diffusion models describe the changes in crater geometry in response to impact flux. Consequently, a method that links the degree of freshness to crater diffusion models also indirectly relates degree of freshness to impact flux. Future studies could also validate the crater saturation hypothesis. Class I and II craters have larger continuous ejecta deposit; thus, their deposits do not saturate as quickly as Class III craters. Therefore, a future study that calibrates the degree of freshness for Class I and II craters to absolute model ages could support that the kink is a result of crater saturation in Class III craters. However, this test only works if the degree of freshness system for Class I and II craters is comparable to the system for Class III craters.

3.5.4 Lifetimes of Crater Morphology

Our calibration allows quick absolute model age determination from looking for the presence or absence of a specific feature on a crater. In addition, we can study the changes in crater morphology with time. Here, we assume that the morphologies disappear and appear at the same degree of freshness, but in reality the timing varies based upon crater size. For a known example, the presence of crater rays is one of the defining features of the Copernican period [*Shoemaker and Hackman*, 1962; *Wilhelms* 1987]. *Pohn and Offield* [1970] recognized that crater rays mature at a degree of freshness of 6.0. From our calibration, we find that a degree of freshness of 6.0 corresponds to about 1.8 Ga. In comparison, *Werner and Medvedev*, [2010] estimated that crater rays disappear at 0.75 Ga, which is ~1 Gyr sooner than our predictions (**Table 3.5**). This result is still within the 95% confidence belt.

We also examine other crater morphologies to determine when they appear or disappear (**Table 3.5**). According to *Pohn and Offield* [1970], crater rays and secondary craters around their parent crater disappear at a degree of freshness of 6.0, which corresponds to 1.8 Ga. *Pohn and Offield* [1970] also noted that craters with a degree of freshness of <5.0 (>3.8 Ga) have already lost their radial grooves and striations. Crater rims subdue at a degree of freshness of 4.5 or at 3.8 Ga. By a degree of freshness of 4.4 (3.8 Ga), the crater loses its circular shape and

become polygonal. The walls of impact craters begin to show indentations and channels at degrees of freshness of 4.2, which corresponds to an age of 3.9 Ga.

Table 3.5: Relationship between crater morphology and time

Morphology Changes in Craters with Respect to Time

Type III Crater Morphologies	Degree of Freshness	Appearance (Ga)	Disapparance (Ga)
Crater Rays	6.0		1.8
Satellitic Craters	6.0		1.8
Radial Facies	5.0		3.8
Rim Crest Sharpness	4.5		3.8
Polygonality	4.4	3.8	
Radial Channels	4.2	3.9	

3.6 Conclusion

We calibrated the degree of freshness of Class III craters dating system created by *Pohn and Offield* [1970] to absolute model ages. In addition, we also converted their degree-of-freshness offset curves from a visual to a numerical correction. These offset curves allows 1–8 km in diameter craters to be comparable to the degree of freshness of larger craters. We validated the calibration with North and South Ray crater and the Apollo 12 site. These trials on Apollo sites demonstrated the capabilities of the degree of freshness as a reconnaissance dating-tool. In all, the method of *Pohn and Offield* [1970] can now be applied to craters from 1–20 km in diameter to yield absolute model ages. Future studies could extend this tool to larger lunar craters as well as to craters on other airless bodies.

The kink between the two regressions (i.e., equation 3.2 and 3.3) is real, but its significance is open to interpretation. This kink either represents a change in the impact flux, an artifact as a result of the method, or a point where saturation dominates the crater continuous ejecta. Until the kink is resolved, we recommend interpreting any crater with a degree of freshness <5.0 to be >3.8 Ga.

A summary of our calibration can be simplified to: 1) If the crater is 8–20 km in diameter and has a degree of freshness between 5.0 to 7.0, then use equation (3.1). Otherwise, 8–20 km craters with degree of freshness of 0.0 to 4.9 are >3.8 Ga. 2) If the crater is 1–8 km in diameter and not younger than a degree of freshness of 6.0, then place the observed degree of freshness and crater diameter to equation (3.5) to obtain the corrected degree of freshness.

CHAPTER 4

THE ORIGIN OF LUNAR CONCENTRIC CRATERS

To Be Submitted To: Journal of Geophysical Research – Planets

Abstract – Lunar concentric craters are a unique class of impact craters because the interior of the crater contains a concentric ridge. The goal of this project is to determine the origin of concentric craters. First, we analyzed data sets from instruments onboard Clementine, Kaguya, and the Lunar Reconnaissance to establish the properties of concentric craters. Specifically, we documented the morphology, spatial distribution, composition, and age of 114 concentric craters. Next, we explored eight different hypotheses that can account for the observations of concentric crates. These observations include: (1) the presence of the concentric ridge structure (2) the shallow depths of concentric craters (3) the concentration of concentric craters near mare margins and in mare pond regions (4) the compositional similarity of the concentric crater to the surrounding area and (5) the tendency for concentric craters to be >3.8 Ga. Afterward, we considered various exogenic and endogenic hypotheses. We find that most exogenic hypotheses cannot explain the spatial and age distribution of concentric craters. As for endogenic hypotheses, we deduced that igneous intrusions are the likely mechanism that forms concentric craters because of the close relationship between concentric craters and floor-fractured craters. In addition, floor-fractured craters are common at crater diameters >15 km. In contrast, concentric craters are common at crater diameters <15 km. Therefore, we suggested that igneous intrusions underneath small craters (<15 km) are likely to form concentric craters, whereas intrusions under large craters (>15 km) produce floor-fractured craters.

4.1 Introduction

The changes in crater geometry and morphology with increasing crater diameter (e.g., *Pike*, [1974, 1980]; *Wood and Andersson*, [1978]) and age (e.g., *Pohn and Offield*, [1970]; *Trask,* [1971]; *Soderblom and Lebofsky*, [1972]; *Head*, [1975]) is well understood. However, these impact crater studies cannot account for the geometry of a class of craters called concentric craters. *Wood* [1978] defined concentric craters as bowl-shaped craters with an inner ring. The inner ring geometry ranges between doughnut-shaped, rounded ridges, steep crater rims, or flattened mounds. In this work, we refine the concentric crater definition as craters with a concentric doughnut-shaped ridge or platform on the crater wall and/or crater floor. We call this 'inner ring' the *concentric ridge* (**Figure 4.1**). Within the concentric ridge is a relatively flat floor or a bowl. The purpose of this project is to determine the origin of concentric craters.

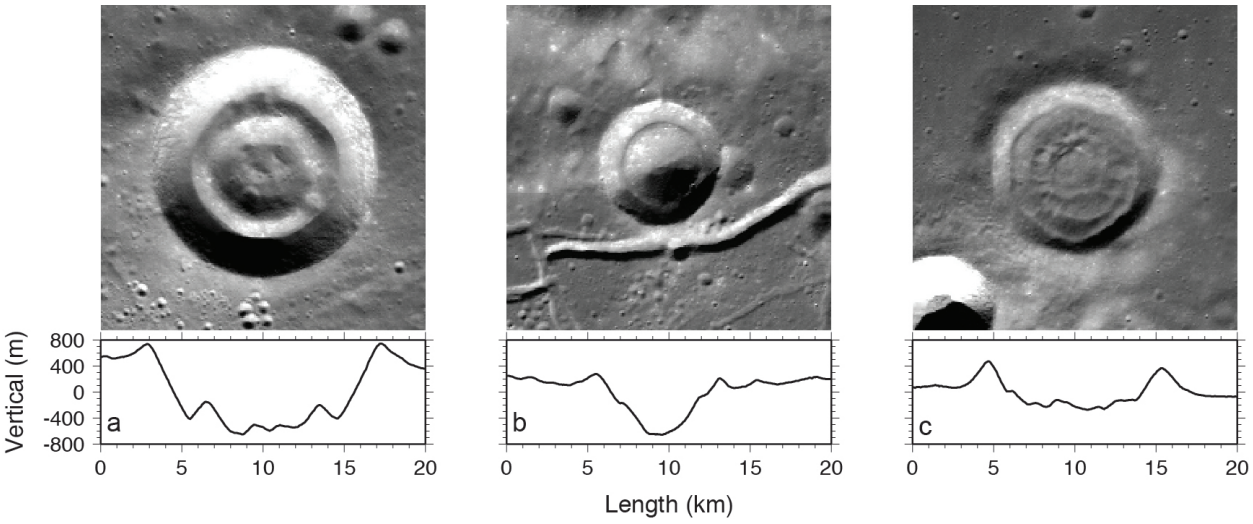

Figure 4.1: The three classes of concentric craters with WAC images of each type along with a LOLA profile through the center of the crater from left to right (exaggerated 4x). (a) Toroid (Hesiodus A) (b) Meniscus (Repsold A) (c) Bubbly (Louville DA)

Currently, there is no consensus about the origin of concentric craters. Most explanations involve impact and igneous-related processes. *Sekiguchi* [1970] hypothesized that concentric craters formed as a result of a tidally split meteoroid that successively impacted the same point on the lunar surface. *Wöhler and Lena* [2009] proposed that concentric craters are a consequence of an impact into a two-layered target, where the surface layer is weaker than the underlying layer.

Previous workers also suggested non-impact related processes. For instance, some workers proposed that lava produced the concentric ridge (e.g., *Schultz*, [1976b]; *Wood*, [1978]). Other volcanic explanations included that the concentric ridge is a product of a ring dike [*Cameron and Padgett*, 1974] or a volcanic dome [*Smith*, 1973]. Another idea involved the accumulation of magma underneath the crater (i.e., igneous intrusions) [*Wöhler and Lena*, 2009]. A non-igneous-related idea suggested that the concentric ridge is a product of mass wasting [*Schultz*, 1976b].

In this work, we describe the properties of concentric craters and use these properties to determine the most likely mechanism to form concentric craters. We categorize the concentric crater properties into four groups: morphology and morphometrics, spatial distribution, composition, and age. Morphology and morphemetrics involve notable features within concentric craters and relationships between concentric crater dimensions (i.e., crater depth, crater diameter, rim height, rim width, concentric ridge height, concentric ridge diameter). Also, we compare concentric crater dimensions to other crater classes (i.e., fresh, degraded, and floor-fractured craters). Next, we examine the spatial distribution of concentric craters and their proximity to major regions (i.e., maria and highlands). Afterward, we measure the elemental abundances of concentric craters to determine the composition of the concentric ridge. Lastly, we approximate the age of concentric craters based upon crater degradation. After studying the concentric crater properties, we assess various exogenic and endogenic mechanisms to determine the likely origin of concentric craters.

The origin of concentric craters is important to understanding planetary surface processes. If concentric craters formed as a result of specific properties of the impactor and/or the target, then this study will provide an opportunity to expand and modify current cratering models. On the other hand, if concentric craters are products of a non-impact process, then this work will allow a better understanding of processes occurring on the lunar surface and subsurface [e.g., *Schultz*, 1976a; *Parmentier and Head*, 1981; *Forsberg-Taylor and Howard*, 2004].

4.2 Methods

4.2.1 Surveying for Lunar Concentric Craters

We create a revised list of concentric craters by integrating a previous study of concentric craters [i.e., *Wood*, 1978] with a new survey of the lunar surface using a high spatial-resolution global map. *Wood* [1978] surveyed Lunar Orbiter and Apollo images and cataloged potential

concentric craters. We examine the craters listed in *Wood* [1978] with the Wide Angle Camera (WAC) mosaic from the Lunar Reconnaissance Orbiter Camera (LROC) to confirm the presence of a concentric ridge. The WAC panchromatic mosaic is a high spatial-resolution (100 m/pixel) map with incidence angles between 60–80°, which accentuate topography [*Robinson et al.*, 2010]; thus, this map accentuates the concentric ridge. Of the 51 potential concentric craters listed in *Wood* [1978], we confirm that 38 of his craters meet our definition of a concentric crater. Also, we resurvey the surface with the WAC mosaic for previously undiscovered concentric craters. We limit our survey to >1 km craters because smaller craters are likely to be a result of an impact into layered targets [e.g., *Quaide and Oberbeck,* 1968; *Wilcox et al.* 2005; *Bart et al.,* 2011]. From this survey, we find an additional 76 concentric craters. In total, we identify 114 concentric craters.

4.2.2 Morphometric Measurements of Craters

We compare and contrast the dimensions of concentric craters to other crater classes (i.e., fresh, degraded, and floor-fractured craters (**Figure 4.2**)). For each crater class, we measure the crater diameter, depth, rim height, and rim width (**Figure 4.3**), these are the same dimensions used in *Pike* [1976, 1980]. In this study, we define fresh craters as bowl-shaped craters with sharp rims and typically exhibit crater rays (**Figure 4.2a**). Fresh craters represent the starting point before the crater becomes modified or degraded. Over time, fresh craters lose their crater rays and develop subdued rims and shallower depths; these craters are degraded craters (**Figure 4.2b**). The degraded crater class illustrates the changes in crater dimensions as a fresh crater transitions to a degraded crater. The causes of crater degradation include space weathering, seismic shaking, mass wasting, and emplacement of ejecta from nearby craters [*McKay et al.*, 1991; *Head*, 1975]. An alternative route for fresh crater is to modify into floor-fractured craters (**Figure 4.2c**). Floor-fractured craters display one or more linear and/or curvilinear rilles on the crater floor [*Schultz*, 1976a]. As opposed to degraded craters, floor-fractured craters are a result of viscous relaxation [e.g., *Baldwin*, 1968; *Daneš*, 1965; *Hall et al*., 1981] or igneous intrusions [e.g., *Young*, 1972; *Brennan*, 1975; *Schultz*, 1976a; *Wichman and Schultz*, 1995; *Wichman and Schultz*, 1996; *Dombard and Gillis*, 2001; *Jozwiak et al.*, 2012].

In concentric craters, we measure two additional dimensions, the height and diameter of the concentric ridge. These two dimensions may reveal the relationships between the concentric ridge and the parent impact crater and the concentric ridge with itself.

We measure the diameters of the parent crater and concentric ridge in JMars for Earth's Moon. The basemap is the WAC panchromatic mosaic. We use the crater counting tool to fit a circle to the crater or the concentric ridge to determine their diameters.

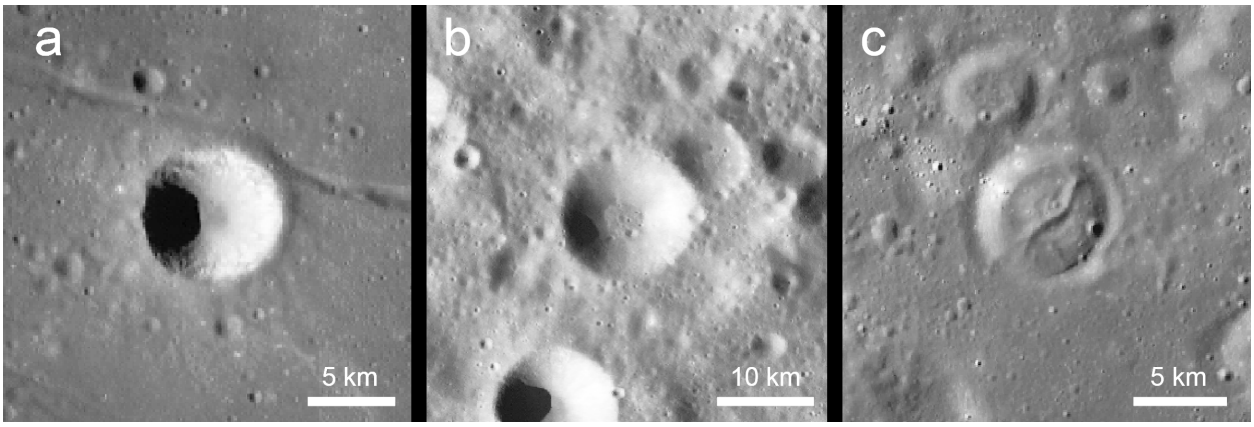

Figure 4.2: WAC images of three additional crater classes that are compared to concentric craters. (a) fresh craters, (b) degraded craters, and (c) floor-fractured craters.

We calculate the crater depth, rim height, rim width, and concentric ridge height from crater profiles. We obtain the profiles from the Lunar Orbiter Laser Altimeter (LOLA) data set. LOLA is a multi-beam laser altimeter where the five beams are oriented in a X-pattern [*Smith et al.*, 2010]. Consequently, each shot consists of five measurements. The separation between each shot is about 50 m. The LOLA track orientation is pole to pole. We only measure craters with a LOLA track that runs directly through the center of the crater (some data tracks are slightly oblique relative to the poles). Without this condition, measurements would overestimate the rim width because the profiles are not radial towards the center of the crater. Additionally, measurements may underestimate the crater depth because the lowest elevation on a crater is usually located at the center. After obtaining the tracks, we bin the data at intervals of 50 m to average out small wavelength topography (e.g., meter-sized craters). We measure the crater depth from the mean elevation of the crater floor to the mean elevation of the north and south rim crests (**Figure 4.3**). We evaluate the rim height and width from the rim crest to the change in slope of the rim flank (**Figure 4.3)**. In concentric craters, we measure the concentric ridge height from the mean elevation of the crater floor to the mean elevation of the northern and southern concentric ridge peaks.

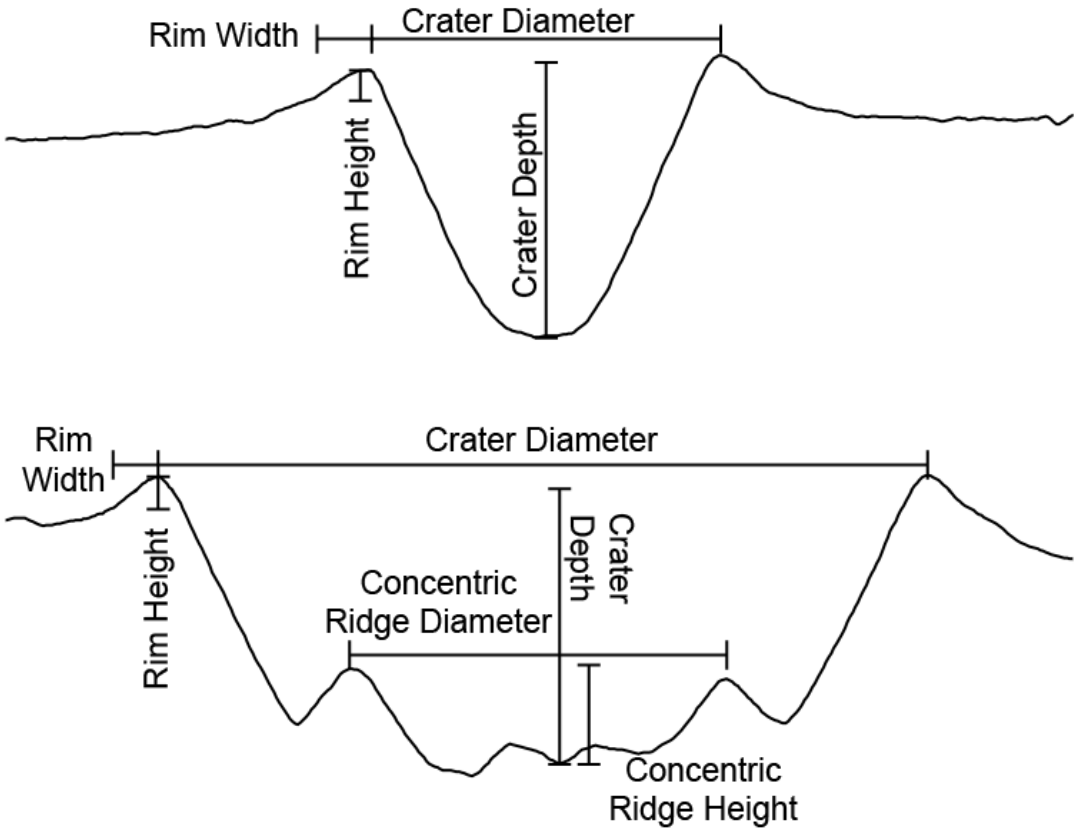

Figure 4.3: These illustrations are of a fresh crater (top) and a concentric crater (bottom) vertically exaggerated four times. This schematic shows the definition of each crater dimension.

4.2.3 Compositional Measurements of Concentric Craters

The concentric ridge composition may provide hints to the origin of concentric craters. In particular, we examine the FeO and TiO_2 abundances of the concentric ridge and compare them to the surrounding area beyond the rim crest. We derive the FeO and TiO_2 abundance maps using the algorithms from *Lucey et al.* [2000a] on Clementine UVVIS data at 100 m/pixel. We calculate the mean FeO and TiO_2 abundances and standard deviation of the concentric crater, but this calculation does not include the area from the concentric ridge to the crater rim crest (i.e., crater wall). Also, we compute the mean FeO and TiO_2 abundances and standard deviation of the surrounding area, which includes the area from the rim crest to one-crater diameter from the rim crest of the concentric crater.

4.2.4 Absolute Modal Age Dating of Concentric Craters

We estimate concentric crater age based upon the morphology of the crater (i.e., *Pohn and Offield*, 1970; *Offield and Pohn*, 1970; *Trang et al.*, *submitted*). *Pohn and Offield* [1970] developed a relative dating system that dates craters from their degradation state, called the degree of freshness. The degree of freshness ranges from 0.0 (oldest) to 7.0 (youngest). This system is dependent on the appearance of the crater floor, wall, and ejecta. Specifically, they used the presence of a continuous ejecta, crater rays, channels on the wall, the smoothness of crater wall and rim, the geometry of the crater, the depth of the floor, the shape of the shadow of the crater rim imposed on the crater floor, and the number of smaller superimposing craters to estimate the degree of freshness. In estimating the degree of freshness of concentric craters, we only take account the appearance of the crater wall, rim, and ejecta, but we do not include the crater floor in the evaluation of the degree of freshness due to the presence of a concentric ridge. This exception includes examination of the shadow of the rim because the concentric ridge distorts the shape of the shadow. In this method, we assume that the age of the crater is an indicator of the age of the concentric ridge as well.

The first step is to evaluate the degree of freshness of each concentric crater. Due to the increased erosion rates of small craters, if the concentric crater is <8 km in diameter, then we correct the observed degree of freshness using eq. 3.6 in Section 3.4.3 [*Offield and Pohn*, 1970; *Trang et al., accepted*]. Next, we convert the corrected degree of freshness of each concentric crater to absolute model ages using eq. 3.1 and 3.2 in Section 3.4.1 [*Trang et al., accepted*].

4.3 Results and Interpretations

4.3.1 Morphology and Morphometrics

4.3.1.1 Morphology

From the observations of concentric crater geometries, we categorize concentric craters into three main classes: *toroid*, *meniscus*, and *bubbly*. We define these three classes based upon the shape of the most prominent concentric ridge and the geometry of the join between the concentric ridge and the crater wall (**Figure 4.1**). In toroid concentric craters, the join between concentric ridge and the crater wall creates a V-shaped valley (**Figure 4.1a**). Similar to the toroid, bubbly concentric craters also display a V-shaped valley, but the concentric ridge exhibits multiple radial troughs extending from the crater center through the concentric ridge (**Figure 4.1c**). In meniscus concentric craters, the concentric ridge forms a continuous platform on the

crater wall (**Figure 4.1b**). In some cases, concentric craters may exhibit characteristics of more than one class. For example, in **Figure 4.1c**, this concentric crater shows both bubbly and meniscus characteristics. If a crater displays more than one concentric ridge, we categorize and measure the most conspicuous concentric ridge.

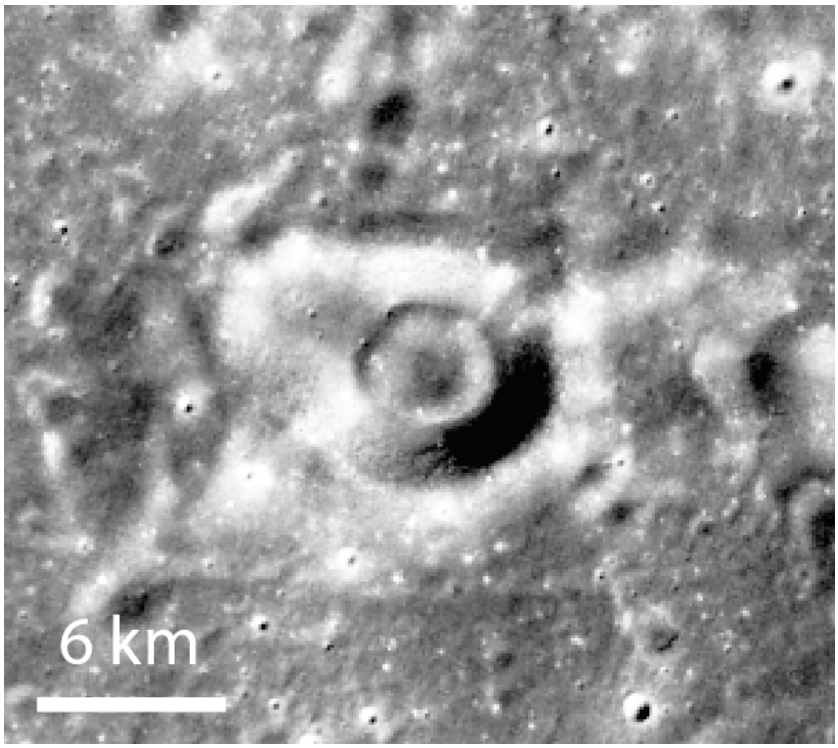

Figure 4.4: An unnamed crater (158.20°E, -60.72°N) with an elongated shape. The shape is attributed to an oblique impact.

Of the 114 concentric craters, nine are elongated craters (**Figure 4.4**). We attribute the elongation to a low-angle impact (<10°) [*Gault and Wedekind*, 1978]. We notice in elongated concentric craters that the shape of the concentric ridge is circular (**Figure 4.4**). Thus, we interpret that the concentric ridge did not form as a result of a low angle impact.

Inside concentric craters, we commonly observe low-albedo material. For the Moon, the low-albedo material is pyroclastic or cryptomare material. The low-albedo material appears on the crater wall (**Figure 4.5a**) or a spot with rays (**Figure 5b**). We interpret these low albedo materials to be cryptomare because their morphology is not consistent with known pyroclastic

deposits. Cryptomaria are mare deposits buried underneath highlands material [e.g., *Schultz and Spudis*, 1979; *Hawke and Bell*, 1981; *Antonenko et al.*, 1995].

In one curious case, the concentric crater Firmicus C has a low-albedo feature on the concentric ridge (**Figure 4.6a**). This low-albedo feature occurs on a fracture that approximately follows the concentric ridge (**Figure 4.6b**). In the high-resolution Narrow Angle Camera (NAC) on the Lunar Reconnaissance Orbiter Camera, the low-albedo material in Firmicus C exhibits diffuse margins, smooth textures (relative to the surrounding), lacks lava flow textures, and mantles the surface (**Figure 4.6c**). The shape of the low-albedo material is round and does not display radial rays, which is a strong indicator of crater rays. Also, this material does not appear to flood topographic lows. The composition of this low-albedo feature is 2.8 wt.% TiO_2 and 8.9 wt.% FeO with a 0.5 wt.% FeO and TiO_2 standard deviation. To determine whether this deposit originated volcanically, we use the six key criteria as summarized by *Gustafson et al.* [2012]. The only criterion this low-albedo feature does not meet is that we do not observe any obvious vents. Although this anomalous low albedo feature only meets five of the six criteria, we interpret that this material originated volcanically.

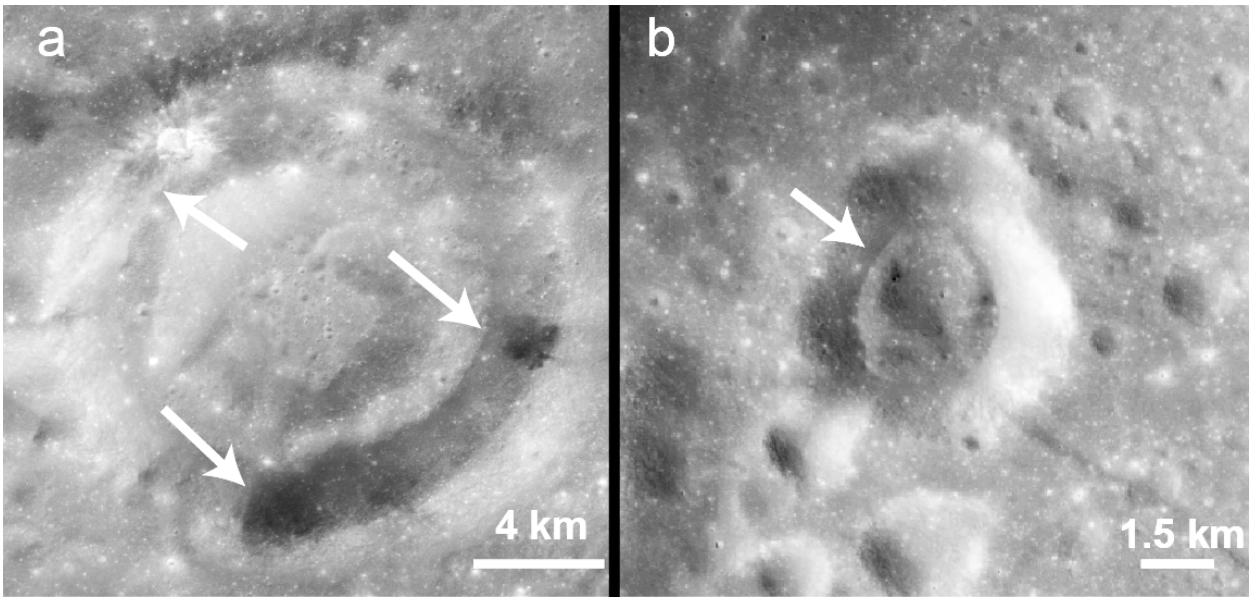

Figure 4.5: Kaguya's Multispectral Imager images (750-nm) of two concentric craters. (a) Bell E exhibits low-albedo material on the walls of the crater (the lower arrows) as well as ejected low-albedo material from a smaller and superimposing crater (upper arrow). (b) This unnamed crater (-78.88°E, 21.91°N) displays low-albedo material (arrow) that was also ejected from a smaller and superimposing crater. These low-albedo deposits are probably due to cryptomare.

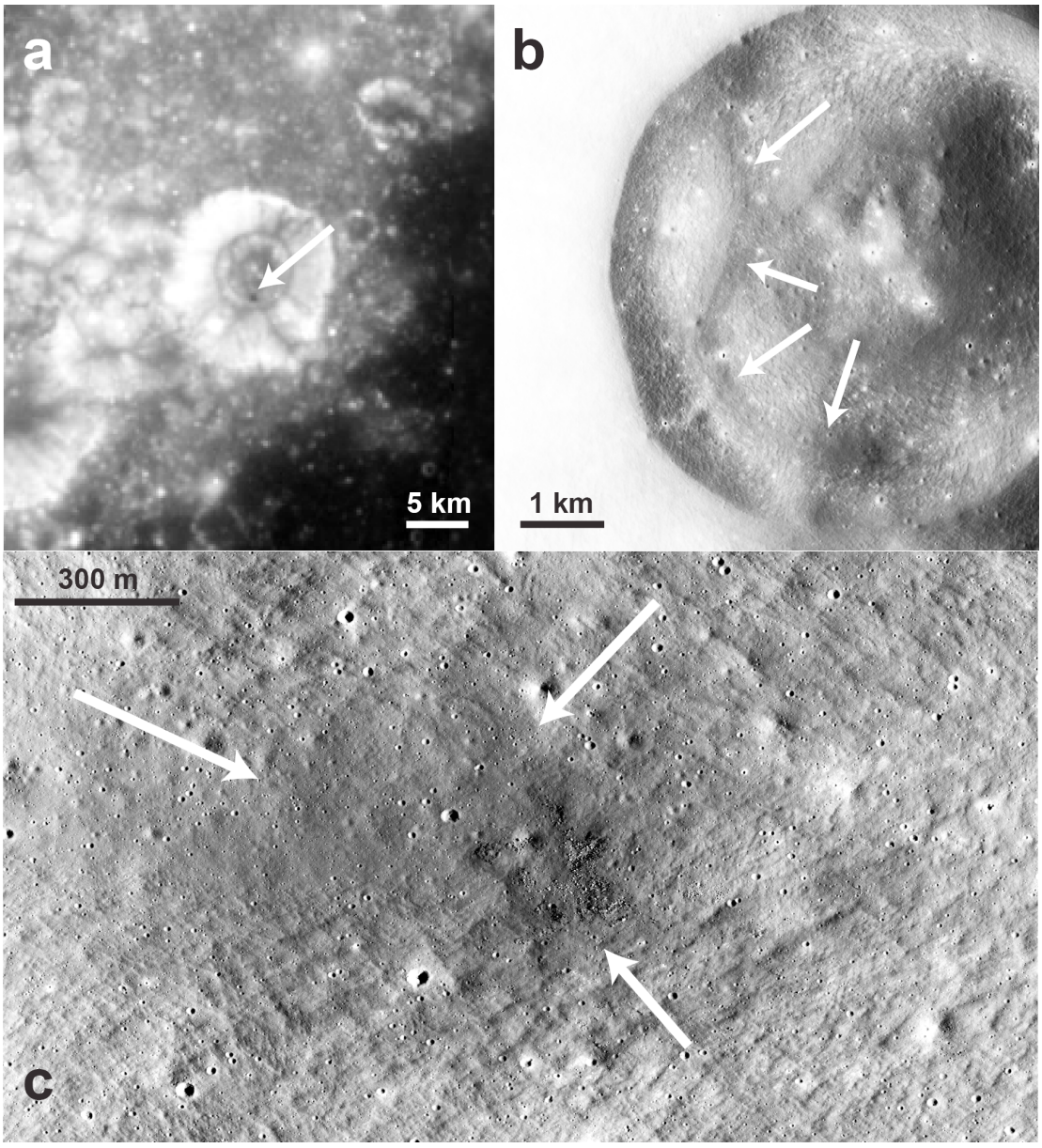

Figure 4.6: (a) A Clementine UVVIS (750-nm) image of the crater, Firmicus C, which shows a low-albedo spot on the concentric ridge (arrow). (b) In this Kaguya Terrain Camera image, the fracture runs along nearly half of the concentric ridge (arrow). The low albedo material is in the southern end of this fracture. (c) The Narrow Angle Camera on LROC shows that the material mantles the pre-existing topography and lacks crater rays (arrow).

Another observation of concentric craters is that we find six concentric craters with lava-flooded interiors (**Figure 4.7)**. These concentric craters display breaches in their crater walls. This imply two possible scenarios; one, lava originated from a location outside the concentric crater and intruded the concentric crater interior. Alternatively, the lava originated from the crater interior and traversed through the wall. The former is the likely case because we do not see any examples of a mare-filled concentric crater without breached walls.

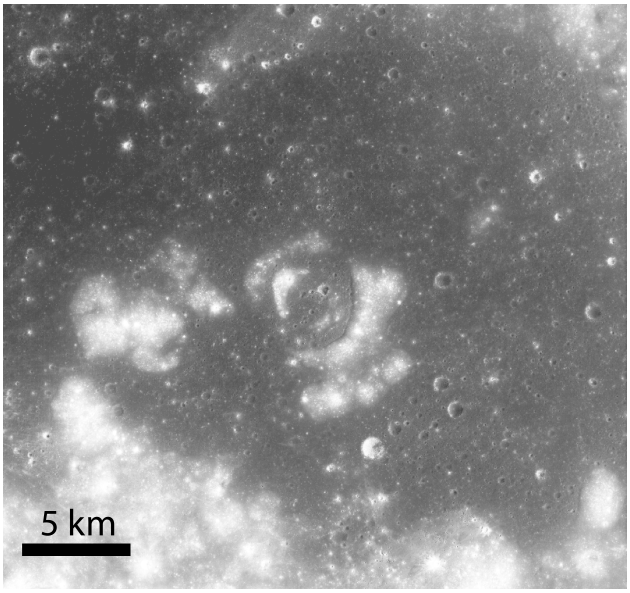

Figure 4.7: An unnamed concentric crater (66.8°E, 4.0°N) exhibits a flooded interior with mare material that flowed into the crater

4.3.1.2 Morphometrics

We search for relationships between concentric ridge dimensions and the concentric ridge dimensions with the parent crater dimensions. In general, the concentric ridge height increases with increasing concentric ridge diameter, but the relationship is weak, which implies that the concentric ridge height is loosely dependent on the concentric ridge diameter (**Figure 4.8a**). Even when we separated the craters into subclasses, we do not observe a relationship between concentric ridge height and diameter.

Next, we compare the concentric ridge against the parent crater dimensions (**Figure 4.8b–c**). The ratio, R_D, is the ratio of the concentric ridge diameter to the parent crater diameter. We note that R_D widely ranges from 0.19 to 0.84 with a mean of 0.49 and standard deviation of 0.13 (**Figure 4.8b**). Therefore, the concentric ridge diameter is probably independent on the

parent crater diameter. Again, we do not see any relationship between R_D and concentric crater class. Also, we examine the relationship between the concentric ridge height with crater depth (**Figure 4.8c**). Between these two dimensions, we do not observe a relationship regardless of concentric crater class.

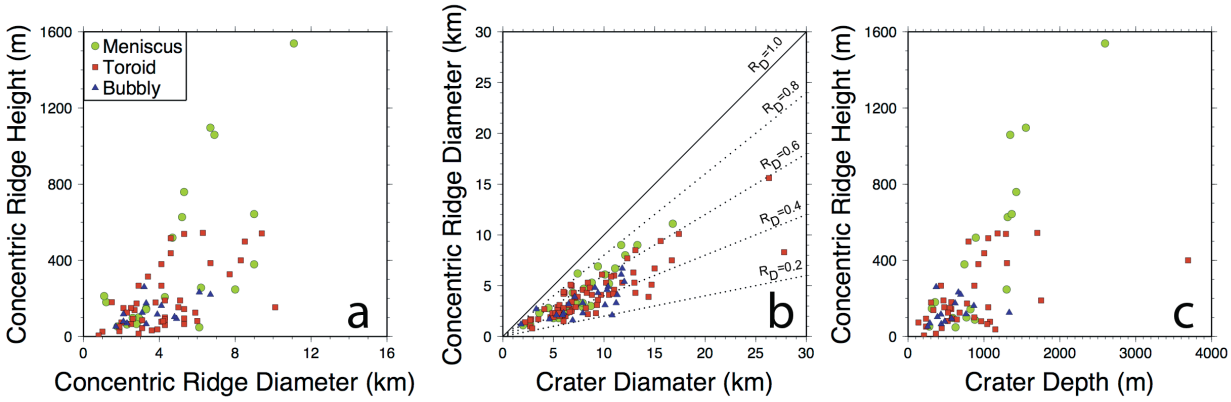

Figure 4.8: Comparisons between the concentric ridge and parent crater dimensions. In all three plots do not show any relationship between the concentric with itself and the parent crater.

This time, we compare the concentric crater dimensions to fresh, degraded, and floor-fractured crater dimensions. The relationships between fresh crater dimensions are well known, especially between the crater depth to diameter (**Figure 4.9a**) [e.g., *Wood and Andersson*, 1978; *Pike*, 1980]. As fresh craters deteriorate or modify, the depth, an observation seen in degraded and floor-fractured craters [e.g., *Soderblom and Lebofsky*, 1972]. For degraded craters, mass wasting and the deposition of ejecta into the crater contributes to the shallower depths [*Head*, 1975] (**Figure 4.9a**). In contrast to floor-fractured craters, igneous intrusions or relaxation uplifts the floor, which results in a decrease in crater depth [e.g., *Schultz*, 1976a; *Hall et al.*, 1981, *Dombard and Gillis*, 2001] (**Figure 4.9a**). Similar to degraded and floor-fractured craters, concentric craters exhibit shallower floors than fresh craters (**Figure 4.9b**). This depth to diameter comparison does not reveal if concentric craters are more similar to degraded craters or floor-fractured craters.

Floor-fractured craters and degraded craters are shallow because of two different processes. Our goal is to find two crater dimensions that separate floor-fractured craters and degraded craters. Those two dimensions are crater depth and rim height. In degraded craters and floor-fractured craters, the rim erodes to a smaller height and some of the material is falling into

the crater causing the crater depth to shallow. Additionally, the depth of floor-fractured craters shallows more than degraded crater because igneous intrusions or viscous relaxation also uplifted the crater floor. Relative to fresh craters, degraded craters appear above or nearly along the fresh crater line, whereas floor-fractured craters are below or along the line (**Figure 4.9c**). As for the concentric craters, they cluster below the fresh crater line (**Figure 4.9d**), similarly to floor-fractured craters.

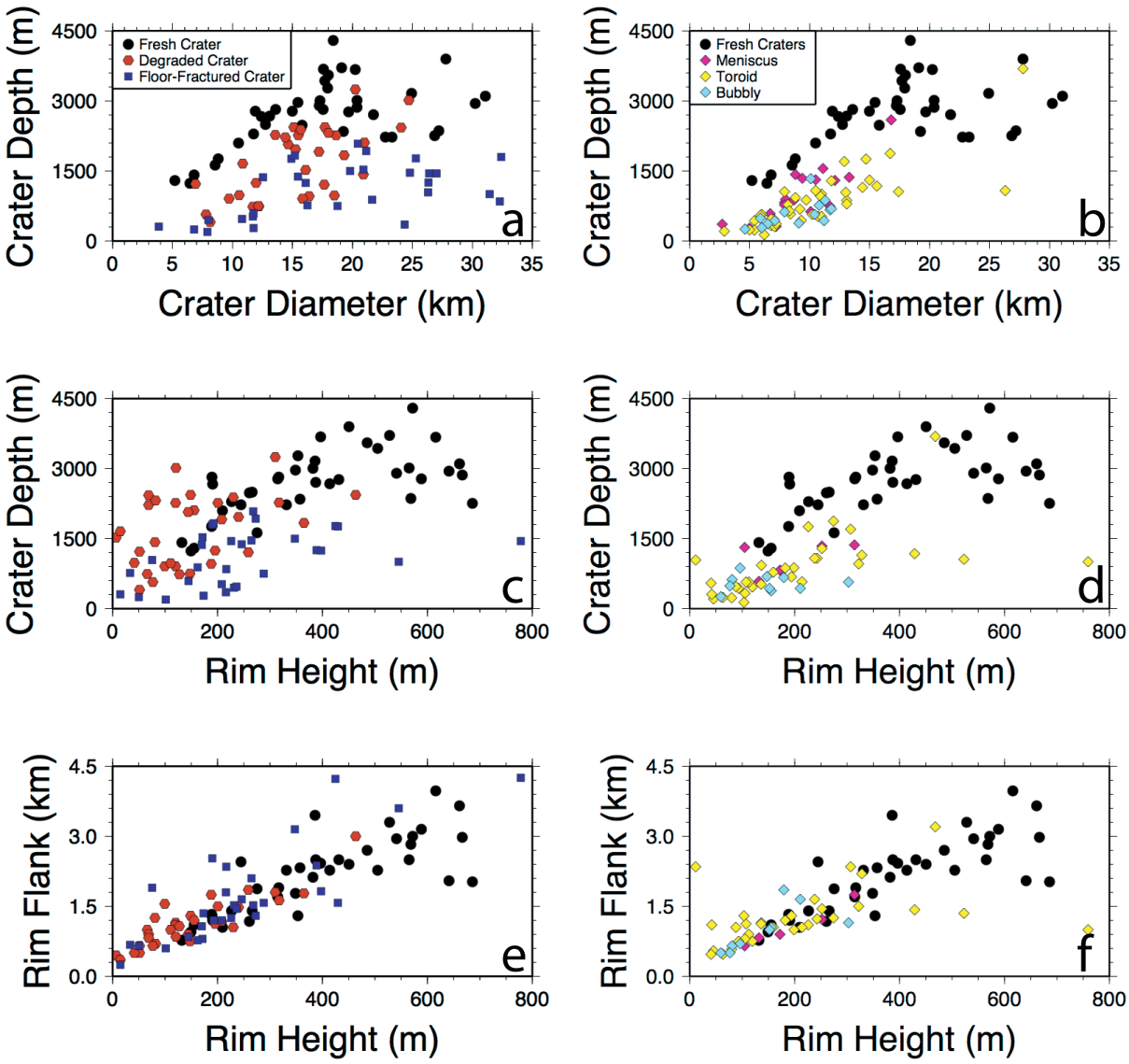

Figure 4.9: (a–b) A comparison between crater diameter to crater depths for fresh, degraded, floor-fractured, and concentric craters. All crater classes show shallower depths than fresh craters. (c–d) These plots compare rim height and crater depth. Above the fresh crater trend are degraded

craters and below are floor-fractured craters. Concentric craters also lies underneath the fresh crater trend. (e–f) In comparing the rim height to rim flank, all crater classes fall along the fresh crater trend.

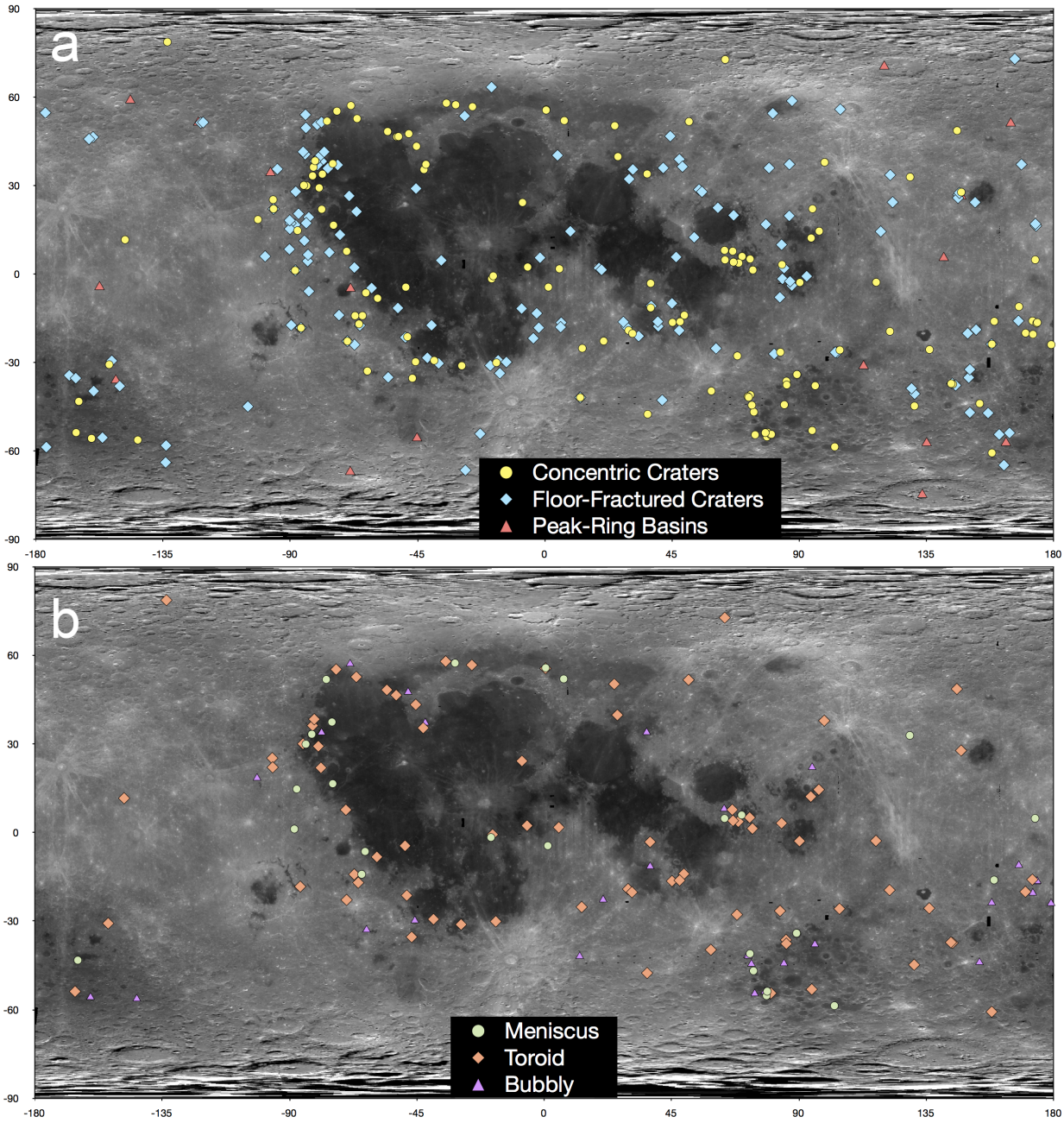

Figure 4.10: a) The distribution of concentric craters, floor-fractured craters [*Jozwiak et al.* 2012], and peak-ring basins [Baker et al., 2011]. b) The distribution of the types of concentric craters. Concentric craters show a similar spatial distribution to floor-fractured craters.

To ensure that the rim height is eroding at the same rate on all three crater-classes, we compare the rim height against the rim width. If this comparison differentiates the classes of craters, then the contrast between degraded craters and floor-fractured craters is not solely due to a process affecting the crater depth. In **Figure 4.9e–f**, we see that degraded, floor-fractured, and concentric craters group in the same area, indicating that the process affecting the rim are the same in all crater classes. Therefore, we interpret that floor-fractured craters and concentric craters have a shallow floor caused by mass wasting and another process.

4.3.2 Spatial Distribution

The spatial distribution of concentric craters exhibits two prominent patterns. First, the concentric crater distribution is along highland/mare boundaries (**Figure 4.10**). Second, concentric craters and floor-fractured craters show similar distributions. There are several examples where floor-fractured craters and concentric craters do not appear together. For example, there are concentric craters in Mare Undarum and Mare Australe, but hardly any floor-fractured craters in these regions. In contrast, adjacent to Mare Nectaris and north of Crisium, there is a large presence of floor-fractured craters, but these areas lack concentric craters.

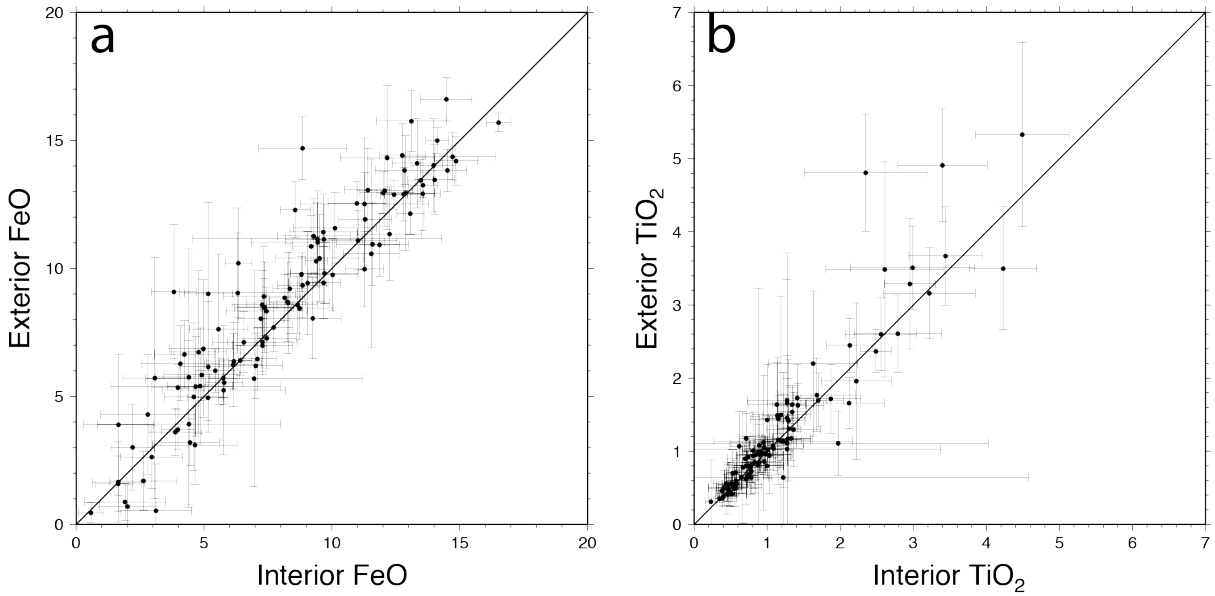

Figure 4.11: The FeO and TiO_2 abundance of the concentric crater and the surrounding area are similar. Thus, the concentric ridge comprises of the same material as the surrounding area. Some outliers exist because concentric craters exist on mare margins where highlands and mare material occur together.

4.3.3 Composition

The interior composition of concentric craters is similar to the surface material surrounding the craters (**Figure 4.11)**. The mean of the absolute difference between the concentric crater and their surrounding surface for FeO is 1.09 wt.% with a standard deviation of 1.03 and for TiO_2 has a mean of 0.19 wt.% with a standard deviation of 0.31. The points that show slight compositional differences between the concentric crater and their surrounding area is because the surrounding region contains both highland and mare material. In one extreme case, Marth (29.3°W, 31.2°S), a concentric crater composed of highlands material lies in the center of a mare region, Palus Epidemiarum.

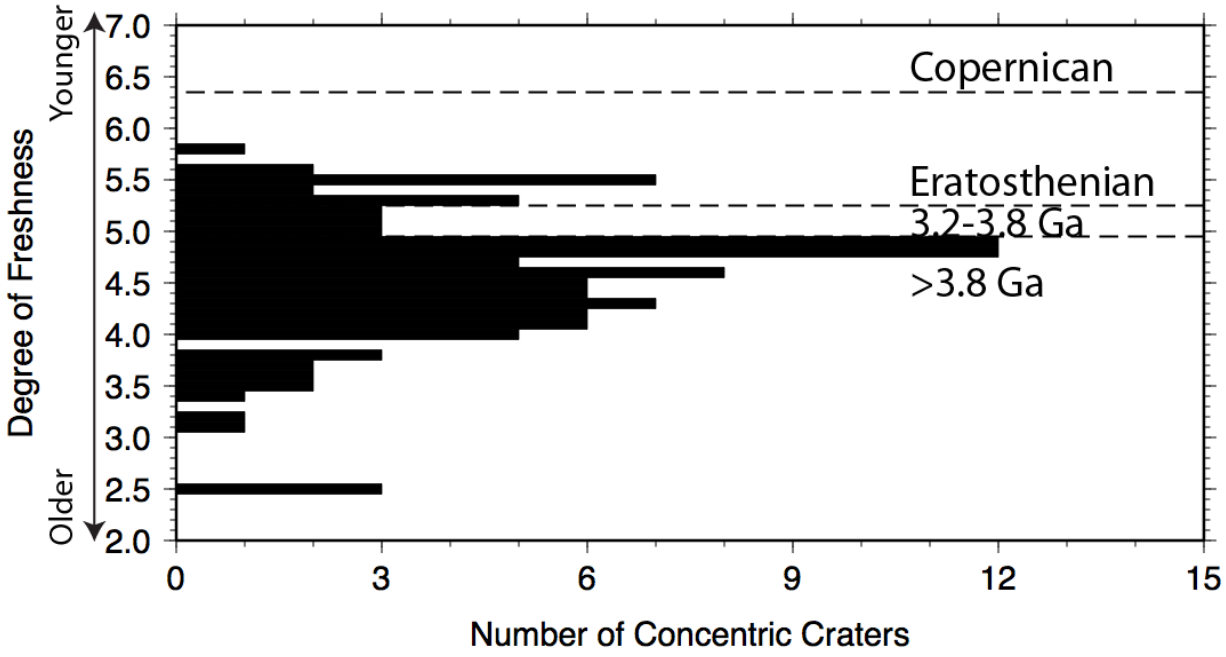

Figure 4.12: The distribution of concentric craters in terms of degree of freshness with marked time periods. Most concentric craters formed during and prior to the Imbrian time period (>3.2 Ga).

4.3.4 Age

We estimate the age of concentric craters using the degree of freshness method. The time stratigraphic periods used in this study are from *Wilhelms* [1987], where the base of the Nectarian, Imbrain, Eratosthenian, and Copernican periods are 3.92, 3.85, 3.2, and 1.1 Ga, respectively. However, we cannot distinguish the base of any time periods beyond 3.8 Ga [*Trang*

et al., in review]. In this method of dating concentric craters, we find that 88 concentric craters formed >3.8 Ga, 9 formed between 3.2–3.8 Ga, and 17 are Eratosthenian-aged craters (**Figure 4.12**). None of the concentric craters are Copernican in age.

4.4 Potential Mechanisms

Now that we established the properties of concentric craters, we deduce which surface process produces the known properties of concentric craters. The surface processes must produce the following observations of concentric craters: (1) the concentric ridge structure (2) the shallow depths of concentric craters (3) the concentration of concentric craters near mare margins and in mare pond regions (4) the compositional similarity of the concentric ridge to the surrounding area (5) the tendency for concentric craters to be >3.8 Ga.

4.4.1 Exogenic

An exogenic process is a surface process group that involves the interaction with the surface and material from space. In this study, we consider the impacting process. The projectile and target properties can affect the geometry of the crater after an impact, such properties include impacting angle, multiple impacts, and composition of the impactor and target. Specifically, we consider two crater classes, peak-ring basins and central-pit craters, which look similar to concentric craters. Also, we explore two processes, multiple impacts and an impact into layered targets.

4.4.1.1 Peak-Ring Basins

Lunar peak-ring basins are renowned features for their inner ring. These basins contain an inner ring and the basin rim (**Figure 4.13**). The inner ring consists of closely-spaced symmetrical peaks [*Hartmann and Wood*, 1971]. The diameter of lunar peak-ring basins ranges from 207–582 km [*Baker et al.*, 2011]. The ratio between the inner ring to basin rim diameter is 0.35–0.56 [*Baker et al.*, 2011]. Peak-ring basins are products of high-energy impacts relative to energies required to form complex and simple craters. The exact mechanism to forming peak-ring basin is still of debate. The two leading hypotheses are: collapse of an over-heightened central peak [*Melosh*, 1982; 1989; *Collins et al.*, 2002] and a nested melt cavity model [*Grieve and Cintala*, 1992; *Head*, 2010; *Baker et al.*, 2011].

The obvious similarity between peak-ring basins and concentric craters is the presence of a topographic ring, which meets observation (1). However, the relative spatial relationship between the rim crest and the topographic ring is different for the two crater classes. The ratio

between the inner-ring diameter and the basin diameter exhibits a narrow range (0.25–0.56) [*Baker et al.*, 2011], whereas the ratio (R_D) between the concentric ridge and crater diameter is 0.1–0.9. Another difference is that the inner ring of peak-ring basins comprises of individual peak. In contrast the concentric ridge is mostly continuous (i.e., toroid and meniscus). Another distinction between the morphology of concentric craters and peak-ring basins is that for peak-ring basins, a flat floor exists between the basin rim and the inner ring, whereas for concentric craters, the concentric ridge is adjacent to the crater wall.

We also investigate the age and spatial distribution of peak-ring basins. Unlike concentric craters, peak-ring basins occur randomly across the highlands. Furthermore, no known peak-ring basins are found in the maria (**Figure 4.10**) because the mare postdates most basins. As for the age, most peak-ring basins are Imbrium-aged [*Wilhelms*, 1987], which is consistent with observation (5). After examining the properties of peak-ring basins, we think that concentric craters formed differently than peak-ring basins.

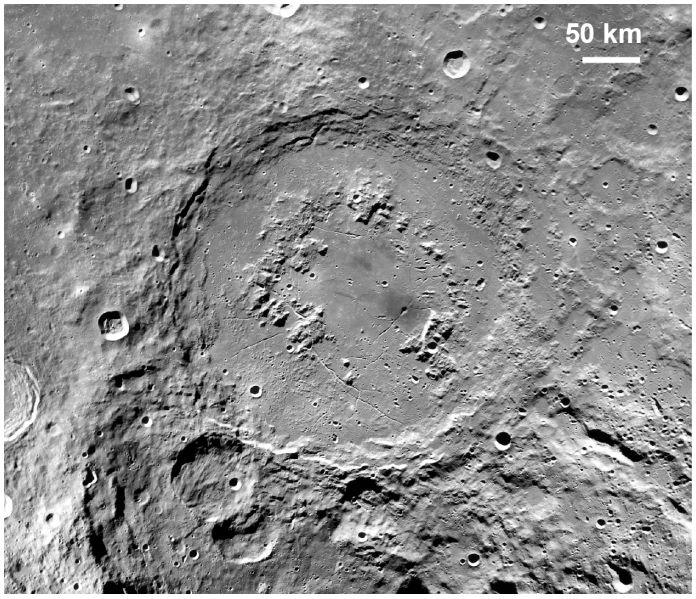

Figure 4.13: Peak-ring basins, such as Schrödinger basin, exhibit an inner ring and a basin rim.

4.4.1.2 Central-Pit Crater

Another crater class that exhibits an additional interior circular feature is central-pit craters. These craters occur on Mars, Ganymede, and Callisto [e.g., *Wood et al.*, 1978; *Schenk*, 1993; *Barlow*, 2010]. On Mars and Ganymede, central-pit craters show a latitude dependency

with a decrease in the number of central-pit craters towards the poles. [*Barlow*, 2010; *Alzate and Barlow*, 2011].

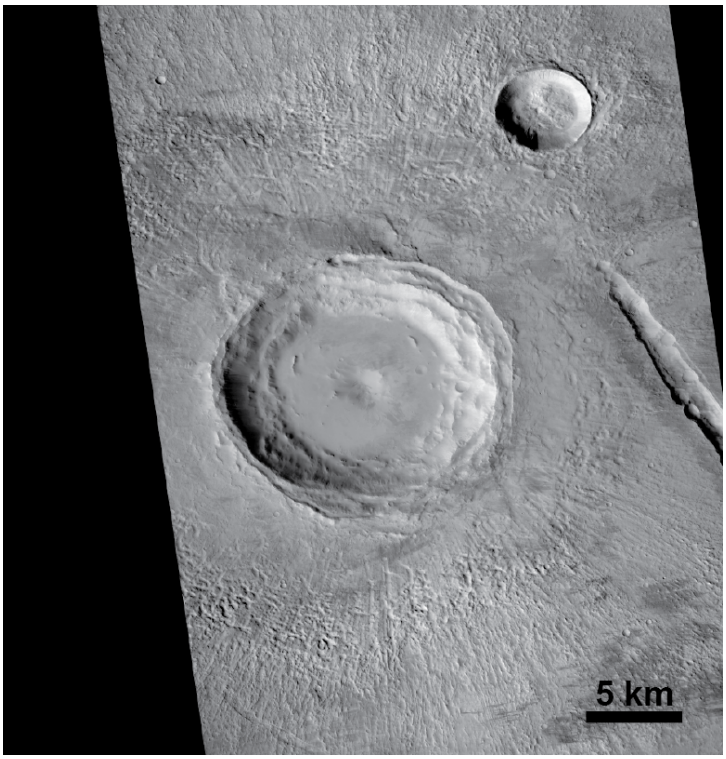

Figure 4.14: This unnamed Martian central-pit crater (116.8°W, 31.2°N) displays a small pit in the interior and a flat floor between the rim and the pit.

The typical central-pit crater geometry displays an outer rim and a circular rimmed depression on the crater floor (**Figure 4.14**) or central peak [*Hodges*, 1978; *Passey and Shoemaker*, 1982]. For craters where the central pit is on the floor, the central pit is usually deeper than the crater floor and surrounded by a circular raised ring. Between the pit and the crater wall is a smooth or hilly floor. On complex craters, the central pit may be present as summit pits [*Wood et al.*, 1978]. In some cases, the central pit can partially or completely replace central peaks or peak rings [*Schenk*, 1993]. On icy satellites, a high-albedo dome sometimes exists inside the central pit [*Passey and Shoemaker*, 1982; *Schenk*, 1993]. The ratio of the central pit diameter to the crater rim diameter is 0.02–0.48 for craters on Mars [*Barlow*, 2010] and 0.1–0.5 [*Schenk*, 1993] for craters on Ganymede and Callisto. Central-pit craters on Mars and Ganymede exhibit pristine to highly degraded morphologies [*Barlow*, 2006; *Barlow*, 2010; Alzate *and Barlow*, 2011]. This observation suggests that central-pit craters have formed

throughout the history of Mars and Ganymede [*Barlow*, 2010]. The occurrence of central-pit craters includes simple craters, complex craters, and peak-ring basins, which implies that central-pit craters could occur on all crater sizes.

Most hypotheses suggested that the formation of central-pit craters require the presence of volatiles in the target. These hypotheses include flash heating of volatiles and leaving behind a central pit [*Wood et al*, 1978; *Barlow*, 2010], collapse of the central peak due weak ice [*Passey and Shoemaker*, 1982], impact into a layered target [*Greeley et al.*, 1982], and drainage of impact melt [*Croft,* 1981; *Elder et al.*, 2012].

We compare the morphology, spatial distribution, and age of central-pit craters to the properties of concentric craters. First, we compare the ratio of the central-pit diameter relative to the crater diameter. The range of the ratio is narrower and smaller (0.02–0.5) than the range of R_D for concentric craters (0.1–0.9). Also, central pits can occur at almost all crater diameters (except mutli-ring basin diameter range), whereas concentric craters are mostly limited to the simple crater diameter range, which is about <20 km on the Moon. Another difference is that central-pit craters exhibit a flat or hilly floor between the pit and crater wall, whereas for concentric craters, the crater wall and concentric ridge is adjacent. On Mars and Ganymede, central-pit craters occur frequently toward the equatorial regions and formed throughout the history of these planetary bodies, whereas concentric craters are absent towards the poles and exhibit preferential distribution based upon the distribution of the mare. Furthermore, concentric craters dominantly formed before 3.8 Ga. From the contrasting properties, we conclude that concentric craters did not form similarly to central-pit craters because of the contrasting properties.

4.4.1.3 Multiple Impacts

The appearance of concentric craters, such as, Hesiodus A (17.1°W, 30.1°S **Figure 4.1a**) led some workers to suggest that they formed as a result of a double impact where the rim of the first impact is the rim crest and the rim of the second impact is the concentric ridge [e.g., *Sekiguchi*, 1970]. In the laboratory, *Oberbeck* [1973] recreated near-simultaneous impacts on the same position where the second impact occurred in the order of milliseconds after the initial impact. When the two impactors were of the same size, he found that the resulting crater is bowl-shaped, which resembled the morphology of a simple crater. On the other hand, when a more

massive impactor followed a less massive impactor, the resulting crater exhibited a central-peak and terrace-like morphology [*Oberbeck*, 1973].

In another impact experiment, *Schultz and Gault* [1985] tested the effects of clustered impacts. An impact from a cluster of projectiles created a crater with a shallow floor, surrounded by a depression, which looks like a multi-ring crater or a concentric crater. The resulting geometry of their experiment agrees with observation (1). Therefore, we test whether concentric craters may be a product of impact clusters.

First, we assume that multiple impacts have the same properties of normal impacts. Thus, if multiple impacts formed concentric craters, then the spatial distribution of concentric craters should be nearly random and almost equally distributed over the lunar surface with slight latitude dependence [e.g., *Gallant et al.*, 2009]. If concentric craters formed from multiple impacts, then concentric craters should exhibit a large range of preservation states. However, these assumed properties of multiple impacts do not agree with observations (3) and (5).

We conclude that concentric craters are not a product of multiple impacts for another reason. In nine instances, we observe a concentric crater with an elongate shape, a consequence of a low-angle impact (**Figure 4.4**). Within the elongated concentric craters, the concentric ridge is circular. This observation implies that if this concentric crater was due to successive impacts, the second impact was not oblique, but the result of a coincidental impact into the same position.

4.4.1.4 Impact into Layered Targets

Sub-kilometer concentric craters, also known as bench craters [*Wilcox et al.*, 2005] or inverted sombrero craters [*Barlow*, 2010], have a "double crater" morphology, which conform with observation (1) (**Figure 4.15a**). To avoid confusion in this study, we will call sub-kilometer concentric craters, bench craters. These bench craters display two rims, an outer crater and inner crater. Between the inner and outer rim is a relatively flat floor. *Quaide and Oberbeck* [1968] reproduced bench craters in the laboratory. They found that bench craters are a consequence of impacting layered targets where the strength of the underlying layer is higher than the strength of the surface layer. However, *Quaide and Oberbeck* [1968] could only produce bench craters when the diameter of the crater was >8 times the thickness of the surficial layer. Otherwise, the crater geometry displayed a different morphology (i.e., flat-floor and central mound craters). In an impact into a layered target, the softer surficial layer ejects more material than the higher strength subsurface layer because the amount of energy required to eject the softer layer is lower

than the higher strength material. Consequently, the softer layer creates a larger crater than the subsurface layer, which creates the bench morphology. The depth of the bench occurs at the depth of the interface of the two layers.

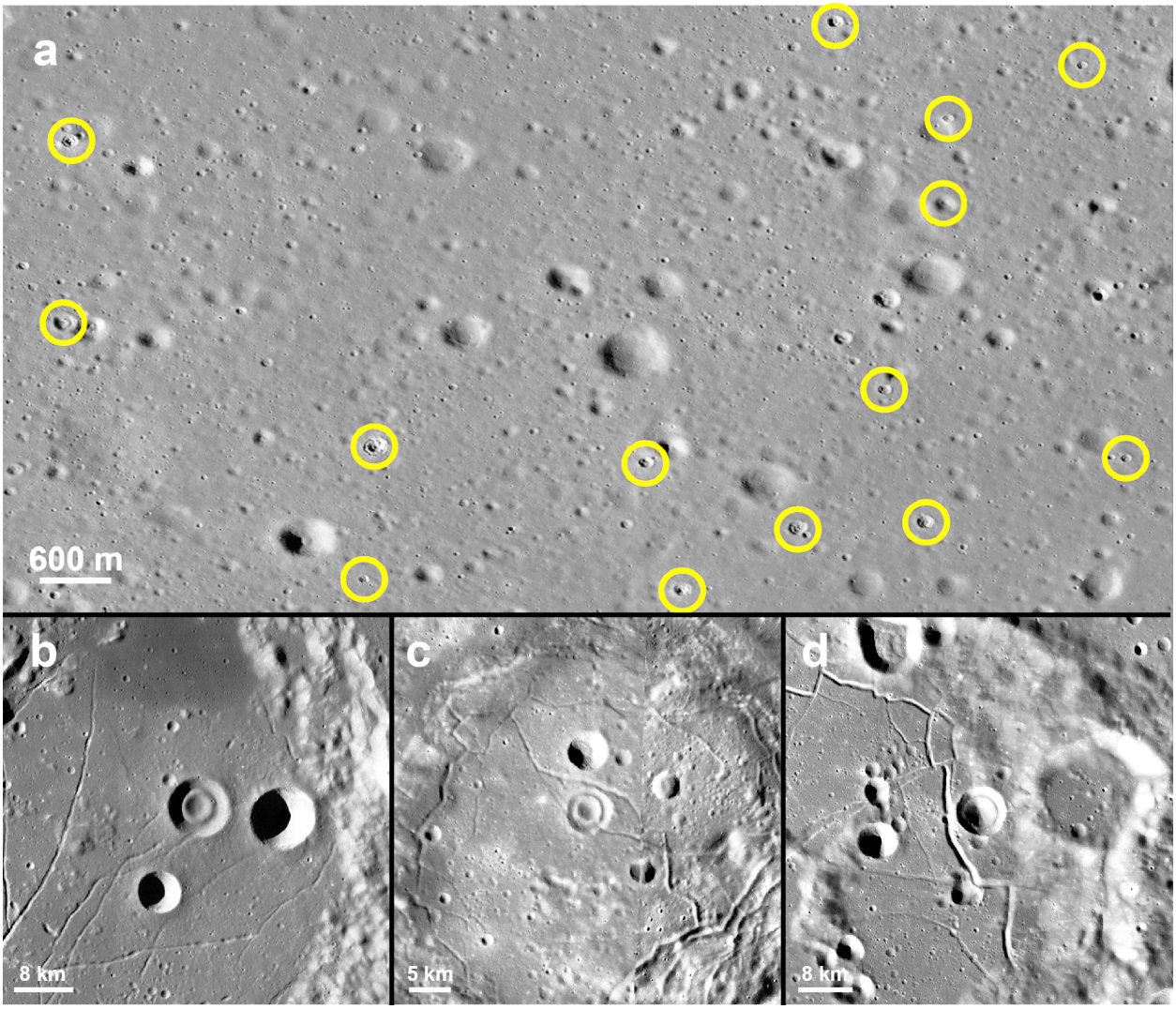

Figure 4.15: (a) A NAC image of bench craters in Oceanus Procellarum (41.6°N, 48.8°W). Bench craters (yellow circles) commonly occur in clusters. (b–d) These WAC images show concentric craters in proximity to simple craters of similar diameter. If the local region contains a layered target, then nearby craters should display a concentric shape. (b) Unnamed crater in Humboldt (26.6°S, 83.4°E) (c) Unnamed crater (38.3°N, 81.2°W) (d) Repsold A.

In regions with two layers, such as the maria, which contain a thin layer of regolith on top of a lava flow, bench craters are abundant (**Figure 4.15a**). If concentric craters formed as a result

of an impact into a layered target, then they would occur in clusters [*Oberbeck*, personal comm.]. Instead, concentric craters are usually isolated. In some cases, concentric craters lie next to unmodified simple craters of the same diameter (**Figure 4.15b–c**). A potential explanation is that these impactors hit shallow and dense igneous bodies embedded in lower strength highlands material in thermally active regions, such as the mare. If this is the case, then we should observe differences in composition between the concentric crater and the surrounding area (e.g., basaltic versus anorthositic) and a larger range of crater degradation because impact into layered target could form at any time.

From a morphological standpoint, bench craters may explain some of the observed morphologies in concentric craters. For instance, the higher strength of the underlying layer may explain the shallow depths (observation 2). However, the V-shaped valley of toroid and bubbly concentric craters is inconsistent with the bench geometry. Impact into layered targets is unlikely to be the mechanism responsible for the origin of concentric craters based upon morphological, compositional, and age arguments.

4.4.2 Endogenic

An endogenic process is a surface process group that involves interactions between the lunar surface and its environment. We consider four possible processes: viscous relaxation, mass wasting, volcanism, and igneous intrusions.

4.4.2.1 Viscous Relaxation

The crater depths on icy bodies (e.g., Ganymede, Callisto, and Enceladus) are usually shallower than craters on rocky bodies because of a process called viscous relaxation [e.g, *Parmentier and Head*, 1981; *Passey and Shoemaker*, 1982; *Dombard and McKinnon*, 2006; *Bland et al*., 2012]. The topography of planetary surfaces relaxes when the crustal material behaves as a fluid due to increasing temperatures with depth below the surface. As a result, viscous relaxation causes long-wavelength topography, which is more likely to interact with deeper low viscosity material, relaxes more than shorter-wavelength topography [*Scott*, 1967]. The consequence of relaxation in craters is that the crater floors shallow and occasionally upbow. However, rims and central peaks, which are short-wavelength topography, preserve their original structure.

There are suggestions that floor-fractured craters are a product of viscous relaxation [e.g., *Bratt et al.*, 1981; *Hall et al.*, 1981]. Observations that support floor-fractured craters are

consistent with the viscous relaxation process include: 1) shallow crater floors, 2) the presence of floor-fractured craters near high thermal regions, 3) the timing of floor-fractured crater formation with impact-basin formation and magmatic activity. The connection between floor-fractured craters and impact basins and mare regions is critical to the viscous relaxation interpretation because impact basins and the mare provided heat to drive this process [*Hall et al.*, 1981].

Hall et al. [1981] and *Dombard and Gillis* [2001] tested the viscous relaxation interpretation on floor-fractured craters through computer simulations. *Hall et al.* [1981] simulated the relaxation of a fresh crater profile. As a result, the model reproduced the profile of a floor-fractured crater. However, the length of time to produce a floor-fractured crater is unknown in *Hall et al.'s* [1981] model. *Dombard and Gillis* [2001] included time in their model and found that the viscous relaxation process requires about 4.5 Gyr to produce a floor-fractured crater; this length in time is equivalent to the age of the Solar System.

The viscous relaxation hypothesis can explain observations (2), (3), and (4) of concentric craters. However, the time to relax a concentric crater is greater than floor-fractured craters because concentric craters have a shorter wavelength topography. Therefore, the time to produce a concentric crater through the viscous relaxation process requires more than 4.5 Ga, which is longer than the age of the Solar System.

4.4.2.2 Mass Wasting

We also consider mass wasting and/or catastrophic collapse of the crater rim as a method of concentric ridge formation. Mass wasting is a common process that occurs across the Moon [e.g., *Lindsay*, 1976; *Xiao et al.*, 2013]. Large impact craters, such as complex craters and peak-ring basins, exhibit features that are mass wasting products. After impacts that result in complex crater and peak-ring basins, their transient craters are gravitationally unstable causing them to collapse, which result in the formation of terraces and scallops [e.g., *Quaide et al.*, 1965]. Terraces are scarps with a relatively flat top [*Settle and Head*, 1979], similar to the meniscus-type concentric craters. Unlike concentric craters, terraces appear in a stair-step pattern toward the crater center and do not occur as a single continuous scarp around the crater. Scallops are multiple arcuate-shaped slump structures on the crater wall and floor [*Settle and Head*, 1979]. Again, the morphology of scallops is not continuous around the entire crater. Therefore, the geometry of terraces and scallops do not meet observation (1).

We also examine degraded craters because mass wasting is a dominant process that erodes crater geometry. Based upon our analysis from Section *3.1.2*, concentric craters are shallower than degraded craters. The interpretation from Section *3.1.2* suggests that concentric craters cannot have formed solely from mass wasting because the crater depths are too shallow. Therefore, mass wasting cannot explain observation (2).

The spatial distribution of concentric craters does not agree with the spatial distribution of degraded craters and complex craters. Degraded craters and complex craters occur on all terrains, but depend on the age of the surface. Therefore, mass wasting cannot account for observation (3)

4.4.2.3 Volcanism

Previous workers suggested that lava extruded inside the crater and formed the concentric ridge [e.g., *Wood*, 1978]. This hypothesis explains observations (2), (3), and (5). The addition of lava on the floor of the concentric crater would explain the extra volume required to shallow the crater depths. Also, the proximity of concentric crater to the margins of the maria and mare ponds suggests the concentric crater formation is related to the nearby volcanic activity. Furthermore, the concentric crater ages coincide to when the Moon was volcanically active. However, if lava created the concentric ridge, then we would observe the composition of the concentric ridge to differ from the surrounding area. From **Figure 11**, the FeO and TiO_2 abundance of the concentric ridge is similar to the surrounding area, which indicate lava flows did not form the concentric ridge. Thus, volcanism does not agree with observation (4).

4.4.2.4 Igneous Intrusions

The alternative model to floor-fractured crater formation is the igneous intrusions model [*Schultz*, 1976a]. Floor-fractured craters show agreement to observations (2), (3), and (5). As shown in **Figure 4.9**, the depths of floor-fractured craters and concentric craters are shallower than degraded craters. Also, in **Figure 4.10**, the spatial distribution of floor-fractured craters and concentric craters are along mare margins. In addition, floor-fractured craters formed when the Moon was thermally active [*Schultz*, 1976a]. Therefore, floor-fractured craters and concentric craters formed at the same time period. However, floor-fractured craters occasionally show mare and pyroclastic deposits on the crater floor, whereas the concentric crater interior does not show any evidence of mare except Firmicus C, which may exhibit a pyroclastic deposit. In contrast to the volcanism hypothesis, the igneous intrusions hypothesis indicates that magma never erupted

into the crater. Therefore, the igneous intrusions hypothesis agrees with observation (4). However, one draw back is that floor-fractured craters do not agree with observation (1).

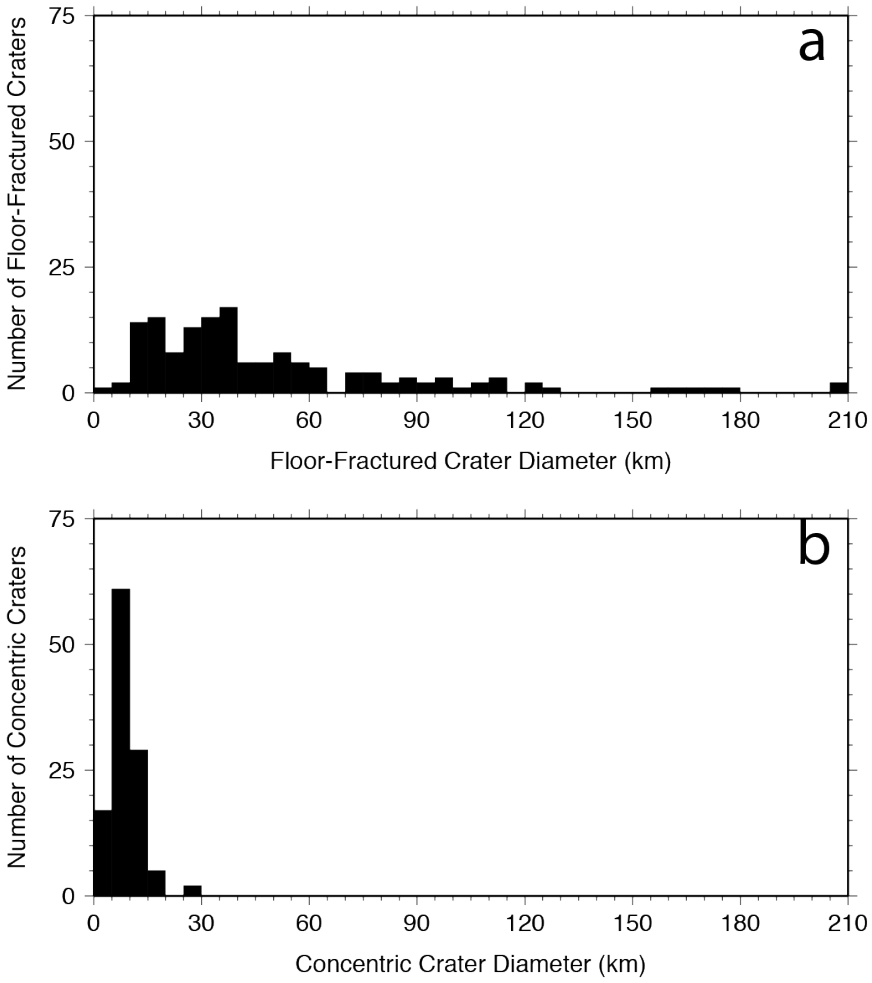

Figure 4.16: (a) The frequency of floor-fractured craters and (b) concentric craters at various diameters. Floor-fractured craters frequently occur in larger craters [Jozwiak et al., 2012], whereas concentric craters (b) are abundant at smaller craters. Floor-fractured craters and concentric craters coexist at 10–15 km in diameter. This range is also the transition between simple to complex craters.

One possible explanation for the disparity of observation (1) is that magmatic intrusions into a large crater result in a different surface expression than intrusions into a smaller crater. In **Figure 4.16**, we observe that floor-fractured craters occur at all crater diameters except at <10 km in diameter range. On the other hand, the diameter of concentric craters is rarely >15 km. The only bin where concentric craters and floor-fractured craters are common is at the 10–15 km

diameter bin. Interestingly, The 10–15 km bin is also the diameter range where simple craters transition to complex craters [*Pike*, 1976; 1980]. Therefore, the structure underneath simple craters is likely different in contrast to complex craters, which may be critical to determining whether igneous intrusions form a concentric crater or a floor-fractured crater. We hypothesize that igneous intrusions underneath <15 km in diameter impact craters may form concentric craters, whereas intrusions underneath >15 km in diameter craters may result in floor-fractured craters.

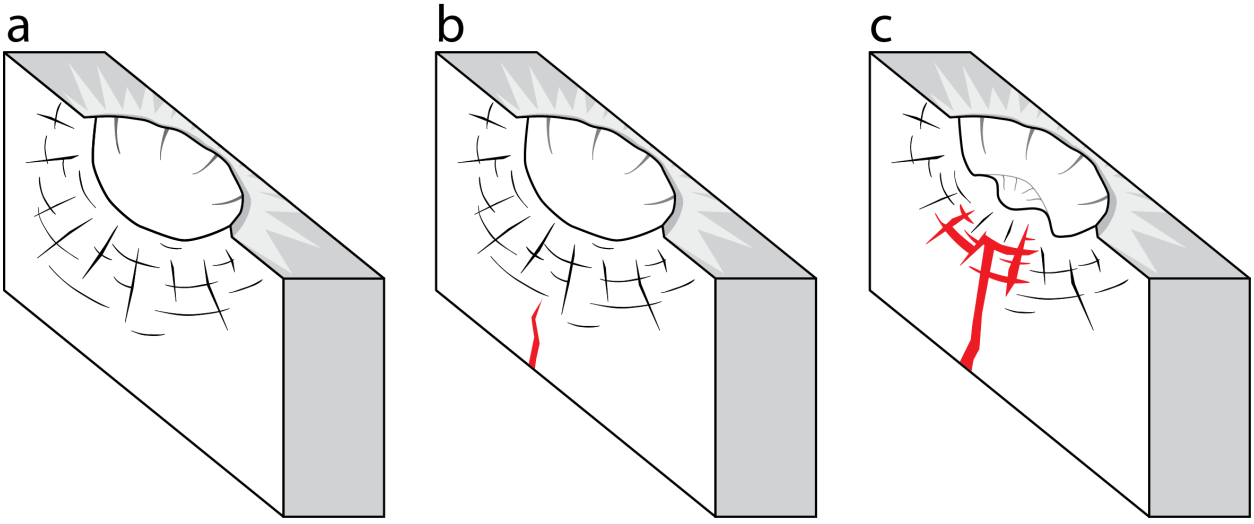

Figure 4.17: A cartoon of concentric crater formation in cross section. a) A simple impact crater. b) Magma intrudes through the surface. c) Magma intrudes into impact-induced fractures and fills them with magma. This addition of volume uplifts the crater floor and produces a concentric ridge.

4.4.3 Conceptual Model

We deduce that the igneous intrusions hypothesis is the best model that accounts for the concentric crater properties. Crater density measurements of the major mare regions show that before the Eratosthenian period, volcanic activity was intense [e.g., *Hiesinger et al.*, 2000; 2010]. During this time, we expect igneous activity to dominant areas in and around the mare regions. Yet, concentric craters are only found on the edges of the mare regions instead of dominating the mare interior. The absence of concentric craters in the mare interior is probably because the mare buried any concentric craters that formed there. The accumulation of lava flows in the center of mare regions is at least hundreds of meters thick [*DeHon*, 1974; 1975; 1977; 1979; *DeHon and Waskom*, 1976] to kilometers thick [*Williams and Zuber*, 1998; *Thomson et al.*, 2009]. If lava

penetrated the interior of concentric craters, then the thickness of the cumulative lava flows only need to be ~100 m, the median height of a concentric ridge, in order to bury a concentric ridge. On the edges of the mare regions, cumulative lava flow thicknesses are thinner than the mare center, which is likely to preserve concentric craters.

We use an identical conceptual model as *Schultz* [1976a] to illustrate concentric crater formation (**Figure 4.17**). The basis of this model is that below an existing ≤15 km impact crater (**Figure 4.17a**), magma filled the impact-induced fractures underneath the crater (**Figure 4.17b**) and formed large magmatic bodies, which uplifted the floor (**Figure 4.17c**). Consequently, the uplifted floor contributes to shallowing the crater depth.

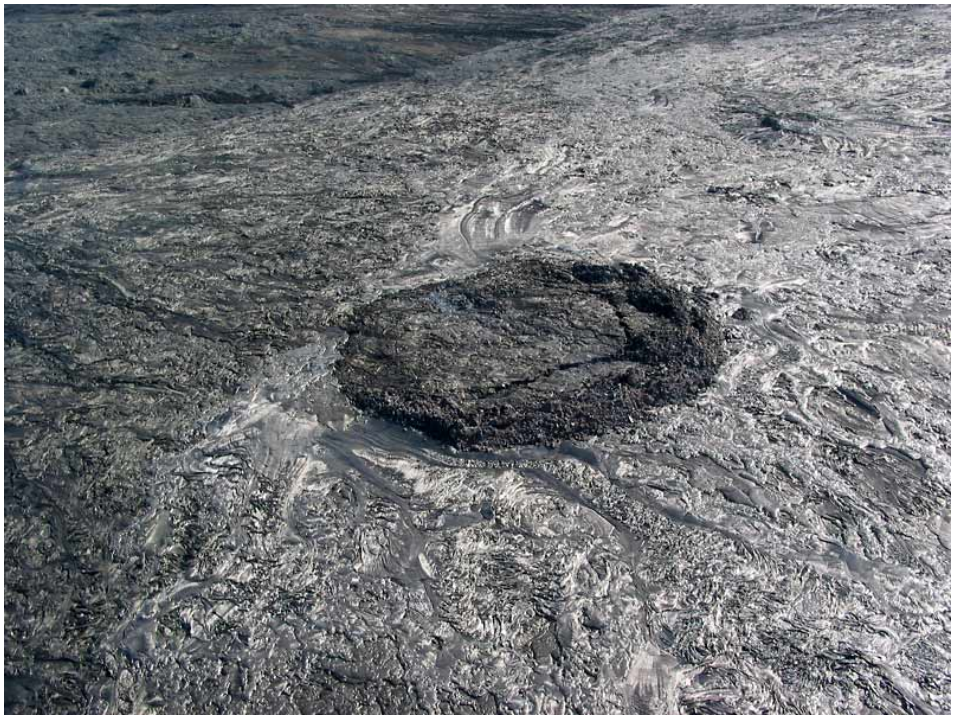

Figure 4.18: A tens of meters wide shatter ring on Kīlauea Volcano. Photo by the Hawaiian Volcano Observatory/United States Geological Survey.

We predict that the accumulated volume and distribution of magma underneath the crater affect the resulting shape of the concentric ridge. Although we observe a relationship between the crater diameter and the crater class (i.e., floor-fractured craters and concentric craters), there are floor-fractured craters that are <10 km in diameter and concentric craters that are >15 km in diameter. Therefore, we suggest that total volume of magma accumulated beneath the crater and

the geometry of the intrusion control the surface expression of the modified crater. We infer that the structure underneath simple craters is different than complex craters, which influences simple craters to modify towards concentric craters and complex craters and peak-ring basins to modify towards floor-fractured craters. Additionally, we suggest that the accumulated volume and distribution of magma underneath simple craters sways concentric craters toward one of the three subclasses (i.e., torid, meniscus, and bubbly).

The formation of a ring structure is possible in the igneous environment. One type of a raised-ring structure is the shatter ring (**Figure 18**). Shatter rings are circular to elliptical features composed of fragmented slabs of pāhoehoe [*Kauahikaua et al.*, 1993; 2003; *Orr*, 2010]. In an overfilled lava tube, the continuous fluctuation in volume of lava through a weakly constructed lava tube results in fragmentation of the roof of the lava tube [*Orr*, 2010]. Consquently, the fragmentation of the roof and the pulsation of the lava tube roof lead to a ring-shaped rubble pile. Therefore, we do not find igneous intrusions forming ring-shaped structures in a crater as a far-fetched hypothesis.

4.5 Concentric Craters on Other Planetary Bodies

4.5.1 Mars

There are instances of concentric-looking craters on other planetary bodies (**Figure 4.19a**), a crater on Mars. *Ormö et al.* [2013] studied three concentric-looking craters on Mars, including Ada. From their studies, they suggested that these concentric craters are a result of impact into layered targets based upon their observation of the contrast in albedo between the walls of the outer and inner crater. In other words, these craters are large bench craters. Therefore, the concentric-looking craters on Mars had a different origin.

4.5.2 Mercury

Several workers found two different geomorphological features related to the igneous intrusions process. *Gillis-Davis et al.* [2009] studied pit-floor craters, which formed from shallow magmatic intrusions underneath the crater to only be later withdrawn; the result of this process created a pit inside the crater. In another study, *Head et al*., [2009] discovered floor-fractured craters [*Head et al.*, 2009] on the surface of Mercury. Thus, we perform an initial survey of the surface of Mercury for concentric craters using the Mercury Dual Imaging System (MDIS) Wide Angle Camera. In this survey, we find at least one concentric crater candidate

(**Figure 4.19b**). Future detailed studies of concentric craters on Mercury will help broaden current understanding of concentric craters.

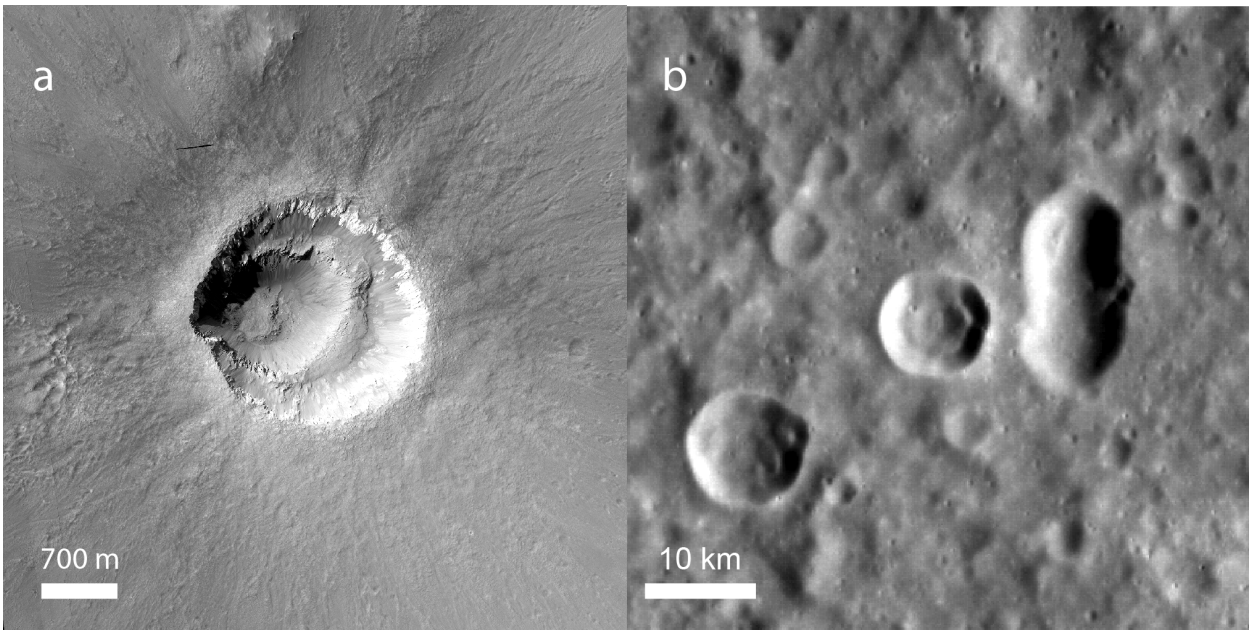

Figure 4.19: (a) Ada crater, a bench crater on Mars. (b) An unnamed potential concentric crater (13.4°S, 58.6°E) on Mercury.

4.6 Conclusion

Lunar concentric craters are craters containing a doughnut-shaped ridge in the interior of the crater called the concentric ridge. We classified concentric craters into three subclasses: toroid, meniscus, and bubbly based upon observations of the relationship between the concentric ridge and the crater wall and continuity of the concentric ridge. In this study, we found a total of 114 concentric craters and examined their morphology, spatial distribution, composition, and age. The concentric ridge exhibits no relationship with itself or the parent crater dimensions. Based upon measurements of the crater depth and rim height, concentric crater depths are shallow, which could not be explained by mass wasting alone. The spatial distribution of concentric craters is similar to the spatial distribution of floor-fractured crater. Specifically, the distribution of concentric craters is along highlands/maria boundaries and in mare ponds. The interior of concentric craters is similar to the surrounding area. The formation of the majority of concentric craters occurred during and before the Imbrium period, which matches the timing of mare

volcanism. We infer that concentric craters formed as a result of igneous intrusions underneath the crater because this hypothesis can explain the concentric crater properties.

CHAPTER 5

THE PHYSICAL AND COMPOSITIONAL PROPERTIES OF LUNAR LOCALIZED PYROCLASTIC DEPOSITS

To Be Submitted To: Journal of Geophysical Research – Planets.

Abstract – An array of instruments onboard Lunar Reconnaissance Orbiter and Kaguya permitted high-spatial resolution and diverse global data sets of the lunar surface. Consequently, we conducted a detailed study of localized pyroclastic deposits. The goal of this work is to (1) describe the physical and compositional properties of 34 previously-identified localized pyroclastic deposits located across the Moon, (2) compare the properties of localized to regional pyroclastic deposits, and (3) find additional methods to differentiate a pyroclastic deposit from a mare pond. We measured and estimated the pyroclastic volume, the juvenile proportion, radar backscatter, surface rock abundance, regolith density, and mineralogical composition in each of the localized pyroclastic deposits. Within these parameters, we found clusters among the relationships between the glass proportion, surface rock abundance, and the maximum deposit thickness. As a result, we categorized pyroclastic deposits into four groups: Glassy, Blocky, Basaltic, and Hybrid based upon the different permutations of high and low surface rock abundances and glass proportions. In comparing the properties of regional to localized pyroclastic deposits, we found that the Glassy and Basaltic group is the most consistent with the properties of regional pyroclastic deposits because of their low surface rock abundances, low radar backscatter, and a range of glassy to crystalline proportions. We also found that seven of the localized pyroclastic deposits in our sample have properties consistent with mare ponds. These deposits have similar regolith densities, surface rock abundance, radar backscatter, and crystalline proportions to the surrounding area.

5.1. Introduction

Lunar pyroclastic deposits are excellent probes of the lunar interior and important future resources. *Delano* [1986] interpreted that pyroclastic material are primitive samples of the lunar interior [*Delano*, 1986]. *Hawke et al.* [1990] and *Hawke and Coombs* [1994] made a strong case that these deposits contain valuable raw materials, such as titanium, iron, oxygen, and helium-3. Thus, pyroclastic deposits are important to understanding the geological history of the Moon and in-situ resource utilization.

Gaddis et al. [1985] divided lunar pyroclastic deposits into two groups based upon areal size: regional pyroclastic deposits (>2500 km^2) and localized pyroclastic deposits (<2500 km^2) [*Gaddis et al.*, 2000]. The properties of regional pyroclastic deposits are well studied from spectral studies [e.g., *Adams et al.*, 1974; *Weitz et al.*, 1998; *Gaddis et al.*, 2003; *Wilcox et al.*, 2006] and radar studies [e.g., *Pieters et al.*, 1973; *Zisk et al.*, 1977; *Gaddis et al*., 1985; *Carter et al.*, 2009]. In contrast, there are only partial descriptions of localized pyroclastic deposits. Most localized pyroclastic deposit studies focus on spectral and albedo characteristics [e.g., *Hawke et al*., 1989; *Gaddis et al*., 2000; *Gaddis et al.*, 2003]. There are more detailed studies (e.g., radar, morphology, composition), but only of the Alphonsus localized pyroclastic deposits [e.g., *Head and Wilson*, 1979; *Coombs et al.*, 1990; *Allen et al.*, 2013], which may not be representative of all localized pyroclastic deposits.

In this study, we investigate 34 previously-identified localized pyroclastic deposits from *Gaddis et al.* [2003] and *Gustafson et al.* [2012]. The goal of this study is to: 1) characterize the physical and compositional properties of localized pyroclastic deposits, 2) compare localized to regional pyroclastic deposits and, 3) find new methods to differentiate a pyroclastic deposit from a mare pond.

5.2. Background

5.2.1 General Properties of Localized Pyroclastic Deposits

There are more than fifty localized pyroclastic deposits on the lunar surface [*Gaddis et al.*, 2003]. Advancements in instrumentation such as those onboard the Lunar Reconnaissance Orbiter and Chandraayan-1, as well as Arecibo assisted in discovering additional pyroclastic deposits [*Carter et al.*, 2009; *Gustafson et al.*, 2012; *Besse et al.*, 2014; *Cambpell et al.*, 2014]. Localized pyroclastic deposits are isolated, low albedo material commonly found in floor-

fractured craters or along mare margins [*Gaddis et al.*, 2000]. The centers of these deposits usually show an irregular-shaped crater [*Gaddis et al.*, 2003].

5.2.2 The Alphonsus Localized Pyroclastic Deposits

The Alphonsus localized pyroclastic deposits are the most thoroughly studied in comparison to other localized pyroclastic deposits. *Head and Wilson* [1979] determined the geometrical properties of the Alphonsus localized pyroclastic deposits. First, they computed the area and volume of the pyroclastic deposits and volcanic craters. From these geometrical properties, they calculated the proportion of juvenile to non-juvenile material for each deposit. In another method, *Allen et al.* [2013] used the Moon Mineralogy Mapper (M^3) to estimate the glass proportion in the Alphonsus pyroclastic deposits. They found that the Alphonsus deposits comprise of low-Ca pyroxene in a pyroclastic glass-rich matrix. Assuming that the juvenile components are pyroclastic glass, then the glass proportion results by *Allen et al.* [2013] agrees with the juvenile proportion calculated by *Head and Wilson* [1979].

Several workers examined the radar backscatter of the Alphonsus deposits. *Head and Wilson* [1979] observed that these pyroclastic deposits exhibit low radar backscatter, similar to regional pyroclastic deposits. This observation suggests that the average grain size in the Alphonsus localized pyroclastic deposits is smaller than the average grain size of non-pyroclastic regolith. *Coombs et al.* [1990] reaffirmed that the radar backscatter in Alphonsus is low. Also, they reported high radar backscatter within the volcanic craters of the Alphonsus deposits, which implies that the volcanic craters are blocky.

Head and Wilson [1979] used their observations and calculations (i.e., geometrical properties, the fraction of non-juvenile material, the absence of visible lava flows) to test various eruptive scenarios. They found that the vulcanian-type eruption is the most likely explosive style to produce the Alphonsus localized pyroclastic deposits.

5.3.3 Global Observations of Localized Pyroclastic Deposits

From studying the spectral characteristics of localized pyroclastic deposits across the nearside of the Moon, *Hawke et al.* [1989] categorized these deposits into three groups: Group I displays highlands and pyroclastic glass signatures; Group II exhibits mare and pyroclastic glass signatures; Group III consists of olivine and orthopyroxene. *Hawke et al.* [1989] interpreted that vulcanian-type eruptions formed Group I and II localized pyroclastic deposits, as this type of eruption would eject entrained local material (i.e., highlands- or mare-bearing material) and

pyroclastic glass. Variation in the eruption conditions would control the proportion of local material into the deposit. In Group III spectra, *Hawke et al.* [1989] interpreted the presence of olivine instead of pyroclastic glass in the spectra because the glass spectral signature is too weak to produce the observed asymmetric 1-μm absorption [*McCord et al.*, 1981]. Thus, *Hawke et al.* [1989] predicted that a vulcanian-type eruption formed Group III where the olivine originated from olivine-bearing magma or devitrification of the pyroclastic glass.

Gaddis et al. [2000; 2003] examined the albedo and band ratios derived from the Clementine UVVIS data set to deduce the maturity, mafic content, and titanium content of various localized pyroclastic deposits across the Moon (i.e., near and farside). *Gaddis et al.* [2003] found that localized pyroclastic deposits exhibit a wide range of albedo and mafic content, but all of the deposits have low-Ti content. Thus, *Gaddis et al.* [2000] proposed that the proportion of local material entrained in the eruption caused the observed diversity of localized pyroclastic deposits. Additionally, *Gaddis et al.* [2003] inferred that maturity is not the cause of the wide range of albedo and mafic contents in pyroclastic deposits.

In this study, we use various data sets and products from the Lunar Reconnaissance Orbiter and Kaguya to describe the physical and compositional properties of localized pyroclastic deposits. We measure the surface and subsurface rock abundance and soil density of each localized pyroclastic deposit. In addition, we model the pyroclastic glass, olivine, orthopyroxene, clinopyroxene, and plagioclase fractions. Lastly, we characterize the geometry and structure of localized pyroclastic deposits with two different digital terrain models (DTM). Afterward, we use these observations to discern the different types of localized pyroclastic deposits.

5.3. Methods

5.3.1 Choosing Localized Pyroclastic Deposits

The lunar surface contains more than fifty localized pyroclastic deposits with areas <1000 km^2 [*Gaddis et al.* 2003]. We elect to study 34 previously-identified localized pyroclastic deposits compiled by *Gaddis et al.* [2003] and identified by *Gustafson et al.* [2012] (**Figure 5.1**) because we want pyroclastic deposits that exist on flat topography to minimize the influence of mass wasting. The consequences of mass wasting on pyroclastic deposits include an increased block population and compositional mixing; factors that would complicate our study of the physical and compositional properties of pyroclastic deposits.

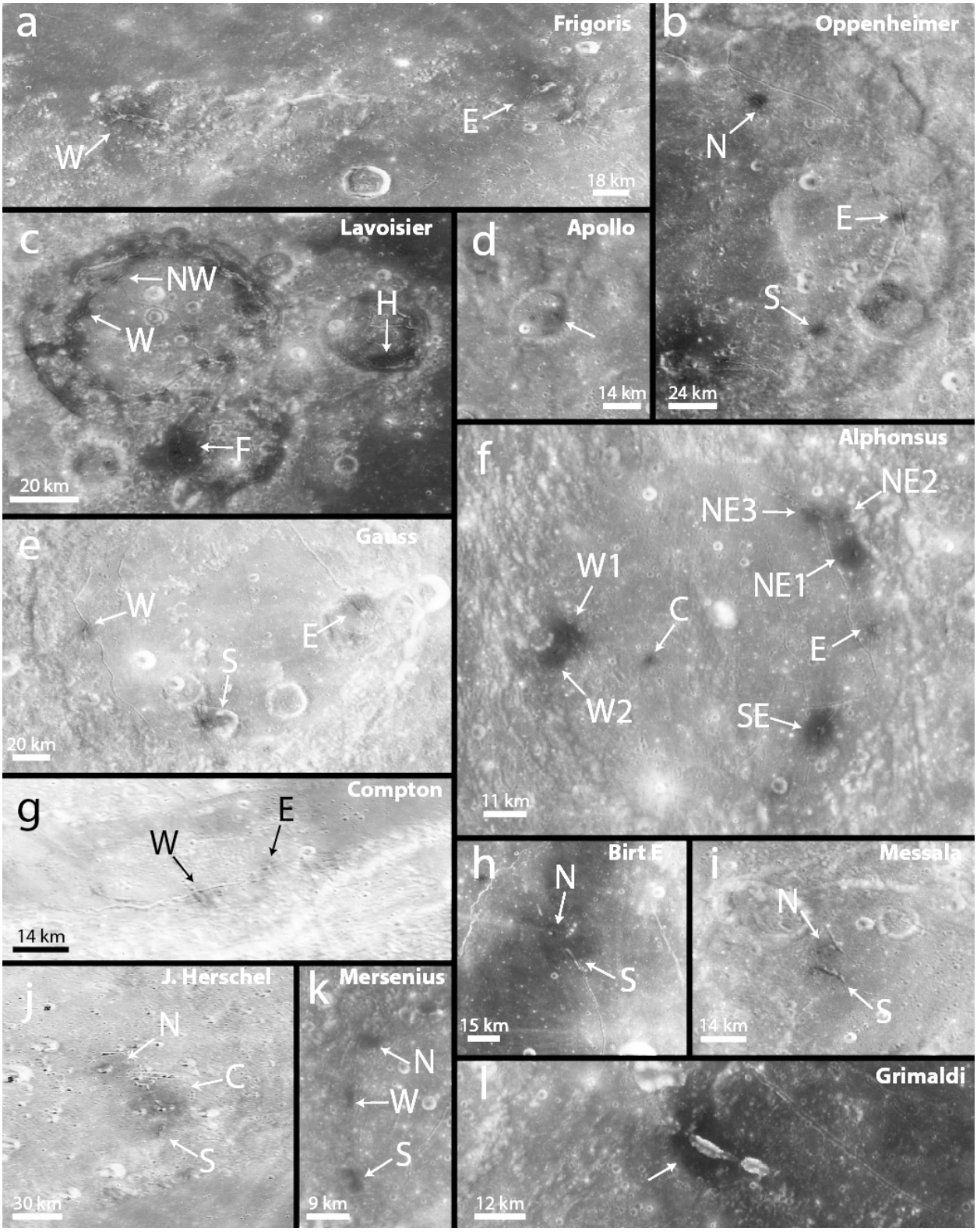

Figure 5.1: Overview images of all the pyroclastic deposits in this study.

5.3.2 Determination of the Physical Properties of Pyroclastic Deposits

5.3.2.1 Volume Calculations of Pyroclastic Deposits

We use the 750 nm albedo maps from the Kaguya Multispectral Imager (MI) to define the boundary of each localized pyroclastic deposits. MI imaged the surface at nine different bands, five in the visible (i.e., 415, 750, 900, 950, 1000 nm) and four in the near infrared (i.e., 1000, 1050, 1250, 1550 nm) [*Ohtake et al.*, 2008]. The spatial resolution of the visible bands is 20 m/pixel and of the near-infrared bands is 62 m/pixel. We looked for the albedo contrast between the pyroclastic deposit and the surrounding area to map the areal extent of the pyroclastic deposits. On four occasions, we divided the pyroclastic deposits into multiple overlapping deposits (**Figure 5.2a**). We drew the boundaries between overlapping pyroclastic deposits from visually inspecting changes in albedo within the overlapping deposits (**Figure 5.2b**).

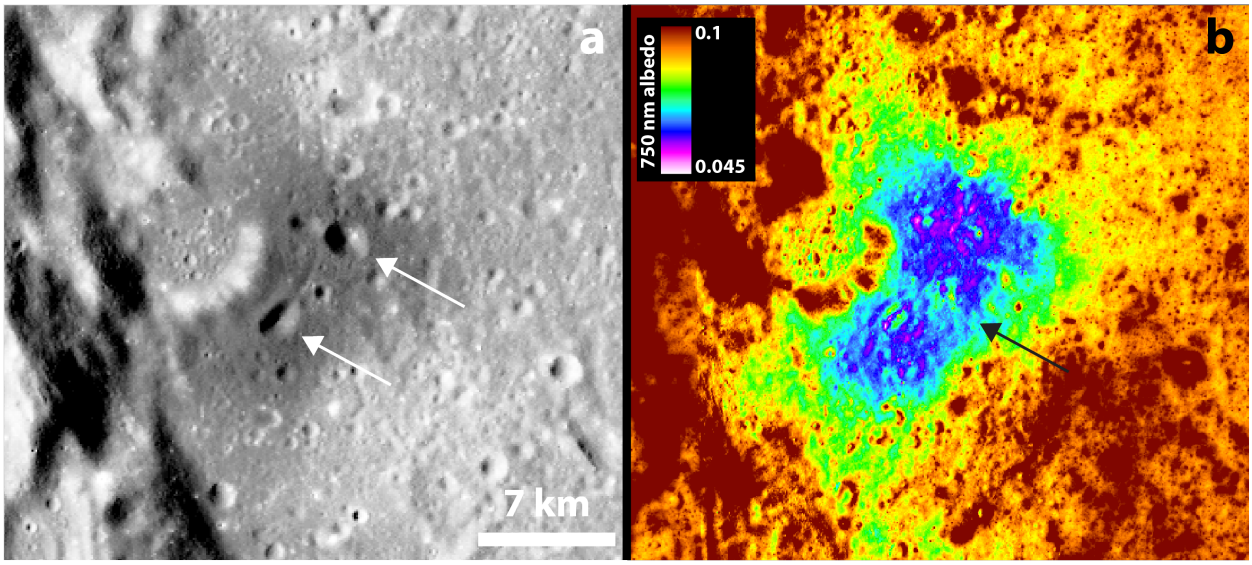

Figure 5.2: a) Alphonsus W1 and W2 localized pyroclastic deposits contains two vents (arrows). b) A Kaguya 750-nm albedo image showing how overlapping deposits are partitioned (arrows).

We outline the vents and nearby structures with the Lunar Reconnaissance Orbiter Camera (LROC) Wide Angle Camera (WAC) global morphologic map. The global morphologic map consists of mosaicked low-sun angle images from LROC WAC with a spatial resolution of 100 m/pixel [*Robinson et al.*, 2010]. The low-sun angle map is useful for enhancing topography. We map vents, nearby rilles and other major topographic features (e.g., crater walls) because

mass wasting from these morphological features could skew the block population and compositional results. In addition, these topographic features could adversely affect our volume calculations of these deposits. We identify vents from their elliptical shape in the center of the deposits (**Figure 5.3a**). When a rille intersects a pyroclastic deposit, we define the vent where the width of the rille is flared and the edges are gentler (**Figure 5.3b**). Occasionally vents are non-circular and instead are elongated or linear (**Figure 5.3c**).

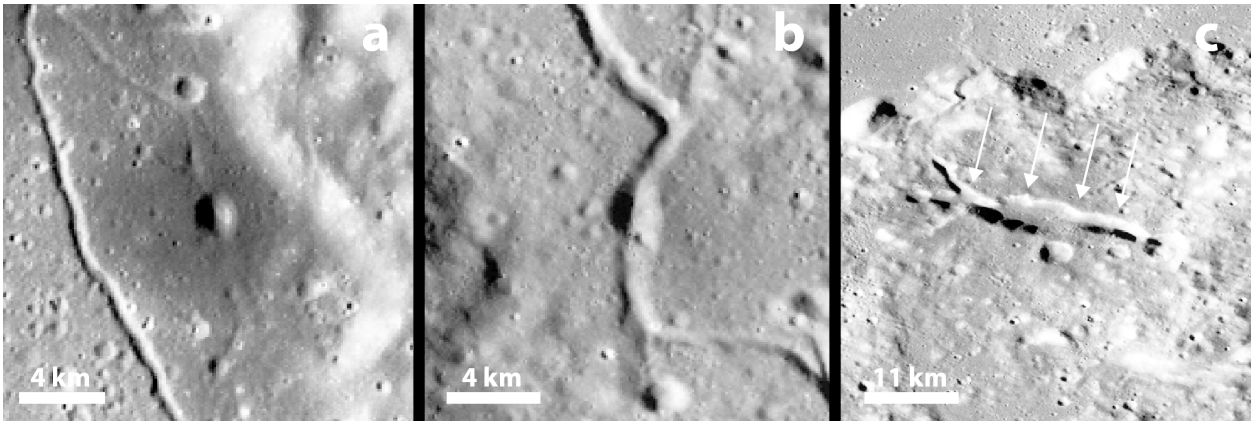

Figure 5.3: a) An elliptical vent at Alphonsus NE1 b) A vent along a rille at Gauss W. This vent is identified by where the width of the rille is flared. c) An elongated vent at Frigoris W.

We use two digital terrain models (DTM), the LROC WAC DTM and the Kaguya Terrain Camera (TC) DTM to calculate the total pyroclastic, juvenile, and non-juvenile volume of each deposit. The purpose of calculating the volumes with two different DTMs is to ensure reproducibility and uncertainty in our results. The LROC DTM data is derived from the WAC data with 100 m/pixel spatial resolution. Globally, the vertical error is <20 m, except for the nearside mare, which has a vertical error of <10 m [*Scholten et al.*, 2012]. In contrast, the Terrain Camera has a spatial resolution of 7.4 m/pixel (4096 pixel/degree) and a vertical error around 3–5 m [*Haruyama et al.*, 2008; *Haruyama et al.*, 2012]. We downsample the TC DTM data to 100 m/pixel because of the large file sizes. We summarize the difference between the WAC DTM and the TC DTM in Appendix E.

We calculate the volume of each pyroclastic deposit by subtracting the pre-erupted topography from the current topography. In this calculation, we employ the same technique to that of *Head and Wilson* [1979]. In order to obtain the total volume of the pyroclastic deposit, we model the pre-erupted surface. For each DTM, we delete all pixels that are within the boundary

of the pyroclastic deposit. Next, we use the pixels adjacent to the pyroclastic deposit area to interpolate the pre-erupted surface. Within ArcGIS, we use an interpolation technique called, "spline with barriers" with a smoothing factor of 0. Occasionally, pyroclastic deposits are next to major topographic features, such as crater walls. When this is the case, we use "barriers" to prevent these large topographic features from affecting our interpolation. As a result of the interpolation, we produce a DTM that models the pre-erupted surface (**Figure 5.4c,f**). Then, we subtract the pre-erupted DTM from the pyroclastic deposit DTM (**Figure 5.4d,g**). Afterward, we evaluate the volume of each positive subtracted pixel within the pyroclastic deposit by multiplying the subtracted pixel value by the size of the pixel (i.e., 100 m^2). The summation of this evaluation results in the total volume of the pyroclastic deposit.

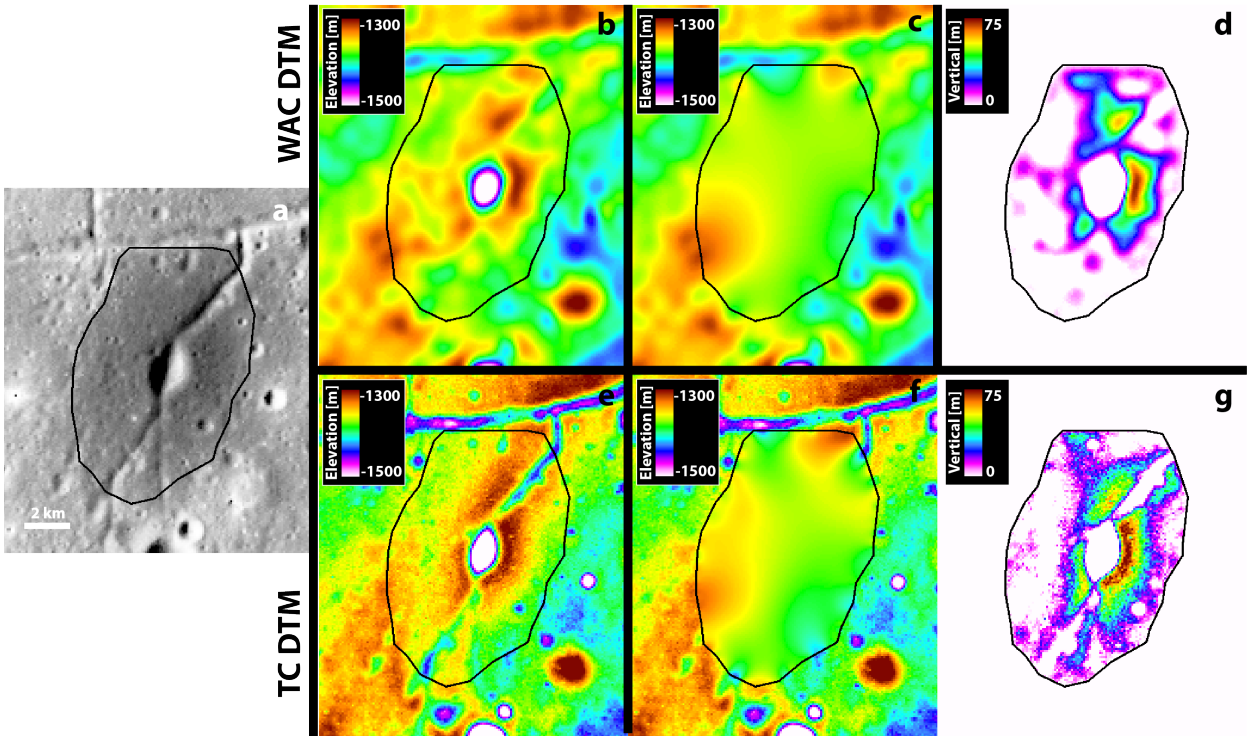

Figure 5.4: a) A localized pyroclastic deposit in Alphonsus. b–d) WAC DTM e–g) TC DTM b,e) DTM of the pyroclastic deposit. c,f) DTM of the pre-erupted surface. d,g) Illustrates the elevation difference between (b) and (c) for WAC or (e) and (f) for TC, which when integrated, yield the volume of the pyroclastic deposit.

In addition to the volume of the pyroclastic deposit, we calculate the volume of the vent, which is an estimation of non-juvenile material within the deposit [*Head and Wilson*, 1979]. First,

we determine the mean rim elevation of each vent. Next, we calculate the vent volume by subtracting each pixel value within the vent from the mean rim elevation and multiplying the result by the area size of the pixel (i.e., 100 m^2). Finally, we sum the volume of each pixel inside the vent, which results in the total vent volume. If we assume that the vent volume is the total amount of non-juvenile material, then we calculate the total juvenile volume from subtracting the volcanic crater volume from the pyroclastic deposit volume.

We also estimate the maximum and mean pyroclastic thicknesses from the WAC DTM data. Using the difference between the DTM data of the pyroclastic deposit (**Figure 5.4b,e**) and the model of the pre-erupted surface (**Figure 5.4c,f**), we calculate the mean and maximum thickness from all positive values within each pyroclastic deposit (**Figure 5.4d,g** and **Table D.1**).

5.3.2.2 Determination of the Physical Properties of Pyroclastic Deposits

We examine the physical properties of localized pyroclastic deposits with three different data products, the radar circular polarization ratio (CPR), surface rock abundance, and density scale height (H) maps. The Miniature Radio-Frequency (Mini-RF) transmits 12.6-cm (S-band) circular polarized waves and receives in two orthogonal linear polarization waves, H and V (horizontal and vertical, respectively) at a spatial resolution of 15 m/pixel [*Raney et al.*, 2007; *Nozette et al.*, 2010]. In this study, we downsample the data to 100 m/pixel to increase the signal to noise ratio. The Mini-RF 12.6-cm CPR map is sensitive to topography, density of the soil, and 1-cm to 1-m blocks on the surface and penetrates to a depth of about ten times the wavelength (i.e., ~1 m). Recall that we only examine deposits on relatively smooth topography. Therefore, topography is not a major contributor to radar backscatter in this study. For each pyroclastic deposit, we calculate the mean CPR value for each pyroclastic deposit. The mean calculation excludes vents and rilles as these features are likely to produce non-volcanically related blocks.

Another data product sensitive to block concentration is the surface rock abundance map. *Bandfield et al.* [2011] derived the surface rock abundance map using the Diviner Lunar Radiometer Experiment. Diviner, a push-broom radiometer instrument on LRO, has seven bands where three of the bands focuses around 8 μm and the other four bands are sensitive to 12–25, 25–50, 50–100, and 100–300 μm [*Paige et al.*, 2010]. On the surface, Diviner can detect blocks larger than 1 m, which continue to be warmer than the surrounding regolith throughout the lunar night. *Bandfield et al.* [2011] separated the thermal emission from >1 m blocks from nighttime regolith to produce a surface rock abundance map at 128 m/pixel. We use the surface rock

abundance map to describe the block distribution on pyroclastic deposits, whereas the CPR data provide a measure of block population on and within the deposit. Similarly with the CPR data, we determine the mean rock abundance of each pyroclastic deposit and exclude pixels covering volcanic craters and rilles.

In contrast to the rock abundance map, the density scale height map is sensitive to regolith properties. After the separation of >1 m rock nighttime thermal emission and nighttime regolith temperatures, *Hayne et al.* [2013] produced a global density scale height map or H-parameter map, where the H value, the density scale height, is the thermal inertia of the top 10 cm of the regolith. Physical properties of the regolith that affect the thermal inertia include compaction, density, and porosity. In this study, we estimate the mean H-value of each pyroclastic deposit as well as the surrounding area. For each pyroclastic deposit, we subtract the background H-value from the pyroclastic deposit, which we will call ΔH. Negative ΔH values indicate that the thermal inertia of the pyroclastic deposit is greater than that of the nearby area, whereas a positive ΔH values indicate the pyroclastic deposit has a lower thermal inertia relative to nearby regolith.

5.3.3 Determination of the Compositional Properties of Pyroclastic Deposits

5.3.3.1 Radiative Transfer

We use the MI data to produce mineral maps of localized pyroclastic deposits. We derive the mineral maps using Hapke's radiative transfer equations [e.g., *Hapke*, 1981; 1993; 2001] and their application to the Moon as described in [*Lucey et al.*, 2014]. In the radiative transfer method we match unknown spectra to a spectra from a spectral library. The spectral library comprises of spectra of lunar-appropriate minerals at a range of proportions and all with an assumed grain size of 17 μm. These minerals include plagioclase from 0–100 vol.% at increments of 1 vol.% and orthopyroxene, clinopyroxene, and olivine at 0–100 vol.% at increments of 10 vol.%. For the mafic minerals, we use a fixed molar (MgO/[MgO+FeO] • 100) of 65 (Mg#). As a result, the spectral library contains 6,601 spectra. The optical constants are based upon *Lucey* [1998], where *Lucey et al.* [2014] later improved and validated the optical constants by using the Lunar Spectral Characterization Consortium (LSCC) data. As a result of this improvement, the mean error decreased to ~8 vol.%. Next, we vary the amount of nanophase iron at seven different intervals, which includes both small and large nanophase iron [e.g., *Britt and Pieters*, 1994; *Hapke*, 2001; *Lucey and Riner*, 2011]. Consequently, this expanded the

spectral library to 46,207 spectra. The final component is the spectra of pyroclastic glass, which is added at varying amounts from 0–100 vol.% at increments of 10 vol.%, which finally results in 508,277 spectra within the spectral library.

For the next step, we derive mineralogical maps by matching spectra from MI to the spectral library. In order to derive the mineral maps, first, we remove continuum in both the MI pixel spectrum and the library spectra, followed by searching for a spectral match within the spectral library based upon an evenly weighted average of correlation and the minimal sum of the absolute difference in reflectance. Due to non-unique solutions in the spectral matching routine, we constrained the FeO abundance to provide additional information on the correct solution. Next, we limit the spectral library to look for spectra within ±2 wt.% FeO of each pixel, where the FeO abundances algorithm is based upon *Lemelin et al.* [in prep.].

After producing plagioclase, orthopyroxene, clinopyroxene, olivine, and pyroclastic glass maps for each of the pyroclastic deposits, we calculate the mean of each phase within each pyroclastic deposit. Due to the possibility of mixing localized pyroclastic material with material within the local area, we limit the mean to include areas of the lowest albedo on the pyroclastic deposit.

5.4. Results and Comparison to Previous Work

After studying the results of the various data sets, we observe a relationship between the maximum pyroclastic thickness, the juvenile volume, the surface rock abundance, and composition. In the following section, we focus on the various relationships between the parameters to understand the diversity of localized pyroclastic deposits. We moved the results of each pyroclastic to Appendix D and the validation observations and other localized pyroclastic deposit observations to Appendix E.

5.4.1 Deposit Thickness

We searched for the pixel with the largest elevation difference between the pyroclastic DTM and the pre-erupted surface DTM to determine the maximum pyroclastic deposit thickness. With the WAC DTM data, we find that the maximum thickness range is 4–641 m with a mean of 103 m and a standard deviation of 121 m. As for the estimates from TC WAC, the maximum thicknesses range from 34–195 m with a mean of 100 m and a standard deviation of 42 m.

Head and Wilson [1979] calculated deposit thickness at the rim of the vent for six pyroclastic deposits in Alphonsus, NE1, NE2, NE3, SE, W1, and W2 (**Figure 5.1f**). They

employed two methods to estimate the thickness of the deposit. In the first method, they interpolated the pre-erupted surface and subtracted the pyroclastic topography from the pre-erupted surface, similar to the method in this study. In their second method, they inspected impact craters that penetrated through the pyroclastic deposit and ejected non-pyroclastic material. We compare our maximum pyroclastic thickness results to *Head and Wilson's* [1979] results and find that our thicknesses are four times larger than *Head and Wilson* [1979]. (**Table 5.1**). We attribute the differences to different interpolation techniques.

Table 5.1 Deposit Thickness and Juvenile Fraction Comparison

Thickness and Juvenile Comparison

Pyroclastic Deposit	*Head and Wilson* [1979]		WAC DTM		TC DTM		MI
	Deposit Thickness at Rim[m]	Juvenile [vol.%]	Deposit Thickness at Rim[m]	Juvenile [vol.%]	Deposit Thickness at Rim[m]	Juvenile [vol.%]	Juvenile [vol.%]
Alphonsus NE1	5-50	68	73.5	60	77.5	37	76
Alphonsus NE2	5-10	18-46	42.1	49	43.7		66
Alphonsus NE3	30-35	6	38.3	52	65.0	44	68
Alphonsus SE	20	52-62	72.9	50	85.2	50	74
Alphonsus W1	27-30	61	106.2	58	90.1	62	75
Alphonsus W2	40	77	119.1	69	110.5	64	74

5.4.2 Proportion of Juvenile Material

We obtained the proportion of juvenile material to non-juvenile material for 19 out of 34 pyroclastic deposits using the WAC DTM and 14 pyroclastic deposits for TC DTM. The percentage of juvenile material estimated from the WAC and TC DTM ranges from 31–88 vol.% (**Table D.1**). The other pyroclastic deposits resulted in negative juvenile volumes, which implies that the estimated volcanic crater volume is larger than the estimated pyroclastic deposit volume. We suspect that these negative juvenile volumes originated from the difficulty in estimating the volume in pixels located in areas of the pyroclastic deposits that are thin. In these thin areas of pyroclastic deposits, the DTM errors are larger than the thickness. Therefore, thin areas may not contribute to the overall pyroclastic volume and the results underestimate the actual pyroclastic volume.

For the Alphonsus pyroclastic deposits, we compare and subtract our juvenile fraction from *Head and Wilson's* [1979] juvenile fraction. The differences between our juvenile fraction

to *Head and Wilson's* [1979] juvenile fraction range from 2–46 vol.% with a median difference of 8 vol.% and a mean difference of 13 vol.% (**Table 5.1**).

5.4.3 Surface Rock Abundance

The mean surface rock abundances of localized pyroclastic deposits range from 0.24–0.54% with a mean of 0.38% and a standard deviation of 0.09% (**Table D.2**). The modal rock abundances for regional pyroclastic deposits, highlands, and maria are 0.3, 0.4, and 0.5%, respectively [*Bandfield et al.*, 2011]. To compare our surface rock abundance results to those of *Bandfield et al.* [2011], first we bin the mean surface rock abundance at intervals of 0.1%. We find the modal surface rock abundance of localized pyroclastic deposit is 0.3%, similar to the modal surface rock abundance of regional pyroclastic deposits.

5.4.4 Compositional Properties

The results from the radiative transfer of pyroclastic deposits display a few consistent relationships across all pyroclastic deposits. In all localized pyroclastic deposits, olivine and orthopyroxene are virtually absent (**Table D.3**). At maximum, the mean olivine abundance is 0 vol.% and the mean orthopyroxene abundance is 10 vol.%. The major components in localized pyroclastic are plagioclase, clinopyroxene, and pyroclastic glass. The glass, clinopyroxene, and plagioclase proportion ranges from 1–80 vol.%, 0–50 vol.%, and 10–60 vol.%, respectively.

We compare the glass proportion based upon the radiative transfer method against the juvenile proportions based upon the DTM interpolation method (**Figure 5.5**). We assume that the glass fraction equates to juvenile fraction. In this test, the radiative transfer predicts higher juvenile proportions in contrast to the interpolation method. There are two possible explanations for this observation: 1) the radiative transfer method is overestimating the juvenile proportion. 2) The interpolation method estimates the juvenile proportion within the pyroclastic volume, whereas the radiative transfer method estimates the juvenile proportion on the surface. If the total volume proportion of juvenile material diverged from the surficial proportion of juvenile material, this observation indicate that more juvenile material exists on the top layers than within the deposit.

We compare our glass proportion results to *Head and Wilson's* [1979] juvenile proportion results of the Alphonsus region. Again, we are assuming that glass and juvenile material are equivalent. We subtracted our glass proportion results of our radiative transfer method from *Head and Wilson's* [1979] juvenile proportion. The difference between the two

results has a median of 16 vol.%, a mean of 23 vol.%, and a range of 3–62 vol.% (**Table 5.1**). Again, we attribute the contrast in the juvenile proportion to the different methodologies.

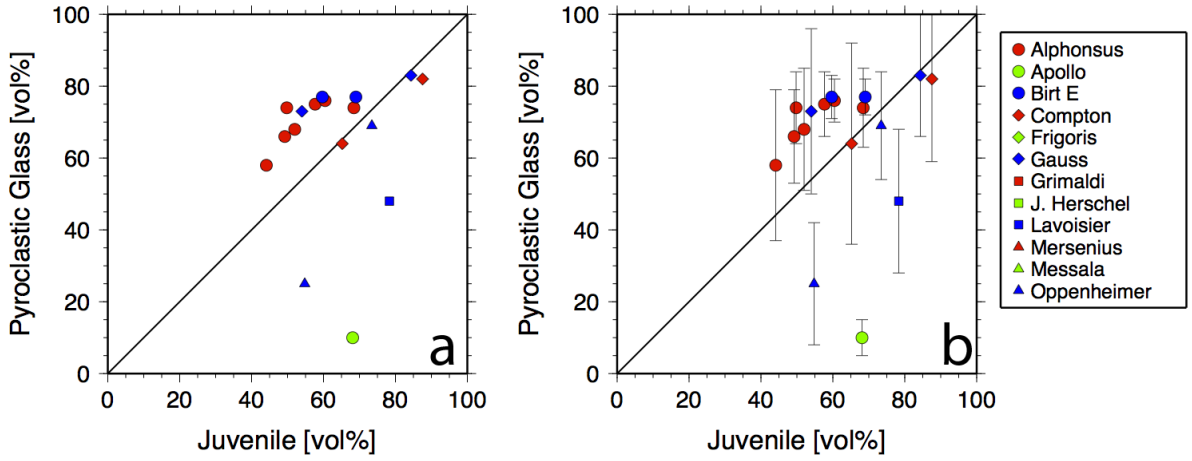

Figure 5.5: Comparison between glass proportion and juvenile proportion calculations. The radiative trasnfer calculation measures higher percentages of juvenile material than the interpolation method.

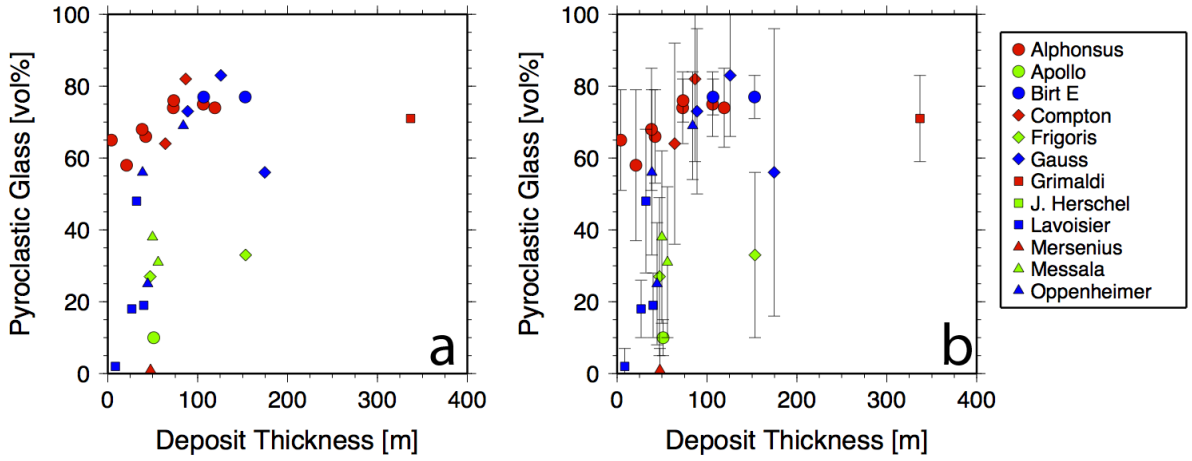

Figure 5.6: Relationship between glass proportion and maximum deposit thickness.

5.4.5 Relationship Between Properties

We notice a relationship between the glass proportion and maximum pyroclastic deposit thickness (**Figure 5.6**) as well as the surface rock abundance (**Figure 5.7**). From about 0–60 vol.% glass, the maximum pyroclastic deposit thickness is consistently ≤50 m. Where the glass proportion is >60 vol.%, the maximum thickness thickens varies from 0 to >300 m. As for the glass proportion and surface rock abundance relationship, we observe two distinct clusters, a cluster with low surface rock abundance and high glass proportion and another cluster with high rock abundance and low glass proportion (**Figure 5.7**). The two groups could be split at ~40 vol.% glass and 0.36% surface rock abundance. This coincides with the lowest mean surface rock abundance of the maria found by *Cahill et al.* [2014].

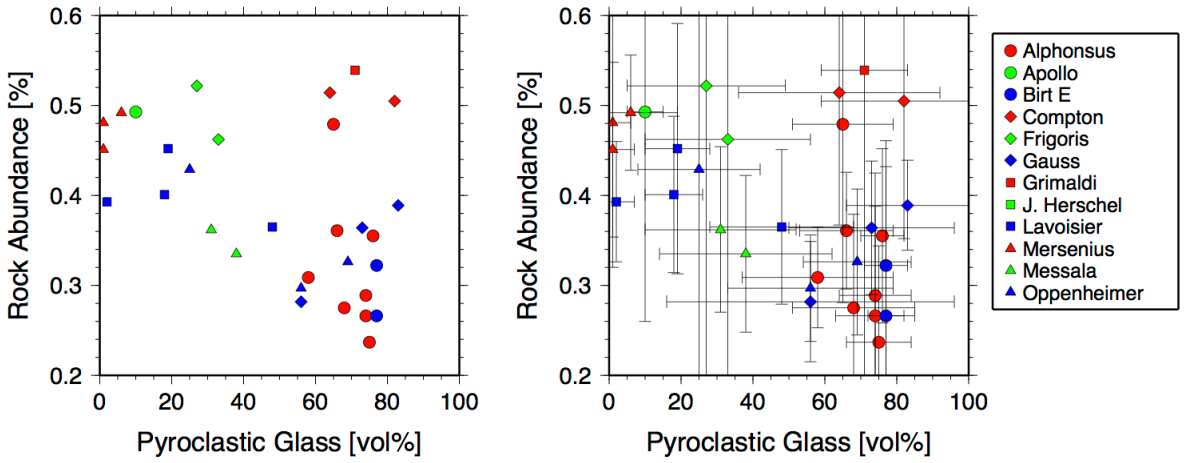

Figure 5.7: Relationship between glass proportions and surface rock abundance. There are two clusters, a low glass proportion and surface rock abundance cluster and a high glass proporiton and surface rock abundance cluster.

5.4.6 Observational Error

In the various figures, we showed both relationships between parameters and their errors (i.e., **Figure 5.5–7** and **E.2–6**). The errors in this study are large, which suggest that the observed trends and clusters are random. However, we used multiple data sets that are sensitive to the same parameter (e.g., CPR and rock abundance) and the data sets validate one another (See Appendix E.1). We infer that local mixing causes the physical and compositional heterogeneity

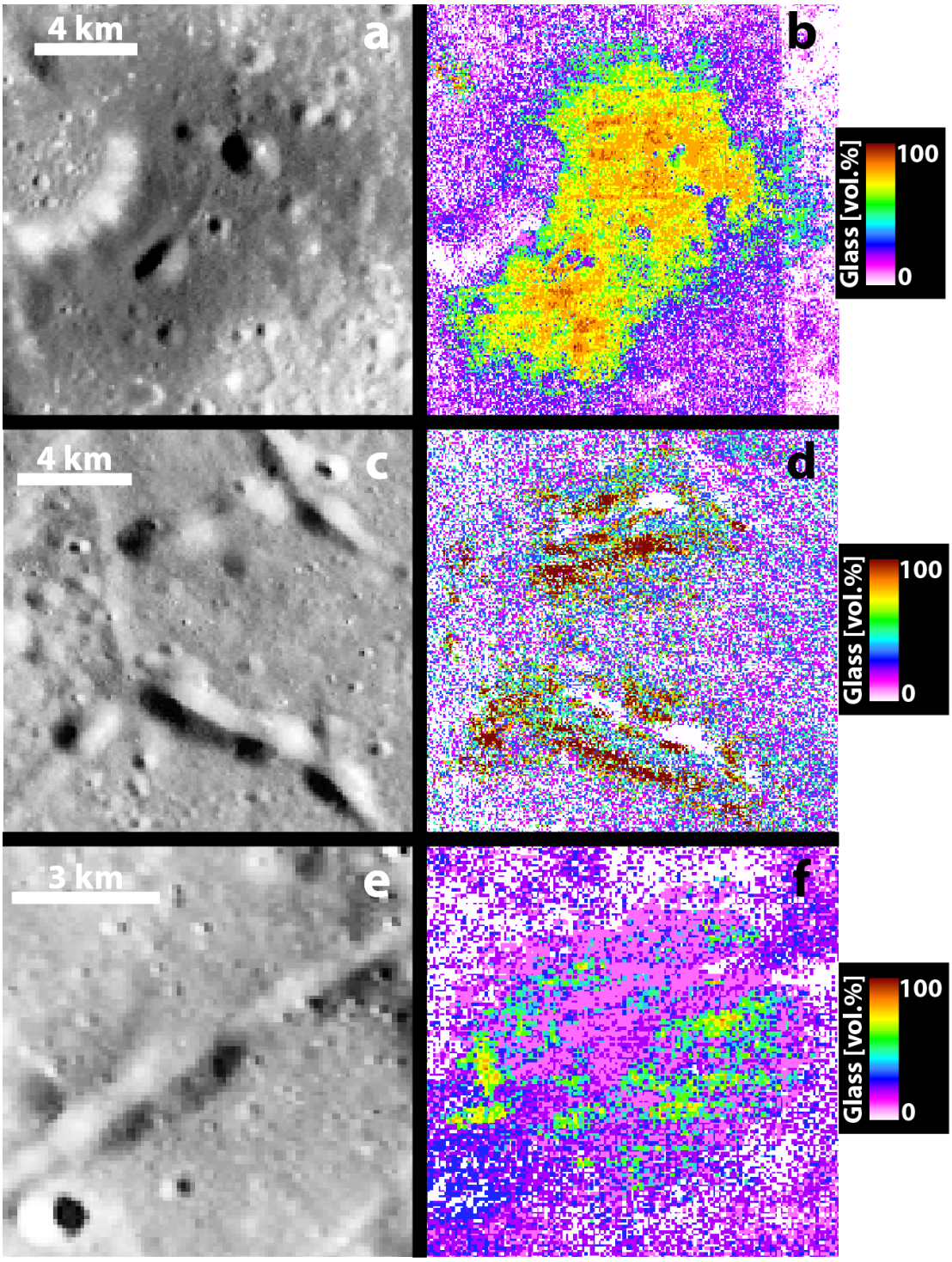

Figure 5.8: a) Alphonsus W1 and W2, a member of the Glassy group, show a mean value of 74–75 vol.% glass (b). C) Messala N and Messala S, part of the Basaltic group, exhibit 31–38 vol.% glass proportion (d). e) Oppenheimer S a representative of the Hybrid group contains 25 vol.% glass.

with localized pyroclastic deposits. If localized pyroclastic deposits formed in the Imbrian period [e.g., *Gaddis et al.*, 2003], then these deposits experienced at least 3 billion years of impacts. If the impacts produce craters large enough to penetrate through the pyroclastic deposit, then the surface rock abundances and glass proportions within and around the crater will evolve towards properties of the substrate. In addition, if impacts occurred near the deposit, the ejecta would land on the pyroclastic deposit; thus, adding local material into the pyroclasatic deposit. We expect that deposit-penetrating and nearby impacts occurred randomly across and nearby the deposit, which increases the heterogeneity of the pyroclastic deposit.

The pyroclastic glass detected with the radiative transfer method could be agglutinate glass. There are two types of glasses on the Moon, pyroclastic glasses and agglutinate. Agglutinate glasses are products of space weathering, whereas the pyroclastic glass are products of volcanism. We are confident that the interference of agglutinate glass on our measurements of pyroclastic glass is negligible for two reasons. 1) These two glass types produce two contrasting spectra. Pyroclastic glasses have a steep continuum in the visible and near infrared, a 1- and 2-μm absorption band, and a large UV absorption [*Bell and Mao*, 1972], whereas agglutinates steepen the continuum, lower the albedo, and decrease spectral contrast [*Hawke et al.*, 1989]. 2) The radiative transfer results showed that the areas around the pyroclastic deposits tend to contain 0–30 vol.% pyroclastic glass, which we attribute to as noise (**Figure 5.8**). The mean glass proportions for the majority of our deposit are >30 vol.%, indicating that the glass presence in the deposits is real.

In another test, we use the radiative transfer technique on the Apollo 17 site, which sampled a pyroclastic deposit, to determine whether we can detect glass and compare its relationship with the surrounding area. Note that we did not include ilmenite, a common mineral found at the Apollo 17 site. Therefore, our radiative transfer technique may over or underestimate the glass proportions (**Figure 5.9**). We observe in **Figure 5.9** that in the high albedo highlands regions (i.e., Sculptured Hills, South Massif, and Bear Mountain) the radiative transfer predicted high plagioclase proportions as expected. Additionally, the highlands deposit north of the South Massif (high albedo) comprises of plagioclase. The low albedo regions exhibit high glass proportions. We expected the low albedo regions to comprise of glass because this region is part of the Tarus-Littrow pyroclastic deposit. However, in the middle of the low albedo

region shows high proportions of clinopyroxene area. This area corresponds to the presence of secondary craters (**Figure 5.9c**). The secondary crater impacts penetrated through the pyroclastic deposit and ejected clinopyroxene [*Weitz et al.*, 1998]; hence the presence of clinopyroxene in this area.

We compare our compositional map to the composition map by *Weitz et al.* [1998]. They also found that the low-albedo regions comprises of glass. Furthermore, they noticed a region exhibiting strong mafic absorptions; this region corresponds to where we observe high proportions of clinopyroxene. We find that our composition map agrees with the map produced by *Weitz et al.* [1998] (see **Figure 3** in *Weitz et al.* [1998]).

5.5. Discussion

5.5.1 Integrating and Interpreting the Data Sets

After examining the relationships between the glass proportion and surface rock abundance and maximum pyroclastic deposit thickness of each pyroclastic deposit (**Table 5.2**), we define four groups: Glassy, with high glass proportions and low surface rock abundance; Blocky, with high glass proportions and surface rock abundance; Basaltic, with low glass proportions and surface rock abundance; and Hybrid, with low glass proportions and high surface rock abundance. We determine the median value for each parameter within each localized pyroclastic deposit group (**Table 5.3**). Also, we redrew **Figure 5.5–7** and **E.2–6** based upon the four groups (**Figure 5.10**).

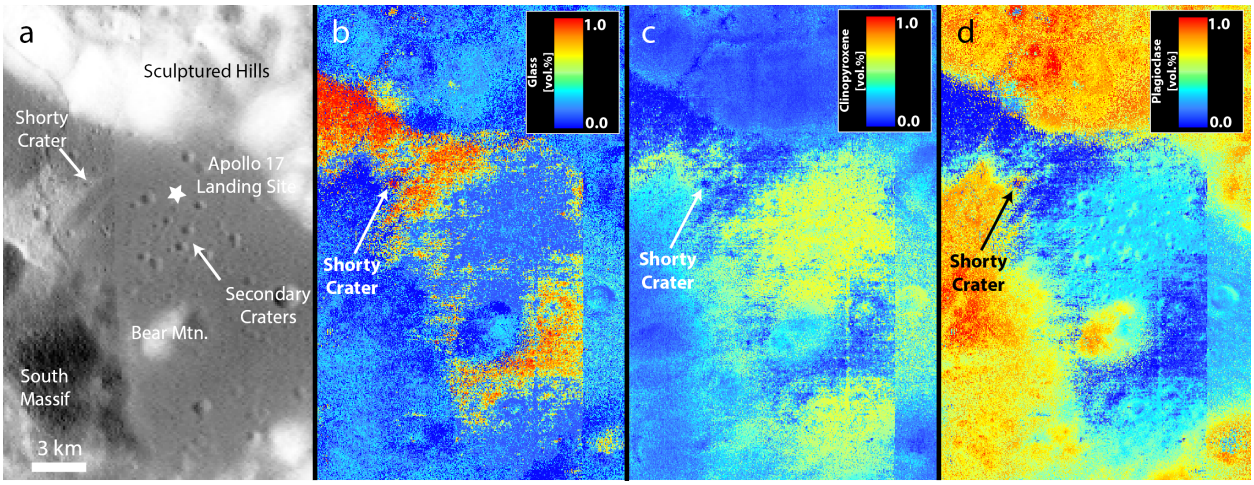

Figure 5.9: Compositonal maps of the Taurus-Littrow region. (a) WAC of Taurus-Littrow (b) glass proportions (c) clinopyroxene proportions (d) plagioclase proportions

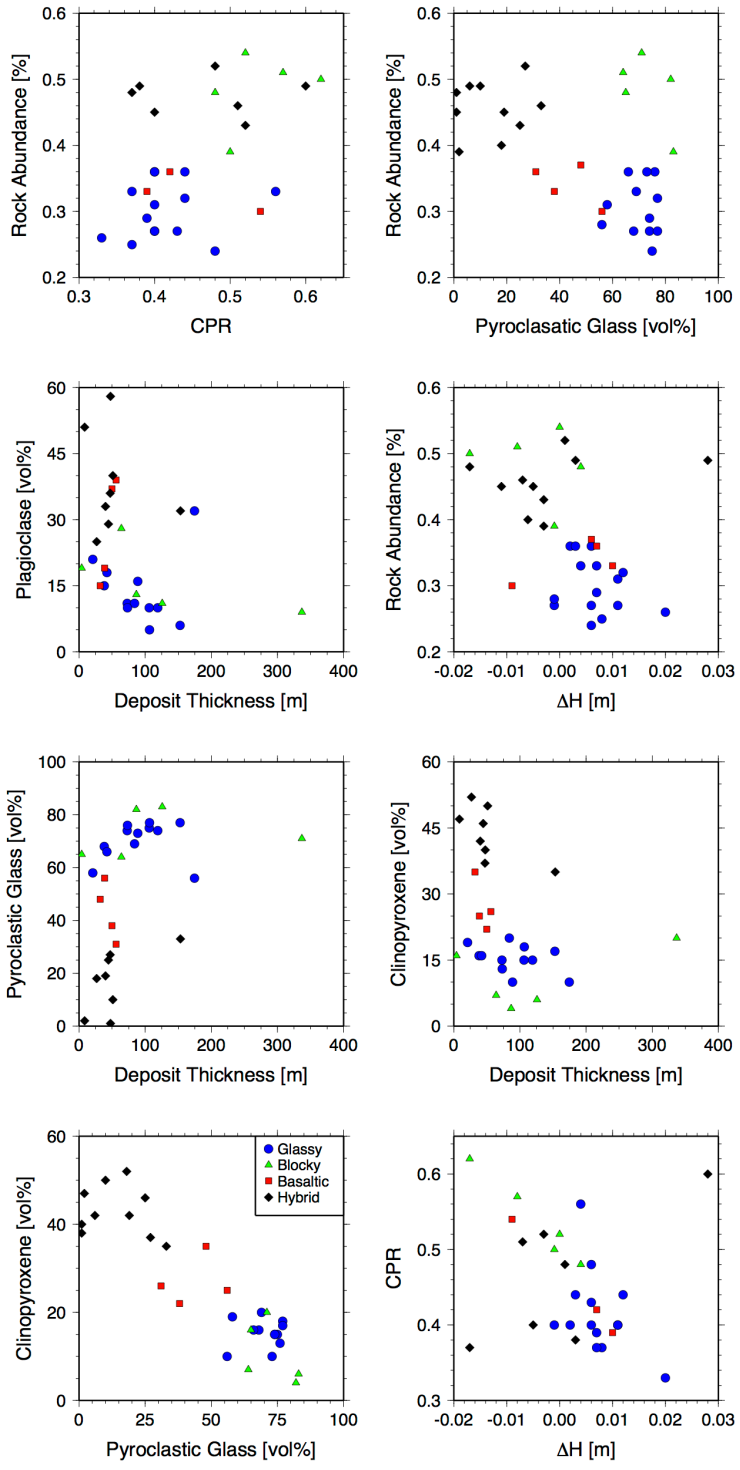

Figure 5.10: A replot of **Figure 5.5–7** and **E.2–6** and an additional clinopyroxene versus glass plot with the four localized pyroclastic groups.

Table 5.2: Key Properties Rearranged by Localized Pyroclastic Deposit Group

Rearrangement of Results of Properties

Pyroclastic	Rock Abund. [%]	CPR	ΔH [m]	Clinopyroxene [vol.%]	Glass [vol.%]	Plagioclase [vol.%]	Maximum Thickness (WAC) [m]	Pyroclastic Group
Alphonsus W1	0.24	0.48	0.006	15	75	10	106.2	Glassy
J. Herschel S	0.25	0.37	0.008				90.2	Glassy
J. Herschel C	0.26	0.33	0.020				641.4	Glassy
Alphonsus W2	0.27	0.43	0.006	15	74	10	119.1	Glassy
Birt E N	0.27	0.40	0.011	18	77	5	106.7	Glassy
Alphonsus NE3	0.27	0.40	-0.001	16	68	15	38.3	Glassy
Gauss E	0.28		-0.001	10	56	32	174.6	Glassy
Alphonsus SE	0.29	0.39	0.007	15	74	11	72.9	Glassy
Alphonsus C	0.31	0.40	0.011	19	58	21	21.0	Glassy
Birt E S	0.32	0.44	0.012	17	77	6	152.7	Glassy
Oppenheimer N	0.33	0.56	0.004	20	69	11	84.2	Glassy
J. Herschel N	0.33	0.37	0.007				257.7	Glassy
Alphonsus NE1	0.36	0.40	0.006	13	76	10	73.5	Glassy
Alphonsus NE2	0.36	0.40	0.002	16	66	18	42.1	Glassy
Gauss S	0.36	0.44	0.003	10	73	16	88.7	Glassy
Gauss W	0.39	0.50	-0.001	6	83	11	125.7	Blocky
Alphonsus E	0.48	0.48	0.004	16	65	19	4.0	Blocky
Compton W	0.50	0.62	-0.017	4	82	13	86.7	Blocky
Compton E	0.51	0.57	-0.008	7	64	28	63.8	Blocky
Grimaldi	0.54	0.52	0.000	20	71	9	336.9	Blocky
Messala N	0.33	0.39	0.010	22	38	37	49.7	Basaltic
Oppenheimer E	0.30	0.54	-0.009	25	56	19	38.5	Basaltic
Messala S	0.36	0.42	0.007	26	31	39	56.2	Basaltic
Lavoisier F	0.37		0.006	35	48	15	32.2	Basaltic

Frigoris W	0.46	0.51	-0.007	35	33	32	153.5	Hybrid
Frigoris E	0.52	0.48	0.001	37	27	36	47.2	Hybrid
Mersenius W	0.48	0.37	-0.017	38	1	60		Hybrid
Mersenius S	0.45	0.40	-0.005	40	1	58	47.5	Hybrid
Mersenius N	0.49	0.38	0.003	42	6	51		Hybrid
Lavoisier W	0.45		-0.011	42	19	33	39.9	Hybrid
Oppenheimer S	0.43	0.52	-0.003	46	25	29	44.4	Hybrid
Lavoisier NW	0.39		-0.003	47	2	51	8.3	Hybrid
Apollo	0.49	0.60	0.028	50	10	40	51.1	Hybrid
Lavoisier H	0.40		-0.006	52	18	25	26.6	Hybrid

5.5.1.1 Properties of the Four Localized Pyroclastic Deposit Groups

Of the 34 pyroclastic deposits, 15 of the deposits fall into the Glassy Localized Pyroclastic Deposit group. The defining features of this group are the high glass proportion and low surface rock abundance (**Figure 5.8a**, **Table 5.3**) Additional key observations include low CPR, low ΔH, low crystalline proportions, and the median maximum-deposit-thickness of these deposits is ≥50 m.

Only 5 of the 34 pyroclastic deposits are in the Blocky Localized Pyroclastic Deposit group. The key features of this group are the high glassy proportion and surface rock abundance (**Table 5.3).** The other important observations of this group are high crystalline proportions, high CPR, similar ΔH to the surrounding area, and the median maximum-deposit-thickness of these deposits is ≥50 m.

The Basaltic Localized Pyroclastic Deposit group is the second smallest group and has four members. The important features of this group are the low glassy proportion and low rock abundance, but high clinopyroxene and plagioclase fraction (**Figure 5.8c**). The median values of other parameters include low CPR, low ΔH, and maximum thicknesses of <50 m.

The second largest group, the Hybrid Localized Pyroclastic Deposit, comprises of 10 deposits. This pyroclastic deposit group displays low to almost absent glass proportion, high crystalline proportions, and high rock abundance (**Figure 5.8e**). Median values of other parameters include high CPR, thermal inertia similar to the surrounding area, and maximum thicknesses <50 m.

Table 5.3: Median Values for Several Properties for Each Group

Median Values of Each Localized Pyroclastic Deposit Group							
Pyroclastic Group	Glass [vol.%]	Clinopyroxene [vol.%]	Plagioclase [vol.%]	Rock Abund. [%]	CPR	ΔH [m]	Maximum Thickness (WAC) [m]
Glassy	74	16	11	0.29	0.40	0.01	90
Blocky	71	7	21	0.50	0.52	0.00	87
Basaltic	43	25	35	0.35	0.42	0.01	38
Hybrid	14	42	38	0.46	0.48	0.00	46

5.5.1.2 Interpretations of the Different Localized Pyroclastic Deposit Groups

After defining the properties of localized pyroclastic deposits and dividing them into groups, we interpret the origin of each group. We base our interpretation for each group on *Head*

and Wilson's [1979] eruptive model. From *Head and Wilson's* [1979] calculations and interpretation of their remote sensing data, they deduced that localized pyroclastic deposits originated from vulcanian-style eruptions. A dike intrusion cools to form a basaltic cap. Underneath the cap, volatiles accumulate, which builds up pressure until explosive decompression. This model is based upon the six localized pyroclastic deposits in Alphonsus, in which we find that these six deposits coincide with the Glassy group in our study. Therefore, we suggest that *Head and Wilson's* [1979] eruptive model is the formation model of the Glassy group.

The Blocky and Glassy group exhibit similar glass proportion and maximum deposit thickness, but differ in surface rock abundance (**Table 5.3**). Our first suggestion for the higher surface rock abundance is that the Blocky group formed identically to the Glassy group, but later, local mixing incorporated non-volcanic material, which increases the surface rock abundance and decreases the glass proportion within the deposit. However, the glass proportion in the Blocky group is equivalent to the Glassy group. Thus, we infer that local mixing is not the cause of the high surface rock abundance of the Blocky group. Another suggestion is that the Blocky group formed identically to the Glassy group, but the eruption resulted in smaller degree of fragmentation, which yields larger grain sizes [*Head and Wilson*, 1979].

The Basaltic and Glassy group exhibit low surface abundance, but they differ in maximum deposit thickness and glassy to crystalline proportions (**Table 5.3**). *Gaddis et al.* [2000] suggested that the compositional variation in localized pyroclastic deposits is because these deposits incorporated different proportions of wall rock, cap rock, and juvenile material, where the differing proportions is related to eruption duration. Adding to *Gaddis et al.'s* [2000] idea, we infer that the thinner deposits and low glass proportions of the Basaltic group suggest the eruptions were short-lived and ejected disrupted cap rock and some glass. In contrast, the thicker deposits and high glass proportion of the Glassy group suggest the eruptions lasted longer and evolved to eject more glass.

The final group is the Hybrid group, which exhibits low glass proportion, high rock abundance, and thin deposits relative to the Glassy group (**Table 5.3**). Even though the Hybrid group exhibits low glass proportions, we noticed that within three pyroclastic deposits (i.e., Frigoris W, Frigoris E, and Oppenheimer S), there are local concentrations of high glass proportions (**Figure 5.17e**). We infer that these deposits originated from explosive eruptions, but

later mare activity buried portions of these deposits. Within the other seven deposits of the Hybrid group (i.e., Mersenius W, Mersenius N, Mersenius S, Lavoisier NW, Lavoisier W, Lavoisier H, and Apollo) we do not observe any pockets of high glass concentration relative to the surrounding area. We interpret that these deposits are consistent with mare ponds. These deposits may have formed explosively, followed by mare burying the pyroclastic deposit. We continue to group these seven deposits into Hybrid because morphological observations from past workers suggest these deposits are consistent with pyroclastic deposits.

5.5.3 Regional versus Localized Pyroclastic Deposits

The compositional and physical properties of regional pyroclastic deposits are better understood than localized pyroclastic deposits because the Apollo 17 sampled a regional pyroclastic deposit in Taurus-Littrow. Samples of the Apollo 17 site showed that regional pyroclastic deposits consist of black crystalline and glass beads [e.g., *Heiken et al.*, 1974]. The black crystalline beads contain olivine with ilmenite crystals [*Adams et al.*, 1974]. Several workers used these samples as ground truth to determine the composition of other pyroclastic deposits through remote sensing observations [e.g., *Lucey et al.*, 1986, *Weitz et al.*, 1998*, Gaddis et al.*, 2003; *Wilcox et al.*, 2006]. These workers found that other regional pyroclastic deposits display a range of glass to crystalline proportions from nearly all glassy to nearly all crystalline. Recently, *Sunshine et al.* [2010] and *Yamamoto et al.* [2013] identified spinel for the first time within a regional pyroclastic deposit.

Regional pyroclastic deposits are prominent in radar observations because they have the lowest radar backscatter on the surface. Radar studies of regional pyroclastic deposits have consistently resulted in low backscatter at multiple wavelengths between 3 cm to 70 cm [*Pieters et al.*, 1973; *Gaddis et al.*, 1985; *Campbell et al.*, 2008; *Carter et al.*, 2009]. The low radar backscatters signifies the lack of blocks on and in the pyroclastic deposits. *Gaddis et al.* [1985] suggested that the unique radar property of pyroclastic deposits is a new method of finding pyroclastic deposits; especially deposits dominantly composed of high albedo glasses (i.e., green glasses and potentially low-FeO bearing glasses).

Now that we established the properties of localized pyroclastic deposits, we compare the difference between localized and regional pyroclastic deposits. The dominant compositions of regional pyroclastic deposits are glass and crystalline beads where the crystalline beads are composed of olivine and ilmenite. In contrast, localized pyroclastic deposits comprise of glass,

clinopyroxene, and plagioclase, but the absence of ilmenite cannot be certain because we did not include ilmenite into our radiative transfer model. In both deposit types, there is a continuum from glassy to crystalline material. The only difference is the crystalline material for regional deposits is the crystalline beads and for localized deposits, the crystalline material is plagioclase or clinopyroxene.

A major contrast between regional and localized deposits is the surface rock abundance and radar properties. *Bandfield et al.* [2011] showed that the modal rock abundance for regional pyroclastic deposits is 0.3%. The modal surface rock abundance for each group (binned at intervals of 0.1%), we find that Glassy and Basaltic groups match regional pyroclastic deposits (0.3%) and the Hybrid and Blocky Groups are similar to modal maria rock abundance (0.5%). Overall, the localized pyroclastic deposits exhibit a large variation in rock abundance.

5.6 Conclusion

We used various data sets from Kaguya and the Lunar Reconnaissance Orbiter to study 34 previously-identified pyroclastic deposits. We described the pyroclastic volume, juvenile proportion, surface rock abundance, radar backscatter, regolith density, and mineralogical composition. Within these observations, we noticed relationships between the glass proportion, the surface rock abundance, and the maximum pyroclastic deposit thickness. Consequently, we divided the deposits into four groups. From this study, we find three major conclusions:

1) The four groups of localized pyroclastic deposits are Glassy, Blocky, Basaltic, and Hybrid. We grouped the pyroclastic deposits based upon the different permutations of high and low surface rock abundances and glass proportions. We infer that the *Head and Wilson's* [1979] eruption model represents the formation of the Glassy group. The Blocky group formed the same way as the Glassy group, but the degree of fragmentation was lower. The Basaltic group were shorter-lived eruptions that ejected basaltic cap rock and some glass, whereas the Glass group were longer-lived eruptions that evolved to eject more glass. The Hybrid group may have formed from explosive eruptons, which were later partially or completely buried by mare.
2) We found two differences between localized and regional pyroclastic deposits. First, both deposits show a continuum from glassy to crystalline proportions, except the crystalline material are crystalline beads for regional deposits and clinopyroxene and plagioclase for localized deposits. Second, we find that the Glassy and Basaltic groups have similar CPR

and surface rock abundance properties as regional pyroclastic deposits, but the Blocky and Hybrid groups exhibit higher CPR and surface rock abundance.

3) Of the 34 deposits in this study, we found that seven of our localized pyroclastic deposits have properties that are consistent with the properties of mare ponds. These deposits tend to have similar regolith densities, surface rock abundances, and glass proportions to the surrounding area.

We obtained all the similar parameters as *Head and Wilson* [1979] in order to provide useful parameters for future eruptive models. These parameters include total volume of pyroclastic material, juvenile to non-juvenile proportion, pyroclastic deposit thickness, block population, regolith density, and composition (Appendix D). These parameters will be useful in future eruptive models to test our hypotheses on the origin of the Basaltic, Blocky, and Hybrid groups.

CHAPTER 6

CONCLUSION AND FUTURE WORK

6.1 Concluding Remarks

In this dissertation, we improved on remote sensing techniques and expanded the knowledge of geomorphological features on the lunar surface. In Chapters 2 and 3, we refined preexisting optical constants for olivine and pyroxene and provided a new technique that constrains ages on geomorphological features and surfaces. In Chapters 3, 4, and 5, these projects resulted in determining the timing of crater degradation, proposed an origin of concentric craters, and categorized localized pyroclastic deposits based upon physical and compositional observations. We summarize the dissertation with the following:

1) Along with refining the optical constants of olivine and pyroxene, we noted other interesting observations. First, we suggested using the RELAB-based olivine optical constants for compositional modeling because the USGS olivine spectra are anomalously dark, which we inferred to be due to differences in spectrometers. Second, the synthetic pyroxene spectra differ from the natural pyroxene spectra. We inferred that the presence of minor elements and zoning in the natural pyroxenes causes the natural pyroxene spectra to diverge from the synthetic pyroxene spectra. Third, cation ordering is an important factor to modeling the strength of the absorption bands. Lastly, the band strengths in olivine displayed a non-linear behavior with increasing Fe^{2+} content. We attributed this behavior to increasing Mn' relative to increasing Fe^{2+} content.
2) We calibrated the degree of freshness to absolute model ages. Therefore, we can obtain absolute model ages for 1-20 km craters through visual inspection of crater degradation states. In testing this calibration with the Apollo 12 and Apollo 16 sites, we demonstrated the robustness of this conversion tool. In addition to developing the technique, we found some interesting observations. First, most geomorphological features in >8 km craters develop or disappear at about 1.8 and >3.8 Ga. Second, in the relationship between degree of freshness and absolute model ages, we observed a kink at about 3.8 Ga (or degree of freshness of 5.0). There are three possible interpretations of this kink, the change in degradation rate, a coincidence of the degree of freshness category, or crater

saturation. Until we determine the origin of the kink, we recommend using an age of >3.8 Ga for any crater with a degree of freshness <5.0.

3) The observations and interpretations of concentric craters show that they are anomalously shallow, lack compositional contrast with the surrounding area, spatially distributed near the maria, and the majority are of Imbrian age or older. Furthermore, the majority of our observations are consistent with the properties of floor-fractured craters. After considering several endogenic and exogenic processes, we concluded that concentric craters are impact craters that were later modified by magma intruding into impact-produced fractures directly below the impact crater.
4) We observed a relationship between surface rock abundance, maximum pyroclastic deposit thickness, and glass proportion. From these relationships, we found localized pyroclastic deposits fit into four groups, Glassy, Block, Basaltic, and Hybrid. All four groups are a result of explosive vulcanian eruptions. The difference is that the Basaltic group erupted some glass and was short-lived, whereas the Glassy group was long-lived and the eruption evolved to eject more glass. The Blocky group formed similarly as the Glassy group, but the degree of fragmentation was lower. The Hybrid group erupted explosively, but mare later partially or completely buried the pyroclastic deposit.

6.2 Future Work

Investigations of these projects have led to potential projects and new hypotheses. We propose a series of additional investigations that can be undertaken in the future to help validate interpretations and refine techniques.

1) Pyroxene cation ordering has a direct relationship with the absorption strengths. If these absorption strengths can be characterized with respect to the degree of cation ordering, then future spectroscopic analyses of pyroxenes can also reveal cooling rate. Additionally, petrological analyses or experiments on synthetic and natural pyroxenes could reveal the differences between our synthetic and natural pyroxene spectra. In olivine, we noticed an odd behavior between band strengths and Mn proportions. Mn is a useful element for petrological models; thus, remote detection of Mn^{2+} on the surfaces of airless bodies may assist in understanding the mantle evolution of a planetary body. A potential useful study is to characterize the optical constants of Mn^{2+}-rich olivine.

2) The kink in the calibration of degree of freshness to absolute model ages could not be resolved in this dissertation. There are several methods in resolving the kink. For example, if the kink is related to crater saturation, calibrating Class I and II craters (i.e. ~20–45 km and >45 km craters, respectively) may provide insight into the origin of the kink. Also, diffusion models could test whether the kink originates from a change in impact flux. In the future, this technique could be carried out to other planetary bodies (e.g., Mercury, Mars, asteroids).
3) In this work, we deduced the most likely mechanism to produce concentric craters, but we did not conduct any models to show how they are formed. Concentric crater formation could be tested with computer simulation models or physical scale models in the laboratory.
4) Now that we are able to describe the physical, and compositional properties of localized pyroclastic deposits, the next step is to produce eruptive models to test our hypotheses to the eruption behavior of Basaltic, Blocky, and Hybrid localized pyroclastic deposits. Future workers could also measure the surface rock abundance, radar backscatter, and glass proportion for potential pyroclastic deposits, such as material in the Dewar and Plato region, to determine whether these deposits fromed explosively.

APPENDIX A

OLIVINE AND PYROXENE SAMPLES AND OPTICAL CONSTANTS RESULTS

Table A.1: Olivine composition

	Sunshine and Pieters, [1998]					Cloutis*				
Wt. %	Havard 103267	GSB	Hawaiian Volc. Bomb	Harvard 118652	Harvard 113637	OLV025	OLV102	OLV106	OLV107	OLV201
SiO_2	41.050	40.420	39.530	33.320	32.470	39.720	40.840	40.480	41.090	40.360
FeO	7.810	11.110	15.640	43.430	42.590					
Fe_2O_3	as FeO	as FeO	1.410	3.830	5.550	n.d.	n.d.	n.d.	n.d.	n.d.
FeO[a]						*13.810*	*9.090*	*9.320*	*10.010*	*12.000*
MgO	51.970	48.250	45.190	19.670	15.390	46.310	50.120	49.680	50.810	47.760
MnO	0.110	0.150	0.220	0.600	5.150	0.220	0.130	0.140	0.170	0.260
ZnO	0.060	0.000	0.100	0.000	0.000	0.000	0.000	0.000	0.000	0.000
NiO	0.390	0.430	0.290	0.040	0.040	0.310	0.450	0.410	0.450	0.010
CaO	0.010	0.190	0.140	0.070	0.100	0.030	0.000	0.080	0.060	tr.
TiO_2	0.030		0.010	0.010	0.010	0.000	0.000	0.000	0.000	tr.
Cr_2O_3	0.010	0.130	0.010	0.000	0.010	0.000	0.000	0.000	0.030	0.020
CoO	0.010	0.040	0.040	0.030	0.000	0.050	0.040	0.060	0.000	0.030
V_2O_5						0.000	0.000	0.000	0.030	0.000
K_2O	0.000	0.000	0.000	0.000	0.010	0.000	0.000	0.000	0.000	0.000
Na_2O	0.030	0.000	0.010	0.010	0.010	0.000	0.000	0.000	n.d.	0.000
Al_2O_3	0.000	0.030	0.050	0.020	0.010	0.000	0.000	0.000	0.000	tr.
Grain Size (µm)†	<45 (22.5)	<45 (22.5)	<45 (22.5)	<45 (22.5)	<45 (22.5)	<45 (22.5) 45–90 (67.5)	<45 (22.5) 45–90 (67.5)	<45 (22.5) 45–90 (67.5)	<45 (22.5)	<45 (22.5)

	Cloutis*										
Wt. %	OLV002	OLV003	OLV005	OLV007	OLV010	OLV011	OLV012	OLV013	OLV020	OLV021	OLV022
SiO_2	39.740	40.640	40.970	41.720	40.420	29.780	40.950	40.680	36.150	40.140	36.500
FeO	12.620	9.250		2.710		61.460					28.520
Fe_2O_3	1.430	0.590	n.d.	0.450	n.d.	5.520	n.d.	n.d.	n.d.	n.d.	8.640
FeO[a]	*13.920*		*9.590*		*11.110*	*66.480*	*8.050*	*9.270*	*34.970*	*13.360*	*36.370*
MgO	46.380	49.130	49.640	54.650	48.250	0.050	50.830	49.670	28.860	45.550	27.730
MnO	0.230	0.090	0.090	0.190	0.150	2.140	0.100	0.130	0.470	0.190	n.d.
ZnO	0.000	0.000	tr.	0.000	0.000	0.540	0.000	tr.	0.000	tr.	n.d.

NiO	0.320	0.330	0.320	0.010	0.430	0.040	0.400	0.360	0.100	0.270	n.d.
CaO	0.130	0.070	0.000	0.630	0.190	0.050	tr.	0.090	0.030	0.030	0.120
TiO_2	tr.	0.000	tr.	0.000	tr.	tr.	0.000	0.000	0.030	0.010	0.010
Cr_2O_3	tr.	0.010	0.000	tr.	0.130	0.000	0.000	tr.	tr.	0.000	n.d.
CoO	0.060	0.040	0.060	0.010	0.040	0.100	0.060	0.040	0.120	0.050	n.d.
V_2O_5	0.000	0.000	0.000	0.000	0.000	0.000	0.000	0.000	0.000	0.000	n.d.
K_2O	0.000	0.000	0.000	0.000	0.000	0.000	0.000	0.000	0.000	0.000	n.d.
Na_2O	0.000	0.000	0.000	0.000	0.000	0.000	0.000	0.000	0.000	0.000	n.d.
Al_2O_3	0.000	tr.	0.000	0.000	0.030	0.000	0.000	0.010	0.000	0.000	0.090
Grain Size (μm)†	<45 (22.5) 45–90 (67.5)	<45 (22.5) 45–90 (67.5)	<45 (22.5) 45–90 (67.5)	<45 (22.5)	<45 (22.5)	<45 (22.5)	<45 (22.5)	<45 (22.5) 45–90 (67.5)	<45 (22.5)	<45 (22.5)	<45 (22.5)

	King and Ridley, [1987]									*Salisbury et al.*, [1987]	*Hunt et al.,* [1973]
Wt. %	KI3005	KI3377	KI3291	KI4143	KI13188	KI3189	KI3054	GDS71	GDS70	NMNH137044	HS285.4B
SiO_2	30.11	31.11	31.98	33.15	34.34	35.47	36.30	40.60	41.09	40.27	
FeO	62.82	59.75	53.65	47.65	41.34	34.63	32.59	7.93	9.16	8.7	
Fe_2O_3											
MgO	4.42	7.71	12.61	18.43	23.80	29.49	32.62	50.70	49.29	52.28	
MnO	1.55	1.30	1.23	0.90	0.73	0.55	0.05	0.12	0.21	0.15	
ZnO											
NiO	0.12	0.12	0.11	0.10	0.07	0.05	0.09	0.28	0.39		
CaO	0.14	0.09	0.35	0.20	0.05	0.09	0.04	0.06	0.03	0.06	
TiO_2	0.07	0.06	0.06	0.04	0.04	0.03	0.03	0.14	0.01	0.01	
Cr_2O_3	0.06	0.07	0.05	0.04	0.04	0.04	0.03	0.06	0.05		
CoO											
V_2O_5											
K_2O										0.01	
Na_2O	0.02									0.02	
Al_2O_3	0.00	0.00	0.00	0.00	0.00	0.00	0.00	0.05	0.00	0.02	
Grain Size	<60 (30)	<60 (30)	<60 (30)	<60 (30)	<60 (30)	<60 (30)	<60 (30)	<60 (30)	<60 (30)	<74 (37)	74–250 (162)

(μm)†		60–104 (82)	60–104 (82) 104–150 (127) 150–250 (200)	74–250 (162)	250–1200 (725)	

* Oxide information generously provided by E.A. Cloutis

n.d. not determined

tr. trace amount (<0.005 wt.%)

a total Fe expressed as FeO

† Mean grain size in parentheses

Table A.2: Pyroxene composition

	1	**2**	**3**	**4**	**5**	**6**	**20**	**21**	**22**	**23**	**24**	**25**	**26**	**28**	**29**	**30**	**33**
SiO2	59.86	56.50	55.73	51.72	50.84	48.53	47.75	46.27	55.92	49.03	47.47	49.73	55.29	48.37	47.07	55.51	54.49
TiO2	0.00	0.00	-0.02	-0.01	-0.02	-0.01	0.01	0.00	0.00	0.01	0.00	0.00	0.00	-0.02	-0.02	-0.02	0.00
Al2O3	0.06	0.03	0.00	0.02	0.00	-0.01	0.00	-0.01	0.08	0.01	0.01	0.10	0.01	0.06	0.03	0.02	0.16
Cr2O3	-0.02	0.00	-0.02	0.01	0.00	0.02	0.00	0.00	0.00	0.01	0.00	-0.01	0.00	0.00	0.01	0.00	0.00
Fe2O3	0.00	0.00	0.00	0.00		0.00	0.00	0.00			0.00		0.00	0.00	0.00	0.00	0.00
FeO	0.06	13.60	15.65	31.07	34.44	43.04	46.85	50.34	16.73	40.66	46.61	38.86	18.23	42.89	48.08	18.55	5.37
MnO	-0.01	-0.01	-0.05	-0.02	0.03	-0.02	-0.03	-0.05	-0.03	0.02	-0.04	-0.03	0.03	0.04	0.02	-0.03	0.01
MgO	39.75	29.94	28.68	17.16	14.54	7.93	5.29	2.47	27.74	9.88	5.42	11.60	26.61	7.84	4.19	26.59	15.78
CaO	0.03	0.02	0.03	0.02	0.04	0.01	0.03	-0.01	0.01	0.01	0.02	-0.01	0.03	0.03	0.02	0.00	25.01
K2O																	0.01
Na2O	-0.11	-0.07	-0.11	-0.03	-0.03	-0.02	-0.11	0.00	-0.07	-0.01	-0.02	-0.02	-0.02	-0.01	-0.05	-0.02	0.00
Total	99.78	100.13	100.08	100.02	99.91	99.57	99.93	99.10	100.50	99.66	99.55	100.31	100.24	99.25	99.44	100.70	100.83

	36	**37**	**39**	**44**	**61**	**64**	**65**	**66**	**67**	**68**	**70**	**71**	**73**	**74**	**75**	**76**	**77**
SiO2	51.38	49.47	51.75	54.32	44.81	59.61	58.19	48.70	55.32	51.20	49.31	51.09	51.97	49.78	54.22	50.06	55.61
TiO2	0.03	0.01	0.00	0.00	0.00	0.00	0.00	0.00	0.00	0.00	0.00	0.01	0.00	0.01	0.00	0.00	0.00
Al2O3	0.06	0.02	0.07	0.01	0.01	0.01	0.02	0.00	0.01	0.06	0.01	0.02	0.02	0.21	0.12	0.05	0.06
Cr2O3	0.01	0.00	0.01	0.01	0.01	0.01	0.00	0.00	0.01	0.01	0.00	0.01	0.00	0.00	0.01	0.01	0.00

Fe2O3																	
FeO	17.13	21.50	14.14	5.33	54.35	1.83	6.69	31.49	6.91	22.63	26.12	20.24	17.48	24.94	6.55	22.69	2.38
MnO	0.01	0.01	0.01	0.01	0.02	0.01	0.00	0.00	0.01	0.01	0.00	0.00	0.03	0.01	0.01	0.01	0.02
MgO	8.37	5.63	10.37	16.42	0.01	38.85	35.50	5.54	21.74	11.10	5.08	8.46	14.25	9.04	18.19	6.68	21.23
CaO	23.02	22.39	23.45	24.59	0.00	0.00	0.01	14.13	16.52	14.50	18.75	20.16	15.40	15.52	20.87	20.69	21.41
K2O	0.01	0.06	0.03	0.00	0.01	0.01	0.01	0.00	0.00	0.00	0.00	0.00	0.00	0.01	0.00	0.01	0.00
Na2O	0.09	0.00	0.00	0.00	0.00	0.00	0.00	0.01	0.00	0.01	0.01	0.01	0.00	0.00	0.00	0.00	0.01
Total	100.10	99.11	99.84	100.70	99.23	100.33	100.44	99.87	100.52	99.54	99.28	100.00	99.16	99.53	99.98	100.22	100.72

	79	**82**	**83**	**85**	**87**
SiO2	53.28	47.95	48.26	49.24	46.46
TiO2	0.00	0.00	0.00	0.10	0.00
Al2O3	0.01	0.06	0.01	0.00	0.01
Cr2O3	0.01	0.00	0.00	0.00	0.01
Fe2O3					
FeO	10.25	28.76	27.97	28.86	44.14
MnO	0.01	0.02	0.01	0.00	0.01
MgO	14.40	0.26	0.00	5.90	0.00
CaO	22.60	21.95	22.91	14.79	9.19
K2O	0.01	0.01	0.00	0.00	0.00
Na2O	0.00	0.00	0.01	0.01	0.01
Total	100.56	99.02	99.18	98.90	99.83

Table A.3: Olivine Optical Parameter Fits

Fo	**1.3 µm center**	**1.3 µm strength**	**1.3 µm width**	**1.1 µm center**	**1.1 µm strength**	**1.1 µm width**	**0.9 µm center**	**0.9 µm strength**	**0.9 µm width**	**0.6 µm continuum**	**1.85 µm continuum**	**Err Mean**	**Err Med**
							RELAB						
0.1	1.300	2.070E-04	0.177	1.085	7.200E-05	0.063	0.985	1.006E-04	0.101	8.674E-05	1.246E-04	1.33E-06	1.05E-06
36	1.265	1.870E-04	0.169	1.085	7.900E-05	0.057	0.970	7.280E-05	0.095	6.008E-05	1.604E-04	2.39E-06	1.62E-06
42	1.260	1.470E-04	0.168	1.075	6.700E-05	0.059	0.970	5.780E-05	0.097	5.444E-05	1.350E-04	1.65E-06	7.34E-07
57.6	1.230	1.570E-04	0.154	1.055	1.170E-04	0.064	0.925	9.880E-05	0.074	7.094E-05	1.519E-04	3.29E-06	2.29E-06

59.5	1.235	1.010E-04	0.158	1.075	5.200E-05	0.059	0.965	6.940E-05	0.088	5.972E-05	1.203E-04	2.64E-06	1.54E-06
84	1.220	5.300E-05	0.164	1.060	3.800E-05	0.061	0.920	1.920E-05	0.095	1.173E-05	1.460E-05	4.91E-07	3.74E-07
85.6	1.200	9.600E-05	0.168	1.045	7.300E-05	0.063	0.875	2.760E-05	0.080	5.859E-06	4.664E-06	4.95E-07	4.26E-07
85.6	1.210	6.500E-05	0.161	1.050	5.200E-05	0.063	0.895	2.100E-05	0.088	1.239E-05	1.731E-05	4.01E-07	2.46E-07
85.7	1.200	8.800E-05	0.160	1.045	7.300E-05	0.063	0.885	2.720E-05	0.087	1.310E-05	2.177E-05	3.45E-07	2.33E-07
85.7	1.205	6.300E-05	0.148	1.050	4.700E-05	0.059	0.915	2.420E-05	0.102	3.443E-05	5.871E-05	1.04E-06	3.83E-07
85.9	1.225	6.700E-05	0.153	1.055	5.100E-05	0.062	0.930	2.580E-05	0.113	2.197E-05	3.365E-05	4.16E-07	2.37E-07
87.6	1.215	6.700E-05	0.158	1.050	5.700E-05	0.062	0.910	2.180E-05	0.087	1.882E-05	3.395E-05	6.02E-07	3.28E-07
88.5	1.220	5.300E-05	0.155	1.055	4.200E-05	0.060	0.915	1.820E-05	0.101	1.266E-05	1.483E-05	3.70E-07	2.43E-07
89	1.215	4.700E-05	0.155	1.055	3.700E-05	0.060	0.915	1.680E-05	0.099	1.019E-05	1.090E-05	3.17E-07	2.02E-07
90	1.245	3.000E-05	0.135	1.060	3.200E-05	0.068	0.960	1.060E-05	0.075	3.598E-05	5.503E-05	6.86E-07	4.55E-07
90	1.245	3.000E-05	0.135	1.060	3.200E-05	0.068	0.960	1.060E-05	0.075	3.598E-05	5.503E-05	6.86E-07	4.55E-07
90.2	1.205	6.300E-05	0.158	1.045	5.300E-05	0.062	0.890	1.920E-05	0.090	1.977E-06	9.223E-07	3.89E-07	3.24E-07
90.2	1.205	4.100E-05	0.159	1.045	3.500E-05	0.061	0.890	1.200E-05	0.086	5.857E-06	8.206E-06	2.34E-07	1.75E-07
90.4	1.210	4.200E-05	0.159	1.050	3.700E-05	0.062	0.890	1.280E-05	0.084	5.208E-06	9.958E-06	2.95E-07	2.35E-07
90.4	1.200	6.500E-05	0.167	1.050	5.300E-05	0.062	0.885	1.760E-05	0.092	2.707E-06	2.338E-06	4.63E-07	4.51E-07
90.4	1.205	6.500E-05	0.164	1.050	5.500E-05	0.062	0.885	2.000E-05	0.090	2.804E-06	2.264E-06	4.44E-07	3.86E-07
90.4	1.205	3.900E-05	0.163	1.050	3.200E-05	0.062	0.890	1.260E-05	0.090	3.687E-06	5.028E-06	2.90E-07	2.35E-07
90.5	1.205	5.800E-05	0.164	1.050	4.700E-05	0.062	0.900	2.020E-05	0.096	3.710E-06	2.304E-06	5.46E-07	4.66E-07
90.5	1.195	5.300E-05	0.165	1.045	4.000E-05	0.060	0.895	1.540E-05	0.093	2.586E-06	2.848E-06	3.57E-07	2.68E-07
90.5	1.205	3.800E-05	0.162	1.050	3.000E-05	0.061	0.905	1.320E-05	0.093	6.518E-06	8.363E-06	2.42E-07	1.55E-07
90.5	1.205	3.100E-05	0.156	1.050	2.500E-05	0.060	0.920	1.240E-05	0.103	7.028E-06	1.052E-05	3.00E-07	1.89E-07
90.8	1.205	4.900E-05	0.155	1.045	4.100E-05	0.061	0.900	1.520E-05	0.099	6.018E-06	1.031E-05	3.28E-07	2.21E-07
90.8	1.210	4.200E-05	0.148	1.050	3.400E-05	0.060	0.925	1.580E-05	0.102	1.343E-05	2.437E-05	5.43E-07	3.12E-07
91.8	1.215	2.700E-05	0.150	1.055	2.300E-05	0.061	0.930	1.080E-05	0.100	9.480E-06	1.307E-05	2.93E-07	2.43E-07
92	1.215	2.800E-05	0.155	1.050	2.300E-05	0.060	0.925	8.800E-06	0.096	8.754E-06	1.378E-05	4.05E-07	3.00E-07
96.9	1.225	1.100E-05	0.162	1.055	1.000E-05	0.062	0.930	4.400E-06	0.107	4.044E-06	5.961E-06	2.03E-07	1.40E-07
							USGS						
11	1.320	1.900E-03	0.180	1.090	6.400E-04	0.063	0.960	5.080E-04	0.079	1.685E-04	4.347E-04	2.18E-05	1.65E-05
18	1.330	1.079E-03	0.260	1.100	1.390E-04	0.079	1.000	4.184E-04	0.160	7.914E-05	2.155E-04	1.04E-05	7.77E-06
29	1.300	2.230E-03	0.176	1.090	7.400E-04	0.060	0.970	6.380E-04	0.098	9.364E-05	2.474E-04	2.37E-05	1.47E-05
41	1.300	9.600E-04	0.168	1.090	2.400E-04	0.059	1.010	3.740E-04	0.101	9.766E-05	3.769E-04	1.62E-05	1.10E-05
51	1.290	9.700E-04	0.160	1.080	2.100E-04	0.054	1.030	4.580E-04	0.102	9.896E-05	4.536E-04	1.88E-05	1.14E-05
60	1.270	9.100E-04	0.167	1.070	2.100E-04	0.051	1.020	3.800E-04	0.103	6.253E-05	2.328E-04	1.22E-05	9.06E-06
66	1.250	1.190E-03	0.161	1.070	5.000E-04	0.059	0.980	4.120E-04	0.087	7.264E-05	3.315E-04	1.68E-05	1.11E-05

80	1.250	2.070E-04	0.130	1.070	1.360E-04	0.064	1.010	9.280E-05	0.073	1.410E-05	1.241E-04	5.97E-06	4.19E-06
89	1.270	2.500E-04	0.133	1.070	2.100E-04	0.072	0.990	7.000E-05	0.072	3.786E-05	1.905E-04	8.02E-06	5.49E-06
89	1.230	5.300E-04	0.158	1.060	2.500E-04	0.049	1.000	2.120E-04	0.114	3.394E-05	9.690E-05	4.79E-06	2.40E-06
89	1.230	5.000E-04	0.157	1.060	2.800E-04	0.057	0.960	1.260E-04	0.111	2.038E-05	4.894E-05	2.61E-06	1.80E-06
89	1.230	5.500E-04	0.153	1.060	3.700E-04	0.059	0.940	1.100E-04	0.111	2.015E-05	4.345E-05	3.38E-06	2.54E-06
91	1.250	1.320E-04	0.186	1.060	1.110E-04	0.092	0.980	4.280E-05	0.096	2.519E-05	1.350E-04	6.19E-06	4.00E-06
91	1.230	3.700E-04	0.149	1.050	3.100E-04	0.063	0.920	6.400E-05	0.082	1.613E-05	9.594E-05	4.13E-06	2.97E-06
92	1.230	2.700E-04	0.161	1.060	1.500E-04	0.057	0.950	7.800E-05	0.093	1.850E-05	6.997E-05	2.12E-06	1.46E-06
92	1.200	5.900E-04	0.169	1.050	4.400E-04	0.055	0.880	7.200E-05	0.073	1.819E-05	5.078E-05	4.01E-06	2.15E-06

Table A.4: Pyroxene Optical Parameter Fits

#	En	Fs	Wo	0.9 µm center	0.9 µm strength	0.9 µm width	1.2 µm center	1.2 µm strength	1.2 µm width	0.8 µm center	0.8 µm strength	0.8 µm width	Err Mean	Err Median
High-Ca Pyroxene														
83	0	49	51	0.945	2.740E-04	0.071	1.140	5.690E-04	0.127	0.795	4.500E-05	0.073	3.50E-06	2.68E-06
85	0	61	39	1.030	7.150E-04	0.057	1.200	9.900E-05	0.142	0.920	7.800E-05	0.055	2.37E-06	1.56E-06
84	0	65	35	1.030	1.937E-03	0.073	1.210	4.780E-04	0.137	0.865	1.570E-04	0.100	1.22E-05	4.23E-06
87	0	71	29	1.015	2.377E-03	0.067	1.250	3.110E-04	0.136	0.885	1.610E-04	0.117	1.07E-05	5.48E-06
86	0	75	25	1.020	2.789E-03	0.072	1.265	3.230E-04	0.116				1.90E-05	1.14E-05
82	1	50	49	1.035	2.960E-04	0.085	1.170	2.540E-04	0.135	0.855	8.900E-05	0.118	6.39E-06	4.06E-06
54	6	70	23	1.000	3.038E-03	0.079	1.260	3.910E-04	0.122	0.755	8.700E-05	0.062	2.15E-05	6.42E-06
70	14	41	45	1.030	9.330E-04	0.060	1.160	2.150E-04	0.147	0.860	9.800E-05	0.121	7.24E-06	1.62E-06
66	15	48	38	1.015	1.090E-03	0.061	1.190	1.250E-04	0.146	0.855	4.900E-05	0.091	6.70E-06	1.40E-06
37	16	35	49	1.040	4.220E-04	0.079	1.195	2.170E-04	0.112	0.855	6.900E-05	0.095	5.54E-06	2.19E-06
76	18	35	46	1.035	8.260E-04	0.067	1.220	1.540E-04	0.096	0.855	3.500E-05	0.097	6.32E-06	3.97E-06
55	18	56	26	1.005	1.581E-03	0.063	1.225	1.290E-04	0.131	0.890	1.160E-04	0.057	7.67E-06	2.58E-06
56	18	60	22	0.980	6.030E-04	0.076	1.230	6.900E-05	0.102				2.19E-06	1.49E-06
50	19	58	23	0.990	2.227E-03	0.073	1.250	1.810E-04	0.107				1.53E-05	6.30E-06
71	23	31	46	1.030	1.052E-03	0.059	1.180	1.910E-04	0.144	0.970	1.440E-04	0.118	6.35E-06	2.36E-06
74	24	37	39	1.015	1.165E-03	0.064	1.200	1.540E-04	0.147	0.820	6.100E-05	0.103	6.24E-06	1.93E-06
36	27	24	49	1.040	4.570E-04	0.077	1.205	2.350E-04	0.122	0.865	9.000E-05	0.073	5.99E-06	3.50E-06
58	28	45	27	1.005	7.140E-04	0.060	1.185	6.000E-05	0.132	0.895	9.400E-05	0.048	3.12E-06	1.20E-06
39	29	22	49	1.040	2.710E-04	0.077	1.165	2.160E-04	0.151	0.840	1.000E-04	0.123	5.29E-06	3.25E-06
68	29	33	38	1.015	1.412E-03	0.060	1.195	1.350E-04	0.144	0.870	6.200E-05	0.062	6.82E-06	1.93E-06

73	36	25	39	1.015	1.168E-03	0.059	1.195	8.200E-05	0.143	0.905	3.300E-05	0.026	8.90E-06	1.94E-06
57	36	39	25	1.000	1.542E-03	0.068	1.250	9.800E-05	0.107				1.56E-05	5.91E-06
79	38	15	47	1.030	1.368E-03	0.061	1.145	2.780E-04	0.179	0.915	6.900E-05	0.037	5.73E-06	3.15E-06
51	39	34	27	1.000	1.250E-03	0.072	1.270	9.000E-05	0.102				1.23E-05	4.19E-06
33	42	8	49	1.040	6.900E-05	0.074	1.190	3.500E-05	0.135	0.885	1.400E-05	0.057	8.93E-07	4.97E-07
44	43	8	49	1.045	2.110E-04	0.058	1.135	1.930E-04	0.158	0.910	5.400E-05	0.060	2.71E-06	1.98E-06
43	45	6	49	1.055	1.170E-04	0.053	1.125	1.040E-04	0.167	0.950	2.500E-05	0.054	1.08E-06	4.17E-07
75	46	9	45	1.030	4.330E-04	0.062	1.240	3.600E-05	0.103				5.84E-06	2.51E-06
77	52	3	45	1.025	3.130E-04	0.056	1.160	3.900E-05	0.141	0.900	1.800E-05	0.037	1.79E-06	9.88E-07
67	52	9	39	1.015	6.690E-04	0.059	1.170	6.600E-05	0.145	0.880	3.400E-05	0.050	2.97E-06	9.85E-07
Low-Ca Pyroxene														
88	0	90	10	0.995	1.159E-03	0.074	1.255	1.710E-04	0.114				1.21E-05	6.64E-06
89	0	93	7	0.975	1.873E-03	0.078	1.240	3.130E-04	0.113				1.44E-05	8.87E-06
91	0	98	2	0.970	1.584E-03	0.098	1.260	5.210E-04	0.105				2.36E-05	1.57E-05
61	0	100	0	0.950	2.573E-03	0.074	1.220	4.230E-04	0.104				2.03E-05	1.06E-05
21	8	92	0	0.945	1.652E-03	0.071	1.210	2.580E-04	0.107				1.07E-05	5.65E-06
49	11	70	19	0.975	2.070E-03	0.076	1.230	2.640E-04	0.118				1.10E-05	6.66E-06
48	14	77	10	0.955	2.290E-04	0.066	1.130	3.600E-05	0.133				2.42E-06	1.51E-06
24	17	83	0	0.945	1.905E-03	0.070	1.215	2.410E-04	0.095				1.59E-05	5.68E-06
20	17	83	0	0.940	1.846E-03	0.070	1.200	2.720E-04	0.107				1.08E-05	5.78E-06
53	23	68	10	0.970	1.632E-03	0.071	1.220	1.490E-04	0.111				6.87E-06	3.22E-06
28	25	75	0	0.935	2.649E-03	0.070	1.195	3.700E-04	0.105				1.74E-05	7.86E-06
23	30	70	0	0.935	3.079E-03	0.070	1.195	3.460E-04	0.097				1.84E-05	8.95E-06
25	35	65	0	0.935	1.110E-03	0.064	1.185	9.800E-05	0.099				7.53E-06	3.39E-06
11	36	50	14	0.965	1.824E-03	0.072	1.225	1.440E-04	0.092				1.24E-05	5.78E-06
8	38	57	5	0.945	1.874E-03	0.070	1.185	1.700E-04	0.106				5.35E-06	3.06E-06
14	39	59	3	0.940	2.195E-03	0.067	1.185	1.530E-04	0.097				2.20E-05	9.70E-06
4	50	50	0	0.930	9.780E-04	0.064	1.180	6.200E-05	0.085				6.74E-06	2.03E-06
26	70	30	0	0.920	4.110E-04	0.060	1.145	1.800E-05	0.089				1.91E-06	9.52E-07
22	75	25	0	0.920	2.660E-04	0.060	1.155	1.000E-05	0.075				2.14E-06	6.12E-07
3	75	25	0	0.920	3.100E-04	0.060	1.150	1.300E-05	0.078				2.03E-06	7.54E-07
2	80	20	0	0.915	5.640E-04	0.060	1.120	2.200E-05	0.093				2.32E-06	1.01E-06
27	80	20	0	0.915	4.680E-04	0.060	1.125	1.800E-05	0.089				1.96E-06	8.66E-07
65	90	10	0	0.910	1.250E-04	0.057	1.110	3.000E-06	0.088				6.88E-07	4.15E-07
64	97.5	2.5	0	0.910	9.800E-05	0.057	1.130	2.000E-06	0.064				1.03E-06	4.48E-07

#	En	Fs	Wo	2.0 µm center	2.0 µm strength	2.0 µm width	0.6 µm continuum	1.3 µm continuum	Err Mean	Err Median
High-Ca Pyroxene										
83	0	49	51	2.445	5.800E-05	0.271	5.899E-05	8.135E-05	1.72E-06	1.31E-06
85	0	61	39	2.320	3.280E-04	0.220	8.781E-05	1.480E-04	2.97E-06	2.26E-06
84	0	65	35	2.310	1.143E-03	0.213	1.558E-04	2.139E-04	9.33E-06	7.94E-06
87	0	71	29	2.315	1.253E-03	0.218	1.475E-04	1.280E-04	9.77E-06	7.23E-06
86	0	75	25	2.320	1.700E-03	0.225	3.639E-04	6.919E-04	1.39E-05	9.58E-06
82	1	50	49	2.325	9.300E-05	0.187	5.378E-05	5.931E-05	1.40E-06	1.02E-06
54	6	70	23	2.315	1.995E-03	0.240	1.860E-04	1.552E-04	1.29E-05	7.19E-06
70	14	41	45	2.325	4.430E-04	0.207	1.103E-04	5.545E-05	4.91E-06	4.16E-06
66	15	48	38	2.335	5.690E-04	0.217	4.459E-05	3.736E-05	4.82E-06	4.17E-06
37	16	35	49	2.280	8.600E-05	0.195	2.317E-04	3.136E-04	7.94E-06	6.78E-06
76	18	35	46	2.335	5.720E-04	0.248	7.159E-04	1.116E-03	6.68E-06	6.03E-06
55	18	56	26	2.330	9.520E-04	0.231	3.566E-05	4.277E-05	6.49E-06	6.74E-06
56	18	60	22	2.220	4.770E-04	0.251	2.239E-05	3.811E-05	6.99E-06	3.76E-06
50	19	58	23	2.290	1.448E-03	0.245	6.098E-05	7.469E-05	9.74E-06	5.83E-06
71	23	31	46	2.325	5.980E-04	0.204	1.851E-04	2.335E-04	8.20E-06	6.66E-06
74	24	37	39	2.335	6.820E-04	0.219	1.109E-04	1.158E-04	5.70E-06	5.22E-06
36	27	24	49	2.275	1.640E-04	0.232	2.013E-04	3.758E-04	8.78E-06	7.21E-06
58	28	45	27	2.315	4.810E-04	0.245	1.650E-05	2.249E-05	4.82E-06	4.23E-06
39	29	22	49	2.335	1.380E-04	0.203	1.079E-04	1.081E-04	2.97E-06	2.32E-06
68	29	33	38	2.350	8.360E-04	0.218	4.105E-05	5.489E-05	8.06E-06	6.81E-06
73	36	25	39	2.335	7.090E-04	0.207	1.683E-04	3.373E-04	9.47E-06	8.56E-06
57	36	39	25	2.300	1.049E-03	0.240	1.852E-04	3.793E-04	1.09E-05	9.18E-06
79	38	15	47	2.325	7.540E-04	0.198	3.419E-04	4.421E-04	9.09E-06	6.96E-06
51	39	34	27	2.320	8.290E-04	0.246	5.071E-05	7.609E-05	7.20E-06	5.84E-06
33	42	8	49	2.345	3.400E-05	0.248	1.177E-05	3.065E-05	1.28E-06	9.21E-07
44	43	8	49	2.305	9.600E-05	0.215	4.569E-05	1.243E-04	4.96E-06	3.06E-06
43	45	6	49	2.325	6.700E-05	0.208	2.661E-05	3.165E-05	2.89E-06	1.89E-06
75	46	9	45	2.345	2.590E-04	0.212	2.229E-05	3.606E-05	4.36E-06	3.65E-06
77	52	3	45	2.340	1.870E-04	0.210	1.964E-05	4.073E-05	4.34E-06	3.38E-06
67	52	9	39	2.345	4.280E-04	0.221	6.304E-05	8.747E-05	7.14E-06	5.58E-06
Low-Ca Pyroxene										

88	0	90	10	2.240	6.900E-04	0.244	1.180E-04	2.713E-04	9.60E-06	4.59E-06
89	0	93	7	2.175	1.232E-03	0.235	7.333E-05	1.753E-04	2.43E-05	1.62E-05
91	0	98	2	2.120	1.445E-03	0.214	5.807E-04	5.954E-04	2.50E-05	1.20E-05
61	0	100	0	2.085	2.017E-03	0.198	2.731E-04	2.639E-04	2.34E-05	1.43E-05
21	8	92	0	2.075	1.290E-03	0.198	2.041E-04	1.489E-04	1.20E-05	9.78E-06
49	11	70	19	2.230	1.540E-03	0.249	1.165E-04	1.593E-04	2.52E-05	1.42E-05
48	14	77	10	2.180	2.110E-04	0.266	6.247E-05	1.025E-04	1.15E-05	8.31E-06
24	17	83	0	2.060	1.500E-03	0.196	1.108E-04	1.284E-04	1.30E-05	1.19E-05
20	17	83	0	2.060	1.678E-03	0.199	1.251E-04	1.324E-04	1.54E-05	1.40E-05
53	23	68	10	2.205	1.114E-03	0.243	4.962E-05	6.910E-05	1.56E-05	1.04E-05
28	25	75	0	2.035	2.807E-03	0.192	1.069E-04	1.782E-04	2.36E-05	2.10E-05
23	30	70	0	2.025	2.676E-03	0.192	1.468E-04	1.789E-04	2.07E-05	1.87E-05
25	35	65	0	2.020	8.180E-04	0.192	1.151E-04	9.583E-05	6.59E-06	5.56E-06
11	36	50	14	2.145	1.252E-03	0.240	6.469E-05	1.070E-04	2.50E-05	2.10E-05
8	38	57	5	2.070	1.477E-03	0.216	6.447E-05	1.191E-04	2.72E-05	2.09E-05
14	39	59	3	2.050	2.134E-03	0.223	3.885E-04	6.608E-04	7.62E-05	3.52E-05
4	50	50	0	1.980	8.130E-04	0.189	1.801E-05	4.888E-05	5.21E-06	4.50E-06
26	70	30	0	1.925	3.250E-04	0.183	5.923E-06	2.023E-05	2.41E-06	2.13E-06
22	75	25	0	1.910	2.030E-04	0.184	9.834E-06	2.095E-05	3.17E-06	2.25E-06
3	75	25	0	1.910	2.460E-04	0.185	7.320E-06	1.649E-05	1.97E-06	1.68E-06
2	80	20	0	1.885	4.220E-04	0.177	7.817E-06	2.226E-05	2.44E-06	2.20E-06
27	80	20	0	1.885	3.530E-04	0.176	6.624E-06	1.848E-05	1.98E-06	1.86E-06
65	90	10	0	1.855	9.500E-05	0.178	8.288E-06	1.329E-05	2.43E-06	8.57E-07
64	97.5	2.5	0	1.825	6.700E-05	0.172	1.704E-05	1.426E-05	2.57E-06	1.10E-06

APPENDIX B

USING THE OPTICAL CONSTANTS PARAMETERS

We provide a simplified version of how to use the optical parameters presented in this study. The value of *k* at some wavelength λ (in microns) is the superposition of the continuum and all the constituent absorptions (Eq. B1),

$$k_\lambda = C_\lambda + \sum_N G_\lambda \text{ (B1)}$$

where k_λ is the value of the imaginary index of refraction, C_λ is the continuum, G_λ are the Gaussians, and *N* is the number of Gaussians (which is three for olivine and pyroxene). The values of C_λ and G_λ can be obtained from the linear and Gaussian functions (Eq. B2 and B3 respectively).

$$C(\lambda) = y_{C1} + \left(\frac{y_{C2}-y_{C1}}{1/\lambda_{C2}-1/\lambda_{C1}}\right)\cdot\left(1/\lambda - 1/\lambda_{C1}\right) \quad \text{(B2)}$$

$$G(\lambda) = s\cdot\exp\left(\frac{-(\lambda-\mu)^2}{2\sigma^2}\right) \quad \text{(B3).}$$

For the continuum (Eq. B2), values for the ordered pairs, (λ_{C1},y_{C1}) and (λ_{C2},y_{C2}), are dependent on the mineral of interest. For olivine, λ_{C1} and λ_{C2} are 0.6 and 1.85 μm, respectively; as for pyroxene, the values are 0.6 and 1.3 μm, respectively. The *k* values for λ_{C1} and λ_{C2} (i.e., y_{C1} and y_{C2}) are derived from functions dependent on mineral chemistry (Eq. B4 or B5).

$$y_{C1,C2} = A + B\cdot(Fo) \text{ (B4: for olivine)}$$

$$y_{C1,C2} = A\cdot(Fs) + B\cdot(Wo) + C \text{ (B5: for pyroxene)}$$

The constants *A*, *B*, and *C* are obtained from **Table 2.1** for olivine and **Table 2.2** for pyroxene (Note: *Ensure that the correct constants A, B, and C are used for the associated parameter*). There are three main Gaussians for olivine (i.e., 0.9-, 1.1-, and 1.3-μm absorptions) and pyroxene (ie., 1.0-, 1.2-, 2.0-μm absorptions). Computing the Gaussians contribution to *k* (Eq. B3) requires caluclating the values of *s*, σ, and μ (Eq. B6 and B7 or B8).

$$\sigma,\mu = A + B\cdot(Fo) \text{ (B6: for olivine)}$$

$$s = A + B\cdot(Fo) + C\cdot(Fo)^2 \text{ (B7: for olivine)}$$

$$s,\sigma,\mu = A\cdot(Fs) + B\cdot(Wo) + C \text{ (B8: for pyroxene)}$$

In summary, the value of k for either olivine or pyroxene is calculated from combining equations Equation B1 through B8 and providing the mineral chemistry and the wavelength of interest. Repeating this method for various wavelengths would produce a k-spectrum.

APPENDIX C

PARAMETERS OF CONCENTRIC CRATERS

Table C.1: Morphology and Morphometrics of Concentric Craters

	Morphology and Morphometrics										
	Name	Longitude	Latitude	Crater Type	Crater Diameter [km]	Concentric Ridge Diameter [km]	Crater Depth [m]	Crater Rim Height [m]	Crater Rim Flank [km]	Conc. Ridge Height [m]	Conc. Ridge Width [km]
1	Archytas G	0.5	55.7	Meniscus	6.9	4.3				206.3	3.5
2	Unnamed	0.5	55.5	Toroid	4.7	1.9				28.5	1.7
3	Egede G	6.9	52.0	Meniscus	7.4	6.2				255.9	
4	Unnamed	24.8	50.2	Toroid	6	4.4					
5	Unnamed	51.0	51.7	Toroid	6.8	2.7	332.0	105.6	0.8	138.1	2.6
6	Unnamed	36.2	33.9	Bubbly	7.9	3.3	621.6	80.7	0.7	174.3	3.9
7	Firmicus E	63.6	8.0	Bubbly	10.1	3.1	1334.8			125.5	
8	Firmicus C	66.5	7.7	Toroid	14.7	5.1	1752.7	226.2	1.1	189.0	4.7
9	Unnamed	83.9	3.1	Toroid	9.8	6.1					
10	Unnamed	72.6	5.0	Toroid	11	6	522.9			81.1	4.8
11	Dubyago V	69.8	5.9	Meniscus	10.1	6.1	626.7			48.3	9.1
12	Unnamed	68.6	3.7	Toroid	5.6	2.5				149.5	2.4
13	Unnamed	66.8	4.0	Toroid	5.6	3.1					
14	Apollonius N	63.8	4.7	Meniscus	10.5	5.2	1312.1	104.4	0.7	626.0	5.5
15	Rhaeticus A	5.2	1.7	Toroid	10.5	4.1	1081.5	243.0	1.2	77.9	3.7
16	Unnamed	73.6	1.3	Toroid	10.2	5.3	570.1	107.2	1.1	144.1	5.2
17	Unnamed	145.9	48.6	Toroid	6.8	5	475.3	88.3	1.1	153.5	
18	Unnamed	129.2	32.8	Meniscus	8.7	3	880.0			87.6	2.8
19	Unnamed	147.3	27.7	Toroid	6.1	4.3				60.0	2.8
20	Unnamed	97.1	14.5	Toroid	7	4.3	467.0	119.3	0.8	190.0	4.1
21	Unnamed	94.2	12.2	Toroid	12.3	7.7				326.6	8.3
22	Unnamed	173.5	4.8	Meniscus	11.1	6.7	1553.7			1096.3	
23	Unnamed	-96.1	25.2	Toroid	16.7	7.5	1875.1	274.0	1.3		
24	Bell E	-95.9	22.0	Toroid	15.6	9.4	1180.5	428.5	1.4	541.6	9.9
25	Dirichlet E	-148.4	11.6	Toroid	27.8	8.3	3689.0	467.7	3.2	399.7	8.3

26	Unnamed	-68.6	57.1	Bubbly	3.3	2.7						
27	Unnamed	-34.8	57.9	Toroid	6.2	2	136.8	103.0	1.3	73.9	1.9
28	Unnamed	-31.5	57.3	Meniscus	5.5	1.8					
29	Unnamed	-25.6	56.7	Toroid	6.7	5.1					
30	Repsold A	-77.0	51.8	Meniscus	8	4.7	892.8			518.0	4.7
31	Unnamed	-66.4	52.7	Toroid	6.5	3.1				85.0	2.5
32	Unnamed	-48.0	47.7	Bubbly	4.6	1.7	258.6	59.1	0.5	51.4	1.3
33	Louville DA	-51.7	46.6	Bubbly	10.4	4.9	572.7	302.7	1.2	93.8	6.4
34	Unnamed	-52.3	46.5	Toroid	6	2.8					
35	Unnamed	-55.6	48.3	Toroid	6	4.2					
36	Louville A	-45.4	43.3	Toroid	8.4	2.2					
37	Unnamed	-81.2	38.3	Toroid	5.4	2.9	434.1	93.7	0.8	266.7	2.9
38	Unnamed	-81.8	36.2	Toroid	5.4	2.6	235.4	80.0	0.6	93.9	2.9
39	Unnamed	-75.0	37.4	Meniscus	2.7	1.2	357.2			179.5	1.6
40	Gruithuisen K	-42.7	35.4	Toroid	6	1.5	571.7	112.5	0.9	179.4	2.9
41	Unnamed	-78.7	33.8	Bubbly	7.9	2.3					
42	Unnamed	-82.1	33.3	Meniscus	7.9	2.9	769.5			99.9	2.5
43	Unnamed	-84.2	29.9	Meniscus	6.7	2.6	588.4	131.9	0.8	97.4	2.3
44	Unnamed	-79.8	29.2	Toroid	6.8	2.5				65.7	3.8
45	MacMillan	-7.9	24.2	Toroid	7.4	3.9					
46	Unnamed	-78.9	21.9	Toroid	5.9	2.1	550.5	40.8	0.5	149.1	
47	Unnamed	-87.4	14.7	Meniscus	12.1	8	1300.6			246.8	
48	Krafft K	-74.7	16.5	Meniscus	11.7	9	742.9			378.3	
49	Cavalerius E	-70.1	7.6	Toroid	9.7	4.1	874.6	198.4	1.0	266.4	4.1
50	Schlüter X	-88.3	1.2	Meniscus	13.3	9	1367.3	314.1	1.8	642.3	9.1
51	Unnamed	-6.0	2.3	Toroid	5	1.9	237.7	63.1	0.5	51.9	2.0
52	Leakey	37.5	-3.2	Toroid	12.9	6.3	1702.2	306.8	2.4	544.6	
53	Crozier H	49.4	-14.0	Toroid	11	4.6	1002.5	759.7	1.0	437.5	5.0
54	Unnamed	37.5	-11.5	Bubbly	11.2	3.3	438.0	210.4	1.7	65.0	1.6
55	Colombo B	45.2	-16.5	Toroid	13	5.3	1043.5	11.3	2.4	65.1	7.2
56	Unnamed	47.9	-16.2	Toroid	8.6	4.8					

57	Unnamed	29.7	-19.2	Toroid	10.7	5.9	525.5	135.8	1.1	124.8	5.5
58	Fracastorius E	31.0	-20.2	Toroid	13.1	4.3	873.3	181.9	1.2	99.8	3.6
59	Unnamed	83.4	-26.6	Toroid	8.8	4.1	927.1	136.9	1.2	379.8	3.9
60	Pontanus E	13.3	-25.3	Toroid	13.1	8.5	796.8			499.2	7.3
61	Unnamed	89.2	-34.1	Meniscus	7.2	3.3	314.4			146.9	3.7
62	Unnamed	85.6	-37.7	Toroid	4.9	2.3					
63	Unnamed	58.9	-39.7	Toroid	4.1	2.7					
64	Maurolycus M	12.6	-41.9	Bubbly	10.8	2.1	762.5			117.5	1.8
65	Unnamed	73.3	-44.5	Bubbly	6.5	3.2	368.6			260.4	3.9
66	Unnamed	84.7	-44.4	Bubbly	11.7	6.1	664.2	179.6	1.9	232.0	4.6
67	Unnamed	74.0	-46.9	Meniscus	5	1.8	279.1			51.9	1.6
68	Unnamed	78.6	-55.3	Meniscus	4.5	2.8				65.5	2.5
69	Unnamed	78.8	-53.8	Meniscus	3.6	2.3				62.5	
70	Unnamed	79.9	-54.5	Toroid	2.8	1.7					
71	Unnamed	80.2	-54.4	Toroid	2.7	1.6					
72	Unnamed	78.0	-53.9	Bubbly	1.8	1.2					
73	Unnamed	90.2	-2.9	Toroid	9.4	3.6				31.7	3.4
74	Unnamed	117.3	-2.8	Toroid	9.3	3.1	442.0			43.6	3.8
75	Unnamed	167.7	-11.1	Bubbly	10.3	4.6					
76	Unnamed	159.0	-16.1	Meniscus	6.4	2.4					
77	Unnamed	172.5	-16.0	Toroid	2.7	1				25.2	1.0
78	Unnamed	174.0	-16.7	Bubbly	6	2.3	287.3			69.2	2.8
79	Unnamed	174.2	-16.5	Bubbly	5.3	2.1					
80	Unnamed	172.7	-20.5	Bubbly	9.4	4.3					
81	Barbier F	158.2	-23.8	Bubbly	11.3	4.1	867.9	96.2	0.7	161.5	6.3
82	Unnamed	136.1	-25.7	Toroid	2.9	0.8	211.2	45.3	0.6	5.2	0.9
83	Unnamed	104.4	-25.8	Toroid	6.6	2.4					
84	Unnamed	95.7	-37.9	Bubbly	5.9	2.1	484.2	76.7	0.5	78.7	2.7
85	Unnamed	143.8	-37.2	Toroid	5.6	2					
86	Unnamed	144.3	-37.4	Toroid	7.1	3.8	304.4	42.1	1.1	178.5	3.4
87	Unnamed	130.8	-44.8	Toroid	9.2	2.3	681.2	194.0	1.3	125.0	2.6

88	Unnamed	153.9	-44.0	Bubbly	7.1	3.9	432.6	151.9	1.0	115.4	3.9
89	Unnamed	94.6	-53.1	Toroid	26.3	15.6	1082.7	237.8	1.7		
90	Unnamed	102.6	-58.7	Meniscus	8.8	5.3	1427.8			759.3	
91	Unnamed	-154.1	-30.8	Toroid	11.8	5.3	1290.3	252.0	1.5	538.9	5.3
92	Unnamed	-164.8	-43.3	Meniscus	9.4	6.9	1345.6	251.9	1.2	1058.8	7.3
93	Unnamed	-165.8	-53.9	Toroid	5.2	2.3					
94	Unnamed	-160.3	-55.8	Bubbly	9.1	4.8	385.8	155.1	1.1	102.0	4.8
95	Unnamed	-18.8	-1.7	Meniscus	2	1.1				212.3	1.3
96	Gambart J	-18.2	-0.7	Toroid	7.2	2.9	366.0			14.1	1.7
97	Damoiseau D	-63.3	-6.5	Meniscus	16.8	11.1	2595.3			1538.9	11.5
98	Damoiseau BA	-59.1	-8.3	Toroid	8.4	5.3	579.4	214.3	1.1	95.1	5.4
99	Crüger F	-64.5	-14.2	Meniscus	7.9	3.3	823.1	171.9	0.9	142.3	3.4
100	Mersenius M	-48.6	-21.3	Toroid	5.5	2.3					
101	Kopff C	-86.2	-18.3	Toroid	14.4	3.9	1148.4	328.2	2.2	37.1	4.0
102	Lamarck B	-69.8	-22.9	Toroid	7.9	4.6	1058.1			515.9	
103	Doppelmayer V	-45.7	-29.8	Bubbly	6.9	1.6					
104	Unnamed	-39.1	-29.4	Toroid	3.5	1.7					
105	Marth	-29.3	-31.2	Toroid	6.8	3.4				314.8	3.1
106	Hesiodus A	-17.1	-30.1	Toroid	15	6.7	1301.9			385.1	7.0
107	Unnamed	-46.8	-35.4	Toroid	8.3	4.3	644.0			89.9	4.0
108	Lagrange T	-62.7	-33.0	Bubbly	12	5.4					
109	Unnamed	-133.5	78.7	Toroid	17.4	10.1	1055.4	522.6	1.4	153.2	9.2
110	Petermann B	63.8	72.7	Toroid	10.9	4.2	963.4	321.9	1.5	79.9	3.3
111	Unnamed	158.2	-60.7	Toroid	8.2	2.8	776.6	159.6	1.1	173.9	2.9
112	Unnamed	-144.0	-56.3	Bubbly	11.8	6.7	692.6	147.4		220.2	6.9
113	Unnamed	1.3	-4.5	Meniscus	4.5	2.8					
114	Unnamed	-65.7	-17.0	Toroid	2.2	1.4					

Table C.2: FeO and TiO_2 of Concentric Craters

		Composition							
	Name	FeO Mean (crater)	FeO Std. Dev. (crater)	FeO Mean (region)	FeO Std. Dev. (region)	TiO_2 Mean (crater)	TiO_2 Std. Dev. (crater)	TiO_2 Mean (region)	TiO_2 Std. Dev. (region)
1	Archytas G	10.1	1.6	11.6	1.4	0.7	0.3	0.6	0.4
2	Unnamed	9.7	1.5	11.1	1.4	0.8	0.3	0.6	0.2
3	Egede G	9.5	2.6	11.0	1.6	1.2	1.0	1.1	0.6
4	Unnamed	9.5	1.7	10.4	1.7	0.8	0.4	0.9	0.4
5	Unnamed	2.8	1.8	4.3	2.3	0.4	0.2	0.4	0.1
6	Unnamed	6.3	2.3	9.0	2.4	0.9	0.3	1.0	2.2
7	Firmicus E	4.4	1.3	5.8	5.0	1.1	0.2	1.5	0.8
8	Firmicus C	3.1	1.3	5.7	4.7	1.0	0.2	1.4	0.8
9	Unnamed	5.0	1.3	6.9	2.7	1.3	0.2	1.5	0.3
10	Unnamed	3.9	1.0	3.6	0.9	0.8	0.1	0.8	0.1
11	Dubyago V	5.8	2.4	5.2	2.5	1.3	0.3	1.5	2.3
12	Unnamed	3.8	0.9	9.1	2.6	1.3	0.3	1.7	0.3
13	Unnamed	11.3	2.5	12.5	2.6	2.8	0.6	2.6	0.5
14	Apollonius N	1.7	1.4	3.9	2.8	0.7	0.2	0.9	0.3
15	Rhaeticus A	6.6	1.2	7.1	1.2	0.9	0.2	0.9	0.2
16	Unnamed	5.6	1.1	7.6	2.9	1.4	0.2	1.7	0.5
17	Unnamed	1.9	1.6	0.9	0.7	0.5	0.2	0.4	0.1
18	Unnamed	3.1	1.4	0.5	1.8	0.5	0.1	0.4	0.2
19	Unnamed	14.0	0.8	13.5	1.4	3.2	0.6	3.2	0.6
20	Unnamed	4.5	1.1	3.2	0.9	0.7	0.2	0.7	0.1
21	Unnamed	9.3	1.1	8.1	1.6	1.9	0.4	1.7	0.5
22	Unnamed	0.6	0.5	0.5	0.4	0.4	0.1	0.4	0.1
23	Unnamed	2.6	1.3	1.7	1.1	0.6	0.1	0.5	0.1
24	Bell E	4.6	1.7	3.1	1.5	0.6	0.2	0.5	0.1
25	Dirichlet E	2.0	1.1	0.7	0.9	0.4	0.1	0.5	0.1
26	Unnamed	4.6	1.1	5.0	2.9	0.2	0.1	0.3	0.6

27	Unnamed	8.9	1.0	9.3	1.3	0.7	0.2	0.6	0.2
28	Unnamed	9.1	0.7	9.4	2.0	0.7	0.2	0.8	0.8
29	Unnamed	12.0	0.9	13.0	0.8	0.5	0.2	0.4	0.2
30	Repsold A	4.7	3.3	5.4	1.9	0.5	0.3	0.5	0.4
31	Unnamed	9.3	1.4	11.3	1.5	1.3	0.5	1.7	0.6
32	Unnamed	11.3	1.0	11.9	1.8	1.2	0.4	1.5	1.6
33	Louville DA	14.0	0.9	14.0	1.8	1.6	0.6	2.2	1.0
34	Unnamed	13.6	0.7	12.9	1.5	1.3	0.2	1.4	0.8
35	Unnamed	12.8	1.2	13.8	0.6	1.0	0.2	0.9	0.2
36	Louville A	9.7	1.3	9.8	1.2	1.2	0.4	1.2	0.4
37	Unnamed	8.7	1.3	8.4	1.2	1.0	0.4	1.0	0.3
38	Unnamed	7.3	1.2	7.0	1.0	0.9	0.3	0.8	0.2
39	Unnamed	13.1	1.4	15.8	1.2	3.0	0.9	3.5	0.6
40	Gruithuisen K	12.8	0.9	14.4	1.2	1.4	0.4	1.6	0.3
41	Unnamed	12.2	1.8	14.3	2.8	2.6	0.8	3.5	1.5
42	Unnamed	11.5	1.1	10.6	3.7	2.2	0.5	2.0	1.1
43	Unnamed	5.2	1.1	6.2	2.6	0.8	0.2	1.0	0.5
44	Unnamed	14.5	1.0	16.6	0.9	3.4	0.6	4.9	0.8
45	MacMillan	11.4	0.9	13.1	1.6	3.0	0.4	3.3	0.9
46	Unnamed	11.3	0.7	10.0	1.5	2.1	0.5	1.7	0.4
47	Unnamed	1.7	1.0	1.7	1.6	0.5	0.1	0.5	0.1
48	Krafft K	14.9	0.8	14.2	0.9	3.4	0.5	3.7	0.7
49	Cavalerius E	7.7	0.8	7.7	0.9	1.1	0.2	1.1	0.2
50	Schlüter X	1.7	0.9	1.6	1.1	0.5	0.1	0.6	0.1
51	Unnamed	13.3	1.0	14.1	1.8	4.5	0.6	5.3	1.3
52	Leakey	9.4	0.4	10.3	0.8	1.3	0.2	1.6	0.3
53	Crozier H	9.2	0.7	10.9	1.2	1.3	0.2	1.1	0.2
54	Unnamed	8.4	0.7	9.2	1.8	1.3	0.2	1.3	0.3
55	Colombo B	8.3	0.7	8.7	1.6	0.9	0.1	1.1	0.3
56	Unnamed	8.2	0.6	8.9	0.9	1.0	0.2	1.1	0.2
57	Unnamed	7.1	0.8	6.5	1.2	1.0	0.2	0.9	0.2

58	Fracastorius E	4.1	1.5	6.3	1.5	0.7	0.2	0.9	0.3
59	Unnamed	3.0	1.2	2.6	1.2	0.5	0.1	0.4	0.1
60	Pontanus E	5.4	0.8	6.0	0.8	0.6	0.1	0.6	0.1
61	Unnamed	10.0	1.0	9.8	1.4	0.9	0.2	1.0	0.2
62	Unnamed	7.4	1.1	8.5	1.8	0.9	0.2	1.0	0.2
63	Unnamed	7.3	1.2	8.5	1.1	0.8	0.2	0.7	0.1
64	Maurolycus M	6.2	1.1	6.4	1.1	0.5	0.2	0.6	0.2
65	Unnamed	7.3	1.6	8.9	2.0	0.7	0.2	0.8	0.2
66	Unnamed								
67	Unnamed								
68	Unnamed	13.5	0.5	13.4	0.8	1.2	0.2	1.1	0.3
69	Unnamed	12.4	0.5	12.9	0.6	1.0	0.2	1.0	0.2
70	Unnamed	12.1	1.1	13.0	1.4	1.2	0.3	1.2	0.6
71	Unnamed	12.3	1.3	11.4	1.8	1.0	0.3	1.0	0.5
72	Unnamed	13.6	0.6	13.3	0.5	1.3	0.3	1.2	0.4
73	Unnamed	11.0	1.5	11.1	1.2	1.7	0.3	1.7	0.4
74	Unnamed	6.4	0.5	6.4	0.6	0.7	0.1	0.6	0.1
75	Unnamed	4.0	0.6	3.7	0.8	0.4	0.1	0.4	0.1
76	Unnamed	5.8	0.6	5.7	0.8	0.6	0.1	0.6	0.1
77	Unnamed	8.6	0.6	12.3	1.1	1.2	0.3	1.5	0.2
78	Unnamed	5.2	1.0	9.0	3.6	0.6	0.1	1.1	0.5
79	Unnamed	4.8	1.1	6.7	3.2	0.5	0.1	0.7	0.3
80	Unnamed	5.8	0.7	5.6	0.9	0.5	0.1	0.5	0.1
81	Barbier F	8.7	0.8	8.6	1.1	0.7	0.2	0.8	0.2
82	Unnamed	5.2	0.8	5.0	0.9	0.8	0.2	0.7	0.2
83	Unnamed	8.3	1.6	8.7	2.0	1.4	0.4	1.3	0.5
84	Unnamed	11.9	0.8	10.9	1.2	1.3	0.3	1.2	0.3
85	Unnamed	4.9	1.5	5.9	1.0	0.6	0.2	0.6	0.2
86	Unnamed	7.0	1.1	6.2	1.3	0.6	0.2	0.6	0.1
87	Unnamed	6.1	1.1	6.3	1.6	0.5	0.1	0.5	0.2
88	Unnamed	9.7	0.7	9.4	1.4	0.8	0.2	0.8	0.4

89	Unnamed	4.8	1.3	5.4	2.3	0.5	0.1	0.5	0.3
90	Unnamed	9.4	4.9	11.2	1.9	2.0	2.1	1.1	0.4
91	Unnamed	7.5	1.6	8.3	1.0	0.4	0.2	0.6	0.1
92	Unnamed	14.7	1.7	14.4	0.9	1.7	0.5	1.8	0.5
93	Unnamed	12.8	0.8	12.9	1.0	0.8	0.3	1.0	0.5
94	Unnamed	14.5	0.8	13.8	0.8	1.1	0.4	1.0	0.3
95	Unnamed	16.5	0.5	15.7	0.4	4.2	0.5	3.5	0.8
96	Gambart J	13.1	0.5	12.1	0.8	2.5	0.2	2.4	0.3
97	Damoiseau D	4.2	1.2	6.6	1.3	0.6	0.1	0.7	0.2
98	Damoiseau BA	11.0	1.1	12.5	0.9	2.1	0.3	2.5	0.4
99	Crüger F	6.4	0.5	10.2	2.1	0.7	0.1	1.2	0.3
100	Mersenius M	7.2	0.9	8.1	0.7	0.8	0.2	0.7	0.2
101	Kopff C	2.2	0.9	3.0	1.7	0.4	0.1	0.5	0.2
102	Lamarck B	4.0	1.0	5.4	0.9	0.6	0.1	0.6	0.1
103	Doppelmayer V	7.3	1.4	7.1	1.3	0.9	0.3	0.8	0.3
104	Unnamed	14.1	0.4	15.0	0.5	2.6	0.5	2.6	0.5
105	Marth	8.9	1.7	14.7	1.2	2.4	0.8	4.8	0.8
106	Hesiodus A	9.7	1.3	11.4	1.5	1.1	0.4	1.6	0.6
107	Unnamed	7.3	1.2	8.6	1.3	0.8	0.2	0.9	0.3
108	Lagrange T	7.5	1.2	7.3	1.2	0.7	0.2	0.8	0.3
109	Unnamed	7.0	4.2	5.7	4.2	1.3	2.1	1.0	2.3
110	Petermann B	4.4	3.6	3.9	3.3	1.2	3.4	0.6	1.4
111	Unnamed	11.6	1.4	11.0	1.6	0.6	0.4	0.5	0.3
112	Unnamed	12.9	1.1	12.9	2.2	1.0	0.5	1.1	0.9
113	Unnamed	8.8	0.6	9.8	0.7	1.0	0.2	1.0	0.2
114	Unnamed					1.0	0.2	0.8	0.2

Table C.3: The Degree of Freshness and Age of Concentric Craters

	Age			
	Name	Degradation	Corrected	Age (Ga)
1	Archytas G	4.8	4.8	3.8
2	Unnamed	4.1	4.4	3.8
3	Egede G	3.8	4.0	3.9
4	Unnamed	2.8	3.2	4.0
5	Unnamed	4.7	4.8	3.8
6	Unnamed	4.7	4.8	3.8
7	Firmicus E	4.1	4.1	3.9
8	Firmicus C	4.5	4.5	3.8
9	Unnamed	3.1	3.1	4.0
10	Unnamed	3.5	3.5	3.9
11	Dubyago V	3.8	3.8	3.9
12	Unnamed	4.2	4.4	3.8
13	Unnamed	3.9	4.1	3.9
14	Apollonius N	4.5	4.5	3.8
15	Rhaeticus A	5.4	5.4	3.0
16	Unnamed	2.5	2.5	4.0
17	Unnamed	4.5	4.6	3.8
18	Unnamed	4.9	4.9	3.8
19	Unnamed	5.3	5.3	3.2
20	Unnamed	4.9	4.9	3.8
21	Unnamed	5.6	5.6	2.6
22	Unnamed	4.8	4.8	3.8
23	Unnamed	5.5	5.5	2.8
24	Bell E	4.9	4.9	3.8
25	Dirichlet E	4.9	4.9	3.8
26	Unnamed	2.2	3.6	3.9
27	Unnamed	4.1	4.3	3.9
28	Unnamed	4.6	4.7	3.8
29	Unnamed	4.3	4.4	3.8
30	Repsold A	4.8	4.8	3.8
31	Unnamed	4.0	4.2	3.9
32	Unnamed	4.1	4.4	3.8
33	Louville DA	5.1	5.1	3.6
34	Unnamed	4.2	4.3	3.9
35	Unnamed	4.5	4.6	3.8
36	Louville A	4.0	4.0	3.9
37	Unnamed	4.1	4.3	3.9
38	Unnamed	4.0	4.2	3.9
39	Unnamed	4.9	5.5	2.8

40	Gruithuisen K	4.4	4.5	3.8
41	Unnamed	4.8	4.9	3.8
42	Unnamed	4.8	4.9	3.8
43	Unnamed	4.5	4.6	3.8
44	Unnamed	4.0	4.2	3.9
45	MacMillan	4.8	4.9	3.8
46	Unnamed	4.5	4.6	3.8
47	Unnamed	4.0	4.0	3.9
48	Krafft K	4.8	4.8	3.8
49	Cavalerius E	4.4	4.4	3.8
50	Schlüter X	5.1	5.1	3.6
51	Unnamed	4.5	4.7	3.8
52	Leakey	5.3	5.3	3.2
53	Crozier H	4.2	4.2	3.9
54	Unnamed	3.8	3.8	3.9
55	Colombo B	4.5	4.5	3.8
56	Unnamed	4.6	4.6	3.8
57	Unnamed	3.6	3.6	3.9
58	Fracastorius E	4.0	4.0	3.9
59	Unnamed	5.1	5.1	3.6
60	Pontanus E	3.4	3.4	3.9
61	Unnamed	4.0	4.2	3.9
62	Unnamed	3.8	4.2	3.9
63	Unnamed	3.9	4.4	3.8
64	Maurolycus M	4.1	4.1	3.9
65	Unnamed	4.2	4.3	3.9
66	Unnamed	4.6	4.6	3.8
67	Unnamed	4.5	4.7	3.8
68	Unnamed	4.7	4.9	3.8
69	Unnamed	4.6	5.0	3.8
70	Unnamed	4.2	5.0	3.8
71	Unnamed	3.8	4.8	3.8
72	Unnamed	4.2	5.6	2.7
73	Unnamed	5.5	5.5	2.8
74	Unnamed	3.5	3.5	3.9
75	Unnamed	3.7	3.7	3.9
76	Unnamed	4.8	4.8	3.8
77	Unnamed	4.5	5.2	3.3
78	Unnamed	3.9	4.1	3.9
79	Unnamed	3.8	4.1	3.9
80	Unnamed	3.7	3.7	3.9
81	Barbier F	4.5	4.5	3.8
82	Unnamed	4.8	5.3	3.1

83	Unnamed	4.5	4.6	3.8
84	Unnamed	4.6	4.7	3.8
85	Unnamed	3.8	4.1	3.9
86	Unnamed	4.2	4.3	3.9
87	Unnamed	3.8	3.8	3.9
88	Unnamed	4.9	4.9	3.8
89	Unnamed	2.5	2.5	4.0
90	Unnamed	4.9	4.9	3.8
91	Unnamed	5.5	5.5	2.8
92	Unnamed	5.5	5.5	2.8
93	Unnamed	4.4	4.6	3.8
94	Unnamed	4.7	4.7	3.8
95	Unnamed	4.9	5.8	2.2
96	Gambart J	4.9	4.9	3.8
97	Damoiseau D	5.4	5.4	3.0
98	Damoiseau BA	5.5	5.5	2.8
99	Crüger F	3.8	4.0	3.9
100	Mersenius M	5.5	5.5	2.8
101	Kopff C	5.3	5.3	3.2
102	Lamarck B	5.2	5.3	3.3
103	Doppelmayer V	4.2	4.3	3.9
104	Unnamed	4.4	4.9	3.8
105	Marth	4.8	4.8	3.8
106	Hesiodus A	5.2	5.2	3.4
107	Unnamed	4.5	4.5	3.8
108	Lagrange T	4.8	4.8	3.8
109	Unnamed	2.5	2.5	4.0
110	Petermann B	4.8	4.8	3.8
111	Unnamed	4.8	4.8	3.8
112	Unnamed	5.0	5.0	3.8
113	Unnamed	3.9	4.3	3.9
114	Unnamed	4.0	5.2	3.4

APPENDIX D

PROPERTIES OF LOCALIZED PYROCLASTIC DEPOSITS

Table D.1: Location and Geometrical Properties of Localized Pyroclastic Deposits

Geometrical Properties and Volume Analysis

Pyroclastic	Latitude	Longitude	Vent Geometry	Pyroclastic Area [km^2]	Vent Area [km^2]
Alphonsus W1	-13.6	-4.1	Elliptical	60.4	4.2
Alphonsus C	-13.8	-3.4	Elliptical	18.3	1.5
Alphonsus SE	-14.4	-1.9	Elliptical	85.8	5.5
Alphonsus NE1	-12.9	-1.6	Elliptical	61.6	4.1
Alphonsus NE2	-12.6	-1.7	Elliptical	15.2	2.1
Alphonsus NE3	-12.5	-2.0	Elliptical	33.8	3.4
Alphonsus E	-13.5	-1.5	Elliptical	9.5	1.6
Alphonsus W2	-13.7	-4.2	Elliptical	44.6	4.0
Apollo	-29.5	-153.0	Elliptical	49.0	4.8
Birt E N	-20.4	-10.0	Elliptical	99.1	6.8
Birt E S	-20.7	-9.7	Elliptical	309.8	14.6
Compton W	54.1	105.4	Elliptical	35.0	7.5
Compton E	54.3	106.0	Elliptical	43.5	5.6
Frigoris W	49.8	27.4	Linear	354.3	83.7
Frigoris E	50.3	34.4	Linear	421.0	43.1
Gauss W	35.8	76.7	Elliptical	123.8	5.2
Gauss S	34.3	78.9	Elliptical	151.5	5.1
Gauss E	36.3	81.4	Elliptical	122.5	18.4
Grimaldi	-0.8	-65.3	Linear	229.7	27.4
J. Herschel N	62.5	-38.3	Elliptical	891.3	57.0
J. Herschel C	61.7	-37.2	Elliptical	788.6	78.8
J. Herschel S	61.3	-37.2	Elliptical	198.4	30.1
Lavoisier W	38.4	-82.0	Linear	54.3	16.4
Lavoisier NW	38.7	-81.6	Linear	19.9	8.4
Lavoisier F	37.0	-81.0	Linear	81.6	21.8
Lavoisier H	37.9	-78.7	Linear	51.7	28.4
Mersenius N	-21.0	-50.1		12.1	
Mersenius W	-21.4	-50.2		8.2	
Mersenius S	-21.9	-50.2	Linear	16.2	1.4
Messala N	40.4	59.4	Elliptical	62.0	8.9
Messala S	40.2	59.5	Elliptical	72.6	15.1
Oppenheimer N	-33.6	-165.5	Elliptical	64.0	7.2
Oppenheimer E	-35.3	-163.3	Elliptical	38.5	6.4
Oppenheimer S	-37.1	-164.6	Elliptical	37.8	4.6

Volume Analysis

Pyroclastic	Crater Volume (WAC) [m^3]	Crater Volume (TC) [m^3]	Pyroclastic Volume (WAC) [m^3]	Pyroclastic Volume (TC) [m^3]	Juvenile Volume (WAC) [m^3]	Juvenile Volume (TC) [m^3]	Juvenile (WAC) [vol.%]	Juvenile (TC) [vol.%]
Alphonsus W1	3.29E+08	4.19E+08	7.79E+08	1.09E+09	4.50E+08	6.74E+08	58	62
Alphonsus C	2.59E+07	9.31E+07	4.64E+07	1.58E+08	2.05E+07	6.49E+07	44	41
Alphonsus SE	4.30E+08	6.12E+08	8.56E+08	1.22E+09	4.26E+08	6.10E+08	50	50
Alphonsus NE1	2.80E+08	4.20E+08	7.08E+08	6.69E+08	4.28E+08	2.49E+08	60	37
Alphonsus NE2	7.62E+07	1.42E+08	1.50E+08	9.52E+07	7.38E+07	-4.66E+07	49	
Alphonsus NE3	1.43E+08	2.83E+08	2.99E+08	5.08E+08	1.56E+08	2.25E+08	52	44
Alphonsus E	3.59E+07	1.17E+08	2.85E+06	4.14E+07	-3.31E+07	-7.57E+07		
Alphonsus W2	2.84E+08	3.71E+08	9.01E+08	1.04E+09	6.17E+08	6.74E+08	69	64
Apollo	1.61E+08	4.12E+08	5.03E+08	7.63E+08	3.42E+08	3.51E+08	68	46
Birt E N	1.60E+08	3.58E+08	1.16E+09	9.52E+08	7.98E+08	5.94E+08	69	62
Birt E S	2.79E+09	3.27E+09	8.13E+09	9.06E+09	4.86E+09	5.79E+09	60	64
Compton W	9.30E+07		7.45E+08		6.52E+08		88	
Compton E	1.84E+08		5.30E+08		3.46E+08		65	
Frigoris W	1.66E+10		3.02E+09		-1.36E+10			
Frigoris E	8.42E+09		1.66E+09		-6.76E+09			
Gauss W	4.37E+08	6.44E+08	2.78E+09	3.46E+09	2.34E+09	2.82E+09	84	81
Gauss S	2.89E+08	3.36E+08	6.29E+08	6.51E+08	3.40E+08	3.15E+08	54	48
Gauss E	3.76E+09	4.15E+09	1.40E+09	2.47E+09	-2.36E+09	-1.68E+09		
Grimaldi	8.96E+09		6.97E+09		-1.99E+09			
J. Herschel N	1.58E+10		4.73E+10		3.15E+10		67	
J. Herschel C	2.59E+10		7.56E+10		4.97E+10		66	
J. Herschel S	2.74E+09		1.16E+09		-1.58E+09			
Lavoisier W	2.73E+08	8.19E+08	1.59E+08	4.26E+08	-1.14E+08	-3.93E+08		
Lavoisier NW	1.05E+08	2.13E+08	1.01E+07	9.33E+07	-9.51E+07	-1.20E+08		
Lavoisier F	3.67E+07	2.41E+08	1.69E+08	5.38E+08	1.32E+08	2.97E+08	78	55
Lavoisier H	1.72E+09	1.68E+09	1.22E+08	4.25E+08	-1.60E+09	-1.26E+09		
Mersenius N								
Mersenius W								
Mersenius S	2.06E+07	1.96E+07	6.33E+06	1.62E+07	-1.43E+07	-3.38E+06		
Messala N	5.26E+08	8.62E+08	4.15E+08	7.24E+08	-1.11E+08	-1.38E+08		
Messala S	6.98E+08	1.47E+09	3.05E+08	6.05E+08	-3.93E+08	-8.61E+08		
Oppenheimer N	3.24E+08	6.45E+08	1.22E+09	1.63E+09	8.96E+08	9.87E+08	73	60
Oppenheimer E	3.33E+08	5.79E+08	8.55E+07	2.01E+08	-2.48E+08	-3.78E+08		
Oppenheimer S	1.20E+08	4.13E+08	2.65E+08	5.96E+08	1.45E+08	1.83E+08	55	31

Pyroclastic Thicknesses

Pyroclastic	Mean Thickness (WAC) [m]	Mean Thickness (TC) [m]	Maximum Thickness (WAC) [m]	Maximum Thickness (TC) [m]
Alphonsus W1	21.1	26.7	106.2	90.1
Alphonsus C	5.8	13.3	21.0	52.8
Alphonsus SE	16.2	21.6	72.9	85.2
Alphonsus NE1	19.4	18.5	73.5	77.5
Alphonsus NE2	13.2	10.9	42.1	43.7
Alphonsus NE3	11.9	21.1	38.3	65.0
Alphonsus E	1.3	8.0	4.0	34.3
Alphonsus W2	29.9	35.1	119.1	110.5
Apollo	18.4	28.6	51.1	114.2
Birt E N	16.9	20.0	106.7	124.6
Birt E S	34.0	38.4	152.7	180.4
Compton W	19.7		86.7	
Compton E	19.1		63.8	
Frigoris W	31.1		153.5	
Frigoris E	8.2		47.2	
Gauss W	34.1	40.0	125.7	149.9
Gauss S	15.0	25.6	88.7	127.6
Gauss E	45.4	49.2	174.6	194.5
Grimaldi	57.2		336.9	
J. Herschel N	82.1		257.7	
J. Herschel C	142.5		641.4	
J. Herschel S	22.3		90.2	
Lavoisier W	9.6	21.2	39.9	94.7
Lavoisier NW	2.4	12.4	8.3	66.8
Lavoisier F	7.0	17.6	32.2	67.9
Lavoisier H	7.2	15.5	26.6	72.2
Mersenius N				
Mersenius W				
Mersenius S	11.7	10.0	47.5	68.4
Messala N	14.6	26.3	49.7	121.0
Messala S	10.5	18.4	56.2	115.4
Oppenheimer N	22.7	34.0	84.2	164.3
Oppenheimer E	9.0	12.9	38.5	63.4
Oppenheimer S	11.4	24.8	44.4	109.8

Table D.2: Physical Properties of Localized Pyroclastic Deposits

Physical Properties										
Pyroclastic	CPR	CPR Std. Dev.	H [m]	H Std. Dev. [m]	Regional H [m]	Regional H Std. Dev [m]	ΔH [m]	ΔH Std. Dev. [m]	Rock Abund. [%]	Rock Abund Std. Dev. [%]
Alphonsus W1	0.48	0.14	0.088	0.006	0.081	0.022	0.006	0.023	0.24	0.11
Alphonsus C	0.40	0.11	0.092	0.027			0.011	0.035	0.31	0.06
Alphonsus SE	0.39	0.11	0.089	0.008			0.007	0.023	0.29	0.10
Alphonsus NE1	0.40	0.11	0.087	0.006			0.006	0.023	0.36	0.10
Alphonsus NE2	0.40	0.11	0.084	0.006			0.002	0.023	0.36	0.07
Alphonsus NE3	0.40	0.11	0.080	0.007			-0.001	0.023	0.27	0.10
Alphonsus E	0.48	0.13	0.085	0.009			0.004	0.024	0.48	0.20
Alphonsus W2	0.43	0.12	0.087	0.006			0.006	0.023	0.27	0.16
Apollo	0.60	0.16	0.127	0.043	0.099	0.030	0.028	0.053	0.49	0.23
Birt E N	0.40	0.11	0.091	0.009	0.081	0.016	0.011	0.019	0.27	0.17
Birt E S	0.44	0.13	0.093	0.009			0.012	0.019	0.32	0.14
Compton W	0.62	0.19	0.076	0.008	0.093	0.049	-0.017	0.050	0.50	0.15
Compton E	0.57	0.17	0.085	0.011			-0.008	0.050	0.51	0.15
Frigoris W	0.51	0.18	0.104	0.024	0.111	0.032	-0.007	0.040	0.46	0.46
Frigoris E	0.48	0.14	0.112	0.022			0.001	0.039	0.52	0.78
Gauss W	0.50	0.14	0.085	0.005	0.086	0.020	-0.001	0.020	0.39	0.05
Gauss S	0.44	0.14	0.089	0.017			0.003	0.026	0.36	0.07
Gauss E			0.085	0.009			-0.001	0.022	0.28	0.07
Grimaldi	0.52	0.19	0.086	0.017	0.086	0.019	0.000	0.025	0.54	0.64
J. Herschel N	0.37	0.15	0.132	0.030	0.125	0.053	0.007	0.061	0.33	0.12
J. Herschel C	0.33	0.12	0.144	0.042			0.020	0.067	0.26	0.11
J. Herschel S	0.37	0.12	0.133	0.030			0.008	0.061	0.25	0.08
Lavoisier W			0.085	0.010	0.096	0.018	-0.011	0.020	0.45	0.14
Lavoisier NW			0.093	0.008			-0.003	0.019	0.39	0.07
Lavoisier F			0.101	0.010			0.006	0.020	0.37	0.09
Lavoisier H			0.090	0.011			-0.006	0.021	0.40	0.09

Mersenius N	0.38	0.10	0.091	0.008	0.088	0.025	0.003	0.026	0.49	0.06
Mersenius W	0.37	0.12	0.071	0.007			-0.017	0.026	0.48	0.16
Mersenius S	0.40	0.13	0.083	0.008			-0.005	0.026	0.45	0.10
Messala N	0.39	0.11	0.106	0.015	0.096	0.032	0.010	0.036	0.33	0.09
Messala S	0.42	0.12	0.103	0.013			0.007	0.035	0.36	0.09
Oppenheimer N	0.56	0.15	0.095	0.010	0.091	0.025	0.004	0.027	0.33	0.08
Oppenheimer E	0.54	0.14	0.082	0.007			-0.009	0.026	0.30	0.06
Oppenheimer S	0.52	0.14	0.087	0.008			-0.003	0.026	0.43	0.24

Table D.3 Compositional Properties of Localized Pyroclastic Deposits

Compositional Properties

Pyroclastic	Clinopyroxene [vol.%]	Clinopyroxene Std. Dev. [vol.%]	Glass [vol.%]	Glass Std. Dev. [vol.%]	Olivine [vol.%]	Olivine Std. Dev. [vol.%]	Orthopyroxene [vol.%]	Orthopyroxene Std. Dev. [vol.%]	Plagioclase [vol.%]	Plagioclase Std. Dev. [vol.%]
Alphonsus W1	15	5	75	9	0	0	0	1	10	4
Alphonsus C	19	8	58	21	0	1	2	5	21	11
Alphonsus SE	15	5	74	10	0	0	0	2	11	4
Alphonsus NE1	13	3	76	6	0	0	0	0	10	3
Alphonsus NE2	16	6	66	13	0	0	0	0	18	7
Alphonsus NE3	16	7	68	17	0	1	1	3	15	8
Alphonsus E	16	5	65	14	0	1	0	1	19	8
Alphonsus W2	15	5	74	11	0	0	0	2	10	4
Apollo	50	4	10	5	0	0	0	1	40	5
Birt E N	18	4	77	5	0	0	0	0	5	2
Birt E S	17	4	77	6	0	0	0	0	6	2
Compton W	4	4	82	23	0	1	0	3	13	17
Compton E	7	5	64	28	0	1	1	3	28	23
Frigoris W	35	12	33	23	0	1	1	3	32	12
Frigoris E	37	10	27	22	0	0	0	2	36	12

Gauss W	6	4	83	17	0	1	0	1	11	12
Gauss S	10	8	73	23	0	2	0	1	16	15
Gauss E	10	8	56	40	2	3	0	0	32	30
Grimaldi	20	8	71	12	0	0	0	0	9	4
J. Herschel N										
J. Herschel C										
J. Herschel S										
Lavoisier W	42	9	19	9	0	1	5	6	33	5
Lavoisier NW	47	4	2	5	0	0	0	1	51	6
Lavoisier F	35	12	48	20	0	0	2	4	15	6
Lavoisier H	52	10	18	8	0	1	5	5	25	4
Mersenius N	42	7	6	13	0	1	1	2	51	8
Mersenius W	38	6	1	5	2	3	0	0	60	4
Mersenius S	40	4	1	6	1	2	0	0	58	4
Messala N	22	9	38	24	0	1	3	5	37	15
Messala S	26	8	31	21	0	1	4	6	39	13
Oppenheimer N	20	9	69	15	0	0	0	3	11	5
Oppenheimer E	25	11	56	23	0	0	0	1	19	12
Oppenheimer S	46	11	25	17	0	0	1	2	29	8

APPENDIX E

VALIDATION OF REMOTE SENSING DATA SETS AND OTHER OBSERVATIONS OF LOCALIZED PYROCLASTIC DEPOSITS

E.1 Validation of Results

E.1.1 DTM Validation

We use the volume of the vents to check the consistency between the WAC DTM and the TC DTM (**Figure E.1**) For the largest vents (i.e., $>10^9$ m^3) the volume measurements of the two data sets agree, however, we observe a deviation between the two DTM data sets for smaller deposits (i.e., $<10^9$ m^3). These observations imply that the TC DTM volume measurements are consistently larger than the WAC DTM measurements. When we examine the WAC DTM and TC DTM data for each pyroclastic deposit, we observe that topography in the WAC DTM is smoother than the TC DTM. Thus, we infer that the interpolation and modeling technique used to derive the DTMs is the source of the differences in the volume measurements (**Figure 5.5 b,e**).

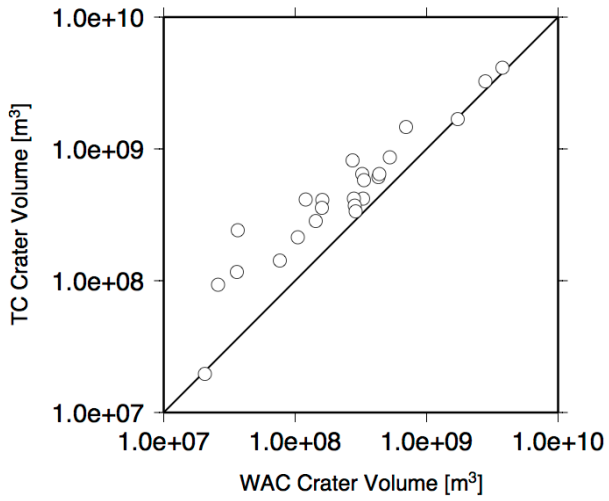

Figure E.1: Volcanic crater volume comparison between the WAC and TC DTM. The TC DTM produced larger volumes than the WAC DTM.

E.1.2 Surface Rock Abundance Validation

E.1.2.1 Radar Properties

Localized pyroclastic deposits range from 0.33–0.62 with a mean and standard deviation of 0.46 and 0.08, respectively (**Table D.2**). We also compare the CPR value of localized

pyroclastic deposits to other regions on the Moon. *Cahill et al.* [2014] used the Mini-RF 12.6 CPR data and calculated the mean CPR of the maria and highlands, which are 0.47 and 0.57, respectively. We find that most localized pyroclastic deposits display a lower CPR than the mean CPR of the maria and highlands.

Our radar observations of the Alphonsus pyroclastic deposits are consistent with previous work. *Head and Wilson* [1979] and *Coombs et al.* [1990] noted that the Alphonsus pyroclastic deposits have relatively low radar backscatter at the 3.0- and 3.8-cm wavelengths compared to the surrounding areas. This radar-dark signature is interpreted as a lack of millimeter-sized and larger rocks within the pyroclastic deposit.

The surface rock abundance and CPR data are sensitive to the same parameter, the presence of blocks. Therefore, we expect a strong correlation between the two data sets. When comparing the two data sets, we note that there is a slight positive trend (**Figure E.2a**). The relationship between the two parameters is not perfect because the CPR data are also sensitive to <1 m blocks and blocks embedded in the subsurface, whereas the surface rock abundance data is only sensitive to >1 m blocks on the surface.

We compare the mean CPR of localized pyroclastic deposits to the mean CPR and surface rock abundance of highlands and maria from *Cahill et al.* [2014] (**Figure E.2a**). We observe that localized pyroclastic deposits cluster in two areas of **Figure E.2a**, one cluster located at low surface rock abundance and low CPR and another cluster located at high surface rock abundance and high CPR. The division between the two clusters in the CPR is 0.45 and 0.4% in the surface rock abundance. In comparison, the high CPR and high surface rock abundance cluster is nearly consistent with the CPR and surface rock abundance of the maria. The cluster with low CPR and low surface rock abundance has CPR and surface rock abundance values lower than those of the maria and the highlands. Furthermore, relative values of the low CPR and low surface rock abundance cluster agree with the expected values of regional pyroclastic deposits (i.e., CPR and surface rock abundance values are lower than the maria and highlands). [i.e., *Bandfield et al.*, 2011; *Pieters et al.*, 1973; *Gaddis et al.*, 1985].

E.1.2.2 Regolith Density Properties

The mean ΔH of localized pyroclastic deposits ranges from -0.02–0.03 m with a mean of 0.00 m and a standard deviation of 0.01 m (**Table D.2**). The mean ΔH of most localized

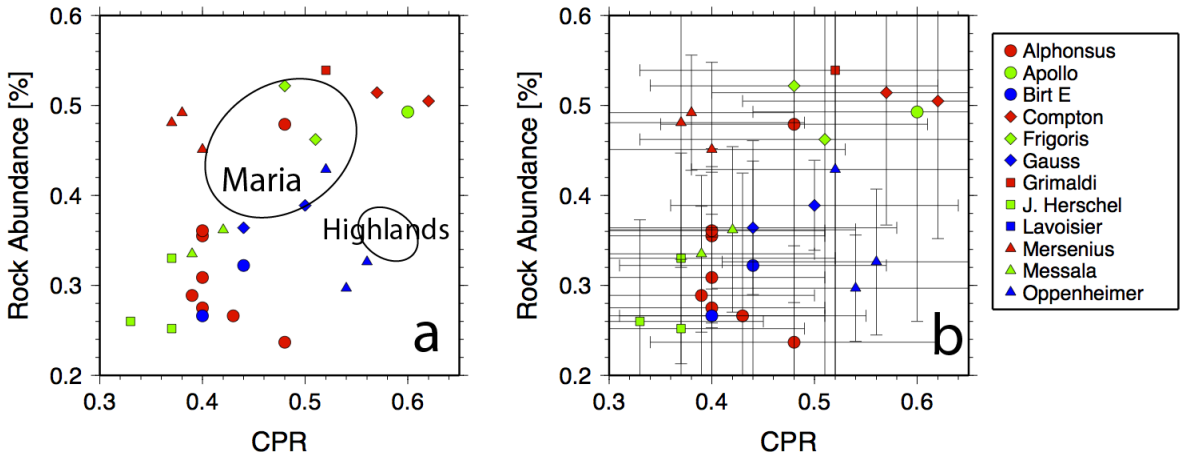

Figure E.2: a) CPR vs. rock abundance, including examples of highland and mare regions from mare regions from *Cahill et al.* [2014]. (b) This plot is the same as (a) with uncertainties.

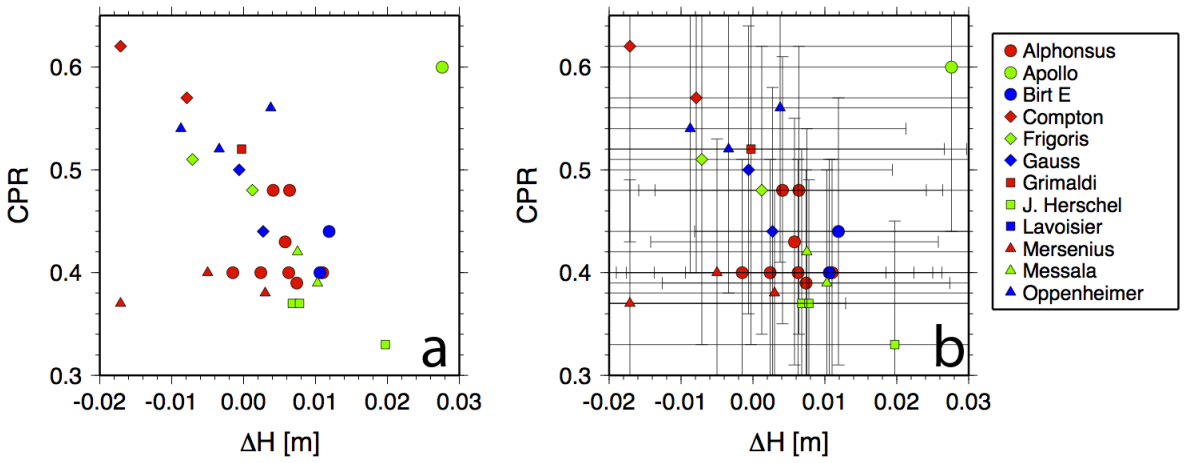

Figure E.3: Inverse relationship between CPR and ΔH.

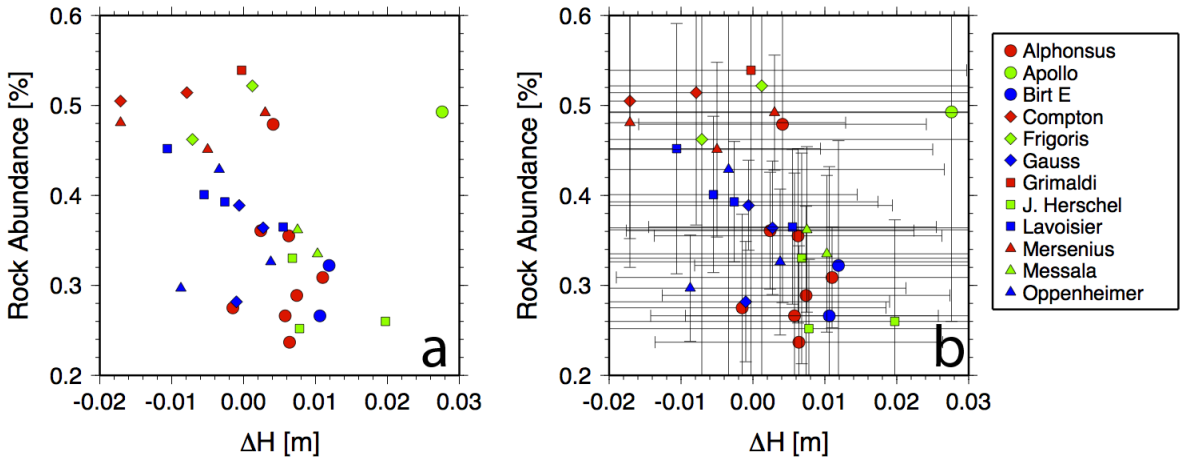

Figure E.4: Inverse relationship between rock abundance and ΔH.

pyroclastic deposit exhibits a positive ΔH value. This implies that most localized pyroclastic deposits consist of material with similar or lower density than non-volcanic regolith.

We compare the results of the mean ΔH to both the mean CPR (**Figure E.3**) and the mean surface rock abundance of the deposits (**Figure E.4**). There is an inverse correlation between ΔH to CPR and to the surface rock abundance mean values. Therefore, these observations show blocky deposits contain a high-density (positive ΔH) regolith and blockless deposits contain a low-density regolith (negative ΔH).

5.4.2 Glass Proportion Validation

We observe a relationship between the glass proportions with the maximum pyroclastic deposit thicknesses (**Figure 5.12**). From 0–60 vol.% glass, the thickness of the pyroclastic deposit is consistently ≤50 m. When the proportion of glass is >60 vol.%, the thickness of the deposits ranges from 0–300 m. Additionally, we also notice the relationships between deposit thickness with the crystalline proportions (i.e., plagioclase and pyroxene) (**Figure E.5–6**). In deposits that contain approximately >20 vol.% clinopyroxene or plagioclase tend to have maximum deposit thickness of ≤50 m, whereas around <20 vol.%, the maximum deposit thickness ranges 0–300 m. These observations sum to thin deposits consists of crystalline material and thick deposits comprises of pyroclastic glass.

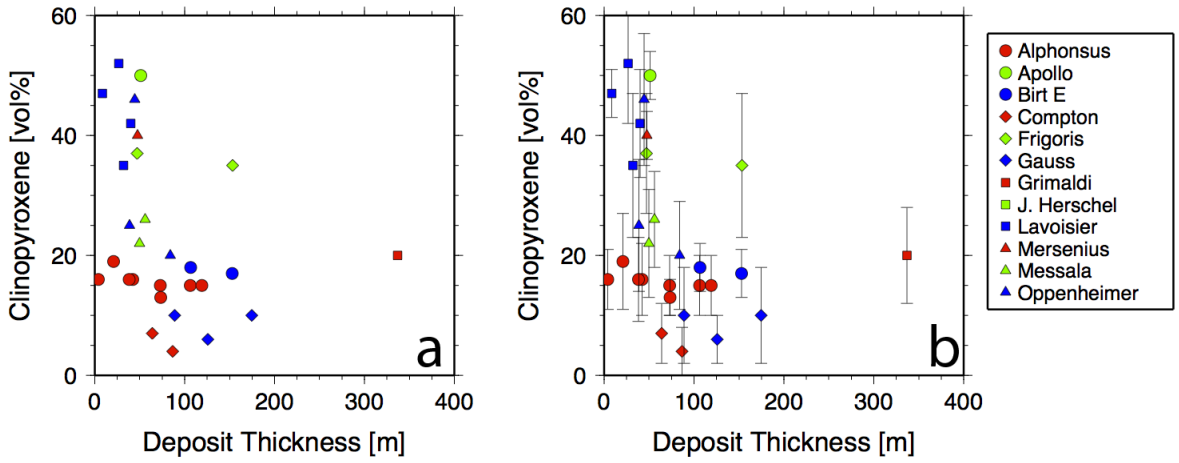

Figure E.5: Relationship between clinopyroxene and maximum deposit thickness. High clinopyroxene proportions exists in thinner deposits.

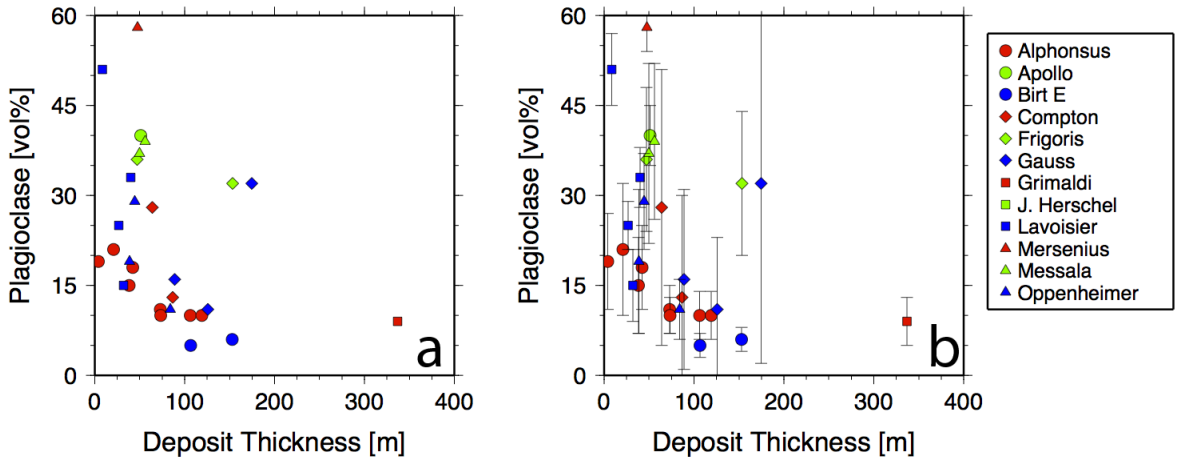

Figure E.6: Another relationship between plagioclase with maximum deposit thickness. High plagioclase proportions occur with thinner deposits.

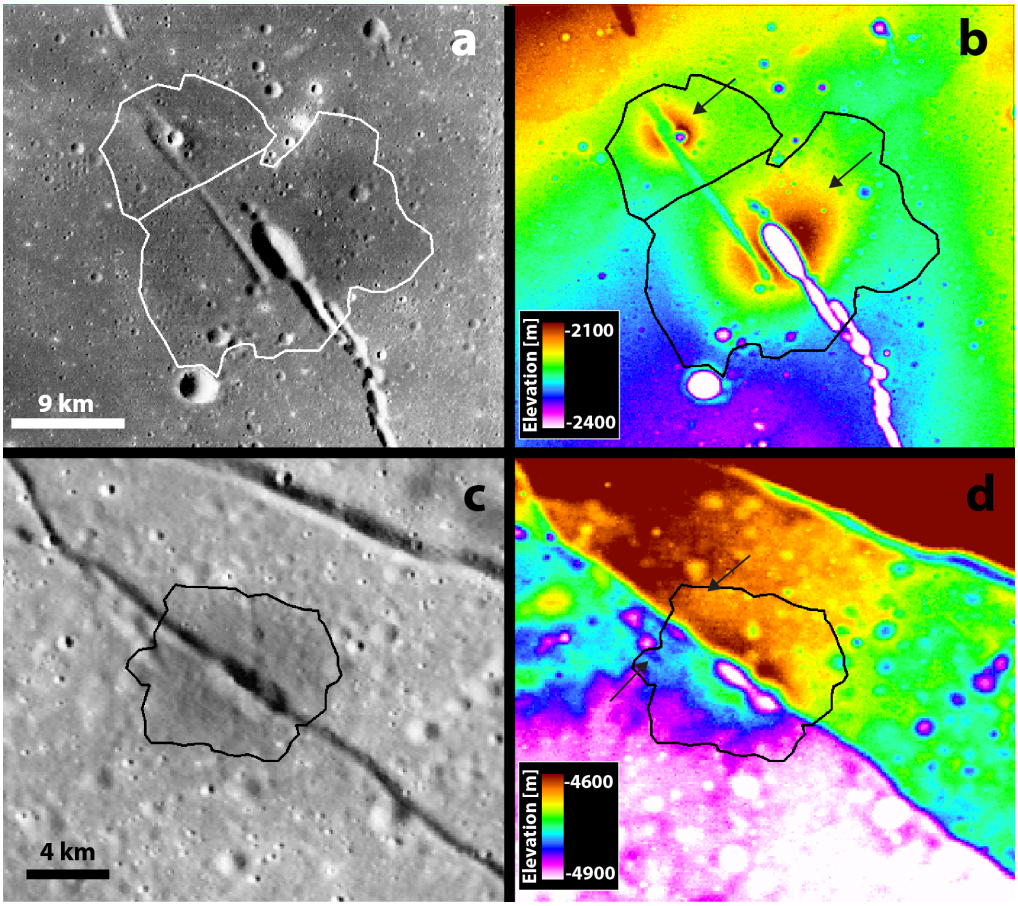

Figure E.7: a) WAC image of Birt E. The low albedo, smooth textured material within the mare is the pyroclastic deposit (outline). b) TC DTM image of Birt E, which shows the two circular topographically high features (arrows) that surround the vents. c) A WAC image of Oppenheimer N. d) A TC DTM of Oppenheimer N. Although the two sides of the rille are at different elevation, the pyroclastic deposit continued to construct a cone-like structure (arrows).

E.2 Other Observations

E.2.1 Localized Pyroclastic Deposit Structures

The high spatial-resolution WAC and TC DTM data allow an examination of the morphology of localized pyroclastic deposits. Birt E is the ideal localized pyroclastic deposit to study localized pyroclastic deposit structure because Birt E formed in the middle of the maria where the topography is flat. In the DTM of this area, we see two rilles en echelon to one another. We observe the flared portions of the rilles centered on ring-like structures (**Figure E.7a–b**). The smaller ring-like structure is associated with the most northwestern most part of the pyroclastic

deposit (Birt E N) and the larger ring-like structure to the southeast (Birt E S). These two structures are ideal to test *McGetchin and Head's* [1973] eruption model. Their model predicted that explosive volcanism on the Moon does not create cinder cones; instead, explosive volcanism build pyroclastic rings because of the lower gravity on the Moon compared to the Earth.

Other localized pyroclastic deposits exhibit a ring-like structure, but unlike Birt E, they are more obscure because other deposits occur in the highlands where the terrain is rough (**Figure E.7d**). Even in relatively flat floor-fractured craters, localized pyroclastic deposits that exist on rilles are not symmetrical because one side of the rille at a higher elevation elevation than the other. Therefore, the structure of localized pyroclastic deposits exists, but observing the structure is difficult (e.g., **Figure E.7d**).

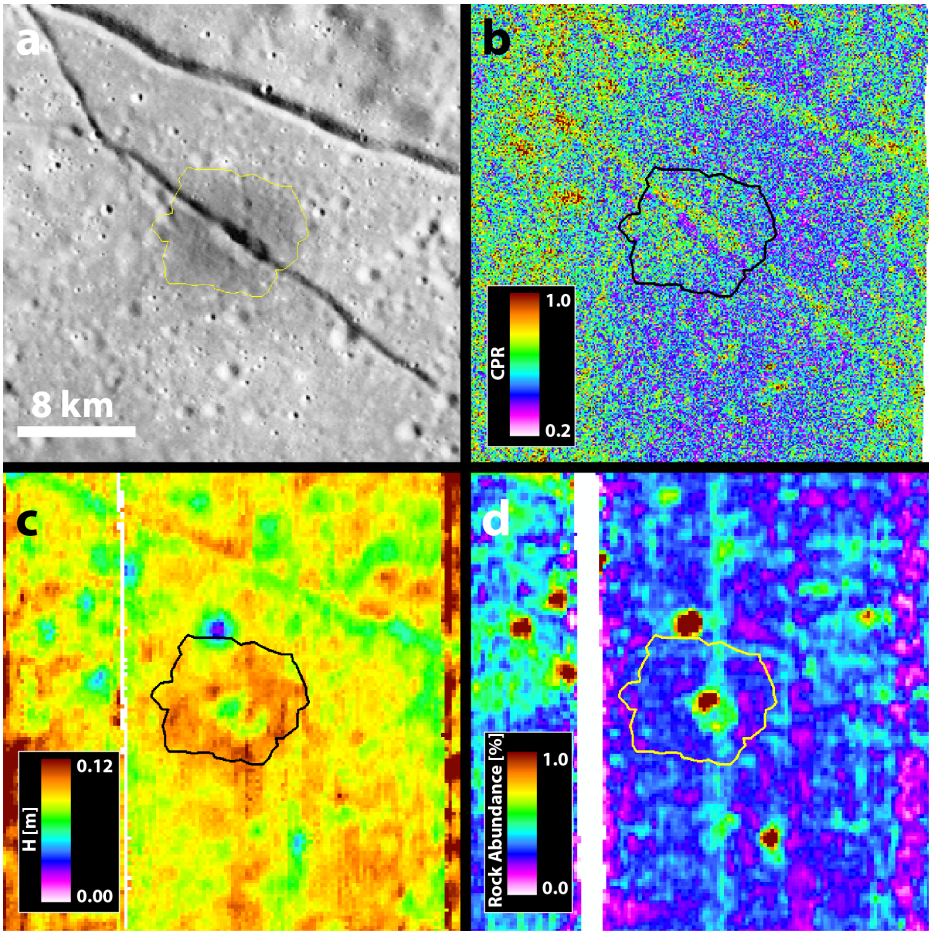

Figure E.8: a) Oppenheimer N outlined in yellow in this WAC image b) CPR image from Mini-RF c) H-parameter map from Diviner, and d) Surface rock abundance data from Diviner. These three maps (b-d) do not show any spatial variation consistent with massive fragments occurring closer to the vent and less massive fragments ejected farther from the vent.

E.2.2 Spatial Distribution of Blocks

Walker et al. [1971] modeled the distribution of fragments from a vent. In a single eruption, the distribution of fragments show that the most massive rocks are located closer to the vent, whereas the less massive rocks are farther away. We examine the CPR, surface rock abundance, and H-parameter map to determine whether this process occurred at these localized pyroclastic deposits. We do not observe any spatial patterns consistent with *Walker et al.'s* [1971] model (**Figure E.8**). If these pyroclastic deposits did exhibit any spatial patterns of blocks at one point, the pattern may have dissipated due to the disintegration of blocks and local mixing over time.

REFERENCES

Adams, J. B. (1975), Interpretation of visible and near-infrared diffuse reflectance spectra of pyroxenes and other rock forming minerals, in *Infrared and Raman Spectroscopy of Lunar and Terrestrial Materials*, edited by C. Karr, pp. 91-116, Academic, San Diego, CA.

Adams, J. B., and R. L. Jones (1970), Spectral Reflectivity of Lunar Samples, *Science*, *167*(3918), 737-739.

Adams, J. B., C. M. Pieters, and T. B. McCord (1974), Orange glass: Evidence for regional deposits of pyroclastic origin of the moon, *Proc. Lunar Conf. 5th*, *5*, 171-186.

Allen, C. C., K. L. Donaldson Hanna, C. M. Pieters, D. P. Moriarty, B. T. Greenhagen, K. A. Bennett, G. Y. Kramer, and D. A. Paige (2013), Pyroclastic Deposits in Floor-Fractured Craters-A Unique Style of Lunar Basaltic Volcanism?, *Lunar Planet. Sci. Conf. 44*, *44*, Abstract #1220.

Alzate, N., and N. G. Barlow (2011), Central pit craters on Ganymede, *Icarus*, *211*, 1274-1283, doi:10.1016/j.icarus.2010.10.015.

Andrews-Hanna, J. C., et al. (2014), Structure and evolution of the lunar Procellarum region as revealed by GRAIL gravity data, *Nature*, *514*, 68-71, doi:10.1038/nature13697.

Antonenko, I., J. W. Head, J. F. Mustard, and B. R. Hawke (1995), Criteria for the detection of lunar cryptomaria, *Earth Moon Planets*, *69*(2), 141-172.

Baker, D. M. H., J. W. Head, C. I. Fassett, S. J. Kadish, D. E. Smith, M. T. Zuber, and G. A. Neumann (2011), The transition from complex crater to peak-ring basin on the Moon: New observations from the Lunar Orbiter Laser Altimeter (LOLA) instrument, *Icarus*, *214*(2), 377-393.

Baldwin, R. B. (1968), Rille Pattern in the Lunar Crater Humboldt, *J. Geophys. Res.*, *73*(10), 3227-3229.

Bandfield, J. L., R. R. Ghent, A. R. Vasavada, D. A. Paige, S. J. Lawrence, and M. S. Robinson (2011), Lunar surface rock abundance and regolith fines temperature derived from LRO Diviner Radiometer data, *J. Geophys. Res.*, *116*, E00H02, doi:10.1029/2011JE003866.

Barlow, N. G. (2006), Impact craters in the northern hemisphere of Mars: layered ejecta and central pit characteristics, *Meteorit. Planet. Sci.*, *41*(10), 1425-1436, doi:10.1111/j.1945-5100.2006.tb00427.x.

Barlow, N. G. (2010), Central pit craters: Observations from Mars and Ganymede and implications for formation models, in *Large Meteorite Impacts and Planetary Evolution IV*, edited by R. L. Gibson and W. U. Reimold, pp. 15-27, The Geological Society of America, Inc., Boulder, CO.

Barrat, J. A., P. Gillet, M. Lesourd, J. Blichert-Toft, and G. R. Poupeau (1999), The Tatahouine diogenite: Mineralogical and chemical effects of sixty-three years of terrestrial residence, *Meteorit. Planet. Sci.*, *34*(1), 91-97.

Bart, G. D., R. D. Nickerson, M. T. Lawder, and H. J. Melosh (2011), Global survey of lunar regolith depths from LROC images, *Icarus*, *215*, 485-490, doi:10.1016/j.icarus.2011.07.017.

Basaltic Volcanism Study Project (1981), *Basaltic Volcanism on the Terrestrial Planets*, 1286 pp., Pergamon Press, Inc.,, New York.

Bell, P. M., and H. K. Mao (1972), Crystal-field effects of iron and titanium in selected grains of Apollo 12, 14, and 15 rocks, glasses, and fine fractions, *Proc. Lunar Conf. 3rd*, *3*, 545-553.

Bell, S. W., B. J. Thomson, M. D. Dyar, C. D. Neish, J. T. S. Cahill, and D. B. J. Bussey (2012), Dating small fresh lunar craters with Mini-RF radar observations of ejecta blankets, *J. Geophys. Res.*, *117*(E12), doi:10.1029/2011JE004007.

Besancon, J. R. (1981), Rate of cation disordering in orthopyroxenes, *Am. Mineral.*, *66*, 965-973.

Besse, S., J. M. Sunshine, and L. R. Gaddis (2014), Volcanic glass signatures in spectroscopic survey of newly proposed lunar pyroclastic deposits, *J. Geophys. Res.*, *119*, doi:10.1002/2013JE004537.

Birlan, M., P. Vernazza, and D. A. Nedelcu (2007), Spectral Properties of nine M-type asteroids, *Astron. Astrophys.*, *475*, 747-754, doi:10.1051/004-6361:20077914.

Birle, J. D., G. V. Gibbs, P. B. Moore, and J. V. Smith (1968), Crystal Structures of Natural Olivines, *Am. Mineral.*, *53*, 807-824.

Bland, M. T., K. N. Singer, W. B. McKinnon, and P. M. Schenk (2012), Enceladus' extreme heat flux as revealed by its relaxed craters, *Geophys. Res. Lett.*, *39*, L17204, doi:10.1029l/2012GL052736.

Boyce, J. M., and A. L. Dial (1975), Relative ages of flow units in Mare Imbrium and Sinus Iridum, *Proc. Lunar Sci. Conf. 6th*, *6*, 2585-2695.

Bray, V. J., et al. (2010), New insight into lunar impact melt mobility from the LRO camera, *Geophys. Res. Lett.*, *37*(21), L21202, doi:10.1029/2010GL044666.

Brennan, W. J. (1975), Modification of Premare Impact Craters by Volcanism and Tectonism, *The Moon*, *12*, 449-461.

Britt, D. T., and C. M. Pieters (1994), Darkening in black and gas-rich ordinary chondrites: The spectral effects of opaque morphology and distribution, *Geochim. Cosmochim. Acta*, *58*(18), 3905-3919, doi:10.1016/0016-7037(94)90370-0.

Brizi, E., G. Molin, and P. F. Zanazzi (2000), Experimental study of intracrystalline Fe2+-Mg exchange in three augite crystals: Effect of composition on geothermometric calibration, *Am. Mineral.*, *85*, 1375-1382.

Brown, G. E. (1982), Olivines and silicate spinels, in *Orthosilicates*, edited by P. H. Ribbe, Mineralogical Society of America.

Burns, R. G. (1970), *Mineralogical Applications of Crystal Field Theory*, 1st ed., 224 pp., Cambridge University Press, New York.

Burns, R. G. (1974), The polarized spectra of iron in silicates: Olivine a discussion of neglected contributions from Fe2+ ions in M(1) sites, *Am. Mineral.*, *59*, 625-629.

Burns, R. G. (1993), *Mineralogical Applications of Crystal Field Theory*, 2nd ed., 551 pp., Cambridge University Press, New York.

Burns, R. G., J. R. Besancon, and S. F. Pratt (1991), Reflectance spectra of Fe(2+)-Mg(2+) disordered pyroxenes: Implications to remote-sensed spectra of planetary surfaces *Reports of Planetary Geology and Geophysics Program N92-10823*, 253-255.

Cahill, J. T., and P. G. Lucey (2007), Radiative transfer modeling of lunar highlands spectral classes and relationship to lunar samples, *J. Geophys. Res.*, *112*, E10007, doi:10.1029/2006JE002868.

Cahill, J. T. S., P. G. Lucey, K. R. Stockstill-Cahill, and B. R. Hawke (2010), Radiative transfer modeling of near-infrared reflectance of lunar highland and mare soil, *J. Geophys. Res.*, *115*, E12013, doi:10.1029/2009JE003500.

Cahill, J. T. S., P. G. Lucey, and M. A. Wieczorek (2009), Compositional variations of the lunar crust: Results from radiative transfer modeling of central peak spectra, *J. Geophys. Res.*, *114*, E09001, doi:10.1029/2008JE003282.

Cahill, J. T. S., et al. (2014), The Miniature Radio Frequency Instrument's (Mini-RF) Global Observations of Earth's Moon, *Icarus*, *In Press*, doi:10.1016/j.icarus.2014.07.018.

Cameron, W. S., and J. L. Padgett (1974), Possible Lunar Ring Dikes, *The Moon*, *9*, 249-294.

Campbell, B. A., L. M. Carter, B. R. Hawke, D. B. Campbell, and R. R. Ghent (2008), Volcanic and impact deposits of the Moon's Aristarchus Plateau: A new view from Earth-based radar images, *Geol.*, *36*(2), 135-138, doi:10.1130/G24310A.1.

Campbell, B. A., B. R. Hawke, G. A. Morgan, L. M. Carter, D. B. Campbell, and M. Nolan (2014), Improved discrimination of volcanic complexes, tectonic features, and regolith properties in Mare Serenitatis from Earth-based radar mapping, *J. Geophys. Res.*, *119*, 313-330, doi:10.1002/2013JE004486.

Campins, H., and E. V. Ryan (1989), The identification of crystalline olivine in cometary silicates, *Astrophys. J.*, *341*, 1059-1066.

Carter, L. M., B. A. Campbell, B. R. Hawke, D. B. Compbell, and M. C. Nolan (2009), Radar remote sensing of pyroclastic deposits in the southern Mare Serenitatis and Mare Vaporum regions of the Moon, *J. Geophys. Res.*, *114*, E11004, doi:10.1029/2009JE003406.

Carter, L. M., C. D. Neish, D. B. J. Bussey, P. D. Spudis, G. W. Patterson, J. T. Cahill, and R. K. Raney (2012), Initial observations of lunar impact melts and ejecta flows with the Mini-RF radar, *J. Geophys. Res.*, *117*, E00H09, doi:10.1029/2011JE003911.

Cintala, M. J., C. A. Wood, and J. W. Head (1977), The effects of target characteristics on fresh crater morphology: Preliminary results for the moon and Mercury, *Proc. Lunar Planet. Sci. Conf. 8th*, *8*, 3409-3425.

Clark, B. E., et al. (2001), Space weathering on Eros: Constraints from albedo and spectral measurements of Psyche crater, *Metorit. Planet. Sci.*, *36*, 1617-1637.

Clark, R. N. (1999), Spectroscopy of rocks and minerals, and principles of spectroscopy, in *Manual of Remote Sensing*, edited by A. N. Rencz, pp. 3-58, John Wiley, Hoboken, N.J.

Clark, R. N., G. A. Swayze, R. Wise, E. Livo, T. Hoefen, R. Kokaly, and S. J. Sutley (2007), USGS digital spectral library splib06a: U.S. Geological Survey, Digital Data Series 231.

Cloutis, E. A. (1985), Interpretive techniques for reflectance spectra of mafic silicates, M.S. thesis, University of Hawai‘i, Honolulu, Hawai‘i.

Cloutis, E. A. (1997), Manganese-rich olivines: Identification from spectral reflectance properties, *J. Geophys. Res.*, *102*(E11), 25,575-525,580.

Cloutis, E. A., and M. J. Gaffey (1991), Pyroxene Spectroscopy Revisited: Spectral-Compositional Correlations and Relationship to Geothermometry, *J. Geophys. Res.*, *96*(E5), 22,809-822,826.

Cloutis, E. A., M. J. Gaffey, T. L. Jackowski, and K. L. Reed (1986), Calibrations of phase abundance, composition, and particle size for olivine-orthopyroxene mixtures from reflectance spectra, *J. Geophys. Res.*, *91*, 11,641-611,653.

Cloutis, E. A., M. J. Gaffey, D. G. W. Smith, and R. S. J. Lambert (1990a), Metal silicate mixtures: Spectral properties and applications to asteroid taxonomy, *J. Geophys. Res.*, *95*, 8323-8338.

Cloutis, E. A., M. J. Gaffey, D. G. W. Smith, and R. S. J. Lambert (1990b), Reflectance spectra of mafic silicate-opaque assemblages with applications to meteorite spectra, *Icarus*, *84*, 315-333.

Collins, G. S., H. J. Melosh, J. V. Morgan, and M. R. Warner (2002), Hydrocode Simulations of Chicxulub Crater Collapse and Peak-Ring Formation, *Icarus*, *157*(1), 24-33, doi:10.1006/icar.2002.6822.

Coombs, C. R., B. R. Hawke, P. G. Lucey, P. D. Owensby, and S. H. Zisk (1990), The Alphonsus Region: A Geologic and Remote-Sensing Perspective, *Proc. Lunar and Planet. Sci. Conf. 20th*, *20*, 161-174.

Crater Analysis Techniques Working Group (1979), Standard Techniques for Presentation and Analysis of Crater Size-Frequency Data, *Icarus*, *37*, 467-474.

Croft, S. K. (1981), On the origin of pit craters, *Lunar and Planetary Science Conference XII*, *12*, 196-198.

Croft, S. K. (1983), A Proposed Origin for Palimpsests and Anomalous Pit Craters on Ganymede and Callisto, *Proc. Lunar Planet. Sci. Conf. 14th*, *14*, B71-B89.

Daneš, Z. F. (1965), Rebound processes in large craters, in *Astrogeologic Studies, Annu. Prog. Rep. A*, edited, pp. 81-100, U.S. Geol. Surv., Washington D.C. .

Davis, J. C. (2002), *Statistics and Data Analysis in Geology, 3rd Edition*, John Wiley & Sons.

Delano, J. W. (1986), Pristine Lunar Glasses: Criteria, Data, and Implications, *Proc. Lunar Planet. Sci. Conf. 16th*, *16*, D201-D213.

Denevi, B. W., P. G. Lucey, E. J. Hochberg, and D. Steutel (2007), Near-infrared optical constants of pyroxene as a function of iron and calcium content, *J. Geophys. Res.*, *112*, E05009, doi:10.1029/2006/JE002802.

Denevi, B. W., P. G. Lucey, and S. B. Sherman (2008), Radiative transfer modeling of near-infrared spectra of lunar mare soils: Theory and measurement, *J. Geophys. Res.*, *113*, E02003, doi:10.1029/2007JE002929.

Dombard, A. J., and J. J. Gillis (2001), Testing the viability of topographic relaxation as a mechanism for the formation of lunar floor-fractured craters, *J. Geophys. Res.*, *106*(E11), 27,901-927,909.

Dombard, A. J., and W. B. McKinnon (2006), Elastoviscoplastic relaxation of impact crater topography with application to Ganymede and Callisto, *J. Geophys. Res.*, *111*, E01001, doi:10.1029/2005JE002445.

Drozd, R. J., C. M. Hohenberg, C. J. Morgan, and C. E. Ralston (1974), Cosmic-ray exposure history at the Apollo 16 and other lunar sites: lunar surface dynamics, *Geochim. Cosmochim. Acta*, *38*(10), 1625-1642, doi:10.1016/0016-7037(74)90178-1.

Elder, C. M., V. J. Bray, and H. J. Melosh (2012), The theoretical plausibility of central pit crater formation via melt drainage, *Icarus*, *221*, 831-843, doi:10.1016/j.icarus.2012.09.014.

Emery, J. P., D. M. Burr, and D. P. Cruikshank (2011), Near-infrared Spectroscopy of Trojan Asteroids: Evidence for Two Compositional Groups, *Astrophys. J.*, *141*, id25, doi:doi:10.1088/0004-6256/141/1/25.

Fassett, C. I. (2013), Crater Degradation of Kilometer-Sized Craters on the Lunar Maria: Initial Observations and Modeling, *Lunar Planet. Sci. Conf. 44th*, *44*, Abstract #2026.

Fassett, C. I., and J. R. Combellick (2014), The rate of crater degradation and topographic evolution on the Moon: Results from the maria and initial comparaisons with the highlands, *Lunar Planet. Sci. Conf. 45th*, *45*, Abstract #1429.

Forsberg-Taylor, N. K., and A. D. Howard (2004), Crater degradation in the Martian highlands: Morphometric analysis of the Sinus Sabaeus region and simulation modeling suggest fluvial processes, *J. Geophys. Res.*, *109*, E05002, doi:10.1029/2004JE002242.

Gaddis, L. R., B. R. Hawke, M. S. Robinson, and C. R. Coombs (2000), Compositional analyses of small lunar pyroclastic deposits using Clementine multispectral data, *J. Geophys. Res.*, *105*(E2), 4245-4262.

Gaddis, L. R., C. M. Pieters, and B. R. Hawke (1985), Remote Sensing of Lunar Pyroclastic Mantling Deposits, *Icarus*, *61*, 461-489.

Gaddis, L. R., M. I. Staid, J. A. Tyburczy, B. R. Hawke, and N. E. Petro (2003), Compositional analyses of lunar pyroclastic deposits, *Icarus*, *161*, 262-280, doi:10:1016/S0019-1035(02)00036-2.

Gallant, J., B. Gladman, and M. Ćuk (2009), Current bombardment of the Earth–Moon system: Emphasis on cratering asymmetries, *Icarus*, *202*(2), 371-382.

Ganguly, J., and M. Stimpfl (2000), Cation ordering in orthopyroxenes from two stony-iron meteorites: Implications for cooling rates and metal-silicate mixing, *Geochim. Cosmochim. Acta*, *64*(7), 1291-1297.

Gault, D. E., and J. A. Wedekind (1978), Experimental studies of oblique impact, *Proc. Lunar Planet. Sci. Conf. 9th*, *9*, 3843-3875.

Ghiorso, M. S., and R. O. Sack (1995), Chemical Mass Transfer in Magmatic Processes. IV. A Revised and Internally Consistent Thermodynamic Model for the Interpolation and Extrapolation

of Liquid-Solid Equilibria in Magmatic Systems at Elevated Temperatures and Pressures, *Contrib. Mineral. Petr.*, *119*, 197-212.

Ghose, S., and S. Hafner (1967), Mg2+-Fe2+ distribution in metamorphic and volcanic orthopyroxenes, *Z. Kristallogr.*, *125*, 157-162.

Gillis-Davis, J. J., D. T. Blewett, R. W. Gaskell, B. W. Denevi, M. S. Robinson, R. G. Strom, S. C. Solomon, and A. L. Sprague (2009), Pit-floor craters on Mercury: Evidence of near-surface igneous activity, *Earth Planet. Sci. Lett.*, *285*, 243-250.

Glotch, T. D., J. J. Hagerty, P. G. Lucey, B. R. Hawke, T. A. Giguere, J. A. Arnold, J.-P. Williams, B. L. Jolliff, and D. A. Paige (2011), The Mairan domes: Silicic volcanic constructs on the Moon, *Geophys. Res. Lett.*, *38*, L21204, doi:10.1029/2011GL049548.

Glotch, T. D., et al. (2010), Highly Silicic Compositions on the Moon, *Science*, *329*, 1510-1513.

Gold, T. (1955), The lunar surface, *Mon. Not. R. Astrono. Soc.*, *115*, 585-604.

Gomes, R., H. F. Levison, K. Tsiganis, and A. Morbidelli (2005), Origin of the cataclysmic Late Heavy Bomardment period of the terrestrial planets, *Nature*, *435*, 466-469.

Greeley, R. (1971), Lava tubes and channels in the lunar Marius Hills, *The Moon*, *3*, 289-314.

Greeley, R., J. H. Fink, D. E. Gault, and J. E. Guest (1982), Experimental Simulation of Impact Cratering on Icy Satellites, in *Satellites of Jupiter*, edited by D. Morrison, pp. 340-378, The University of Arizona Press, Tucson, AZ.

Grier, J. A., A. S. McEwen, P. G. Lucey, M. Milazzo, and R. G. Strom (2001), Optical maturity of ejecta from large rayed lunar craters, *J. Geophys. Res.*, *106*(E12), 32,847-832,862, doi:10.1029/1999JE001160.

Grieve, R. A. F., and M. J. Cintala (1992), An analysis of differential impact melt-crater scaling and implications for the terrestrial impact record, *Meteoritics*, *27*(5), 526-538, doi:10.1111/j.1945-5100.1992.tb1074.x.

Guest, J. E., and J. B. Murray (1976), Volcanic features of the nearside equatorial lunar maria, *J. Geol. Soc. London*, *132*(3), 251-258, doi:10.1144/gsjgs.132.3.0251.

Gustafson, J. O., J. F. Bell III, L. R. Gaddis, B. R. Hawke, and T. A. Giguere (2012), Characterization of previously unidentified lunar pyroclastic deposits using Lunar Reconnaissance Orbiter Camera data, *J. Geophys. Res.*, *117*, E00H25, doi:10.1029/2011JE003893.

Hagerty, J. J., D. J. Lawrence, B. R. Hawke, D. T. Vaniman, R. C. Elphic, and W. C. Feldman (2006), Refined thorium abundances for lunar red spoits: Implications for evolved, nonmare volcanism on the Moon, *J. Geophys. Res.*, *111*, E06002, doi:10.1029/2005JE002592.

Hall, J. L., S. C. Solomon, and J. W. Head (1981), Lunar floor-fractured craters: Evidence for viscous relaxation of crater topography, *J. Geophys. Res.*, *86*, 9537-9552.

Hapke, B. (1981), Bidirectional Reflectance Spectroscopy 1. Theory, *J. Geophys. Res.*, *86*(B4), 3039-3054.

Hapke, B. (1981), Bidirectional Reflectance Spectroscopy 1. Theory, *J. Geophys. Res.*, *86*(B4), 3039-3054.

Hapke, B. (1993), *Theory of Reflectance and Emittance Spectroscopy*, 469 pp., Cambridge University Press, New York.

Hapke, B. (2001), Space weathering from Mercury to the asteroid belt, *J. Geophys. Res.*, *106*(E5), 10,039-010,073, doi:10.1029/2000JE001338.

Harker, D. E., D. H. Wooden, C. E. Woodward, and C. M. Lisse (2002), Grain Properties of Comet C/1995 O1 (Hale-Bopp), *Astrophys. J.*, *580*, 579-597.

Hartmann, W. K. (1984), Does Crater "Saturation Equilibrium" Occur in the Solar System?, *Icarus*, *60*, 56-74.

Hartmann, W. K., and C. A. Wood (1971), Moon: Origin and Evolution of Multi-Ring Basins, *The Moon*, *3*, 3-78.

Haruyama, J., et al. (2012), Lunar Global Digital Terrain Model Dataset Produced from SELENE (Kaguya) Terrain Camera Stereo Observations, *Lunar Planet. Sci. Conf. 43rd*, *43*, Abstract #1200.

Haruyama, J., et al. (2009), Possible lunar lava tube skylight observed by SELENE cameras, *Geophys. Res. Lett.*, *36*, L21206, doi:10.1029/2009GL040635.

Haruyama, J., et al. (2008), Planned radiometrically calibrated and geometrically corrected products of lunar high-resolution Terrain Camera on SELENE, *Adv. Space Res.*, *42*, 310-316, doi:10.1016/j.asr.2007.04.062.

Hawke, B. R., and J. F. Bell (1981), Remote sensing studies of lunar dark-halo impact craters: Preliminary results and implications for early volcanism, *Proc. Lunar Planet. Sci. Conf. 12B*, *12*, 665-678.

Hawke, B. R., D. T. Blewett, P. G. Lucey, G. A. Smith, J. F. Bell, B. A. Campbell, and M. S. Robinson (2004), The origin of lunar crater rays, *Icarus*, *170*, 1-16, doi:10.1016/j.icarus.2004.02.013.

Hawke, B. R., and C. R. Coombs (1994), A remote sensing evaluation of lunar pyroclastic deposits, *Engineering, Construction, and Operations in SPACE IV*, 1008-1019.

Hawke, B. R., C. R. Coombs, and B. Clark (1990), Ilmenite-rich Pyroclastic Deposits: An Ideal Lunar Resource, *Proc. Lunar Planet. Sci. Conf. 20th*, *20*, 249-258.

Hawke, B. R., C. R. Coombs, L. R. Gaddis, P. G. Lucey, and P. D. Owensby (1989), Remote Sensing and Geologic Studies of Localized Dark Mantle Deposits on the Moon, *Proc. Lunar and Planet. Sci. Conf. 19th*, *19*, 255-268.

Hayne, P. O., R. R. Ghent, J. L. Bandfield, A. R. Vasavada, M. A. Siegler, B. T. Greenhagen, J.-P. Williams, and D. A. Paige (2013), Formation and evolution of the Moon's upper regolith: Constraints from Diviner Thermal Measurements, *Lunar Planet. Sci. Conf. 44th*, *44*, Abstract #3003.

Hazen, R. M., P. M. Bell, and H. K. Mao (1978), Effects of compositional variation on absorption spectra of lunar pyroxene, *Proc. Lunar and Planet. Sci. Conf. 9th*, *9*, 2919-2934.

Hazen, R. M., H. K. Mao, and P. M. Bell (1977), Effects of compositional variation on absorption spectra of lunar olivine, *Proc. Lunar and Planet. Sci. Conf. 8th*, *8*, 1081-1090.

Head, J. W. (1975), Processes of Lunar Crater Degradation Changes in Style with Geologic Time, *The Moon*, *12*, 299-329.

Head, J. W. (1976), Lunar volcanism in space and time, *Rev. Geophys.*, *14*, 265-300, doi:10.1029/RG014i002p00265.

Head, J. W. (2010), Transition from complex craters to multi-ringed basins on terrestrial planetary bodies: Scale-dependent role of the expanding melt cavity and progressive interaction with the displaced zone, *Geophys. Res. Lett.*, *37*, L02203, doi:10.1029/2009GL041790.

Head, J. W., et al. (2009), Evidence for intrusive activity on Mercury from the first MESSENGER flyby, *Earth Planet. Sci. Lett.*, *285*, 251-262.

Head, J. W., and L. Wilson (1979), Alphonsus-type dark-halo craters: Morphology, morphometry and eruption conditions, *Proc. Lunar and Planet. Sci. Conf. 10th*, *10*, 2861-2897.

Head, J. W., and L. Wilson (1979), Alphonsus-type dark-halo craters: Morphology, morphometry and eruption conditions, *Proc. Lunar and Planet. Sci. Conf. 10th*, *10*, 2861-2897.

Heiken, G. H., D. S. McKay, and R. W. Brown (1974), Lunar deposits of possible pyroclastic origin, *Geochim. Cosmochim. Acta*, *38*, 1703-1718.

Hiesinger, H., J. W. Head, U. Wolf, R. Jaumann, and G. Neukum (2003), Ages and stratigraphy of mare basalts in Oceanus Procellarum, Mare Nubium, Mare Cognitum, and Mare Insularum, *J. Geophys. Res.*, *108*(E7), 5065, doi:10.1029/2002JE001985.

Hiesinger, H., J. W. Head, U. Wolf, R. Jaumann, and G. Neukum (2010), Ages and stratigraphy of lunar mare basalts in Mare Frigoris and other nearside maria based on crater size-frequency distribution measurements, *J. Geophys. Res.*, *115*, E03003, doi:10.1029/2009JE00380.

Hiesinger, H., R. Jaumann, G. Neukum, and J. W. Head (2000), Ages of mare basalts on the lunar nearside, *J. Geophys. Res.*, *105*(E12), 29239-29275.

Hinrichs, J. L., and P. G. Lucey (2002), Temperature-Dependent Near-Infrared Spectral Properties of Minerals, Meteorites, and Lunar Soil, *Icarus*, *155*, 169-180, doi:10.1006/icar.2001.6754.

Hiroi, T., and C. M. Pieters (1994), Estimation of grain sizes and mixing ratios of fine powder mixtures of common geologic materials, *J. Geophys. Res.*, *99*, 10,867-810,879.

Hiroi, T., C. M. Pieters, F. Vilas, S. Sasaki, Y. Hamabe, and E. Kurahashi (2001), The mystery of 506.5 nm feature of reflectance spectra of Vesta and Vestoids: Evidence for space weathering?, *Earth Planet. Sci. Lett.*, *53*, 1071-1075.

Hodges, C. A. (1978), Central Pit Craters on Mars, *Lunar and Planetary Science IX*, *9*, 521-522.

Howard, K. A. (1973), Avalanche Mode of Motion: Implications from Lunar Examples, *Science*, *180*, 1052-1055.

Huggins, F. E. (1973), Cation Order in Olivines: Evidence From Vibrational Spectra, *Chem. Geol.*, *11*, 99-109.

Huguenin, R. L., and J. L. Jones (1986), Intelligent Information Extraction From Reflectance Spectra: Absorption Band Positions, *J. Geophys. Res.*, *91*(B9), 9585-9598.

Hunt, G. R., J. W. Salisbury, and C. J. Lenhoff (1973), Visible and near-infrared spectra of minerals and rocks: VI. Additional silicates, *Modern Geology*, *4*, 85-106.

Isaacson, P. J., and C. M. Pieters (2010), Deconvolution of lunar olivine reflectance spectra: Implications for remote compositional assessment, *Icarus*, *210*(1), 8-13.

Jolliff, B. L., J. J. Gillis, L. A. Haskin, R. L. Korotev, and M. A. Wieczorek (2000), Major lunar crustal terranes: Surface expressions and crust-mantle origins, *J. Geophys. Res.*, *105*(E2), 4197-4216.

Jolliff, B. L., C. K. Shearer, D. A. Papanastassiou, L. Alkalai, and M. Team (2010), MoonRise: South Pole-Aitken Basin Sample Return Mission for Solar System Science, *Annual LEAG Meeting*, Abstract #3072.

Jolliff, B. L., et al. (2011), Non-mare silicic volcanism on the lunar farside at Compton-Belkovich, *Nat. Geosci.*, *4*, 566-571.

Jozwiak, L. M., J. W. Head, M. T. Zuber, D. E. Smith, and G. A. Neumann (2012), Lunar floor-fractured craters: Classification, distribution, origin and implications for magmatism and shallow crustal structure, *J. Geophys. Res.*, *117*, E11005, doi:10.1029/2012JE004134.

King, T. V. V., and W. I. Ridley (1987), Relation of the Spectrscopic Reflectance of Olivine to Mineral Chemistry and Some Remote Sensing Implications, *J. Geophys. Res.*, *92*(B11), 11,457-411,469.

Klima, R. L., M. D. Dyar, and C. M. Pieters (2011), Near-infrared spectra of clinopyroxenes: Effects of calcium content and crystal structure, *Meteorit. Planet. Sci.*, *46*(3), 379-395.

Klima, R. L., C. M. Pieters, and M. D. Dyar (2007), Spectroscopy of synthetic Mg-Fe pyroxenes I: Spin-allowed and spin-forbidden crystal field bands in the visible and near-infrared, *Meteorit. Planet. Sci.*, *42*(2), 235-253.

Kneissl, T., S. van Gasselt, and G. Neukum (2011), Map-projection-independent crater size-frequency determination in GIS environments - New software tool for ArcGIS, *Planet. Space Sci.*, *59*(11-12), 1243-1254.

Lawrence, S. J., and P. G. Lucey (2007), Radiative transfer mixing models of meteoritic assemblages, *J. Geophys. Res.*, *112*, E07005, doi:10.1029/2006JE002765.

Levison, H. F., L. Dones, C. R. Chapman, and S. A. Stern (2001), Could the Lunar "Late Heavy Bombardment" Have Been Triggered by the Formation of Uranus and Neptune?, *Icarus*, *151*, 286-306.

Lindsay, J. F. (1976), Energy at the Lunar Surface, in *Lunar Stratigraphy and Sedimentology*, edited by Z. Kopal and A. G. W. Cameron, pp. 19-64, Elsevier Scientific Publishing Company, Amsterdam.

Longhi, J. (1991), Comparative liquidus equilibria of hypersthene-normative basalts at low pressure, *Am. Mineral.*, *76*, 785-800.

Lucey, P. G. (1998), Model near-infrared optical constants of olivine and pyroxene as a function of iron content, *J. Geophys. Res.*, *103*(E1), 1703-1713, doi:10.1029/97JE03145.

Lucey, P. G. (2004), Mineral maps of the Moon, *Geophys. Res. Lett.*, *31*, L08701, doi:10.1029/2003GL019406.

Lucey, P. G., D. T. Blewett, and B. L. Jolliff (2000b), Lunar iron and titanium abundance algorithms based on final processing of Clementine ultraviolet-visible images, *J. Geophys. Res.*, *105*(E8), 20297-20305, doi:10.1029/1999JE001117.

Lucey, P. G., D. T. Blewett, G. J. Taylor, and B. R. Hawke (2000b), Imaging of lunar surface maturity, *J. Geophys. Res.*, *105*(E8), 20377-20386.

Lucey, P. G., B. R. Hawke, C. M. Pieters, J. W. Head, and T. B. McCord (1986), A Compositional Study of the Aristarchus Region of the Moon Using Near-Infrared Reflectance Spectroscopy, *Proc. Lunar and Planet. Sci. Conf. 16th*, *16*, D344-D354.

Lucey, P. G., J. A. Norman, S. T. Crites, G. J. Taylor, B. R. Hawke, and M. Lemelin (2014), A large spectral survey of small lunar craters: Implications for the composition of the lunar mantle, *Am. Mineral.*, *In Press*.

Lucey, P. G., J. A. Norman, S. T. Crites, G. J. Taylor, B. R. Hawke, and M. Lemelin (In Press), A large spectral survey of small lunar craters: Implications for the composition of the lunar mantle, *Am. Mineral.*

Lucey, P. G., and M. A. Riner (2011), The optical effects of small iron particles that darken but do not redden: Evidence of intense space weathering on Mercury, *Icarus*, *212*(2), 451-462.

Markwardt, C. B. (2009), Non-Linear Least Squares Fitting in IDL with MPFIT, paper presented at Astronomical Data Analysis Software and Systems XVIII, Astronomical Society of the Pacific, Québec City, QC, Canada.

McCallister, R. H., L. W. Finger, and Y. Ohashi (1976), Intracrystalline Fe2+-Mg equilibria in three natural Ca-rich clinopyroxenes, *Am. Mineral.*, *61*, 671-676.

McCord, T. B., R. N. Clark, B. R. Hawke, L. A. McFadden, P. D. Owensby, C. M. Pieters, and J. B. Adams (1981), Moon: Near-Infrared Spectral Reflectance, A First Good Look, *J. Geophys. Res.*, *86*(B11), 10883-10892.

McCord, T. B., and M. J. Gaffey (1974), Asteroids: Surface Composition from Reflection Spectroscopy, *Science*, *186*(4161), 352-355, doi:10.1126/science.186.4161.352.

McCord, T. B., and T. V. Johnson (1970), Lunar Spectral Reflectivity (0.30 to 2.50 Microns) and Implications for Remote Mineralogical Analysis, *Science*, *169*(3948), 855-858, doi:10.1126/science.169.3948.855.

McGetchin, T. R., and J. W. Head (1973), Lunar Cinder Cones, *Science*, *108*(4081), 68-71.

McKay, D. S., G. Heiken, A. Basu, G. Blanford, S. Simon, R. Reedy, B. M. French, and J. Papike (1991), The Lunar Regolith, in *Lunar Sourcebook A User's Guide to the Moon*, edited by G. H. Heiken, D. T. Vaniman and B. M. French, Cambridge University Press.

Melosh, H. J. (1982), A schematic model of crater modification by gravity, *J. Geophys. Res.*, *87*(B1), 371-380, doi:10.1029/JB087iB01p00371.

Melosh, H. J. (1989), *Impact cratering: a geologic process*, Oxford University Press, Inc., New York, NY.

Melosh, H. J., and E. A. Whitaker (1994), Lunar crater chains, *Nature*, *369*, 713-714, doi:10.1038/369713a0.

Meyer, C., D. S. McKay, D. H. Anderson, and P. Butler (1975), The source of sublimates on the Apollo 15 green and Apollo 17 orange glass samples, *Proc. Lunar Sci. Conf. 6th*, *6*, 1673-1699.

Michael, G. G., and G. Neukum (2010), Planetary surface dating from crater size-frequency distribution measurements: Partial resurfacing events and statistical age uncertainty, *Earth Planet. Sci. Lett.*, *294*, 223-229.

Molster, F. J., and L. B. F. M. Waters (2003), The Mineralogy of Interstellar and Circumstellar Dust, in *Astromineralogy*, edited by T. K. Henning, pp. 121-170, Springer Berlin / Heidelberg.

Neukum, G., B. A. Ivanov, and W. K. Hartmann (2001), Cratering Records in the Inner Solar System in Relation to the Lunar Reference System, *Space Sci. Rev.*, *96*, 55-86, doi:10.1023/A:1011989004263.

Nozette, S., C. L. Lichtenberg, P. Spudis, R. Bonner, W. Ort, E. Malaret, M. Robinson, and E. M. Shoemaker (1996), The Clementine Bistatic Radar Experiment, *Science*, *274*, 1495-1498.

Nozette, S., et al. (2010), The Lunar Reconnaissance Orbiter Miniature Radio Frequency (Mini-RF) Technology Demonstration, *Space Sci. Rev.*, *150*, 285-302, doi:10.1007/s11214-009-9607-5.

Oberbeck, V. R. (1973), Simulatneous impact and lunar craters, *The Moon*, *6*, 83-92.

Oberbeck, V. R. (1975), The Role of Ballistic Erosion and Sedimentation in Lunar Statigraphy, *Rev. Geophys. Space Ge*, *13*(2), 337-362, doi:10.1029/RG013i002p00337.

Offield, T. W., and H. A. Pohn (1970), Lunar Crater Morphology and Relative-Age Determination of Lunar Geologic Units-Part 2, Applications, *U.S. Geol. Survey Prof. Paper*, *700-C*, C163-C169.

Ohtake, M., J. Haruyama, T. Matsunaga, Y. Yokota, T. Morota, C. Honda, and L. team (2008), Performance and scientific objectives of the SELENE (KAGUYA) Multiband Imager, *Earth Planets Space*, *60*, 257-264.

Ormö, J., A. P. Rossi, and K. R. Housen (2013), A new method to determine the direction of impact: Asymmetry of concentric impact craters as observed in the field (Lockne), on Mars, in experiments, and simulations, *Meteorit. Planet. Sci.*, *48*(3), 403-419, doi:10.1111/maps.12065.

Ostrach, L. R., M. S. Robinson, B. W. Denevi, and P. C. Thomas (2011), Effects of Incidence Angle on Crater Counting Observations, *Lunar Planet. Sci. Conf. 42nd*, *42*, Abstract #1608.

Ottonello, G., F. Princivalle, and A. Della Giusta (1990), Temperature, Composition, and fO2 Effects on Intersite Distribution of Mg and Fe2+ in Olivines, *Phys. Chem. Miner.*, *17*, 301-312.

Paige, D. A., et al. (2010), The Lunar Reconnaissance Orbiter Diviner Lunar Radiometer Experiment, *Space Sci. Rev.*, *150*, 125-160, doi:10.1007/s11214-009-9529-2.

Parmentier, E. M., and J. W. Head (1981), Viscous Relaxation of Impact Craters on Icy Planetary Surfaces: Determination of Viscosity Variation with Depth, *Icarus*, *47*, 100-111.

Pasqual, D., G. Molin, and M. Tribaudino (2000), Single-crystal thermometric calibration of Fe-Mg order-disorder in pigeonites, *Am. Mineral.*, *85*, 953-962.

Passey, Q. R., and E. M. Shoemaker (1982), Craters and basins on Ganymede and Callisto: Morphological indicators of crustal evolution, in *Satellites of Jupiter*, edited by D. Morrison, pp. 379-434, The University of Arizona Press, Tucson, AZ.

Pieters, C. M. (1978), Mare basalt types on the front side of the moon: A summary of spectral reflectance data, *Proc. Lunar Planet. Sci. Conf. 9th*, *9*, 2825-2849.

Pieters, C. M. (1982), Copernicus Crater Central Peak: Lunar Mountain of Unique Composition, *Science*, *215*(4528), 59-61, doi:10.1126/science.215.4528.59.

Pieters, C. M. (1983), Strength of Mineral Absorption Features in the Transmitted Component of Near-Infrared Reflected Light: First Results From RELAB, *J. Geophys. Res.*, *88*(B11), 9534-9544, doi:10.1029/JB088iB11p09534

Pieters, C. M. (1986), Composition of the Lunar Highland Crust From Near-Infrared Spectroscopy, *Rev. Geophys.*, *24*(3), 557-578.

Pieters, C. M., et al. (2011), Mg-spinel lithology: A new rock type on the lunar farside, *J. Geophys. Res.*, *116*, E00G08, doi:10.1029/2010JE003727.

Pieters, C. M., and T. B. McCord (1973), Lunar Black Spots and Nature of the Apollo 17 Landing Area, *J. Geophys. Res.*, *78*(26), 5867-5875.

Pieters, C. M., M. I. Staid, E. M. Fischer, S. Tompkins, and G. He (1994), A Sharper View of Impact Craters from Clementine Data, *Science*, *266*, 1844-1848.

Pike, R. J. (1971), Some Preliminary Interpretations of Lunar Mass-Wasting Processes from Apollo 10 Photography, in *Analysis of Apollo 10 Photography and Visual Observations*, edited, Washington D.C.

Pike, R. J. (1974), Depth/Diameter relations of fresh lunar craters: Revisions from spacecraft data, *Geophys. Res. Lett.*, *1*(7), 291-294.

Pike, R. J. (1976), Crater Dimensions From Apollo Data and Supplemental Sources, *The Moon*, *15*, 463-477.

Pike, R. J. (1980), Geometric Interpretation of Lunar Craters, *U.S. Geol. Survey Prof. Paper*, *1046-C*, C1-C77.

Pohn, H. A., and T. W. Offield (1969), Lunar Crater Morphology and Relative Age Determination of Lunar Geologic Units, in *Interagency Report: Astrogeology 13*, edited, pp. 1-35.

Pohn, H. A., and T. W. Offield (1970), Lunar crater morphology and relative age determination of lunar geologic units - Part 1, Classification, *U.S. Geol. Survey Prof. Paper*, *700-C*, C153-C162.

Princivalle, F. (1990), Influrence of Temperature and Composition on Mg-Fe2+ Intracrystalline Distribution in Olivines, *Miner. Petrol.*, *43*, 121-129.

Princivalle, F., and L. Secco (1985), Crystal Structure Refinement of 13 Olivines in the Forsterite-Fayalite Series from Volcanic Rocks and Ultramafic Nodules, *Tschermaks Mineralogische und Petrographische Mitteilungen*, *34*, 105-115.

Quaide, W. L., D. E. Gault, and R. A. Schmidt (1965), Gravitative Effects on Lunar Impact Structures, *Ann. NY Acad. Sci.*, *123*, 563-572.

Quaide, W. L., and V. R. Oberbeck (1968), Thickness Determinations of the Lunar Surface Layer from Lunar Impact Craters, *J. Geophys. Res.*, *73*(16), 5247-5270.

Raney, R. K. (2007), Hybrid-Polarity SAR Architecture, *IEEE T. Geosci. Remote.*, *45*(11), 3397-3404, doi:10.1109/TGRS.2007.895883.

Redfern, S. A. T., G. Artioli, R. Rinaldi, C. M. B. Henderson, K. S. Knight, and B. J. Wood (2000), Octahedral cation ordering in olivine at high temperature. II: an in situ neutron powder diffraction study on synthetic MgFeSiO4 (Fa50), *Phys. Chem. Miner.*, *27*, 630-637.

Rinaldi, R., G. Artioli, C. C. Wilson, and G. McIntyre (2000), Octahedral cation ordering in olivine at high temperature. I: in situ neutron single-crystal diffraction studies on natural mantle olivines (Fa12 and Fa10), *Phys. Chem. Miner.*, *27*, 623-629.

Robbins, S. J. (2013), Revised lunar cratering chronology for planetary geological histories, *Lunar Planet. Sci. Conf. 44th*, *44*, Abstract #1619.

Robbins, S. J., et al. (2014), The variability of crater identification among expert and community crater analysts, *Icarus*, *234*, 109-131, doi:10.1016/j.icarus.2014.02.022.

Robinson, M. S., et al. (2010), Lunar Reconnaissance Orbiter Camera (LROC) Instrument Overview, *Space Sci. Rev.*, *105*(1-4), 81-124, doi:10.1007/s11214-010-9634-2.

Roush, T. L., and R. B. Singer (1986), Gaussian Analysis of Temperature Effects on the Reflectance Spectra of Mafic Minerals in the 1-μm Region, *J. Geophys. Res.*, *91*(B10), 10,301-310,308.

Salisbury, J. W., L. W. Walter, and N. Vergo (1987), Mid-Infrared (2.1-25μm) Spectra of Minerals: First Edition, *U.S. Geological Survey Open File Report 87-263*.

Schaber, G. G. (1973), Lava flows in Mare Imbrium: Gelogic evaluation from Apollo orbital photography, *Proc. Lunar Sci. Conf. 4th*, *1*, 73-82.

Schaber, G. G., J. M. Boyce, and H. J. Moore (1976), The scarcity of mappable flow lobes on the lunar maria: Unique morphology of the Imbrium flows, *Proc. Lunar Sci. Conf. 7th*, *7*, 2783-2800.

Schenk, P. M. (1993), Central Pit and Dome Craters: Exposing the Interiors of Ganymede and Callisto, *J. Geophys. Res.*, *98*(E4), 7475-7498.

Scholten, F., J. Oberst, K.-D. Matz, T. Roatsch, M. Wählisch, E. J. Speyerer, and M. S. Robinson (2012), GLD100: The near-global lunar 100 m raster DTM from LROC WAC stereo image data, *J. Geophys. Res.*, *117*, E00H17, doi:10.1029/2011JE003926.

Schultz, P. H. (1976a), Floor-Fractured Lunar Craters, *The Moon*, *15*, 241-273.

Schultz, P. H. (1976b), *Moon morphology: Interpretations based on Lunar Orbiter photography*, 626 pp., University of Texas Press, Austin, Texas.

Schultz, P. H., and D. E. Gault (1975), Seismic Effects from Major Basin Formations on the Moon and Mercury, *The Moon*, *12*, 159-177.

Schultz, P. H., and D. E. Gault (1985), Clustered Impacts: Experiments and Implications, *J. Geophys. Res.*, *90*(B5), 3701-3732.

Schultz, P. H., and P. D. Spudis (1979), Evidence for ancient mare volcanism, *Proc. Lunar Planet. Sci. Conf. 10th*, *10*, 2899-2918.

Scott, R. F. (1967), Viscous Flow of Craters, *Icarus*, *7*, 139-148.

Sekiguchi, N. (1970), On the Fissions of a Solid Body Under Infuence of Tidal Force; with Application to the Problem of Twin Craters on the Moon, *The Moon*, *1*, 429-439.

Settle, M., and J. W. Head (1979), The Role of Rim Slumping in the Modification of Lunar Impact Craters, *J. Geophys. Res.*, *84*(B6), 3081-3096.

Shoemaker, E. M., and R. J. Hackman (1962), Stratigraphic Basis for a Lunar Time Scale, in *The Moon*, edited by Z. Kopal and Z. K. Mikhailov, pp. 289-300, Academic Press.

Singer, R. B., and T. L. Roush (1985), Effects of Temperature on Remotely Sensed Mineral Absorption Features, *J. Geophys. Res.*, *90*(B14), 12,434-412,444.

Smith, D. E., et al. (2010), The Lunar Orbiter Laser Altimeter Investigation on the Lunar Reconnaissance Orbiter Mission, *Space Sci. Rev.*, *150*, 209-241, doi:10.1007/s11214-009-9512-y.

Smith, E. I. (1973), Identification, Distribution and Significance of Lunar Volcanic Domes, *The Moon*, *6*, 3-31.

Soderblom, L. A. (1970), A Model for Small-Impact Erosion Applied to the Lunar Surface, *J. Geophys. Res.*, *75*(14), 2655-2661, doi:10.1029/JB075i014p02655.

Soderblom, L. A., and L. A. Lebofsky (1972), Technique for Rapid Determination of Relative Ages of Lunar Areas from Orbital Photography, *J. Geophys. Res.*, *77*(2), 279-296.

Stimpfl, M., J. Ganguly, and G. Molin (1999), Fe2+-Mg order-disorder in orthopyroxene: equilibrium fractionation between the octahedral sites and thermodynamic analysis, *Contrib. Mineral. Petr.*, *136*, 297-309.

Stopar, J. D., B. R. Hawke, M. S. Robinson, B. W. Denevi, T. A. Giguere, and S. D. Koeber (2014), Occurrence and mechanisms of impact melt emplacement at small lunar craters, *Icarus*, *243*, 337-357, doi:10.1016/j.icarus.2014.08.011.

Sunshine, J. M., et al. (2010), Hidden in Plain Sight: Spinel-rich Deposits on the Nearside of the Moon as Revealed by Moon Mineralogy Mapper (M3), *Lunar Planet. Sci. Conf. 41st*, *41*, Abstract #1533.

Sunshine, J. M., and C. M. Pieters (1993), Estimating Modal Abundances From the Spectra of Natural and Laboratory Pyroxene Mixtures Using the Modified Gaussian Model, *J. Geophys. Res.*, *98*(E5), 9075-9087.

Sunshine, J. M., and C. M. Pieters (1998), Determining the composition of olivine from reflectance spectrscopy, *J. Geophys. Res.*, *103*(E6), 13,675-613,688.

Sunshine, J. M., C. M. Pieters, and S. F. Pratt (1990), Deconvolution of Mineral Absorption Bands: An Improved Approach, *J. Geophys. Res.*, *95*(B5), 6955-6966.

Swann, G. A., and V. S. Reed (1974), A method for estimating the absolute ages of small Copernican craters and its application to the determination of Copernican meteorite flux, *Proc. Lunar Sci. Conf. 5th*, *5*, 151-158.

Tera, F., D. A. Papanastassiou, and G. J. Wasserburg (1974), Isotopic evidence for a terminal lunar cataclysm, *Earth Planet. Sci. Lett.*, *22*(1), 1-21.

Thompson, T. W., S. H. Zisk, R. W. Shorthill, P. H. Schultz, and J. A. Cutts (1981), Lunar Craters with Radar Bright Ejecta, *Icarus*, *46*, 201-225.

Thomson, B. J., D. B. J. Bussey, J. T. S. Cahill, C. D. Neish, R. K. Raney, and D. Trang (2013), Global Distribution of Radar-Bright Halos on the Moon Detected by LRO Mini-RF, *Lunar Planet. Sci. Conf. 44th*, *44*, Abstract #2107.

Thomson, B. J., E. B. Grosfils, D. B. J. Bussey, and P. D. Spudis (2009), A new technique for estimating the thickness of mare basalts in Imbrium Basin, *Geophys. Res. Lett.*, *36*, L12201, doi:10.1029/2009GL037600.

Titley, S. R. (1966), Seismic energy as an agent of morphologic modification on the Moon, in *Astrogeologic Studies Annual Progress Report - Part A*, edited, pp. 87-103, United States Geological Survey.

Trang, D., J. J. Gillis-Davis, and J. M. Boyce (accepted), Absolute Model Ages to Crater Degradation, *J. Geophys. Res.*

Trang, D., P. G. Lucey, and J. J. Gillis-Davis (2011), The Optical Constants of Olivine in the Near-Infrared as a Function of Iron Content, *Lunar Planet. Sci. Conf. 42nd*, *42*, Abstract #2745.

Trask, N. J. (1971), Geologic comparison of mare materials in the lunar equatorial belt, including Apollo 11 and Apollo 12 landing sites, *U.S. Geol. Survey Prof. Paper*, *750-D*, D138-D144.

Turnock, A. C., D. H. Lindsley, and J. E. Grover (1973), Sythesis and Unit Cell Parameters of Ca-Mg-Fe Pyroxenes, *Am. Mineral.*, *58*, 50-59.

van der Bogert, C. H., H. Hiesinger, A. S. McEwen, C. Dundas, V. Bray, M. S. Robinson, and J. B. Plescia (2010), Discrepancies between crater size-frequency distributions on ejecta and impact melt pools at lunar craters: An effect of different target properties?, *Lunar Planet. Sci. Conf. 41st*, *41*, Abstract #2165.

Virgo, D., and S. S. Hafner (1970), Fe2+,Mg Order-Disorder in Natural Orthopyroxenes, *Am. Mineral.*, *55*, 201-223.

Walker, G. P. L., L. Wilson, and E. L. G. Bowell (1971), Explosive Volcanic Eruptions-I the Rate of Fall of Pyroclasts, *Geophys. J. Roy. Astr. S.*, *22*, 377-383.

Weitz, C. M., J. W. Head, and C. M. Pieters (1998), Lunar regional dark mantle deposits: Geologic, multispectral, and modeling studies, *J. Geophys. Res.*, *103*(E10), 22725-22759.

Werner, S. C., and S. Medvedev (2010), The Lunar rayed-crater population - Characteristics of the spatial distribution and ray retention, *Earth Planet. Sci. Lett.*, *295*, 147-158, doi:10:1016/j.epsl.2010.03.036.

Wichman, R. W., and P. H. Schultz (1995), Floor-fractured craters in Mare Smythii and west of Oceanus Procellarum: Implications of crater modification by viscous relaxation and igneous intrusion models, *J. Geophys. Res.*, *100*(E10), 21,201-221,218, doi:10.1029/95JE02297.

Wichman, R. W., and P. H. Schultz (1996), Crater-Centered Laccoliths on the Moon: Modeling Intrusion Depth and Magmatic Pressure at the Crater Taruntius, *Icarus*, *122*, 193-199.

Wilcox, B. B. (2005), Constraints on the depth and variability of the lunar regolith, *Meteorit. Planet. Sci.*, *40*(5), 695-710, doi:10.1111/j.1945-5100.2005.tb00974.x.

Wilcox, B. B., P. G. Lucey, and B. R. Hawke (2006), Radiative transfer modeling of compositions of lunar pyroclastic deposits, *J. Geophys. Res.*, *111*, E09001, doi:10.1029/2006JE002686.

Wilcox, B. B., P. G. Lucey, and B. R. Hawke (2006), Radiative transfer modeling of compostions of lunar pyroclastic deposits, *J. Geophys. Res.*, *111*, E09001, doi:10.1029/2006JE002686.

Wilhelms, D. E. (1987), The Geologic History of the Moon, *U.S. Geol. Survey Prof. Paper*, *1348*.

Williams, K. K., and M. T. Zuber (1998), Measurement and Analysis of Lunar Basin Depths from Clementine Altimetry, *Icarus*, *131*, 107-122, doi:10.1006/icar.1997.5856.

Wöhler, C., R. Lena, and G. L. R. G. Group (2009), Lunar intrusive domes: Morphometric analysis and laccolith modelling, *Icarus*, *204*(2), 381-398, doi:10.1016/j.icarus.2009.07.031.

Wood, C. A. (1978), Lunar Concentric Craters, *Lunar Planet. Sci. Conf. 9th*, *9*, 1264-1266.

Wood, C. A., and L. Andersson (1978), New morphometric data for fresh lunar craters, *Proc. Lunar Planet. Sci. Conf. 9th*, *9*, 3669-3689.

Wood, C. A., J. W. Head, and M. J. Cintala (1978), Interior morphology of fresh martian craters: The effects of target characteristics, *Proc. Lunar Planet. Sci. Conf. 9th*, *9*, 3691-3709.

Wooden, D. H., D. E. Harker, C. E. Woodward, H. M. Butner, C. Koike, F. C. Witteborn, and C. W. McMurtry (1999), Silicate Mineralogy of the Dust in the Inner Coma of Comet C/1995 01 (Hale-Bopp) Pre- and Postperihelion *Astrophys. J.*, *517*(2), 1034-1058, doi:10.1086/307206.

Xiao, Z., Z. Zeng, N. Ding, and J. Molaro (2013), Mass wasting features on the Moon - how active is the lunar surface?, *Earth Planet. Sci. Lett.*, *376*, 1-11, doi:10.1016/j.epsl.2013.06.015.

Yamamoto, S., et al. (2013), A new type of pyroclastic deposit on the Moon containing Fe-spinel and chromite, *Geophys. Res. Lett.*, *40*, 4549-4554, doi:10.1002/grl.50784.

Young, R. A. (1972), Lunar volcanism: Fracture patterns and rilles in marginal premare craters, in *Apollo 16 Preliminary Science Report, NASA Spec. Publ.*, edited, pp. 29-89-29-90.

Young, R. A. (1975), Mare crater size-frequency distributions: Implications for relative surface ages and regolith development, *Proc. Lunar Sci. Conf. 6th*, *6*, 2645-2662.

Zanetti, M., A. Stadermann, T. Krüger, C. van der Bogert, H. Hiesinger, and B. L. Jolliff (2014), Mapping crater density variation on copernican ejecta blankets: Evidence for auto-secondary cratering at Tycho and Aristarchus, *Lunar Planet. Sci. Conf. 45th*, *45*, Abstract #1528.

Zuber, M. T., D. E. Smith, F. G. Lemoine, and G. A. Neumann (1994), The Shape and Internal Structure of the Moon from the Clementine Mission, *Science*, *266*, 1839-1843.